Indirect Dark Matter Search with Neutrinos in JUNO and THEIA
-
A Sensitivity Study

Dissertation

der Mathematisch-Naturwissenschaftlichen Fakultät
der Eberhard Karls Universität Tübingen
zur Erlangung des Grades eines
Doktors der Naturwissenschaften
(Dr. rer. nat.)

vorgelegt von
David Samuel Blum
aus Tübingen

Tübingen
2022

Gedruckt mit Genehmigung der Mathematisch-Naturwissenschaftlichen
Fakultät der Eberhard Karls Universität Tübingen.

Tag der mündlichen Qualifikation:	26.04.2022
Dekan:	Prof. Dr. Thilo Stehle
1. Berichterstatter:	Prof. Dr. Tobias Lachenmaier
2. Berichterstatter:	Prof. Dr. Josef Jochum

Abstract

Extensive evidence from various astrophysical observations suggests that most of the matter in the universe is dark matter. However, the nature of dark matter is still unknown and remains one of the most prominent unanswered questions in physics today. A potential way to search for dark matter is the indirect dark matter search with neutrinos. It is based on the hypothesis that dark matter particles self-annihilate into neutrinos. This would result in a neutrino flux, which could be measured by neutrino detectors at Earth. In case of no excess signal is observed, a limit on the dark matter self-annihilation cross section can be set. The future neutrino detectors JUNO and THEIA can search for dark matter, especially for light dark matter particles with masses ranging from MeV to GeV. The search for such light dark matter particles has gained in importance in the last years as it extends the typical WIMP search to the sub-GeV mass range.
In this work, the sensitivities of JUNO and THEIA to measure neutrinos from dark matter self-annihilation in the Milky Way as an excess over backgrounds are determined in detail for the first time. The work focuses on direct self-annihilation of light dark matter particles with masses ranging from 15 MeV to 100 MeV into neutrino-antineutrino pairs. The expected electron antineutrino signal measured through the inverse β decay (IBD) reaction and all background contributions occurring in the visible energy region from 10 MeV to 100 MeV are determined for both detectors. To effectively reduce IBD-like background events of atmospheric neutrinos interacting via neutral current and of fast neutrons in JUNO, pulse shape discrimination is studied and applied in this work. THEIA would feature the separate measurement of Cherenkov and scintillation light. As a consequence, selection cuts on the ratio of measured Cherenkov to scintillation light and on the number of reconstructed Cherenkov rings are determined in this work, which can suppress atmospheric neutral current and fast neutron background events in THEIA with high efficiency.
The sensitivities of JUNO and THEIA are determined using a Bayesian analysis and Markov Chain Monte Carlo sampling for dark matter masses ranging from 15 MeV to 100 MeV. JUNO will achieve the highest sensitivity for indirect dark matter search with neutrinos among existing neutrino detectors and will take a leading role in the indirect dark matter search in the upcoming years. The results of this work show for the first time that JUNO will improve the best currently existing 90 % C.L. upper limit of neutrino detectors on the dark matter self-annihilation cross section by a factor of 2 to 9 for 10 years of data taking. JUNO's potential to discover an electron antineutrino signal from dark matter self-annihilation in the Milky Way as an excess over backgrounds will be between 3σ and 5σ for most dark matter masses from 15 MeV to 100 MeV assuming an annihilation cross section that corresponds to the 90 % C.L. upper limit on the annihilation cross section of Super-K. This work moreover demonstrates that THEIA, if realized, could achieve a sensitivity comparable to JUNO.

Zusammenfassung

Zahlreiche astrophysikalische Beobachtungen weisen darauf hin, dass der größte Teil der Materie im Universum in Form von Dunkler Materie vorliegt. Die Natur der Dunklen Materie ist jedoch bis heute unbekannt und stellt eine der bedeutendsten Fragen der Physik dar. Ein möglicher Ansatz das Rätsel über die Dunkle Materie zu lösen ist die indirekte Suche nach Dunkler Materie mit Neutrinos. Diese basiert auf der Hypothese, dass Dunkle Materie in Neutrinos annihiliert. Ein daraus resultierender Neutrinofluss könnte von Neutrinodetektoren auf der Erde gemessen werden. Falls kein Signal beobachtet wird, kann eine Obergrenze für den Annihilations-Wirkungsquerschnitt der Dunklen Materie bestimmt werden. Die zukünftigen Neutrinodetektoren JUNO und THEIA können nach Dunkler Materie, insbesondere nach leichter Dunkler Materie mit einer Masse im Bereich von MeV bis GeV, suchen. Die Suche nach leichter Dunkler Materie wurde in den letzten Jahren immer bedeutsamer, da sie die übliche Suche nach WIMPs auf den Massenbereich zwischen MeV und GeV erweitert.
In dieser Arbeit werden zum ersten Mal die Sensitivitäten von JUNO und THEIA für die indirekte Suche nach Dunkler Materie bestimmt. Dabei wird nach einem Überschuss an Neutrinos, welche durch Selbstannihilation von Dunkler Materie in der Milchstraße erzeugt werden, gegenüber Untergrundereignissen gesucht. Der Fokus dieser Arbeit liegt auf der direkten Annihilation von leichter Dunkler Materie mit einer Masse zwischen 15 MeV und 100 MeV in Neutrino-Antineutrino Paare. Das zu erwartende Signal der Elektron-Antineutrinos, welche durch den inversen β-Zerfall (IBD) gemessen werden, und alle Untergrundbeiträge, die im sichtbaren Energiebereich von 10 MeV bis 100 MeV auftreten, werden für beide Detektoren bestimmt. Um Untergrundereignisse schneller Neutronen und atmosphärischer Neutrinos, die über den neutralen Strom (NC) wechselwirken, sehr effektiv reduzieren zu können, wird im Rahmen dieser Arbeit die Pulsformunterscheidung in JUNO untersucht und angewendet. THEIA könnte in Zukunft realisiert werden und würde sich dadurch auszeichnen, dass Cherenkov- und Szintillationslicht getrennt voneinander gemessen werden können. In dieser Arbeit werden Auswahlkriterien auf das Verhältnis von gemessenem Cherenkov- zu Szintillationslicht und auf die Anzahl der rekonstruierten Cherenkov Ringe bestimmt, wodurch Untergrundereignisse atmosphärischer NC Wechselwirkungen und schneller Neutronen in THEIA mit großer Effizienz reduziert werden können.
Die Sensitivitäten von JUNO und THEIA werden basierend auf einer bayesschen Analyse mit Markov Chain Monte Carlo Sampling für Massen der Dunklen Materie von 15 MeV bis 100 MeV bestimmt. JUNO wird die höchste Sensitivität für die indirekte Suche nach Dunkler Materie mit Neutrinos unter den derzeit existierenden Neutrinodetektoren erreichen und in den kommenden Jahren eine führende Rolle bei der indirekten Suche nach Dunkler Materie einnehmen. Die Ergebnisse dieser Arbeit zeigen zum ersten Mal, dass JUNO die beste derzeit existierende Obergrenze von Neutrinodetektoren auf den Annihilations-Wirkungsquerschnitt der Dunklen Materie nach einer Laufzeit von 10 Jahren um den Faktor 2 bis 9 verbessern wird. Das Entdeckungspotenzial JUNOs für ein Signal von Elektron-Antineutrinos aus der Annihilation Dunkler Materie wird für die meisten untersuchten Massen im Bereich zwischen 3σ und 5σ liegen, wenn die 90 % C.L. Obergrenze des Annihilations-Wirkungsquerschnitts von Super-Kamiokande angenommen wird. Diese Arbeit zeigt außerdem, dass THEIA, wenn es realisiert wird, eine mit JUNO vergleichbare Sensitivität erreichen könnte.

Contents

Abstract iii

Zusammenfassung iv

1. Introduction 1

2. Dark Matter 3
2.1. Evidence for Dark Matter . . . 3
2.2. Dark Matter Models and Candidates . . . 6
2.3. Dark Matter Detection Techniques . . . 7
2.3.1. Direct Dark Matter Search . . . 7
2.3.2. Dark Matter Search at the Large Hadron Collider . . . 9
2.3.3. Indirect Dark Matter Search . . . 11
2.4. Indirect Dark Matter Search with Neutrinos . . . 13
2.4.1. Dark Matter with Mass above 1 GeV . . . 13
2.4.2. Dark Matter with Mass below 1 GeV . . . 14

3. The Jiangmen Underground Neutrino Observatory 21
3.1. JUNO's Neutrino Physics Program . . . 21
3.1.1. Neutrino Physics in General . . . 21
3.1.2. Reactor Neutrinos . . . 25
3.1.3. Solar Neutrinos . . . 28
3.1.4. Geo-Neutrinos . . . 28
3.1.5. Supernova Burst Neutrinos . . . 29
3.1.6. Diffuse Supernova Neutrino Background . . . 30
3.1.7. Atmospheric Neutrinos . . . 30
3.1.8. Neutrinos from Dark Matter Annihilation . . . 30
3.2. Neutrino Interactions in JUNO . . . 31
3.3. The JUNO Detector . . . 33
3.3.1. JUNO Detector Setup . . . 33
3.3.2. Energy Resolution of JUNO . . . 37
3.4. The JUNO Simulation and Analysis Framework . . . 38
3.4.1. Detector Simulation . . . 39
3.4.2. Electronics Simulation . . . 39
3.4.3. Calibration and Waveform Reconstruction . . . 39
3.4.4. Energy and Vertex Reconstruction . . . 40

4. Neutrinos from Dark Matter Annihilation in JUNO 41
4.1. Neutrino Flux from Galactic Dark Matter Annihilation . . . 42
4.2. Antineutrino Signal from Dark Matter Annihilation in JUNO . . . 44
4.3. IBD Selection Criteria and JUNO's Detection Efficiency . . . 45
4.4. Visible Energy Spectrum in JUNO . . . 49

5. Background Sources in JUNO **53**
5.1. Reactor Electron Antineutrino Background . . . 53
5.2. Diffuse Supernova Neutrino Background . . . 57
5.3. Atmospheric Neutrino Background . . . 59
5.3.1. Atmospheric Neutrino Flux at JUNO site . . . 60
5.3.2. Atmospheric Charged Current Neutrino Background . . . 61
5.3.3. Atmospheric Neutral Current Neutrino Background . . . 67
5.4. Muon-induced Background . . . 74
5.4.1. Background from Cosmogenic Isotopes . . . 74
5.4.2. Fast Neutron Background . . . 75
5.4.3. Background from Decaying Muons . . . 76
5.5. Additional Background Sources . . . 77
5.6. Summary of Backgrounds in JUNO . . . 79

6. Background Reduction by Pulse Shape Discrimination in JUNO **81**
6.1. Pulse Shape Analysis . . . 82
6.2. JUNO's Pulse Shape Discrimination Performance . . . 84
6.3. Final Visible Energy Spectrum in JUNO . . . 88

7. JUNO's Sensitivity for Indirect Dark Matter Search **93**
7.1. Analysis Method . . . 93
7.1.1. Principle of Bayesian Analysis . . . 93
7.1.2. Bayesian Analysis for JUNO . . . 94
7.2. Sensitivity of JUNO . . . 97
7.3. Discussion and Comparison with Limits from other Experiments . . . 104
7.4. Possible Improvements for Indirect Dark Matter Search with JUNO . . . 108
7.4.1. Optimization of Detector Properties . . . 108
7.4.2. Additional Detection Channels and Background Reduction Methods 108
7.4.3. Directional Information in JUNO . . . 109

8. Indirect Dark Matter Search with THEIA **115**
8.1. The THEIA Detector . . . 117
8.2. Antineutrino Signal from Galactic Dark Matter Annihilation in THEIA . . . 119
8.3. Background Sources in THEIA . . . 123
8.3.1. Reactor Neutrino Background . . . 123
8.3.2. Diffuse Supernova Neutrino Background . . . 123
8.3.3. Atmospheric Charged Current Background . . . 124
8.3.4. Atmospheric Neutral Current Background . . . 128
8.3.5. Muon-induced Background . . . 132
8.3.6. Summary of Backgrounds in THEIA . . . 134
8.4. Background Reduction in THEIA . . . 136
8.4.1. Cherenkov Ring Counting . . . 136
8.4.2. Cherenkov to Scintillation Ratio . . . 138
8.5. THEIA's Sensitivity for Indirect Dark Matter Search . . . 145
8.5.1. Bayesian Analysis for THEIA . . . 145
8.5.2. Sensitivity of THEIA . . . 146
8.5.3. Discussion and Comparison with Limits of other Experiments . . . 151

9. Summary **155**

Appendix **159**
A. Distributions of the Simulation Data from the JUNO Simulation Framework 159
A.1. Distributions of Simulated IBD Events . . . 159

A.2. Distributions of Simulated Atmospheric NC Events 162
B. Total Visible Energy Spectra in JUNO 164
C. Distributions of the Simulation Data for THEIA25 from the RAT-PAC Simulation Framework 166
C.1. Distributions of Simulated IBD Events 166
C.2. Distributions of Simulated Atmospheric NC Events 168
D. Cherenkov Ring in THEIA25 170
E. Total Visible Energy Spectra in THEIA25 171

List of Figures **173**

List of Tables **177**

List of Acronyms **179**

Bibliography **183**

Danksagung **201**

1. Introduction

Several astrophysical and cosmological observations yield evidence for the existence of dark matter and therefore physics beyond the Standard Model of Particle Physics [1]. Although dark matter constitutes more than 80 % of the total matter density of the universe, its nature is still unknown and remains one of the most prominent unsolved puzzles in particle physics of the last decades [2, 3].
A large variety of experiments aim to detect dark matter based on different assumptions of the underlying theoretical models and on different detection techniques. One specific detection technique is the indirect dark matter search. Indirect dark matter search experiments look for an anomalous flux of standard model particles produced in self-annihilation (or decay) of dark matter particles [1]. In particular, dark matter self-annihilation could result in a potential flux of neutrinos and antineutrinos that can be measured with neutrino detectors at Earth [4]. Therefore, neutrino detectors contribute to the search for dark matter and could help to solve the puzzle of the dark matter's nature.

The Jiangmen Underground Neutrino Observatory (JUNO), a large-scale liquid scintillator detector with a broad neutrino physics program and currently under construction [5], and the prospective neutrino detector THEIA, which would represent a new kind of detector type on the basis of a water-based liquid scintillator target [6], provide ideal detectors to search for neutrinos produced in dark matter self-annihilation of dark matter particles with masses in the range from few MeV to around 100 MeV.

In this work, the sensitivities of JUNO and THEIA for the indirect dark matter search with neutrinos are studied for the first time. This is done by determining JUNO's and THEIA's sensitivity to measure a potential flux of neutrinos produced in dark matter self-annihilation in the Milky Way as an excess over backgrounds.
The thesis is structured as follows: evidence for the existence of dark matter, dark matter models and corresponding candidates, and techniques to detect dark matter particles, in particular indirect dark matter search with neutrinos, are presented in chapter 2. Chapter 3 introduces the Jiangmen Underground Neutrino Observatory (JUNO) with its neutrino physics program and the detector's design and setup. In the following chapters, the indirect dark matter search with neutrinos in JUNO studied in this work is presented including the calculation of the expected electron antineutrino signal from dark matter self-annihilation in the Milky Way (chapter 4), potential background sources and their corresponding spectra (chapter 5), background reduction by pulse shape discrimination (chapter 6) and the

resulting sensitivity of JUNO (chapter 7). The sensitivity for the indirect dark matter search of the prospective neutrino detector THEIA is determined and discussed in chapter 8. A summary of the thesis and its results is given in chapter 9.

2. Dark Matter

According to current knowledge, only 16 % of the total matter density of the universe is baryonic matter as described by the Standard Model of Particle Physics [1–3, 7]. Thus, the nature of 84 % of the universe's matter density is unknown yet which makes the search for so called *dark matter* to one of the major topics of astro and particle physics in the last decades [1–3, 7].
This introductory chapter aims to shortly summarize the current state of knowledge about dark matter physics. The evidence for the existence of dark matter based on several observations is reported in section 2.1. Section 2.2 introduces a selection of well-motivated dark matter models and their corresponding dark matter candidates concentrating on particle dark matter. Different techniques to detect dark matter particles are presented in section 2.3. In section 2.4, the indirect dark matter search approach via neutrinos is discussed and existing results and predicted sensitivities of neutrino experiments contributing to the search for dark matter are reviewed.
Extensive information about dark matter can be found in [1–3, 7], on which this chapter is based.

2.1. Evidence for Dark Matter

Evidence for the existence of large amounts of non-luminous matter in the universe is deduced from astrophysical and cosmological observations. This evidence for dark matter (DM) is observed in different astronomic structures ranging from galactic scales through scales of galaxy clusters to the cosmological scale.

A direct evidence for DM on the galactic scale are measurements of rotation curves of galaxies [2]. Rotation curves describe the radial velocity of stars and gas in a galaxy as a function of their distance to the galactic center and were first observed and studied by Vera Rubin in the 1960s [8]. It was shown, also in many following measurements [9–13], that the observed radial velocities remain almost constant at large distances from the galactic center and moreover even beyond the edge of the visible galactic disk [2]. Contrary to this, it was expected that the radial velocity, given as $v(r) = \sqrt{\frac{GM(r)}{r}}$ in Newtonian dynamics with the integrated mass $M(r)$, should decrease with increasing distance to the center under the assumption that the mass of a galaxy is distributed like the luminous matter. So, the observation of a constant radial velocity at larger radii can be explained by a halo of non-luminous matter with integrated mass $M(r) \propto r$ at large radii. This "missing"

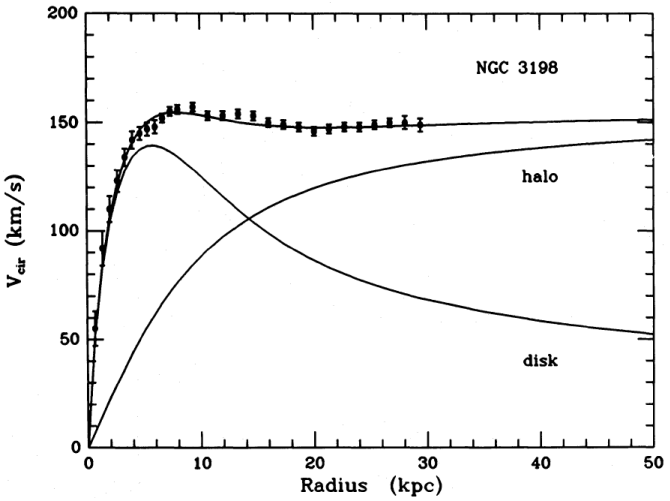

Figure 2.1.: Measured rotation curve of galaxy NGC 3198 (dots with error bars). The fit (black curve through data points) is based on the combined integrated mass $M(r)$ of a luminous matter disk and a dark matter halo resulting in constant radial velocities as function of the radii. Taken from [14].

mass to expound the observation is attributed to dark matter. In figure 2.1, a measured rotation curve of galaxy NGC 3198 is shown exemplarily. It illustrates that the measured radial velocities cannot be solely explained by the luminous disk, but by introducing an additional non-luminous halo. The combined integrated mass of both parts, luminous disk and non-luminous halo, leads to a constant radial velocity at larger radii, which agrees with the observations.

The first indication for the existence of non-luminous matter was reported even before the measurements of galactic rotation curves by Zwicky in 1933 after observing a cluster of galaxies [15]. From measurements of the velocity distribution of galaxies in the Coma cluster, he estimated the mass of the cluster using the virial theorem and claimed a ratio of the total mass to the luminous mass of around 400. Based on this observation, he postulated the need of additional non-luminous mass and introduced the term *dark matter* [15].
Another way to estimate the total mass in galaxy clusters is by the effect of gravitational lensing. According to Einstein's theory of general relativity, light from distant objects is bent when passing gravitational fields. The distortion of the light propagation caused by the gravitational mass of the cluster can be used to infer its mass [2]. Again, observations show a discrepancy between the gravitationally interacting mass of the galaxy clusters and their luminous mass [16–18].
Another evidence for the existence of dark matter at the scale of clusters of galaxies is the observation of the Bullet cluster, which consists of two galaxy clusters that have collided. Figure 2.2 shows an image of the Bullet cluster composed of different observations: optical and infrared light of the galaxies (white and orange), X-ray emission of hot intracluster gas (pink) and the total mass distribution obtained from gravitational lensing (blue). The intracluster gas (pink) contains the majority of the baryonic matter in the two clusters [19, 20]. The bullet-shaped clump on the right represents the intracluster gas from the smaller cluster, which passed through the hot gas of the other, larger cluster during the collision [21]. After the collision, most of the gravitational matter in the clusters (blue) obtained by the gravitational lensing effect is invisible and clearly separated from the baryonic matter (pink). This spatial separation and the measured gravitational lensing effect confirms the strong evidence of the existence of non-baryonic dark matter in the universe [22]. The fact that the dark matter clump is undisturbed by the collision

Figure 2.2.: Composite image of the Bullet cluster (1E 0657-558). Optical and infrared light from galaxies observed by Magellan and the Hubble Space Telescope are shown in orange and white. Hot intracluster gas, measured by Chandra via X-rays, is illustrated in pink. The mass distribution of the two clusters determined by the gravitational lensing effect is shown in blue. Image credit: [24].

of the clusters further implies a small DM self-interaction cross section [23]. Moreover, a small interaction cross section between dark matter and the baryonic intracluster gas can be assumed, since the dark matter mass distribution doesn't follow the distribution of the gas.

The most convincing indications for the presence of DM at the cosmological scale are the observations of the cosmic microwave background (CMB) and the study of structure formation in the universe, which allows to determine the total amount of DM in the present universe.
The CMB represents the residual photon radiation released in the early universe around 400,000 years after the Big Bang [25]. At this time, the universe became transparent to photons since electrons and protons recombined to neutral hydrogen. Due to the expansion of the universe, the CMB nowadays can be observed as sea of photons with an average temperature of 2.7 K [25]. Its first observation by Penzias and Wilson dates back to 1964 [26]. The key feature of the CMB are small fluctuations of the temperature in the order of 10^{-4} K. Figure 2.3 shows the currently most precise measurement of the CMB's fluctuations provided by the Planck satellite [27]. The bulk of cosmological information is encoded in these small fluctuations, since they represent small density anisotropies in the early universe. The angular correlations of these deviations can be decomposed into spherical harmonics and mapped into an angular power spectrum of the CMB, which depends on the matter density of the universe and its different components [28]. Therefore, measurements of the power spectrum yield a precise determination of the baryon matter and dark matter density in the universe (for more details see [25]).
The anisotropies of the CMB caused by density fluctuations can furthermore be considered as seeds for large scale structure formation in the universe and are used as input for N-body simulations to investigate the universe's evolution [2]. Predictions of these simulations are compared to large scale structure observations of large sky surveys, like e.g. SDSS [29], and agree notably well with the measurements, if non-relativistic (i.e. cold) dark matter is assumed. Cold DM clusters earlier than ordinary matter because it only interacts gravitationally [28]. Hence, baryonic matter follows the dark matter and structures are formed from smaller to larger scales. These results also rule out a significantly large contribution of ultra-relativistic hot DM to the total DM density, since its large kinetic energy would prevent the formation of clusters in the early universe.
The described observations together with other astrophysical measurements lead to the cosmological standard model (ΛCDM)[1]. Based on recent Planck data, the ΛCDM model

[1]For detailed information about the ΛCDM model see [30].

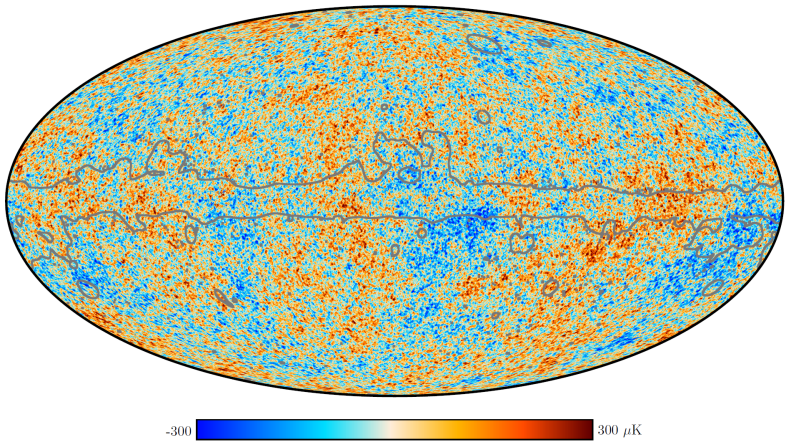

Figure 2.3.: Sky map of the CMB temperature from 2018 Planck data. The color map ranges from $-300\,\mu$K (blue) to $+300\,\mu$K (red). Foreground sources as well as solar and orbital dipoles are subtracted. The CMB map has been masked and inpainted in regions, where residuals from foreground emission are expected to be substantial. This mask, mostly around the galactic plane, is delineated by a gray line (for more details see [27]). Image taken from [32].

predicts an energy composition of the universe of 5.0 % baryonic matter, 26.5 % dark matter and 68.5 % dark energy at the present day [31].

2.2. Dark Matter Models and Candidates

Today, the existence of dark matter is generally accepted and supported by a variety of observations[2]. From these observations several properties can be attributed to dark matter, however the nature of this unseen matter is still unclear. In the following, additional particles not present in the SM that can explain the nature of DM are presented.
Dark matter is non-baryonic, gravitationally interacting matter with vanishing electromagnetic interaction [1]. Moreover, the self-interaction of DM is very small and its lifetime must be long compared to cosmological time scales [34]. From the standpoint of structure formation, DM must have negligible, non-relativistic velocities (it must be cold). However, a weak interaction between dark and baryonic matter is possible and the spin, i.e. if DM is fermionic or bosonic, is not yet determined [1].
Since there is no SM particle that fulfills the properties of DM and explains the observations presented in section 2.1 completely by its own, the search for unknown DM particles extend the current knowledge about particle physics beyond the SM. Many different models and theories have arisen in the past and are claiming possible DM candidates. These models partially differ, because the constraints on DM characteristics mostly come from gravitational observations and therefore don't provide much information about the particles' nature [7]. So, many different DM candidates are proposed in an extremely broad mass range from masses of around 10^{-15} eV to more than a few solar masses (for an exhaustive summary and more details about several DM models and candidates, see [1,2,7]). This and the following sections focus on weakly interacting massive particles (WIMPs) as DM candidates as well as so-called light DM with masses from MeV to GeV.
WIMPs are one of the most popular DM candidates and describe non-baryonic particles participating in the weak interaction and gravitation (no strong and electromagnetic

[2]There are also alternative theories that can describe some of the observations above without requiring the existence of additional non-luminous matter by modifying Newton's law of gravity at large scales [33]. Nevertheless, these Modified Newtonian Dynamics (MOND) can neither predict the observed anisotropic power spectrum of the CMB nor explain the observations of colliding clusters [1, 22].

interaction) [7]. Their appeal arises mainly from the fact that a particle with an annihilation cross section comparable to that of the weak interaction naturally reproduces the DM relic density [28]. Thermally produced DM particles like WIMPs are expected to self-annihilate into SM products, if no symmetry forbids this. At some point in the early universe, the expansion rate of the universe became larger than the thermally-averaged self-annihilation cross section, which prevents further annihilation into SM particles [4]. This so-called *freeze-out* of the DM particles defines the observed relic DM abundance today. WIMPs with masses from 2 GeV to around 10 TeV predict this relic abundance of DM regardless of the final annihilation channel for a thermally-averaged self-annihilation cross section of $\langle \sigma \, \mathrm{v} \rangle \simeq 3 \times 10^{-26} \, \mathrm{cm^3 s^{-1}}$ [4]. The WIMP's lower mass bound of 2 GeV is due to the Lee-Weinberg limit [35], as WIMPs with a smaller mass than 2 GeV would result in a lower self-annihilation cross section[3]. Therefore, the thermal freeze-out would have occurred earlier in time, which would have yielded in a larger relic DM density than observed nowadays. Another reason for the popularity of WIMPs as DM particles is the existence of well-motivated WIMP candidates in theoretical extensions of the SM. Models like e.g. supersymmetry (SUSY) [2, 37] naturally contain possible WIMP candidates as side products of the theory [38].
In contrast to the general WIMP scenario with large DM masses, light DM describes DM particles with masses below 1 GeV, more precisely in the MeV to GeV range. Due to the Lee-Weinberg limit, fermionic DM with standard weak interaction and masses less than few GeV would result in a larger relic DM density in the universe than observed and is therefore ruled out [2, 35]. Nevertheless, light DM particles with no significant or drastically reduced direct coupling to the Z boson do not appear excluded [39–41]. If scalar DM particles interact with ordinary matter through the exchange of new fermions or a new light gauge boson, the annihilation cross section would depend on the two low masses of the DM candidate and the exchange particle or, moreover, could be largely independent of the dark matter mass at all [39]. This would evade the Lee-Weinberg limit to lower DM masses and still produce the correct observed relic DM density [39].
The coupling of scalar DM particles with masses from MeV to GeV either to a new light neutral fermion with negligible coupling to the Z boson or to a new light gauge boson increases the DM self-annihilation cross section and satisfies cosmological constraints [39, 41, 42]. Hence, light DM serves as valid DM candidate with masses from approximately 1 MeV to around 1 GeV. Especially the 1 MeV to 100 MeV DM mass range appeared as interesting region for dark matter search in the last years [7] and is investigated within this thesis.

2.3. Dark Matter Detection Techniques

The search for these, yet still hypothetical, dark matter particles is a very diverse and challenging field in astro and particle physics. Focusing on WIMPs and light DM particles as introduced above, the search for dark matter can be separated into three different detection methods: direct detection, dark matter production at colliders and indirect detection. The concept and recent results of each technique is briefly presented in this section. A review of additional dark matter search methods, like e.g. axion searches, can be found in [1].

2.3.1. Direct Dark Matter Search

Direct dark matter detection generally describes the observation of elastic or inelastic scattering of DM particles from the galactic halo with atomic nuclei or electrons in the

[3] The annihilation cross section for non-relativistic particles weakly interacting with ordinary matter is in the order of $\sigma_{anni.}^{non-rel.} \sim \frac{m_{DM}^2}{M_Z^4}$ with WIMP mass m_{DM} and mass of the Z boson M_Z as mediator [36].

target material of detectors operated on Earth. Most of these experiments aim to measure the recoil energy of the target nuclei scattering off WIMPs with masses in the order of GeV to TeV because the recoil energy of the atomic nuclei in this case is large due to their similar masses[4] [43]. Typical nuclear recoil energies for WIMPs are predicted to range from 0 keV to around 100 keV [43].
The expected event rate R in a detector depends on the DM mass m_{DM}, its scattering cross section σ_{scat} with the target material and, since the Earth is traversing the galactic DM halo, also on the local DM density ρ_0 and the velocity of DM. Furthermore, both, the event rate and the recoil energy, depends on the number of targets N and the mass m_N of the target type itself [1]. The rate is

$$R \approx N \frac{\rho_0}{m_{DM}} \langle \sigma_{scat}\, \mathrm{v} \rangle \,, \tag{2.1}$$

where $\langle \sigma_{scat}\, \mathrm{v} \rangle$ is the scattering cross section averaged over the relative DM velocity with respect to the detector [2].
The exact expression for the cross section depends on the nature of the coupling. In direct detection experiments one generally distinguishes between spin-independent (SI) and spin-dependent (SD) interactions. For both interactions, coherent scattering can be assumed because the wavelength of the DM particle is usually large compared to the size of the nucleus. For SD interactions only target nuclei with non-vanishing nuclear spin can contribute [28].
The observation of very small recoil energies together with low event rates is very challenging. Various experiments aim to measure DM scattering in their detectors, mainly in the form of ionization, scintillation or lattice vibration of the target material. Most currently operated detectors simultaneously measure two types of these signals to distinguish between electron and nuclear recoils and to reject backgrounds due to the coincident measurement of the two signal types. Backgrounds are due to radioactivity of detector components and cosmic muons and their secondaries. The cosmic muon background and muon-induced secondary particles are mainly suppressed by going deep underground and equipping the detector with an active muon veto. Internal radiation is reduced by surrounding the target material with dedicated shielding structures and excessive screening of the incorporated materials. An irreducible background occurs from neutrinos, e.g. of the Sun or atmosphere, interacting through elastic neutrino-electron scattering or coherent elastic neutrino-nucleus scattering (CEνNS) with the detector material [1].
The most sensitive experiments are either based on noble liquid, solid-state cryogenic or superheated liquid detectors and are introduced in the following. It must be mentioned here that none of the detectors measured DM signals, apart of some anomalies that can be excluded by other DM experiments, with required significance of 5σ so far. Hence, the experiments only can set upper limits on the DM-nucleon scattering cross section. The currently best limits on the SI and SD DM-nucleon scattering cross section from direct detection experiments are shown in figure 2.4 and figure 2.5, respectively.
Noble liquid experiments are either using liquid xenon or liquid argon as DM target material and consist of time projection chambers measuring recoil energies from scintillation and ionization. Detectors based on liquid xenon, like XENON100/XENON1T at LNGS [45], LUX at SURF [46] and PandaX-II at CJPL [47], measure the SI as well as the SD scattering cross section and provide the best constraints on DM-nucleon interaction for a wide

[4] WIMP-electron scattering experiments become important for very light WIMPs of few MeV masses, since they will not transfer sufficient momentum to the target nucleus to generate a detectable nuclear recoil signal. Results for the DM-electron scattering are determined e.g. by the XENON collaboration or the DarkSide-50 experiment setting limits on the DM-e^- cross section of $\sim 10^{-30}\,\mathrm{cm}^2$ to $\sim 10^{-38}\,\mathrm{cm}^2$ for DM masses from 1 MeV to 1 GeV. For detailed information and results see [43, 44].

range of DM masses. The liquid argon experiment DarkSide-50 [48], located at LNGS, provides the best sensitivity of SI scattering for DM masses from 2 to 5 GeV.
Solid-state cryogenic experiments are optimized for low-mass DM searches down to masses of around 0.2 GeV by using the bolometric method together with charge or light signals, respectively [1]. They give the most stringent limits on the SI DM-nucleon scattering cross section below a mass of around 2 GeV. The most sensitive experiments are CDMSlite at Soudan utilizing germanium targets [49] and CRESST at LNGS deploying $CaWO_4$ as target [50].
Measurements of the spin-dependent scattering cross section require target nuclei with uneven total angular momentum. Fluorine, especially ^{19}F, is part of the target material using superheated liquids in bubble chamber experiments like PICASSO [51] and its follow-up experiment PICO-60 [52], both located at SNOLAB.

2.3.2. Dark Matter Search at the Large Hadron Collider

Various searches for a broad range of DM models, including different DM candidates, interactions, couplings, mediators and DM masses, are investigated mainly by the ATLAS and CMS collaboration at the LHC at CERN. For such searches it is assumed that DM particles are produced in *pp* collisions and leave the detector unimpeded leading to a significant amount of missing energy and momentum [1]. Therefore, precise observations of different types of signals, e.g. measurements of imbalance in the transverse momentum in an event due to the presence of DM particles, the determination of a bump in the di-jet or di-lepton invariant mass distributions or measurements of an excess of events in the di-jet angular distribution produced by a dark matter mediator, are performed (for detailed reviews and information see [63], [64] and [65]).
Up to now, no signal from DM production have been observed at the LHC, but limits on the DM production cross section, the DM-nucleon scattering cross section and the coupling between DM and SM particles have been set [54, 61, 66]. These results strongly depend on the assumed model and underlying mechanism that couples DM and SM particles [54]. Hence, and due to the fact that many different models and couplings are investigated, the interpretation of these results and the comparison to observations of direct and indirect DM experiments is difficult. On the other hand, DM production experiments are independent of cosmological assumptions. As an example for the sensitivity of the ATLAS experiment [54,61], the currently best limits on the SI (SD) DM-nucleon scattering cross section for a simplified DM model assuming vector (axial-vector) coupling to a spin-1 mediator Z' are shown in figure 2.4 and 2.5, respectively (in both cases a coupling of the mediator to quarks of $g_q = 0.25$, coupling of the mediator to DM of $g_{DM} = 1$ and, that the mediator has no couplings other than g_q and g_{DM}, is assumed). To be able to compare the ATLAS limits with limits from direct detection experiments, the resulting SI and SD DM-nucleon scattering cross section of ATLAS are defined as $\sigma_{SI} \simeq 6.9 \cdot 10^{-43}\,\mathrm{cm}^2 \left(\frac{g_q g_{DM}}{0.25}\right)^2 \left(\frac{1\,\mathrm{TeV}}{M_{med}}\right)^4 \left(\frac{\mu_{n\,DM}}{1\,\mathrm{GeV}}\right)^2$ and $\sigma_{SD} \simeq 2.4 \cdot 10^{-42}\,\mathrm{cm}^2 \left(\frac{g_q g_{DM}}{0.25}\right)^2 \left(\frac{1\,\mathrm{TeV}}{M_{med}}\right)^4 \left(\frac{\mu_{n\,DM}}{1\,\mathrm{GeV}}\right)^2$ with the DM-nucleon reduced mass $\mu_{n\,DM} = \frac{M_n\, m_{DM}}{M_n + m_{DM}}$ (for details see [67]).
Data of the LHC is also used to study the DM-neutrino interaction using a simplified model, where DM particles only interact with the SM through a neutrino and a new mediator [68]. In this simplified model, minimal DM-neutrino interaction is assumed, which can be parametrized by a single coupling constant. The DM particles, as well as the mediators, are assumed to be fermionic or scalar, respectively. In [68], the bounds on the DM-neutrino coupling are derived from mono-lepton results [69] and invisible Z width measurements [70] provided by the ATLAS experiment. These bounds are translated to a limit on the thermally-averaged DM self-annihilation cross section $\langle \sigma\, \mathrm{v} \rangle$ (times the relative velocity of the annihilating particles) into neutrinos ($DM + DM \rightarrow \nu + \bar{\nu}$) for DM

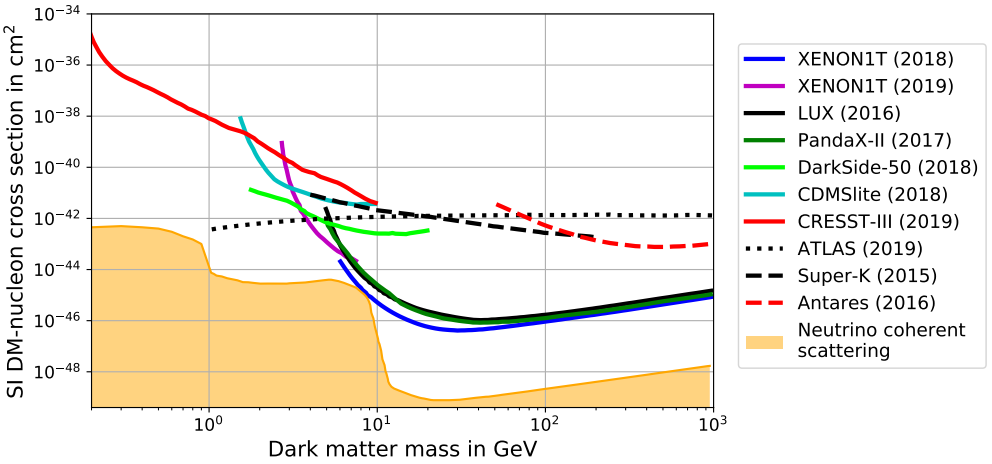

Figure 2.4.: Current experimentally allowed parameter space for the spin-independent DM-nucleon scattering cross section as function of the DM mass. Results from direct DM detection experiments (solid lines), DM production at colliders (dotted line) and indirect DM search with neutrinos (dashed lines) are displayed. Recent upper limits of XENON1T (from 2018 [45] and 2019 [53]), LUX [46], PandaX-II [47], DarkSide-50 [48], CDMSlite [49] and CRESST-III [50], together with the current limit of ATLAS [54] (details in section 2.3.2) are shown. Moreover, upper limits of the neutrino experiments Super-Kamiokande [55] and ANTARES [56] for the annihilation channel $DM + DM \rightarrow \tau^+\tau^-$ are presented. The space above the upper limits is excluded at 90 % confidence level (for ATLAS at 95 % C.L.). The orange region represents the irreducible background from coherent elastic neutrino-nucleus scattering (CEνNS) and limits the parameter space for direct detection experiments from below (see [50] for $m_{DM} < 1\,\text{GeV}$ and [57] for $m_{DM} > 1\,\text{GeV}$).

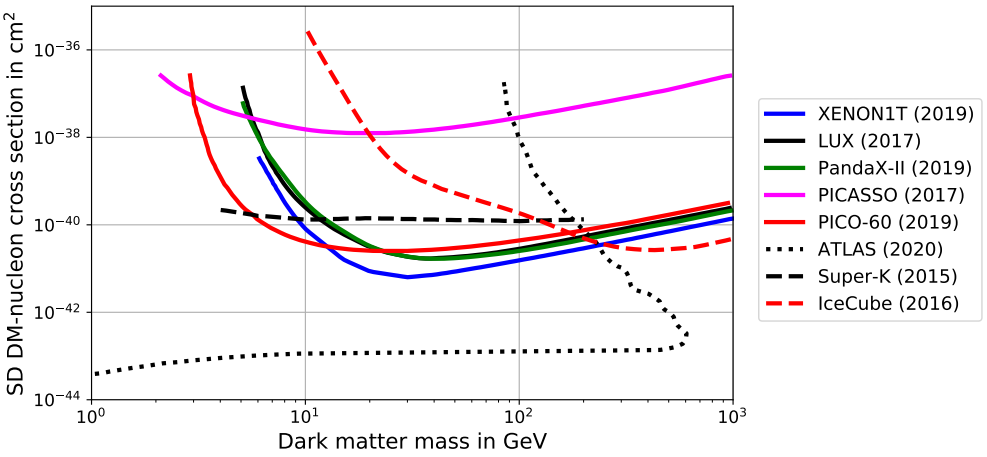

Figure 2.5.: Current experimentally allowed parameter space for the spin-dependent DM-nucleon scattering cross section as function of the DM mass. Results from direct DM detection experiments (solid lines), DM production at colliders (dotted line) and indirect DM search with neutrinos (dashed lines) are displayed. Recent upper limits of XENON1T [58], LUX [59], PandaX-II [60], PICASSO [51] and PICO-60 [52], together with the current limit of ATLAS [61] (details in section 2.3.2) are shown. Also upper limits from the neutrino experiments Super-Kamiokande [55] and IceCube [62] for the annihilation channel $DM + DM \rightarrow \tau^+\tau^-$ are presented. The space above the upper limits is excluded at 90 % confidence level for all experiments.

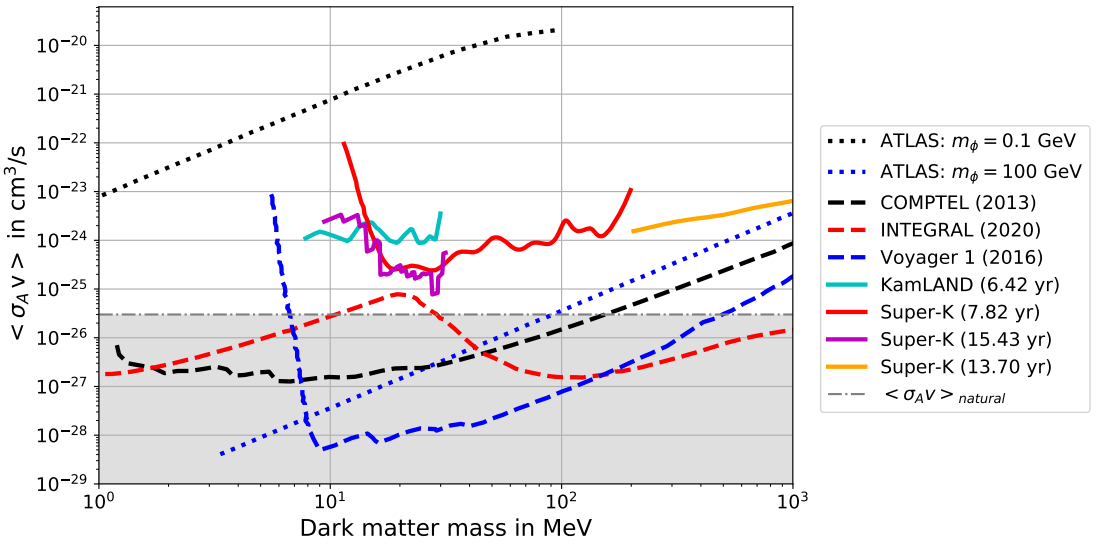

Figure 2.6.: Current experimental limits on the DM annihilation cross section $\langle \sigma_A \, \mathrm{v} \rangle$ in the DM mass region from 1 MeV to 1 GeV. Results from DM production at colliders (dotted lines), indirect DM searches with photons and cosmic rays (dashed lines) and indirect DM detection with neutrino detectors (solid lines) are displayed. The limits of the ATLAS experiment from [68] assuming fermionic DM and the simplified model described in section 2.3.2 are shown exemplarily for mediator masses of $m_\phi = 0.1$ GeV (black dotted) and $m_\phi = 100$ GeV (blue dotted). Limits of X-ray measurements of INTEGRAL from [71] (red dashed) and low energy gamma ray detection of COMPTEL from [72] (black dashed) for the annihilation channel $DM + DM \rightarrow e^+ + e^-$ are plotted. The bound of Voyager-1 on the DM annihilation channel $DM + DM \rightarrow e^+ + e^-$ from [73] by measuring cosmic positrons is displayed as blue dashed line. Furthermore, current limits of neutrino detectors for the annihilation channel $DM + DM \rightarrow \nu + \bar{\nu}$ are shown (see section 2.4): KamLAND from [74] (cyan solid) and Super-K from [75] (red solid), [4] (magenta solid) and [68] (orange line). All limits are given at 90 % confidence level. The gray line represents the natural scale $\langle \sigma_A \, \mathrm{v} \rangle_{natural} \approx 3 \cdot 10^{-26}$ cm^3/s of the DM annihilation cross section required to explain the observed relic DM abundance from thermal freeze-out [76]. Limits projecting into the gray region below this natural scale exclude a velocity-independent thermal annihilation cross section for the observed channel and made assumptions.

masses from 1 MeV to 100 GeV and different mediator masses [68]. The limits on the DM annihilation cross section of this specific simplified model from collider results can be compared to constraints of model-independent indirect DM searches, which is displayed in figure 2.6. Under the assumptions of this simplified model and of large mediator masses of few hundreds of GeV, a velocity-independent thermal DM annihilation cross section could be ruled out by ATLAS for DM masses below around 100 MeV (see figure 2.6).

2.3.3. Indirect Dark Matter Search

Indirect searches for dark matter are based on the detection of an anomalous flux of photons, neutrinos or cosmic-rays produced in self-annihilation or decay of DM particles gravitationally accumulated in cosmological objects like e.g. galaxy clusters, galaxies or the Sun [77]. Expressions for the production rate and the expected flux of these particles can be separated into two different parts: a particle physics factor and an astrophysical factor. The particle physics factor mainly contains the DM mass, the annihilation cross

section (or DM lifetime for decay searches), the number of final-state particles originating from one annihilation (or decay) and the expected energy spectrum of these final products. In contrast to that, the astrophysical factor only depends on the observed region of interest and how the DM particles are distributed inside of it [1, 78]. Detailed information about these two parts is given in section 2.4 and chapter 4.
Experiments searching for the final products of DM annihilation or decay are separated into three groups depending on the particle type they are measuring: photons, charged cosmic rays and neutrinos. This section focuses on indirect DM detection with photons and charged cosmic rays, whereas DM annihilation into neutrinos is explicitly discussed in section 2.4.
Dark matter annihilation or decay to nearly any final state produces photons, especially gamma rays and X-rays in case of DM masses from MeV to few TeV [1], which implies that a sizable fraction of the final annihilation or decay products ends up as photons. Furthermore, photons travel to the observer without deflection allowing to map the sources of the signals and carry important spectral information that can be used to characterize the dark matter particle in the case of a detection [78]. Target regions to observe gamma and X-ray emission from DM annihilation or decay are for example the galactic center of the Milky Way or dwarf satellite galaxies [1]. Experiments contributing to the indirect DM search via gamma and X-ray observations are either satellites, since the Earth's atmosphere is opaque to gammas and X-rays, or ground-based imaging atmospheric Cherenkov telescopes detecting Cherenkov light produced by particle showers and induced by high energetic gamma rays in the atmosphere [78]. Up to now, none of the various gamma and X-ray telescopes has obtained a significant detection in their search for dark matter signals investigating various annihilation and decay channels and observing plenty of sources [77, 79]. For DM masses above $\sim$ GeV, the most encouraging limits on the annihilation cross section and DM lifetime are provided from gamma ray measurements by the Cherenkov telescopes H.E.S.S. [80, 81] and MAGIC [82, 83] and by the space telescope Fermi-LAT [83, 84]. For lower DM masses in the range of few MeV to few GeV, satellites like the X-ray telescope INTEGRAL [71] and the COMPTEL telescope [85], which measures low energetic gamma rays, are sensitive to constrain the annihilation cross section and DM lifetime. The current limits on the DM self-annihilation cross section for the annihilation channel $DM + DM \rightarrow e^+ + e^-$ from INTEGRAL [71] and COMPTEL [72] are shown in figure 2.6 for sub-GeV DM masses as an example.
Another prime target for indirect DM searches is cosmic radiation contained of stable charged particles that are produced either directly in DM annihilation/decay processes or through decays of annihilation/decay products [1]. The reconstruction of the source and primary energy of cosmic rays is challenging, since these charged particles are bent by magnetic fields and lose energy through inverse Compton scattering and synchrotron radiation during propagation. However, due to the measurements of relatively rare particle types like positrons, antiprotons and antinuclei, the signal to noise ratio can be maximized [78]. This allows cosmic ray detectors like space-based instruments such as PAMELA [86] and AMS-02 [87] and balloon-borne experiments such as ATIC [88] to put constraints on the DM annihilation cross section and the DM lifetime. Moreover, also gamma ray detectors like Fermi-LAT, H.E.S.S. and MAGIC, and the ultra-high-energy cosmic ray Pierre Auger observatory [89, 90] contribute to indirect DM searches with charged cosmic rays [78]. The currently best limit on the DM annihilation cross section of cosmic ray detectors for sub-GeV DM masses obtains the LECP experiment on the spacecraft Voyager-1 [91, 92] by measuring cosmic positrons. Its limit on the annihilation channel $DM + DM \rightarrow e^+ + e^-$ is displayed in figure 2.6 exemplarily.
In summary, it can be stated that the described indirect DM search experiments give strong bounds on the dark matter self-annihilation into photons and positrons. Figure 2.6 shows that the current limits of INTEGRAL, COMPTEL and Voyager-1 are even below

the natural scale $\langle \sigma_A \, \mathrm{v} \rangle_{natural} \approx 3 \cdot 10^{-26}$ cm^3/s of the DM annihilation cross section, which describes the value of the annihilation cross section required to explain the observed relic DM abundance by thermal freeze-out [76]. Therefore a velocity independent thermal DM self-annihilation into photons and positrons can be excluded[5] at 90 % C.L. for DM masses from 1 MeV to 1 GeV.

2.4. Indirect Dark Matter Search with Neutrinos

The observation of neutrinos or antineutrinos from DM annihilation or decay completes the list of indirect DM searches and have become a very active field of investigation. In this section, recent results of neutrino experiments according to dark matter annihilation are reviewed. For details about the decay of DM particles into neutrinos, see e.g. [93–95]. Neutrinos can be produced either directly from DM self-annihilation or by the decay of heavy states such as muons, quarks or weak bosons originating from DM annihilation. Since neutrinos are neutral and only weakly interacting with SM particles, they are not deflected by magnetic fields and can leave also optically dense environments without significant interaction [4] (more information about neutrinos and their characteristics is given in chapter 3). Moreover, in contrast to photons or charged particles, the small ν-SM interaction cross section makes neutrinos the least detectable particles in the SM and constraints on the DM annihilation cross section into neutrinos allow to set a conservative bound on the total DM annihilation cross section into SM particles [96]. Until now, no neutrino signal from DM self-annihilation has been observed in neutrino experiments [1].
In the following, DM self-annihilation into neutrinos for typical WIMP masses between 1 GeV and few TeV and corresponding experiments are described. Afterwards neutrinos produced in DM annihilation of light DM particles in the mass range from 1 MeV to 1 GeV and experiments aiming to measure these neutrinos are reviewed in detail, since it is directly correlated to the work developed within this thesis.

2.4.1. Dark Matter with Mass above 1 GeV

WIMP annihilation searches with neutrinos as final products focus on three different objects: the Milky Way, the Sun and the Earth.
To study WIMP annihilation in the Milky Way, neutrino experiments search for an excess in the observed neutrino flux either from the entire Milky Way or only from the galaxy's core above the expected background. With precise measurements of the neutrino flux and sophisticated analysis methods to extract a possible signal from the background, constraints on the DM self-annihilation cross section are determined by several neutrino experiments. The most stringent bounds for WIMP masses above few GeV are set by the Cherenkov experiments ANTARES in the Mediterranean Sea measuring $\nu_\mu/\bar{\nu}_\mu$ [97], IceCube at South Pole observing $\nu/\bar{\nu}$ interactions in the ice [98] and the Super-Kamiokande experiment detecting $\nu_\mu/\bar{\nu}_\mu$ in a 50 kton water Cherenkov detector [99]. Dark matter annihilation channels into $b\bar{b}$, W^+W^-, $\tau^+\tau^-$, $\mu^+\mu^-$ and directly into $\nu\bar{\nu}$ as well as different DM density profiles have been assumed in these experiments resulting in upper limits of the DM annihilation cross section into neutrinos of $\sim 10^{-25}$ cm^3/s to $\sim 10^{-23}$ cm^3/s for WIMP masses from 4 GeV to 100 TeV (for details see [99, 100]).
Dark matter can be captured in celestial objects in significant amounts, which makes the Sun another possible source of neutrinos from DM self-annihilation [1]. The Sun travels through the DM halo of the Milky Way and, after losing energy by scattering off nuclei

[5] DM annihilation depending on its velocity, as well as DM self-annihilation into other SM particles like e.g. neutrinos, is not ruled out yet.

in the Sun, the DM particles' velocity can be too small to escape the gravitational potential of the Sun. So, DM can be trapped inside the Sun[6]. Due to the gravitational pull of the Sun and further scattering off its nuclei, DM particles sink to the Sun's core and accumulate there [103]. This whole process can be express in the solar DM capture rate C_c that is proportional to the SI and SD DM-nucleon scattering cross section [104]. Captured WIMPs could then pair-annihilate in the Sun's core into ordinary matter and produce neutrinos as final products that can leave the Sun and be detected by neutrino experiments on Earth [55]. Under the assumption that the solar DM capture rate C_c and the DM annihilation rate Γ_A in the Sun, which is proportional to the annihilation cross section [104], are in equilibrium[7], neutrino detectors can set constraints on the DM-nucleon scattering cross section by measuring the neutrino flux from the Sun, which can be compared to results from direct DM detection experiments [1]. The neutrino experiments ANTARES [56], IceCube [62] and Super-K [55] have measured the neutrino flux from the Sun and compared it to the expected neutrino energy spectrum of several DM annihilation channels like $DM + DM \rightarrow b\bar{b}$, W^+W^-, $\tau^+\tau-$. These neutrino energy spectra are simulated taking into account the interaction of neutrinos in the solar plasma as well as neutrino oscillations inside the Sun and on their way from the Sun to the detector. For each annihilation channel, a branching ratio of 100 % is assumed [56]. The currently best limits on the spin-independent DM-nucleon scattering cross section from neutrino experiments due to dark matter annihilation into neutrinos in the Sun are provided by Super-K and ANTARES and shown in figure 2.4, whereas the most stringent limits on the spin-dependent scattering cross section come from Super-K and IceCube and are displayed in figure 2.5.
ANTARES [105] and IceCube [106] also investigated dark matter self-annihilation inside the Earth's core. DM can also be accumulated in the gravitational field of the Earth through DM-SM interactions and produce neutrinos via self-annihilation. By measuring the flux of up-going neutrinos, these experiments set upper limits on the spin-independent DM-nucleon scattering cross section of $\sigma^{SI}_{scat} \approx 10^{-41}$ cm^2 for WIMP masses from 10 GeV to 10 TeV (for more information, see [105–107]). Nevertheless, the most constraining limits in this mass range from direct DM detection experiments shown in figure 2.4 are around four orders of magnitudes better.

2.4.2. Dark Matter with Mass below 1 GeV

Since the subject of this thesis is the determination of the sensitivity of the future neutrino experiments JUNO and THEIA to detect neutrinos from DM self-annihilation for DM masses below 1 GeV, neutrino experiments contributing to the search in this mass region and their current results are reviewed here. Moreover, also the expected sensitivity of the proposed Hyper-Kamiokande experiment is discussed.
The most auspicious region to search for neutrinos from pair-annihilation of light DM particles with masses between 1 MeV and 1 GeV is our galaxy, for which reason this section focuses on the Milky Way. The Sun is ruled out as feasible source, since DM

[6] Since the scattering cross section between DM and solar nuclei is very small ($\lesssim 10^{-41}$ cm^2), DM particles interact only occasionally and can thermally evaporate from the Sun before being captured. This evaporation effect has a strong impact on WIMPs with masses below ~ 4 GeV and therefore rules out WIMP capture in the Sun for these masses. In contrast, evaporation of WIMPs with masses above 4 GeV in the Sun is negligible (see [101, 102])

[7] The time derivative of the number of WIMPs N in the Sun is given as $\dot{N} = C_c - C_e N - C_a N^2$ with the capture rate C_c, the evaporation rate C_e and the annihilation rate $\Gamma_A = 1/2\, C_a N^2$ [104]. In equilibrium of capture and annihilation rate, and neglecting the evaporation rate (for $m_{DM} \gtrsim 4$ GeV), the annihilation rate is given as $\Gamma_A = 1/2\, C_a N^2 = {}^{C_c}/_2$ and proportional to the scattering cross section [103].

particles with $m_{DM} \lesssim 4$ GeV are not captured sufficiently due to the evaporation effect [101, 102]. Furthermore, the expected neutrino flux from self-annihilation of light DM inside the Earth is negligible. Inside the Earth, significant DM capture only occurs by scattering of DM particles off the most abundant elements ^{16}O, ^{24}Mg, ^{24}Si, ^{56}Fe and their isotopes. Therefore, DM capture and corresponding self-annihilation inside the Earth for $m_{DM} \ll m_{^{16}\mathrm{O}} \approx 14.9\,\mathrm{GeV}$ is unlikely [107].
The expected neutrino (or antineutrino) flux per flavor on Earth originating from DM self-annihilation in the Milky Way can be divided into one part defined by the underlying particle physics and one astrophysical part and is given as [96]

$$\frac{\mathrm{d}\phi_\nu}{\mathrm{d}E_\nu} = \left[\frac{\langle\sigma_A\,\mathrm{v}\rangle}{m_{DM}^2}\,\frac{1}{\kappa_1\,\kappa_2}\,\frac{\mathrm{d}N_\nu}{\mathrm{d}E_\nu}\right]\cdot\left[R_0\rho_0^2\,J_{avg}\right] \tag{2.2}$$

The particle physics part describes the annihilation process and depends on the thermally averaged DM self-annihilation cross section $\langle\sigma_A\,\mathrm{v}\rangle$, the DM mass m_{DM}, the number of neutrinos (or antineutrinos) of one flavor produced in one annihilation (described by the factors κ_1 and κ_2) and the expected neutrino energy spectrum $^{\mathrm{d}N_\nu}/_{\mathrm{d}E_\nu}$ according to the assumed annihilation channel. The most studied annihilation channel in this context is the direct annihilation of dark matter particles into neutrinos $DM + DM \rightarrow \nu + \bar{\nu}$, which represents the most invisible channel in terms of particle detection[8]. Assuming direct annihilation into neutrinos, the expected neutrino energy spectrum is monoenergetic with $E_\nu = m_{DM}$; $^{\mathrm{d}N_\nu}/_{\mathrm{d}E_\nu} = \delta(E_\nu - m_{DM})$. Moreover, annihilation with equal branching ratios into the three neutrino flavors ($\nu_e : \nu_\mu : \nu_\tau = 1 : 1 : 1$) is assumed in the following, which is considered in equation 2.2 by setting $\kappa_2 = 3$. Even in case of annihilation predominantly into one neutrino flavor, neutrino oscillation between the production point and the detector would generate the two other flavors with comparable intensity[9], which guarantees a flux of neutrinos in all flavors [96]. The factor κ_1 is defined by the DM particle type: $\kappa_1 = 2$ for Majorana DM (DM is its own antiparticle) and $\kappa_1 = 4$ for Dirac DM (DM is not its own antiparticle) [4, 68].
The astrophysical part is characterized by the dark matter distribution in the observed region, i.e. in the Milky Way. R_0 is defined as distance from the solar system to the galactic center and ρ_0 describes the local DM density (i.e. the DM density at R_0). The dimensionless angular-averaged J-factor J_{avg} is defined as integral over the squared DM density ρ in the halo along the line of sight l averaged over the Milky Way halo and describes the angular-averaged DM intensity over the whole Milky Way [75, 96]:

$$J_{avg} = \frac{1}{2\,R_0\,\rho_0^2}\int_{-1}^{+1}\int_0^{l_{max}} \rho^2(r)\,\mathrm{d}l\,\mathrm{d}(\cos\psi) \tag{2.3}$$

with $r = \sqrt{R_0^2 - 2lR_0\cos\psi + l^2}$, the angle ψ between the galactic center and the line of sight, and the upper limit of the integration $l_{max} = \sqrt{R_{halo}^2 - \sin^2\psi R_0^2} + R_0\cos\psi$, which depends on the size of the halo R_{halo}. J_{avg} remains approximately unchanged for $R_{halo} \gtrsim 30$ kpc [4], as the contribution at large scales is negligible. Here, a value of $R_{halo} = 40$ kpc is assumed.
The angular-averaged J-factor J_{avg} strongly depends on the DM density profile in the

[8] Every other annihilation channel produces photons, electrons or positrons as final products, either directly or through decay of heavier particles, which will always be easier to detect (unless annihilation occurs in optical thick environments) [4].

[9] Pure annihilation into electron neutrinos would result in a flavor composition at the detector of $\nu_e : \nu_\mu : \nu_\tau \approx 1.65 : 0.75 : 0.6$, pure annihilation into muon neutrino would give a composition of $\nu_e : \nu_\mu : \nu_\tau \approx 0.75 : 1.08 : 1.14$ and pure annihilation into tau neutrinos would yield $\nu_e : \nu_\mu : \nu_\tau \approx 0.57 : 1.14 : 1.29$ [4].

Milky Way. There are many different DM profile models parameterizing the galactic DM halo, which tend to agree at large radii, but can differ significantly in the inner region. Therefore, the largest uncertainty in the neutrino flux from DM annihilation of equation 2.2 comes from the lack of knowledge of the DM density profile. To quantify this uncertainty, several DM halo profiles and their effects on the neutrino flux have been investigated. Details about the most prominent models and their resulting angular-averaged J-factors are given in section 4.1. Most experiments assume a halo average value of $J_{avg} = 5$ as the canonical value for better comparison [108].
In the following, current results of the neutrino experiments KamLAND and Super-Kamiokande and the predicted sensitivity of Hyper-Kamiokande for measuring neutrinos from DM self-annihilation in the Milky Way as an excess over backgrounds are presented. A verbose review of DM annihilation into neutrinos in the Milky Way over a DM mass range from MeV to ZeV for a great number of neutrino experiments can be found in [4].

KamLAND [74, 109] is a liquid scintillator neutrino detector in Japan. Its target volume contains 1 kt of ultra-pure liquid scintillator and is surrounded by a buffer volume to shield the scintillator from external radiation. The scintillation light is detected by about 1880 photomultiplier tubes resulting in a total photocathode coverage of 34 %. In addition to the buffer volume, a 3.2 kt water Cherenkov detector shields the inner detector from cosmic muons acting as an active muon veto. The whole detector itself is located underground at 2700 m.w.e., which reduces the cosmic muon flux by almost five orders of magnitudes. The main detection channel in KamLAND is the inverse β decay (IBD: $\bar{\nu}_e + p \rightarrow e^+ + n$), which allows an efficient background suppression due to the spatial and temporal coincidence of the prompt energy deposition of the positron and the delayed neutron capture signal on hydrogen (for details about the IBD, see section 3.2). The emitted scintillation light in the liquid scintillator detector is nearly isotropic, which does not allow to reconstruct the antineutrino source direction properly [74]. However, KamLAND has a very low energy threshold of 0.7 MeV with an energy resolution of $6.4\,\%/\sqrt{E[\mathrm{MeV}]}$ and a vertex reconstruction resolution of $\sim 12\,\mathrm{cm}/\sqrt{E[\mathrm{MeV}]}$ [109].
In [74], constraints on the DM annihilation cross section of the KamLAND experiment are presented for DM masses from 7.5 MeV to 30 MeV. Direct annihilation of Majorana DM particles into neutrinos in the entire Milky Way with equal annihilation into all flavors is assumed. Moreover, an angular-averaged J-factor of $J_{avg} = 5$, $R_0 = 8.5\,\mathrm{kpc}$ and $\rho_0 = 0.3\,\mathrm{GeV/cm^3}$ is used to predict the electron antineutrino flux from DM self-annihilation as given in equation 2.2. KamLAND uses measurements of the $\bar{\nu}_e$ flux via the IBD detection channel of 2343 live-days (6.42 years) with a fiducial volume of 0.7 kt for prompt positron energies between 7.5 MeV and 30 MeV and observes 25 IBD events in this energy range[10]. Estimated background components and their number of events N for prompt energies between 7.5 MeV and 30 MeV are: random coincidences with $N = 0.22 \pm 0.01$, reactor antineutrinos with $N = 2.2 \pm 0.7$, cosmogenic isotopes with $N = 4.0 \pm 0.3$, fast neutrons with $N = 3.2 \pm 3.2$ and atmospheric neutrinos with $N = 17.3 \pm 5.4$. The total number of background events is estimated to 26.9 ± 5.7. The data is analyzed using an unbinned maximum likelihood fit to the event spectrum to search for an excess from a monoenergetic $\bar{\nu}_e$ flux over the estimated background spectra. The resulting upper limit for a monoenergetic $\bar{\nu}_e$ flux from DM annihilation is then translated into a 90 % C.L. upper limit for the DM annihilation cross section, which is displayed as "KamLAND (6.42 yr)" in figure 2.6. The limit on $\langle \sigma_A \, \mathrm{v} \rangle$ varies weakly over the DM mass according to the limited statistics [74].

[10] The observed energy region between 7.5 MeV and 30 MeV is limited by the reactor antineutrino background present below 7.5 MeV and the presence of atmospheric neutrino background events above 30 MeV.

The currently most stringent constraints on the DM annihilation cross section of neutrino detectors for DM masses up to 1 GeV are provided by the Super-Kamiokande experiment. The Super-Kamiokande detector is a cylindrical water Cherenkov detector with a total mass of 50 kt located in Japan approximately 2700 m.w.e. underground [110]. It is divided into an inner and outer detector. The outer detector contains 18 kt ultra-pure water, surrounds the inner one and is optically separated from it. The main purpose of the outer detector is to act as active Cherenkov veto. The inner detector serves as neutrino target containing 32 kt ultra-pure water and is instrumented with about 11,150 PMTs to detect the emitted Cherenkov light, which results in a photocathode coverage of 40 %. The fiducial volume of the Super-K detector is 22.5 kt. Neutrino interactions are detected via Cherenkov light produced by charged particles inside the fiducial volume. A charged particle traversing a dielectric medium with refractive index $n > 1$, like e.g. water, radiates Cherenkov light, if its velocity v is larger than the phase velocity of light in the medium ($v > c/n$). The emission is due to an asymmetric polarization of the medium in front and at the rear of the particle track and known as *Cherenkov effect* [111]. The size, shape and orientation of the detected Cherenkov light pattern is used to identify the particle's type, measure its energy and obtain the directional information of the incoming neutrino [110]. In contrast to liquid scintillator detectors, the Super-K detector can reconstruct the direction of the incoming neutrino with an angular resolution of around 25° at 10 MeV [112]. However, the energy resolution of Super-K with 14.2 % at 10 MeV [113] is worse compared to scintillator detectors, since the photon light yield of Cherenkov detectors, i.e. the number of photons produced per deposited energy, is around two orders of magnitudes smaller than in liquid scintillator detectors [114]. Another disadvantage of Cherenkov detectors is the large energy threshold in comparison to LS detectors (for Super-K approximately $E_{thr.} \approx 4.5$ MeV [110]), which does not allow to measure the 2.2 MeV γ's released in the delayed neutron capture on hydrogen in the inverse β decay reaction channel. Nevertheless, Super-K is an excellent detector to search for neutrinos from DM self-annihilation.

In the DM mass range from 10 MeV to 130 MeV, data of the Super-Kamiokande detector originally measured to search for the diffuse supernova neutrino background (DSNB) is analyzed to set upper limits on the DM self-annihilation cross section (details about the DSNB are given in section 3.1.6 and 5.2).
In [75], data of three Super-K phases (SK-I, SK-II, SK-III), which corresponds to 2853 days ($\sim$ 7.82 years) of data taking, for positron energies from 18 MeV to 88 MeV[11] and a fiducial volume of 22.5 kt is analyzed using the specific energy resolution, thresholds and efficiencies of each phase. Self-annihilation of Majorana DM particles in the entire Milky Way directly into neutrinos with equal flavor composition is assumed similar to the limit of KamLAND discussed above. Moreover, an angular-averaged DM intensity of $J_{avg} = 5$, a local DM density of $\rho_0 = 0.3$ GeV/cm^3 and a distance between solar system and galactic center of $R_0 = 8.5$ kpc is presumed. Neutrino interactions of electron antineutrinos with free protons, i.e. inverse β decay, and interactions of ν_e and $\bar{\nu}_e$ with bound nucleons of the oxygen nuclei ($\nu_e + {}^{16}\mathrm{O} \rightarrow e^- + {}^{16}\mathrm{F}$ and $\bar{\nu}_e + {}^{16}\mathrm{O} \rightarrow e^+ + {}^{16}\mathrm{N}$) are investigated. The two main backgrounds for the search of a monoenergetic neutrino flux from DM annihilation in the Super-K detector are atmospheric electron (anti-)neutrinos and Michel positrons/electrons from the decay at rest of invisible muons. If the kinetic energy of muons produced by atmospheric muon neutrinos in the detector is below the energy threshold of muons for emitting Cherenkov radiation ($E_{\mu,thr.} = 54$ MeV), the muons are invisible for the detector. These invisible muons are slowed down and subsequently decay by emitting Michel electrons/positrons, which cannot be distinguished from the e^-/e^+

[11] The maximum observed positron energy $E_{e,max} = 88$ MeV corresponds to a maximum neutrino energy of around 130 MeV. Therefore, the corresponding DM mass region is also limited to $m_{DM} = 130$ MeV.

signal. Therefore, invisible muons from atmospheric ν_μ and $\bar{\nu}_\mu$ constitute the dominant background in water Cherenkov detectors. The background from invisible muons could be significantly suppressed by a factor of 5 [115], if the delayed neutron capture signal on hydrogen from the inverse β decay reaction emitting a 2.2 MeV γ could be tagged. This is not possible in pure water Cherenkov detectors like Super-K because of its energy threshold of 4.5 MeV. However, by adding a small amount of gadolinium into the water, neutrons could be captured by gadolinium releasing a total energy of around 8 MeV, which is above the threshold. This would allow to tag neutron capture signals, reduce the background from invisible muons and improve the limit on the annihilation cross section [115]. In summer 2020, the Super-K collaboration started to dissolve Gd sulfate into the Super-K water tank [116], but no sensitivity studies for indirect DM search with Super-K plus Gd have been published until now. Not included into the analysis in [75] is the DSNB and the subleading backgrounds from neutral current elastic events and low-energy muons and pions misidentified as positrons and electrons, since the results are not significantly affect by these. It should be noted here, that no directional information, neither for the signal nor for the background events, is used. The upper limit of the DM event rate is then converted into a 90 % C.L. upper limit on the DM annihilation cross section derived for a constant velocity-independent annihilation cross section (details about the analysis and the used χ^2 fit can be found in [96] and [75]). The resulting upper limit on $\langle \sigma_A \, \mathrm{v} \rangle$ for DM masses from around 10 MeV to 130 MeV is shown as "Super-K (7.82 yr)" in figure 2.6.
In [4], the upper limit of Super-K from [75] described above was updated for the DM mass region from 10 MeV to 30 MeV by considering additional data from the latest Super-K phase SK-IV (2778 days of data taking). The analysis of low energy data of 5631 live-days ($\sim$ 15.43 years) from SK-I to SK-IV leads to an upper limit on the relic supernova $\bar{\nu}_e$ flux published in [117]. In [117], the upper limit of the number of signal events is calculated in a model-independent way based on background estimations and was derived by the Rolke method [118] implemented in the ROOT toolkit [119]. The upper limit of the number of events in each bin was translated into an upper limit of the $\bar{\nu}_e$ flux in [117] and is then converted into an 90 % C.L. upper limit on the DM annihilation cross section in [4]. Besides the larger dataset, also directional information of the background events is used in the analysis of [4]. The upper limit on $\langle \sigma_A \, \mathrm{v} \rangle$ in the DM mass range from 10 MeV to 30 MeV is improved by a factor of 1.5 on average[12] compared to the previous limit of Super-K and is displayed as "Super-K (15.43 yr)" in figure 2.6. In contrast to [75], the limit in [4] is determined assuming $J_{avg} = 4.56$, $\rho_0 = 0.4$ GeV/cm^3 and $R_0 = 8.127$ kpc (all other assumptions are the same). Therefore, the limit displayed in figure 2.6 is scaled according to the "usual" values of $J_{avg} = 5.0$, $\rho_0 = 0.3$ GeV/cm^3 and $R_0 = 8.5$ kpc for better comparison.

Also, measurements of the Super-K detector of the atmospheric neutrino flux, both $\nu_e + \bar{\nu}_e$ and $\nu_\mu + \bar{\nu}_\mu$, in the neutrino energy range from 100 MeV to 100 GeV are reinterpreted by [4] and [68] to derive the bound on the DM annihilation cross section for DM masses from around 200 MeV to 100 GeV. In both references [4] and [68], the atmospheric flux measurements for data of SK-I to SK-III with parts of the data of SK-IV (in total around 5000 days or $\sim$ 13.70 years of livetime) published by the Super-Kamiokande collaboration in [120] are analyzed. Here, only the more stringent constraint on the DM annihilation cross section of [68] shall be discussed. In the cited work, a monoenergetic $\nu_e + \bar{\nu}_e$ neutrino flux from DM self-annihilation directly into neutrinos with equal branching ratios per flavor in the whole Milky Way is assumed. With this assumed flux and the atmospheric

[12] Considering only the larger statistics, an improvement by a factor of 15.43 yr/7.82 yr $\approx$ 2 is expected. However, the limit obtained in [4] is weaker, since additional background contributions of reactor antineutrinos, spallation products, atmospheric neutral current events and accidental coincidences are considered (for details see [4] and [117]).

flux measurements of Super-K ($\sim$ 13.70 years of runtime and 22.5 kt fiducial volume), a bound on the annihilation cross section is determined using the least square fitting method by comparing the observed and predicted atmospheric neutrino flux. The underlying χ^2 function is defined by the predicted and observed atmospheric electron neutrino flux and the neutrino flux from DM annihilation. In figure 2.6, the 90 % C.L. upper limit on the DM annihilation cross section for DM masses from 200 MeV to 1 GeV of [68] is shown as "Super-K (13.70 yr)". The limit presented in figure 2.6 is again scaled to be comparable with the other limits provided by neutrino detectors[13], since the annihilation of Dirac DM particles (i.e. $\kappa_1 = 4$ in equation 2.2), $J_{avg} = 3.34$ and $\rho_0 = 0.471$ GeV/cm^3 is assumed in [68].

To finalize the section about indirect DM search with neutrinos from DM self-annihilation in the Milky Way, the prospective sensitivity of the future Hyper-Kamiokande experiment investigated in detail in [121] is summarized here[14]. The construction of the Hyper-Kamiokande experiment began in 2020 and start of data taking is predicted to be in 2025 [122]. The design of the Hyper-K water Cherenkov detector will be very similar to the well established Super-K detector, but on a larger scale. In the first phase the detector will consist of one water tank with a total volume of 258 kt, corresponding to a fiducial volume of 187 kt, and be located underground at a depth of around 650 m ($\sim$ 1750 m.w.e.) [122]. The detector will be instrumented with around 40,000 20-inch PMTs providing a photo-sensitive coverage of 40 % to measure the Cherenkov light released in neutrino interactions. The energy resolution is expected to be 12.7 % for deposited energy of 10 MeV. An extensive description about the design and the physics potential of Hyper-K can be found in [122]. Especially due to its large fiducial volume, Hyper-K should essentially improve the existing limits on the annihilation cross section of Super-K for DM masses below 1 GeV.
In [121], the sensitivity of Hyper-K is estimated by using a dedicated detector simulation framework, which is in principle a scaled-up version of the Super-K detector simulation. A monoenergetic neutrino flux produced from direct annihilation of light Majorana DM particles in the Milky Way with $R_0 = 8.5$ kpc and $\rho_0 = 0.3$ GeV/cm^3 is assumed similar to the previously discussed studies. Moreover, also an all-sky analysis, i.e. taking into account the entire Milky Way as source for DM annihilation, with an angular-averaged J-factor based on the NFW model (details in section 4.1) and similar to the canonical value of $J_{avg} = 5$ is performed. The study in [121] concentrates on quasielastic neutrino interactions of ν_e and $\bar{\nu}_e$ on free protons and bound nucleons ($\bar{\nu}_e + p \rightarrow e^+ + n$, $\nu_e + {}^{16}\mathrm{O} \rightarrow e^- + {}^{16}\mathrm{F}$, $\bar{\nu}_e + {}^{16}\mathrm{O} \rightarrow e^+ + {}^{16}\mathrm{N}$), since these are the dominant neutrino interaction modes for neutrino energies below 1 GeV. In addition to the expected neutrino signal from DM annihilation, also possible background events are generated with the Hyper-K detector simulation. The dominant background for neutrino energies above around 50 MeV is due to atmospheric neutrinos, whereas muon-induced spallation products act as main background below 16 MeV and prohibit the search in this low energy region. For energies from 16 MeV to around 50 MeV, Michel electrons and positrons from invisible muons and the DSNB cause background events, which are considered in the simulations. A 90 % C.L. upper limit on the DM annihilation cross section of the Hyper-K detector is predicted in [121] for a fiducial volume of 187 kt and after 20 years of data taking. This limit (estimated for 20 years of data taking with Hyper-K) would improve the currently

[13] In [68], the limit of $\langle \sigma_A \, \mathrm{v} \rangle$ is determined from the flux defined by equation 2.2 using $\kappa_1 = 4$, $J_{avg} = 3.34$ and $\rho_0 = 0.471$ GeV/cm^3 in contrast to the other discussed neutrino experiments, where $\kappa_1 = 2$, $J_{avg} = 5.0$ and $\rho_0 = 0.3$ GeV/cm^3 is assumed. Furthermore, the total $\nu_e + \bar{\nu}_e$ flux and not only the $\bar{\nu}_e$ flux is used to constrain the annihilation cross section. Therefore, to be able to compare the limits correctly, the limit of [68] is scaled in the following way: $\langle \sigma_A \, \mathrm{v} \rangle_{scaled} = 2/4 \cdot 3.34/5.0 \cdot 0.471^2/0.3^2 \cdot 2/1 \cdot \langle \sigma_A \, \mathrm{v} \rangle$.
[14] A very basic sensitivity study about Hyper-Kamiokande was previously published in [115].

most stringent limits of Super-K (shown in figure 2.6 and presented above) in the whole DM mass range from 17 MeV to 1 GeV by a factor of 3 to 24 mainly due to the larger exposure.
Furthermore, also the sensitivity of Hyper-K after adding gadolinium at a level of 0.1 % into the water is discussed in [121]. As already mentioned above, this would allow to tag the neutron capture of inverse β decay reactions due to gadolinium's large neutron capture efficiency and the released neutron capture energy of around 8 MeV, which surpasses the energy threshold $E_{thr.} \sim 4.5$ MeV of water Cherenkov detectors. The possibility of neutron tagging in the IBD channel would reduce the background of invisible muons by 70 % and further improves Hyper-K's estimated limit on the annihilation cross section below 70 MeV by factor of around 2 [121].

To further extend and improve the existing and proposed limits on the DM annihilation cross section of neutrino experiments presented in this section, the sensitivity to measure neutrinos from DM self-annihilation in the Milky Way as an excess over backgrounds with two future neutrino experiments, JUNO and THEIA, is investigated within this thesis. Chapters 3 to 7 introduce the JUNO experiment and study JUNO's sensitivity for indirect DM search with neutrinos. THEIA's sensitivity is determined in chapter 8.

3. The Jiangmen Underground Neutrino Observatory

The Jiangmen Underground Neutrino Observatory (JUNO) is a multi-purpose neutrino experiment with a large and versatile physics program. The collaboration consists of 670 members from 77 institutes in 18 countries. The observatory is sited in South China in the Jiangmen prefecture and currently under construction. It is planned to be fully setup to start data taking by mid of 2023. The location at medium-baseline to two powerful nuclear power plants (NPPs) opens JUNO the opportunity to answer one of today's most important open questions of neutrino physics, the neutrino mass ordering. Moreover, JUNO also provides great physics potential for almost all fields of neutrino physics, which is described in section 3.1. In section 3.2, possible neutrino interaction channels in JUNO are discussed. The instrument to achieve the physics goals is the JUNO detector, a 20 kt liquid scintillator detector, which is introduced in section 3.3. JUNO's offline simulation and analysis framework is presented in section 3.4. This chapter is mostly based on [5,123,124], where also more detailed information can be found.

3.1. JUNO's Neutrino Physics Program

JUNO will explore a broad field of neutrino physics in the upcoming years. This section introduces general information about neutrinos and covers the extensive neutrino physics program of JUNO. Section 3.1.1 summarizes neutrino physics in general from its fundamental characteristics through the principle of neutrino oscillations to the currently open questions in neutrino physics. In the subsequent sections 3.1.2 to 3.1.8, different neutrino sources are introduced in general terms and, furthermore, JUNO's potential and ability to measure neutrinos from these different sources are presented.

3.1.1. Neutrino Physics in General

Since 1930, when Pauli postulated the neutrino as hypothetical particle to explain the continuous energy spectrum of the β-decay without breaking the law of energy and momentum conservation [125], physicists are aiming to measure neutrinos and their properties. Cowan and Reines succeeded in the first measurement of neutrinos, more precisely of electron antineutrinos, 26 years later, in 1956 [126].
In the Standard Model of Particle Physics (SM), neutrinos are massless elementary Dirac fermions without electric charge and only interacting via the weak interaction [1, 127].

They are produced and observed in three different flavors (electron neutrino ν_e, muon neutrino ν_μ and tau neutrino ν_τ, with their antiparticles $\bar{\nu}_e$, $\bar{\nu}_\mu$ and $\bar{\nu}_\tau$) associated to the corresponding charged lepton. Neutrinos (antineutrinos) occur only in left-handed (right-handed) chirality because of the violation of parity symmetry in the weak interaction [128–130]. The fact that neutrinos are only weakly interacting results in very small interaction cross sections of neutrinos with matter [131] and therefore makes it challenging to investigate and determine their properties.
Neutrinos can originate from various sources, which can be divided into two groups: natural neutrino sources (like e.g. the Earth, the Sun, the atmosphere and supernovae) and artificial neutrino sources (like NPPs and particle accelerators).

Neutrino Oscillations in General

The need to extend the neutrino model described in the SM first came up after the measurements of Davis et al. [132]. They observed a significant deficit in the flux of electron neutrinos from the Sun compared to predictions of the solar standard model (SSM). The measured electron neutrino flux covered only around one third of the expected flux of the SSM. This lack of ν_e's could neither be explained by statistical or systematical effects from the detector setup [133] nor with modifications of the SSM [134] and was further confirmed by subsequent solar neutrino experiments as Gallex/GNO and SAGE [135–137]. This deficit, also denoted as solar neutrino problem, could be solved and explained by a periodic change from one neutrino flavor to another [5], the *neutrino oscillation*. Neutrino oscillation requires the mixing of lepton flavors and finite neutrino masses, which results in violating the individual lepton flavor conservation and the existence of at least one massive neutrino (i.e. non-vanishing neutrino mass differences). Thus, neutrino oscillation gives evidence to neutrino physics beyond the SM [5].
The formalism to describe neutrino flavor mixture can be introduced corresponding to the Cabbibo-Kobayashi-Maskawa (CKM) formalism of flavor mixing in the quark sector [1]. The terms for neutrino flavor mixing are on the one hand non-vanishing neutrino mass differences and on the other hand, that neutrino flavor eigenstates of the weak interaction differ from neutrino mass eigenstates. The flavor eigenstates couple to $W^\pm$ bosons in the weak interaction, whereas the mass eigenstates diagonalize the Hamiltonian of the free neutrino and therefore describe its evolution in time and propagation in space [1]. Both eigenstates form a complete and orthonormal basis of neutrino states within the SM and are related to each other by the unitary Pontecorvo-Maki-Nakagawa-Sakata (PMNS) matrix U [5]:

$$|\nu_\alpha\rangle = \sum_k U_{\alpha k} |\nu_k\rangle \text{ and } |\nu_k\rangle = \sum_k U^*_{\alpha k} |\nu_\alpha\rangle \tag{3.1}$$

with the mass eigenstates $|\nu_k\rangle$ ($k = 1, 2, 3, ...$) and the flavor eigenstates $|\nu_\alpha\rangle$ ($\alpha = 1, 2, 3, ...$).
In standard three-neutrino theory, where the mixing of all three neutrino flavors (ν_e, ν_μ, ν_τ) and mass eigenstates (ν_1, ν_2, ν_3) of the SM is considered, the PMNS matrix U reduces to a 3×3 unitary matrix and can be parametrized with three mixing angles θ_{ij} ($ij = 12, 13, 23$) and one CP violating phase δ:

$$
\begin{aligned}
U &= \begin{pmatrix} U_{e1} & U_{e2} & U_{e3} \\ U_{\mu 1} & U_{\mu 2} & U_{\mu 3} \\ U_{\tau 1} & U_{\tau 2} & U_{\tau 3} \end{pmatrix} \\
&= \begin{pmatrix} 1 & 0 & 0 \\ 0 & c_{23} & s_{23} \\ 0 & -s_{23} & c_{23} \end{pmatrix} \begin{pmatrix} c_{13} & 0 & s_{13}e^{-i\delta} \\ 0 & 1 & 0 \\ -s_{13}e^{i\delta} & 0 & c_{13} \end{pmatrix} \begin{pmatrix} c_{12} & s_{12} & 0 \\ -s_{12} & c_{12} & 0 \\ 0 & 0 & 1 \end{pmatrix},
\end{aligned} \tag{3.2}
$$

where $s_{ij} \equiv \sin\theta_{ij}$ and $c_{ij} \equiv \cos\theta_{ij}$ are defined [5].
The spatial propagation and temporal evolution of neutrinos in their mass eigenstates $|\nu_k\rangle$ can be described with the standard Hamiltonian. This results in

$$
|\nu_k(x,t)\rangle = e^{i(p_k x - E_k t)} \, |\nu_k(x=0,t=0)\rangle \tag{3.3}
$$

assuming a relativistic neutrino with momentum p and energy E at position x after time t. If a neutrino was generated via the weak interaction in the flavor eigenstate $|\nu_\alpha\rangle$, this neutrino can be detected in a weak interaction process in the flavor eigenstate $|\nu_\beta\rangle$ after traveling a distance L. The transition probability that a neutrino produced as ν_α is detected as ν_β is:

$$
P_{\nu_\alpha \to \nu_\beta} = |\langle \nu_\beta \,|\, \nu_\alpha(E,L)\rangle|^2 = \left| \sum_k U^*_{\alpha k} U_{\beta k} e^{-i\frac{m_k^2 L}{2E}} \right|^2 . \tag{3.4}
$$

Introducing the squared mass difference $\Delta m^2_{kj} = m^2_k - m^2_j$, this can be written more conveniently as:

$$
\begin{aligned}
P_{\nu_\alpha \to \nu_\beta}(E,L) = \delta_{\alpha\beta} &- 4 \sum_{k>j} \mathrm{Re}\left(U^*_{\alpha k} U_{\beta k} U_{\alpha j} U^*_{\beta j}\right) \sin^2\left(\frac{\Delta m^2_{kj} \, L}{4E}\right) \\
&+ 2 \sum_{k>j} \mathrm{Im}\left(U^*_{\alpha k} U_{\beta k} U_{\alpha j} U^*_{\beta j}\right) \sin\left(\frac{\Delta m^2_{kj} \, L}{2E}\right).
\end{aligned} \tag{3.5}
$$

The survival probability of electron antineutrinos in the three flavor vacuum oscillation model is given as an example in equation 3.6. This $\bar{\nu}_e$ survival probability opens the possibility to determine the neutrino mass ordering, which is described in section 3.1.2 in more detail.

$$
\begin{aligned}
P_{\bar{\nu}_e \to \bar{\nu}_e} = 1 &- \sin^2(2\theta_{12}) c_{13}^4 \sin^2\left(\frac{\Delta m^2_{21} L}{4E}\right) \\
&- \sin^2(2\theta_{13}) \left[c_{12}^2 \sin^2\left(\frac{\Delta m^2_{31} L}{4E}\right) + s_{12}^2 \sin^2\left(\frac{\Delta m^2_{32} L}{4E}\right) \right]
\end{aligned} \tag{3.6}
$$

The flavor oscillation of neutrinos is a well established model and its existence was finally proven by the Sudbury Neutrino Observatory (SNO) [138,139] and the Super-Kamiokande experiment [140, 141]. Nowadays, neutrino oscillation has been observed in various other experiments and for nearly all kinds of flavor transitions, see e.g. KamLAND [109],

Table 3.1.: Three flavor oscillation parameters from fit to global data as of July 2020 for normal (NO) and inverted (IO) neutrino mass ordering. The results are obtained with the inclusion of the tabulated χ^2 data on atmospheric neutrinos provided by the Super-Kamiokande collaboration [149]. Note that Δm^2_{3l} defines the large mass difference with $\Delta m^2_{3l} = \Delta m^2_{31} > 0$ for NO and $\Delta m^2_{3l} = \Delta m^2_{32} < 0$ for IO. Data taken from [150].

	Normal ordering (best fit)	Inverted ordering ($\Delta\chi^2 = 7.1$)
	best fit $\pm 3\sigma$	best fit $\pm 3\sigma$
$\sin^2\theta_{12}$	$0.304^{+0.039}_{-0.035}$	$0.304^{+0.039}_{-0.035}$
θ_{12} in $^\circ$	$33.44^{+2.42}_{-2.17}$	$33.45^{+2.42}_{-2.18}$
$\sin^2\theta_{23}$	$0.573^{+0.043}_{-0.158}$	$0.575^{+0.042}_{-0.156}$
θ_{23} in $^\circ$	$49.2^{+2.5}_{-9.1}$	$49.3^{+2.5}_{-9.0}$
$\sin^2\theta_{13}$	$0.02219^{+0.00191}_{-0.00187}$	$0.02238^{+0.00190}_{-0.00186}$
θ_{13} in $^\circ$	$8.57^{+0.36}_{-0.37}$	$8.60^{+0.36}_{-0.36}$
δ_{CP} in $^\circ$	197^{+172}_{-77}	282^{+70}_{-89}
Δm^2_{21} in $10^{-5}\,\mathrm{eV}^2$	$7.42^{+0.62}_{-0.60}$	$7.42^{+0.62}_{-0.60}$
Δm^2_{3l} in $10^{-3}\,\mathrm{eV}^2$	$+2.517^{+0.081}_{-0.082}$	$-2.498^{+0.084}_{-0.083}$

T2K [142], NOvA [143], MINOS [144], Double Chooz [145], DayaBay [146], RENO [147] and OPERA [148].
The current best fit values of all oscillation parameters (i.e. the three mixing angles, two squared mass differences and the CP violating phase) can be determined by using a complete set of available experimental data. The best fit values of this global fit are shown in table 3.1. The sign of Δm^2_{3l} determines the still unknown neutrino mass ordering, which will be discussed in section 3.1.2. Moreover, the octant of θ_{23} and the CP violating phase δ_{CP} are unidentified until now as illustrated in table 3.1.

Open Questions in Neutrino Physics

The fact that neutrinos are massive particles[1], which is proven by the existence of neutrino oscillations, raised further questions on their properties and the underlying model. In the following, the main open questions in neutrino physics are presented exemplarily [5]:

- **Neutrino mass ordering:** The neutrino mass ordering, i.e. the sign of the large mass difference, is not yet determined. Several experiments aim to identify the mass ordering in the near future, e.g. JUNO [5], NOvA [151], DUNE [152, 153], Hyper-Kamiokande [122] or IceCube-PINGU [154]. JUNO's sensitivity to the mass ordering determination is discussed in section 3.1.2 in detail.

- **Absolute neutrino mass:** The neutrino mass can either be investigated in direct neutrino mass measurements with β-endpoint spectroscopy, like e.g. in KATRIN [155] and ECHo [156], or with neutrino-less double β ($0\nu\beta\beta$) decay experiments, since the effective neutrino mass $\langle m_{\beta\beta}\rangle = \left|\sum_i U^2_{ei} m_{\nu_i}\right|$ is correlated with the lifetime of the $0\nu\beta\beta$ decay. Corresponding experiments are e.g. GERDA [157], LEGEND [158] and KamLAND-Zen [159]. The currently best limit on the electron antineutrino mass from direct mass measurements is $m_{\bar{\nu}_e} < 1.1$ eV (90 % C.L.) provided by KATRIN [155]. The limit from $0\nu\beta\beta$ experiments on the effective mass

[1] At least two of the three neutrino mass eigenstate have finite mass.

is $\langle m_{\beta\beta} \rangle \leq 0.061 - 0.165$ eV (90 % C.L.) obtained by KamLAND-Zen [159] only valid, if neutrinos are Majorana particles[2]. Moreover also model-dependent upper limits on the sum of neutrino mass eigenstates can be derived from analyses of the cosmic microwave background (CMB) and structure formation in the universe. The most robust constraints are given by the Planck collaboration with $\sum m_\nu < 0.12$ eV (95 % C.L.) [160].

- **Dirac or Majorana particle:** The neutrino's particle character can be either Dirac or Majorana. By definition, a Majorana particle is its own antiparticle [161]. A massive Majorana neutrino would lead to lepton number violation as a direct consequence [5]. At present the only experimentally feasible way to probe the Majorana nature of neutrinos is the observation of $0\nu\beta\beta$ decays, as it is done e.g. in GERDA [157] or its follow-up experiment LEGEND. Until now, no evidence for neutrinos being of Majorana character has been established.

- **CP violation:** Violation of the CP symmetry, the symmetry of physical behavior of particles and antiparticles, was already observed in the quark sector and is assumed to be also present in the neutrino sector, which would partially explain the observed particle-antiparticle imbalance in the universe [5]. Several existing and up-coming experiments like NOvA, DUNE, Hyper-K and T2K aim to measure the CP-violating phase δ in the neutrino sector.

- **Sterile neutrinos:** One fundamental question in neutrino physics and cosmology is whether there exist extra species of neutrinos, which do not directly participate in the standard weak interactions [5]. These sterile neutrinos cannot be detected directly, but would either slightly modify the oscillation pattern of the three flavor oscillation or violate the unitarity of the 3×3 PMNS mixing matrix. High precision measurements of the mixing parameters with e.g. JUNO , DUNE and Hyper-K could prove the unitarity of the PMNS matrix and the existence of sterile neutrinos in the future.

3.1.2. Reactor Neutrinos in General and in JUNO

Reactor neutrinos are electron antineutrinos emitted from subsequent β-decays of instable fission fragments produced in nuclear fission processes in NPPs [5]. They represent the largest amount of artificially produced neutrinos on Earth. This section first introduces reactor neutrinos in general and then concentrates on the expected reactor neutrino spectrum in JUNO and JUNO's potential to determine the neutrino mass ordering and to quantify neutrino oscillation parameters precisely by measuring the reactor spectrum.
This section will focus on reactor neutrinos from pressurized water reactors (PWR), since all NPPs close to the JUNO detector site are PWRs. In these reactors, the fission of the four fuel isotopes ^{235}U, ^{238}U, ^{239}Pu and ^{241}Pu constitute more than 99.7 % of the thermal power and reactor electron antineutrinos [5]. Reactor neutrino fluxes per fission of each isotope $\phi_{f,i}$ can be determined either by the inversion of the measured β-spectra of the four isotopes [162, 163] or by the summation of β-decay branches of the fission products [164, 165]. The reactor electron antineutrino flux is given by

$$\frac{\mathrm{d}\phi_{\bar{\nu}_e}^{reactor}(E_{\bar{\nu}_e})}{\mathrm{d}E_{\bar{\nu}_e}} = W_{th} R_f \sum_{i=0}^{3} F_i \frac{\mathrm{d}\phi_{f,i}(E_{\bar{\nu}_e})}{\mathrm{d}E_{\bar{\nu}_e}} \tag{3.7}$$

[2]The upper limit of $\langle m_{\beta\beta} \rangle$ of KamLAND-Zen is obtained under the assumption that the $0\nu\beta\beta$ decay mechanism is dominated by exchange of a pure-Majorana Standard model neutrino and includes the uncertainties in U_{ei} and the neutrino mass splitting. Moreover, it can be translated to a 90 % C.L. upper limit of $m_{lightest} < (0.18 - 0.48)$ meV [159].

with the total thermal power W_{th}, the fission rate R_f (i.e. the number of fission per released thermal energy) and the fission fraction F_i of each fission isotope, which can be estimated with core simulations and thermal power measurements [5].
The reactor neutrino flux and its corresponding spectrum at a certain detector site depends on the distance of the detector to the specific NPP due to neutrino oscillations. This spatial dependency allows the observation of different oscillation parameter spaces. Short baseline experiments with distances between detector and reactor core of around 1 km and an additional detector close to the reactor as reference, like DayaBay [146], Double Chooz [145] and RENO [147], are sensitive to the mixing angle θ_{13}. Moreover these short baseline experiments provide the most precise measurements of the reactor neutrino flux. In particular, DayaBay measured the reactor $\bar{\nu}_e$-flux with a total uncertainty of 1.5 % [166]. Medium baseline experiments like JUNO enable precision measurements of θ_{12}, Δm^2_{21} and $|\Delta m^2_{ee}| = |\cos^2\theta_{12}\Delta m^2_{31} + \sin^2\theta_{12}\Delta m^2_{32}|$ and furthermore the determination of the neutrino mass ordering.

Reactor Neutrino Spectrum in JUNO

The JUNO detector is located around 53 km away from two NPPs, the Taishan NPP and Yangjiang NPP. At the beginning of JUNO's data taking in 2023, the combined thermal power will be 26.6 GW, while a combined thermal power of 35.8 GW is expected as soon as all reactor cores are running (for more details see [5]).
The expected reactor neutrino spectrum $\frac{\mathrm{d}N^{reactor}}{\mathrm{d}E_{\bar{\nu}_e}} \propto \sigma_{IBD}\ \phi^{reactor}_{\bar{\nu}_e}\ P_{\bar{\nu}_e\to\bar{\nu}_e}$ in JUNO, measured via the inverse β decay (IBD) interaction channel with the IBD interaction cross section σ_{IBD} (details in section 3.2), can be derived from the reactor neutrino flux $\phi^{reactor}_{\bar{\nu}_e}$ of equation 3.7 by considering the three flavor oscillations $P_{\bar{\nu}_e\to\bar{\nu}_e}$ introduced in section 3.1.1. After defining the phase ϕ as [5]

$$\sin\phi = \frac{\cos^2\theta_{12}\sin\left(2\sin\theta_{12}\Delta_{21}\right) - \sin^2\theta_{12}\sin\left(2\cos^2\theta_{12}\Delta_{21}\right)}{\sqrt{1-\sin^2(2\theta_{12})\sin^2\Delta_{21}}} \tag{3.8}$$

and with $\Delta_{ij} = \frac{\Delta m^2_{ij} L}{4E}$, the survival probability of electron antineutrinos of equation 3.6 is given by

$$\begin{aligned} P_{\bar{\nu}_e\to\bar{\nu}_e} = 1 &- \sin^2(2\theta_{12})\cos^4\theta_{13}\sin^2\Delta_{21} \\ &- \frac{1}{2}\sin^2(2\theta_{13})\left[1 - \sqrt{1-\sin^2(2\theta_{12})\sin^2\Delta_{21}}\cdot\cos\left(2|\Delta_{ee}| \pm \phi\right)\right], \end{aligned} \tag{3.9}$$

where the ± sign depends on the neutrino mass ordering, i.e. "+" for normal mass ordering and "-" for inverted mass ordering.

The resulting electron antineutrino spectrum of JUNO is shown in figure 3.1. The mixing angles θ_{12} and θ_{13} fix the oscillation amplitudes, while the oscillation frequency is set by the squared mass differences Δm^2_{21} and Δm^2_{32}.

Neutrino Mass Ordering Determination with JUNO

The ordering of the neutrino masses is one of the main open questions of neutrino oscillation and neutrino physics. As already mentioned in previous sections and shown in table 3.1, the sign of the large squared mass difference is unknown. Since the mass ordering of the small squared mass difference $\Delta m^2_{21} = m^2_2 - m^2_1 > 0$ was ascertained by matter-induced oscillation for solar neutrinos [37], two possibilities remain for the arrangement of mass eigenstate m_3:

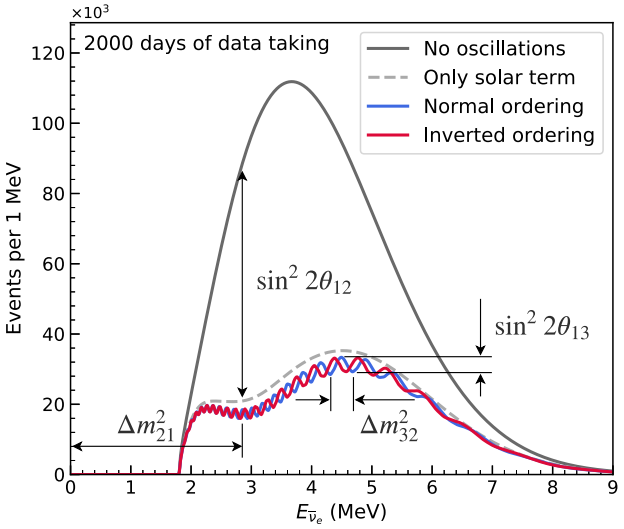

Figure 3.1.: Expected reactor electron antineutrino spectrum, $\frac{\mathrm{d}N^{reactor}}{\mathrm{d}E_{\bar{\nu}_e}} \propto \sigma_{IBD}\ \phi^{reactor}_{\bar{\nu}_e}\ P_{\bar{\nu}_e \to \bar{\nu}_e}$, for the location of JUNO at baseline of $L = 53\,\mathrm{km}$. The expected reactor spectrum without neutrino oscillations is shown as solid gray line, whereas the spectrum taking account of the reduction due to the solar oscillation term (first part of equation 3.9) is shown as dashed gray line. Moreover the spectrum with full three flavor oscillation is illustrated for normal (blue) and inverted (red) neutrino mass ordering. Around 83 IBD events from reactor electron antineutrinos per day are expected in JUNO [5]. Image provided by JUNO collaboration.

1. m_3 is heavier than m_1 and m_2 ($m_1 < m_2 < m_3$), called **normal neutrino mass ordering (NO)**, or
2. m_3 is lighter than m_1 and m_2 ($m_3 < m_1 < m_2$), called **inverted neutrino mass ordering (IO)**.

Both cases are sketched in figure 3.2.

The model-independent determination of the mass ordering is the main goal of JUNO and can be derived from high precision measurements of JUNO's reactor neutrino spectrum shown in figure 3.1. The small differences in the spectrum originate from the $\pm$ sign of phase ϕ in equation 3.9 and are represented by a phase-shift in the fast oscillation pattern. The observed reactor spectrum can be fitted to the expectations of neutrino oscillation patterns of equation 3.9 and a frequency analysis of the spectrum can determine the sign of phase ϕ [5]. This results in a preferred sign of ϕ, where a positive phase corresponds to normal mass ordering and a negative phase to inverted mass ordering, respectively [123]. Considering uncertainties depending on the detector performance, the background distribution and the reactor neutrino flux, and taking into account the spatial distribution of the reactor cores (see [5]), a median sensitivity of JUNO to determine the mass ordering of $\sim 3\,\sigma$ is expected after six years of data taking [5]. This sensitivity can be further improved by combining atmospheric and reactor neutrino measurements in JUNO, which will shortly be discussed in section 3.1.7.
The determination of the neutrino mass ordering has profound impacts on our understanding of the neutrino physics, neutrino astronomy and neutrino cosmology [5]. It helps to define the goals of $0\nu\beta\beta$ search experiments and is a crucial information to understand the origin of neutrino mass generation and for measuring the CP violating phase in the lepton sector. Moreover it is also a key parameter of neutrino astronomy and neutrino cosmology, e.g. to probe the neutrino mass scale with cosmological constraints or to investigate the

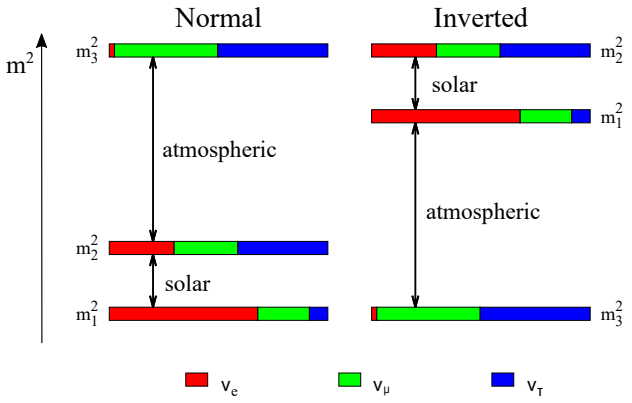

Figure 3.2.: Illustration of the arrangement of neutrino mass eigenstates in normal and inverted mass ordering. Mass eigenstate m_1 is by definition the one with highest ν_e contribution. The flavor content of each mass eigenstate is indicated color-coded. Taken from [5].

supernova nucleosynthesis further.

Precision Measurements of Neutrinos with JUNO

The study of neutrino oscillation parameters with high precision is possible in JUNO, since it will simultaneously measure neutrino oscillation driven by the solar, $\Delta m^2_{solar} \equiv \Delta m^2_{21}$, and atmospheric, $\Delta m^2_{atm} \equiv |\Delta m^2_{32}| \approx |\Delta m^2_{31}|$, squared mass differences in one reactor neutrino spectrum from one source [123]. JUNO aims to measure the oscillation parameters $\sin^2\theta_{12}$, Δm^2_{21} and $|\Delta m^2_{ee}|$ with uncertainties of less than 1 % after a detector runtime of ten years [5]. With these high precision measurements better constraints on the unitarity of the PMNS matrix can be provided, which will help to clarify the existence of additional neutrino flavors.

3.1.3. Solar Neutrinos in General and in JUNO

Solar neutrinos are created in the Sun's core in thermonuclear fusion processes. The main fusion process in the Sun is the proton-proton reaction chain (pp-chain) initiated by proton-proton fusion. The neutrinos are labeled depending on their production reaction as *pp*-, *pep*-, *hep*-, ^{7}Be- and ^{8}B-neutrinos. The second process is the catalytic carbon-nitrogen-oxygen cycle (CNO-cycle), which only contributes less than around 1 % to the solar luminosity [167]. Solar neutrinos are electron neutrinos with an average energy of $\langle E_{\nu_e} \rangle \approx 0.53$ MeV (up to around 19 MeV) [168]. All neutrinos of the pp-chain, except of *hep*-neutrinos, were measured by several solar neutrino experiments like e.g. Borexino [167, 169] and SNO [138, 139]. In 2020, the Borexino collaboration first reported experimental evidence for neutrinos produced in the CNO-cycle in the Sun [170].
JUNO will also contribute to the investigation of solar neutrinos due to its instrumentation and high energy resolution (see section 3.3) by measuring ^{7}Be- and ^{8}B-neutrinos [5, 171]. The expected signal spectrum of ^{8}B-neutrinos together with the background spectra in JUNO after 10 years of data taking is shown in figure 3.3.

3.1.4. Geo-Neutrinos in General and in JUNO

Geo-neutrinos originate from decays of radionuclides naturally occurring in the Earth and can give information about the chemical composition of the Earth's core, mantle

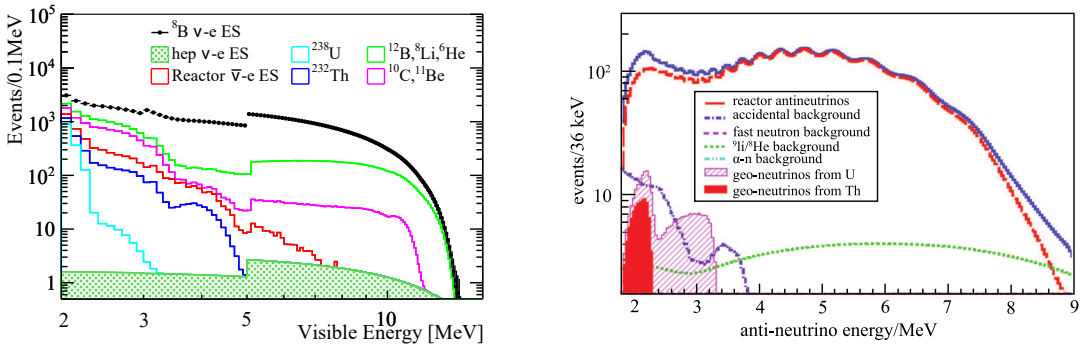

Figure 3.3.: Left: Expected signal spectrum of ^{8}B-neutrinos and the corresponding background spectra in JUNO after ten years of data taking, with all selection cuts and muon veto methods applied. The energy dependent fiducial volumes to reduce the external radioactivity background account for the discontinuities at 3 MeV and 5 MeV. Details in [171]. Right: Expected energy spectra of geo-neutrinos, reactor antineutrinos, and other non-antineutrino backgrounds in JUNO for one year of data-taking. The total spectrum, i.e. geo-neutrino signal and backgrounds, is indicated as solid blue line. Geo-neutrinos from ^{232}Th are marked as red area, geo-neutrinos from ^{238}U as pink hatched area. Details in [177].

and crust. Geo-neutrinos are electron antineutrinos with energies up to 3.27 MeV [172] mainly produced in β-decay chains of ^{238}U, ^{232}Th and ^{40}K [3]. These isotopes account for more than 99 % of the present-day radiogenic heat generated inside the Earth [5]. KamLAND [173, 174] and Borexino [175, 176] have measured geo-neutrinos from β-decay of ^{238}U and ^{232}Th up to now.
Due to its size, its low energy threshold and great energy resolution, the detection of an unprecedented number of geo-neutrinos is possible with JUNO, which gives the opportunity to explore the origin and thermal evolution of the Earth further [177]. In figure 3.3, the expected geo-neutrino spectrum in JUNO simulated for one year of data taking and the corresponding background spectra are shown.

3.1.5. Supernova Burst Neutrinos in General and in JUNO

99 % of a supernova's energy is carried away by a burst of neutrinos and antineutrinos of all flavors in a time interval of about 10 seconds. Due to this high expected neutrino flux, neutrino detectors can represent one main part of multi messenger astronomy in case of a galactic supernova [5]. Moreover, neutrino observatories can act as an early warning alert for supernovae to be used to direct other telescopes to the part of the sky, where the supernovae explosion occurred [178].
In case a galactic supernova appears during JUNO's operation time, JUNO will provide high statistics of supernova neutrinos of all flavors as a large scale neutrino detector. Assuming a core-collapse supernova with typical supernova parameters at a typical galactic distance of around 10 kpc, JUNO will measure approximately 5000 neutrino events from the inverse β decay channel, around 2000 events from all-flavor elastic neutrino-proton scattering and circa 300 neutrino-electron scattering events [5]. Therefore JUNO could help to clarify open questions about supernovae like the neutrino-driven explosion mechanism and nucleosynthesis.

[3] Geo-neutrinos from the β-decay of ^{40}K cannot be detected in liquid scintillator detectors via IBD reactions, since their energy is below the IBD threshold.

3.1.6. Diffuse Supernova Neutrino Background in General and in JUNO

The integrated neutrino flux from all past core-collapse supernovae in the visible universe forms the diffuse supernova neutrino background (DSNB), containing information about the cosmic star formation rate, the average core-collapse supernova neutrino spectrum and the rate of failed supernovae [5, 179]. Until now, the DSNB was not measured by present neutrino experiments, but upper limits on the diffuse supernova $\bar{\nu}_e$-flux are set. The currently best limit is provided by Super-Kamiokande setting an upper limit of $(2.8-3.0)\,\mathrm{cm}^{-2}\mathrm{s}^{-1}$ on the $\bar{\nu}_e$-flux at 90 % C.L. for $E_{\bar{\nu}_e} \geq 17.3$ MeV [180].
JUNO could be one of the first experiments to measure the DSNB successfully with a signal prediction of 5.5 events per year because of measurements of electron antineutrinos via the inverse β decay and effective background reduction [179]. A DSNB detection significance of $4\,\sigma$ after 10 years of data taking is expected for JUNO [179]. Detailed information about the DSNB in JUNO is given in section 5.2.

3.1.7. Atmospheric Neutrinos in General and in JUNO

Atmospheric neutrinos are produced in the atmosphere of the Earth as a result of cosmic ray interactions and weak decays of secondary mesons, in particular pions and kaons [5]. These atmospheric neutrinos can have energies from MeV to the PeV scale [181]. For energies below around 1 GeV, their production is dominated by the following decay channels [5]:

$$\pi^+ \to \mu^+ + \nu_\mu, \qquad \mu^+ \to e^+ + \bar{\nu}_\mu + \nu_e \tag{3.10}$$

$$\pi^- \to \mu^- + \bar{\nu}_\mu, \qquad \mu^- \to e^- + \nu_\mu + \bar{\nu}_e \tag{3.11}$$

The flux ratio $(\phi_{\nu_\mu}+\phi_{\bar{\nu}_\mu})/(\phi_{\nu_e}+\phi_{\bar{\nu}_e})$ is around two at ~ 1 GeV and increases as the energy increases, since more muons are likely to reach the Earth's surface without decaying [182]. The atmospheric neutrino flux at Earth, which depends on the location on Earth according to the geomagnetic field, contains all three neutrino and antineutrino flavors because of neutrino oscillation [181]. The existence of changes of neutrino flavor eigenstates was first discovered by measuring atmospheric neutrinos in Super-K [140]. The leading atmospheric neutrino oscillation parameters θ_{23} and $|\Delta m^2_{31}|$ have been measured by several experiments like e.g. Super-K [183], IceCube [184] and MINOS [185]. Moreover, future atmospheric neutrino detectors as e.g. Hyper-K [122], INO [186], IceCube-PINGU [154] and KM3NeT/ORCA [187] will be sensitive to sub-dominant three-flavor oscillation effects like the neutrino mass ordering, the octant of θ_{23} and CP violation [188].
JUNO will have great potential to measure the low energetic atmospheric neutrino spectrum from 100 MeV to 10 GeV and will be one of the few liquid scintillator detectors contributing to atmospheric neutrino measurements [182]. Moreover, for upward atmospheric neutrinos, the oscillation probabilities $P_{\nu_\mu\to\nu_\mu}$ and $P_{\nu_e\to\nu_\mu}$ differ for NO and IO due to the MSW matter effect [5]. JUNO can reach a conservative NMO sensitivity of $0.9\,\sigma$ (and an optimistic sensitivity of $1.8\,\sigma$) for 10 years of data taking by measuring atmospheric neutrinos, which is complementary to the NMO sensitivity from the JUNO reactor neutrino results discussed in section 3.1.2 and will further improve JUNO sensitivity to determine the NMO (for more details about the analysis see [189]).

3.1.8. Neutrinos from Dark Matter Annihilation in General and in JUNO

Neutrino detectors can contribute to indirect DM searches as already discussed in detail in section 2.4. JUNO's sensitivity to measure neutrinos produced in WIMP self-annihilation

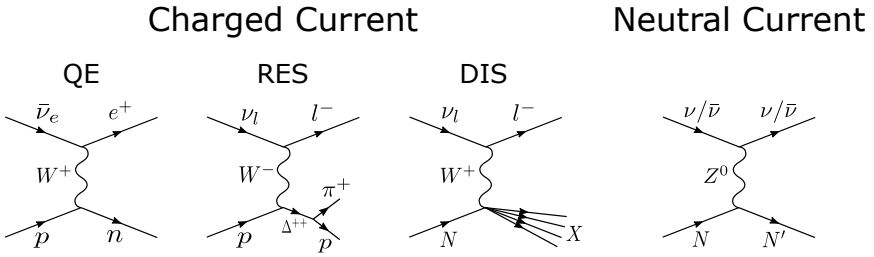

Figure 3.4.: Feynman diagrams of typical charged and neutral current neutrino interactions: quasielastic (QE) scattering (the IBD channel is shown here), resonant neutrino scattering (RES) and deep inelastic scattering (DIS) of CC interactions, and NC interactions in general.

in the Sun for DM masses from 4 GeV to 20 GeV is investigated in [5] and [190] similar to studies of Super-Kamiokande described in section 2.4. In [190], three annihilation channel ($DM + DM \rightarrow \nu\bar{\nu}, \tau^+\tau^-, b\bar{b}$) are studied and JUNO's ability to measure the $\nu_e/\bar{\nu}_e$ signal spectra of these channels is simulated. This is translated into a 90 % C.L. upper limit on the spin-independent and spin-dependent DM-nucleon scattering cross section (σ^{SI}_{scat} and σ^{SD}_{scat}) taking into account selection efficiencies and atmospheric neutrino background from charged and neutral current interactions. Additionally, in [5], a similar study is performed for JUNO according to an expected $\nu_\mu/\bar{\nu}_\mu$ signal, which results in nearly identical limits. The predicted upper limits of JUNO after an assumed runtime of 10 years and for the annihilation channel into $\tau^+\tau^-$ are $\sigma^{SI}_{scat} \approx (0.4 - 2.0) \cdot 10^{-41}$ cm^2 and $\sigma^{SD}_{scat} \approx 3 \cdot 10^{-40}$ cm^2 in the DM mass range from 4 GeV to 20 GeV. They are a factor of 1.5 to 3.5 less stringent than the limits obtained by Super-K for 10.7 years of data discussed in section 2.4 and shown in figure 2.4 and 2.5.
Beyond that, JUNO's sensitivity to measure neutrinos from annihilation of light DM particles with masses from 10 MeV to 100 MeV is investigated within this thesis for the first time.

3.2. Neutrino Interactions in JUNO

The fact that neutrinos only interact with matter via weak processes entails two important characteristics. On the one hand neutrinos are perfectly suited to study the weak interaction theory precisely, but on the other hand interaction cross sections of neutrinos with matter are small compared to electromagnetic and strong interactions.
Neutrino reactions with matter can be separated into two groups depending on the exchanged gauge boson. The exchange of a neutral Z boson is called neutral current (NC) interaction, where the neutrino's flavor is unaffected and no charge is exchanged. In contrast to that, the exchange of a charged $W^\pm$ boson describes the charged current (CC) interaction, transforming neutrinos to leptons of the same family and vice versa. Depending on the neutrino's energy it can be further distinguished between elastic/quasielastic scattering, resonant neutrino scattering and deep inelastic scattering [131]. In figure 3.4, Feynman diagrams for typical CC and NC neutrino interactions are shown exemplarily.

The target material in liquid scintillator (LS) detectors like JUNO consists of organic molecules for the most part. Therefore, neutrino interactions on free protons, ^{12}C nuclei and electrons arise. The dominant neutrino cross sections on these target particles are presented in figure 3.5 for energies of the incoming neutrinos up to 100 MeV.

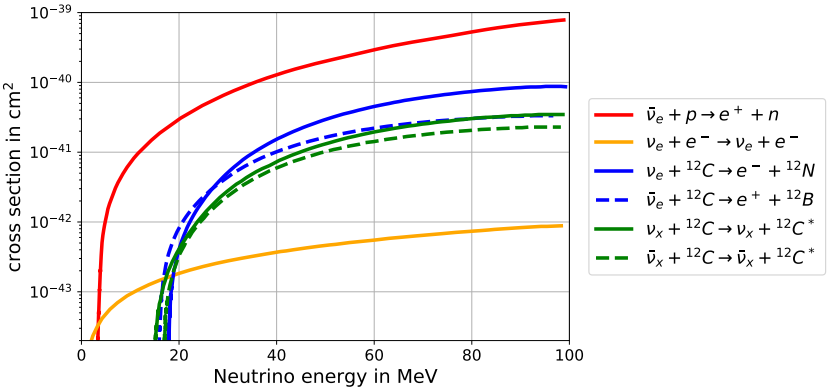

Figure 3.5.: Cross sections of different neutrino interaction channels for energies up to 100 MeV. The dominating cross section of the CC-QE IBD reaction $\bar{\nu}_e + p \to e^+ + n$ is shown in red. Cross sections of CC-QE interactions on ^{12}C ($\nu_e + {}^{12}\text{C} \to e^- + {}^{12}\text{N}$ (solid) and $\bar{\nu}_e + {}^{12}\text{C} \to e^+ + {}^{12}\text{B}$ (dashed)) are displayed in blue. NC interaction cross sections on ^{12}C for neutrinos (solid) and antineutrinos (dashed) are posed in green (ν_x represents all three neutrinos flavors ν_e, ν_μ, ν_τ). The cross section for elastic scattering of electron neutrinos on electrons, $\nu_e + e^- \to \nu_e + e^-$, is shown in orange and contains both, CC and NC, interactions. Figure based on [191].

The main neutrino detection channel in JUNO below few hundred MeV is the inverse β decay (IBD), the charged current quasielastic reaction of an electron antineutrino on a free proton creating a positron and a neutron:

$$\bar{\nu}_e + p \to e^+ + n. \tag{3.12}$$

The major part of the $\bar{\nu}_e$'s kinetic energy E_ν is directly transferred to the positron, except of the positron's rest mass m_e, the proton-neutron mass difference $\Delta = M_n - M_p$ and a small recoil energy carried away by the neutron [123]. Hence, the IBD energy threshold is $E_{thr.,IBD} = \frac{(M_n+m_e)^2 - M_p^2}{2M_p} \simeq 1.8\,\text{MeV}$ [192]. The positron deposits its kinetic energy $E_{e,kin}$ in the liquid scintillator volume within a few nanoseconds and finally annihilates with an electron into two gammas with 511 keV each [5]. This fast energy deposition defines the prompt IBD signal with a visible energy of $E_{vis} \simeq E_{e,kin} + 2m_e$. In contrast to that, the neutron scatters off atoms in the LS medium and thermalizes until it is captured by hydrogen of the LS emitting a 2.2 MeV gamma or by carbon [4]. This neutron capture process is delayed in time by $\tau \approx 220\,\mu\text{s}$ compared to the prompt signal and therefore labeled as delayed IBD signal [5]. The temporal and spatial coincidence between the prompt and delayed signal results in a clear detection signature of IBD events. This allows a very effective discrimination and suppression of background events and, together with the comparably large interaction cross section (see figure 3.5), makes the IBD reaction the main antineutrino detection channel of liquid scintillator detectors like JUNO.
Besides the IBD reaction of electron antineutrinos, also muon and tau antineutrinos interact via CC-QE scattering on free protons of the target material: $\bar{\nu}_\mu + p \to \mu^+ + n$ and $\bar{\nu}_\tau + p \to \tau^+ + n$. However, due to the large masses of the corresponding charged leptons ($m_\mu \simeq 105.65\,\text{MeV}$, $m_\tau \simeq 1.78\,\text{GeV}$ [1]) and the resulting large energy threshold, these reactions only occur for high energetic antineutrinos (more details in section 5.3.2).

[4] Neutron capture on ^{12}C also occurs by releasing a 4.9 MeV gamma and can be measured, but is strongly suppressed, since the neutron capture cross section on ^{12}C is around 100 times smaller than on hydrogen [193, 194].

Another reaction channel is the CC interaction of neutrinos and antineutrinos of all flavors on ^{12}C nuclei: $\nu_x + {}^{12}\mathrm{C} \rightarrow x^- + {}^{12}\mathrm{N}$ and $\bar{\nu}_x + {}^{12}\mathrm{C} \rightarrow x^+ + {}^{12}\mathrm{B}$ ($x = e, \mu, \tau$). The residual isotopes ^{12}N and ^{12}B can be in ground or excited state depending on the interaction process (QE, RES or DIS; for more details see section 5.3.2). In figure 3.5, the CC interaction cross sections of electron neutrinos and antineutrinos on ^{12}C are shown as example.
In addition to CC interactions, also NC neutrino reactions on free protons and ^{12}C nuclei can be measured with liquid scintillator detectors [195]. In NC reactions, all neutrinos and antineutrinos participate: $\nu_x/\bar{\nu}_x + p \rightarrow \nu_x/\bar{\nu}_x + p$ and $\nu_x/\bar{\nu}_x + {}^{12}\mathrm{C} \rightarrow \nu_x/\bar{\nu}_x + {}^{12}\mathrm{C}$ (g.s. or e.s.). Especially NC interactions on ^{12}C are a critical background for IBD event searches, which is extensively discussed in 5.3.3. Cross sections of NC interaction channels on ^{12}C are shown exemplarily in figure 3.5.

3.3. The JUNO Detector

The instrument to achieve the physics goals described in section 3.1 and furthermore to enable the search for neutrinos from dark matter annihilation (see chapter 4) is the JUNO detector. In this section, the setup of the detector together with its subsystems is introduced (section 3.3.1) and the estimated resulting energy resolution is presented (section 3.3.2).
The location of JUNO is optimized to have the best sensitivity for neutrino mass ordering determination by measuring reactor neutrinos [124]. This is realized by a distance of about 53 km from the experimental site to each of the two NPPs, which provide a total thermal power of at least 26.6 GW and therefore strong sources for electron antineutrinos. The JUNO detector will be deployed in a newly built underground laboratory with rock overburden of around 650 m ($\sim$ 1900 m.w.e.). This reduces the cosmic muon flux in the central detector by a factor of around 60,000 to 0.0041 $\mu/(\mathrm{s\,m^2})$ with a mean muon energy of $\langle E_\mu \rangle \approx 207$ GeV [124, 196].

3.3.1. JUNO Detector Setup

The JUNO detector consists of the central detector and two veto systems. The detector's design and setup is primarily chosen to reach an energy resolution of $3\,\%/\sqrt{E[\mathrm{MeV}]}$ to be able to resolve the small differences in the oscillation pattern of figure 3.1 (more details in section 3.3.2). An overview about the setup of the JUNO detector is given in figure 3.6.
The whole detector is situated within a cylindrical cavern with a diameter of 43.5 m and a height of 44.5 m [124]. In the center of the cavern, the JUNO central detector, an acrylic sphere filled with 20 kt of liquid scintillator (LS), is set up. The acrylic sphere has an inner diameter of 35.4 m with a wall thickness of 12 cm and separates the inner LS volume from the outer water pool. The central detector is held by a stainless steel support structure with a diameter of 40.1 m. At this steel structure, also the PMTs are mounted. Around 17,700 20-inch PMTs together with circa 25,000 3-inch PMTs are oriented towards the central detector volume with the small 3-inch PMTs located in between the gaps of the large 20-inch PMTs. The distance from the PMT photocathode to the center of the acrylic sphere is around 19.6 m. In addition to that, approximately 2,400 20-inch PMTs are facing outwards to the water pool and are labeled as veto PMTs. The water pool itself contains 35 kt of ultra-pure water, in which the central detector, the stainless steel frame and the PMTs are embedded. On top of the detector, the calibration unit and the top tracker system is mounted [124].

Liquid Scintillator

The liquid scintillator serves as target material for the detection of neutrinos and antineutrinos. JUNO's liquid scintillator is based on the solvent linear alkyl-benzene (LAB), which

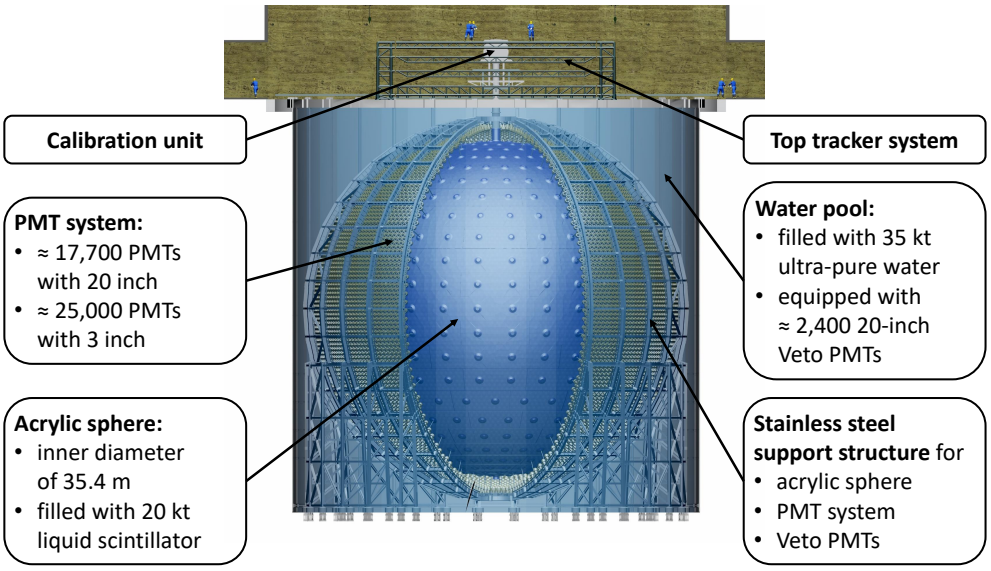

Figure 3.6.: Overview about the setup of the JUNO detector. The cylindrical cavern has a diameter of 43.5 m and a height of 44.5 m. The acrylic sphere, the stainless steel support structure and the PMT system are embedded into the water pool [124]. Image provided by JUNO collaboration.

is an organic compound featuring a benzene ring (chemical formula $C_6H_5C_nH_{2n+1}$). Two additional supplements are dissolved in the LS at low concentrations: 2,5-diphenyloxazole (PPO) with 2.5 g/l as the fluor and p-bis-(o-methylstyryl)-benzene (bis-MSB) with $1 - 4$ mg/l as the wavelength shifter [197]. This composition contains $7.25 \cdot 10^{31}$ free protons per kt of LS and $4.41 \cdot 10^{31}$ ^{12}C atoms per kt.
Ionizing particles excite the benzene rings of the LAB molecules in the region of the energy deposition. This excitation energy is partly transferred to the PPO molecules by non-radiative processes. Scintillation photons generated from the de-excitation of the PPO molecules are re-shifted compared to the LAB photon spectrum (see figure 3.7) and overlap with the absorption spectrum of the bis-MSB molecules. bis-MSB acts as wavelength shifter and re-emits photons with wavelengths of about 430 nm [124]. The structure of the molecules and the photon absorption and emission spectra are illustrated in figure 3.7. Since LAB is not transparent to its own fluorescence light at around 280 nm, the wavelength shift of the emitted photons to around 430 nm is crucial to avoid self-absorption in the LAB (see figure 3.7) and thus to increase the transparency. Therefore, together with complex purification and cleaning procedures to ensure a great radio-purity [124], JUNO's LS will have a high transparency with an attenuation length of at least 20 m at 430 nm [5].

Moreover, an excellent photon light yield of around 10^4 scintillation photons per MeV of deposited energy can be achieved in JUNO [5]. This, in combination with the fast light emission of the excited states in the LS of few nanoseconds, allows effective event reconstruction.
The photon light yield and the temporal light emission depend on the type of the ionizing particle and its energy. Heavier particles, like protons, deuterons or alpha particles, lead to an increased ionization density along their trajectories in the LS. This results in a decreased number of photons compared to lighter particles, like electrons, positrons or photons, with same deposited energy, since the light emission in the scintillator saturates. The saturation effect is called quenching and can be described by Birk's law:

[5] An attenuation length of 20 m at 430 nm corresponds to an absorption length of approximately 60 m and a Rayleigh scattering length of around 30 m [124].

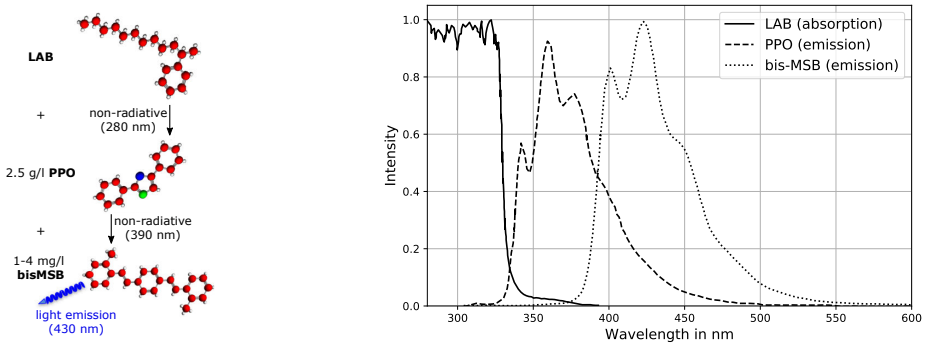

Figure 3.7.: Left: Scheme of the molecular structure of LAB, PPO and bis-MSB together with their concentrations in the LS and the wavelengths of the emitted photons. Image based on [198]. Right: Light absorption by LAB and photon emission by PPO and bis-MSB as function of the wavelength. Figure based on [199] and [200].

$$\frac{\mathrm{d}L}{\mathrm{d}x} = L_0 \frac{\mathrm{d}E/\mathrm{d}x}{1 + k_b \cdot \mathrm{d}E/\mathrm{d}x}, \tag{3.13}$$

where L is the luminescence of the particle, L_0 the expected luminescence for minimum-ionizing particles and k_b the material and particle specific Birk's constant [70].
The time profile of the light emission is defined by the decay time constants of the excited states of the LS. Since different particles types excite different states of the LS with different weights and the de-excitation is affected by the ionization density, the time profile of light emission depends on the particle type [201]. The photon emission time profile can be described by the sum of several exponential functions:

$$P(t) = \sum_i \frac{\omega_i}{\tau_i} e^{-t/\tau_i} \tag{3.14}$$

with the decay time constants τ_i and weights ω_i of the corresponding decay processes [201]. As consequence of the correlation between photon emission time profile and the particle type, the temporal signal evolution in the LS can be used to discriminate between different particles. This is discussed in section 6 explicitly.
In addition to the dominant emission of scintillation photons, also Cherenkov photons can be emitted in the LS medium via the Cherenkov effect, but with a photon light yield of less than 10 % compared to the scintillation light yield.

Photomultiplier Tubes

The light emitted by JUNO's LS is detected by two independent PMT systems, both mounted at the stainless steel support structure and facing towards the central detector volume. The ultra-pure water between the PMTs and the acrylic sphere around 1.7 m away acts as buffer against internal radiation of the PMTs.
The main PMT system consists of 17,613 large PMTs with diameter of 20 inches: 5,000 dynode PMTs from Hamamatsu (R12860 HQE) [206] and 12,613 microchannel plate (MCP) PMTs from Northern Night Vision Technology Ltd. (NNVT) [207]. The coverage of the 20-inch PMTs' photocathodes is around 75 % and, therefore, the large PMTs form the main light collection system of JUNO. Besides the large 20-inch PMTs, additional 25,000 smaller 3-inch PMTs from HZC Photonics (type XP72B22 [208]) are placed in the gaps between the large PMTs. The photocathode coverage of these small PMTs

Table 3.2.: Main characteristics of the different PMT types used in the JUNO detector. The photon detection efficiency (PDE) is given for a wavelength of 430 nm. The mean PDE of all 20-inch PMTs is 29.6 % [202]. The mean dark count rate (DCR) of all 20-inch PMTs is 40.5 kHz. The transit time spread (TTS) is given as FWHM of the transit time distribution and defines the timing resolution of the PMTs. Data from [203–205].

	20-inch dynode PMTs	20-inch MCP PMTs	3-inch PMTs
mean PDE	~ 28.4 %	~ 30.0 %	~ 32.8 %
mean DCR	~ 15.3 kHz	~ 49.0 kHz	~ 550 Hz
mean TTS	~ 2.8 ns	~ 16.7 ns	< 5.0 ns

is around 3 %. Therefore a total photocathode coverage of about 78 % can be achieved in JUNO. Moreover, the independence of these two systems makes the JUNO detector to a double calorimetric system that enables the control of systematics by determining the non-linear response of the 20-inch PMTs, and increases the dynamic range to improve the muon reconstruction resolution and the detection of near supernovae [209].
The main characteristics of the PMTs, i.e. the photon detection efficiency[6], the dark count rate and the transit time spread, are summarized in table 3.2. The reliable performance and the accomplishment of these PMT properties is very crucial to reach the targeted energy resolution of the JUNO detector. Therefore all 20-inch PMTs are tested before being mounted into the detector to prove their characteristics and reject bad-performing PMTs [123, 210].

Veto Systems

The JUNO detector consists not only of the central detector, but also of two veto systems. The water pool is filled with 35 kt ultra-pure water and equipped with around 2,400 20-inch veto PMTs as illustrated in figure 3.6. On the one hand the water pool shields the central detector against external background from the surrounding rock material and on the other hand it can be used as active water Cherenkov veto [124]. The MCP-type veto PMTs can detect Cherenkov light from cosmic muons and other charged particles, that enter the detector and possibly penetrate the central detector. To increase the light detection of the veto PMTs, the entire surface of the water pool is covered with Tyvek [124]. In addition to the Cherenkov veto, the top tracker system is mounted on top of the detector covering an area of around 60 % (see figure 3.6). The top tracker is built of three layers of crossing plastic scintillator panels and can track traversing particles, e.g. cosmic muons, very precisely. A muon detection efficiency above 95 % can be achieved with the Cherenkov veto and the top tracker [211].

Calibration

The calibration system of the JUNO detector includes several sub-systems to monitor and verify the detector's performance and to calibrate physics and instrument non-linearities. Physics non-linearity describes e.g. the quenching effect, whereas instrument non-linearity is affected from the PMTs, the electronics and the position inside the detector and characterizes the nonlinear response between the number of created photons and the measured charge [212].
The calibration unit on top of the detector (see figure 3.6) houses three calibration systems: the automatic calibration unit (ACU), the cable loop system (CLS) and the remotely operated vehicle (ROV). With these systems, radioactive sources can be lowered into the

[6] The photon detection efficiency (PDE) is defined as product of quantum efficiency (QE) and collection efficiency (CE): $\mathrm{PDE}(\lambda) = \mathrm{QE}(\lambda) \cdot \mathrm{CE}$

LS volume through a chimney to measure the energy response of the detector at different positions. To calibrate the non-uniformity at the boundary of the central detector, guide tubes (GTs) are instrumented outside of the acrylic sphere. Further, the laser system AURORA monitors the attenuation and scattering length of the LS. More details on JUNO's calibration strategy can be found in [212].

OSIRIS and TAO

Besides the JUNO detector, two accompanying detectors, OSIRIS and TAO, are also part of the Jiangmen Underground Neutrino Observatory and briefly introduced here. For detailed information about OSIRIS and TAO see [213] and [214], respectively.
The Online Scintillator Internal Radioactivity Investigation System (OSIRIS) is a 20 ton sub-detector at the end of the liquid scintillator filling chain of JUNO to finally validate the radiopurity of the LS before being filled into the central detector. Natural radioactivity in the LS is having a direct impact on the sensitivity and detection performance of JUNO. Therefore, the contamination level of the LS with uranium and thorium chain elements may not exceed a stringent upper limit of $\leq 10^{-15}\,\mathrm{g/g}$ to reach the predicted NMO sensitivity[7] [213]. OSIRIS will monitor the radiopurity by measuring the residuals of natural U/Th contamination and, additionally, can serve as test bench for further development of liquid scintillators and other applications (e.g. measurement of the solar *pp* neutrino flux) after the filling of JUNO is finished [213].
The Taishan Antineutrino Observatory (TAO) is a satellite experiment of JUNO to measure the reactor antineutrino spectrum with sub-percent energy resolution. The ton-level LS detector will be placed only around 30 m away from one core of the Taishan NPP and will provide a reference spectrum for JUNO and other future reactor neutrino experiments and a benchmark measurement to test nuclear databases [214].

3.3.2. Energy Resolution of JUNO

The main physics goal of JUNO is the determination of the neutrino mass ordering (see section 3.1.2) by the precise measurement of the reactor spectrum shown in figure 3.1. In order to identify the true mass ordering with the aimed significance of $\sim 3\,\sigma$ after six years, the oscillation pattern and its small features must be resolved with high accuracy [5]. This entails that the energy resolution of the JUNO detector has to be at least the size of the ratio of the two oscillation frequencies:

$$\frac{\Delta m^2_{21}}{\Delta m^2_{ee}} \sim \frac{7.42 \cdot 10^{-5}\,\mathrm{eV}^2}{2.51 \cdot 10^{-3}\,\mathrm{eV}^2} \sim 3\,\%, \tag{3.15}$$

using the values from table 3.1.
Therefore, one of the main design goals of the JUNO detector, besides of its location and large target volume, is to reach a 3 % energy resolution at 1 MeV to enable the neutrino mass ordering determination and also to accomplish the physics goals described in chapter 4 and section 3.1. The detector's energy resolution σ_E/E can be described using a generic parametrization:

$$\frac{\sigma_E}{E} = \sqrt{\left(\frac{a}{\sqrt{E}}\right)^2 + b^2 + \left(\frac{c}{E}\right)^2} \tag{3.16}$$

[7] For the measurement of solar neutrinos an even more stringent contamination level of $\leq 10^{-16\div 17}\,\mathrm{g/g}$ is required [213].

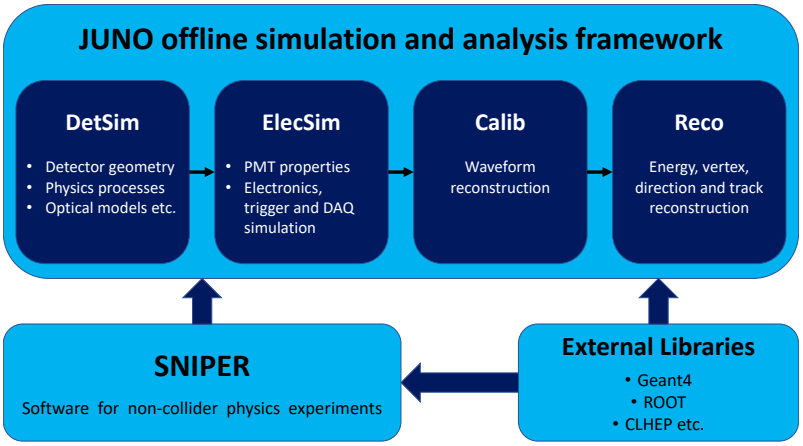

Figure 3.8.: Working principle and offline processing chain of the JUNO simulation and analysis framework.

with the visible energy E of the signal in MeV [5]. The term a is given by photon statistics, which depends on the photon light yield, the total PMT photocathode coverage, the PMT quantum efficiency and the attenuation length of the liquid scintillator. b and c factor in detector effects like PMT dark count rates, variation of the PMT quantum efficiency and smearing of the reconstructed vertices [5].
The targeted energy resolution is realized with an attenuation length in the LS of 20 m at 430 nm wavelength, a total optical coverage of the central detector of at least 75 % and a high PMT quantum efficiency in the order of 30 % with only moderate dark count rate [5,124]. This can be translated to a light yield of $\sim$ 1200 p.e./MeV of visible energy taking the photon light yield of 10^4 photons/MeV into account. From Monte Carlo simulations of the JUNO detector (details in section 3.4) with these characteristics, the parameters of equation 3.16 are determined as $a = 2.973\,\%$, $b = 0.768\,\%$ and $c = 0.970\,\%$ resulting in an energy resolution of around 3.2 % at 1 MeV [215].

3.4. The JUNO Simulation and Analysis Framework

The main topic of this thesis is the investigation of JUNO's sensitivity to measure neutrinos emitted from DM annihilation in the Milky Way as an excess over backgrounds. Such sensitivity studies require a precise and reliable prediction of the detector's performance and its response to different signal and background events. Therefore, a dedicated Monte Carlo (MC) simulation and analysis framework of the JUNO detector is necessary being the most important source of information before data is taken.
The simulation framework is used to manage detector geometries and materials, event data and physics processes, and is a substantial part of the development and optimization of the detector design [124,216,217]. The JUNO offline simulation and analysis framework is based on SNIPER (Software for Non-collider Physics ExpeRiments), which is tailored to the requirements of neutrino experiments. It focuses on an efficient and flexible execution and acts as interface to standard libraries like e.g. ROOT [119], CLHEP [218] and Geant4 [219], that are well established in particle physics [220]. Moreover, the JUNO offline simulation and analysis framework is a serial full detector Monte Carlo simulation and includes the simulation of the JUNO detector and its electronics, the reconstruction of PMT waveforms and of the energy and vertex of events. The working principle and processing chain of the offline simulation software will shortly be introduced in the following and is visualized in figure 3.8.

3.4.1. Detector Simulation

The detector simulation (DetSim) simulates the different detector systems and the interaction of particles within these systems. As input for the detector simulation either data from event generators for many physics processes can be used or information of initial particles of an event, like particle type, mass, momentum, position and direction can be included via a particle gun or in HEPEVT-file format [124].
At first, the detector itself is implemented into the simulation including the geometries of all sub-systems, their properties and the used materials introduced in section 3.3.1. Especially all characteristics of JUNO's liquid scintillator like the composition, photon light yield, quenching, refraction index, re-emission probability and absorption and Rayleigh scattering length are considered. An optical model of the PMTs is included taking the reflection on the interface between water and PMT glass and the conversion of photon hits into photo-electrons into account. This conversion is based on the wavelength-dependent PDE of each PMT [221].
In the second step of DetSim, the initial particles are placed inside the geometry and propagated through the detector by Geant4 considering all possible interactions. All particles, either initial or secondary, are tracked and simulated until they stop inside or leave the detector volume. The produced scintillation and Cherenkov photons, that hit a PMT photocathode and produce photo-electrons according to the optical model of the PMTs, are stored as hits with their corresponding hit times in the output of DetSim. This output ROOT file contains all MC truth data of the simulation (like e.g. the number of p.e. per PMT, hit times, initial position of the particles, deposited energy, ...) and can be either directly analyzed or further processed to the electronics simulation [124].

3.4.2. Electronics Simulation

In the electronics simulation (ElecSim), the response of the PMTs and the digitization electronics is simulated to get the full waveform sampling of the PMTs. To achieve this and to produce realistic waveforms, the signal generation of the PMTs considering dark count rate, transit time spread and pre- and after-pulses is simulated. Furthermore, also the properties of the JUNO electronics like thresholds and trigger conditions can be set and characteristics such as overshoot, saturation effects and electronic noise are considered. More detailed information about the PMT signals and the simulation of trigger, electronics and DAQ can be found in [123, 222] and [124, 216, 223], respectively.

3.4.3. Calibration and Waveform Reconstruction

The digitized PMT waveforms of ElecSim, that describe the FADC traces of the PMT read-out electronics, contain the charge and time information of the measured photo-electrons. This charge and time information can be reconstructed from each waveform within the calibration and waveform reconstruction package (Calib) and calibrated to ensure the correct charge response. Calib provides different reconstruction methods: the deconvolution method, the waveform fitting method, the waveform integration method and the PMT and hit counting methods [224]. Here, only the deconvolution method will be introduced, since it is applied and used later in section 6.
The waveform results from the convolution of the photon hit distribution on the PMT photocathode with a single p.e. spectrum and additional noise. The deconvolution method reconstructs the charge and time of each photon hit based on a discrete Fourier transformation in the frequency domain [224]. The charge is then calibrated due to a measured single p.e. waveform. This method is a powerful tool to deal with electronics noises, overshoot and reflections in the waveform and therefore used as default waveform reconstruction algorithm [225].

3.4.4. Energy and Vertex Reconstruction

In the last step of the JUNO offline simulation and analysis chain, the charge and time information from Calib is used to reconstruct the energy and vertex of the simulated events. Different reconstruction algorithms, based on analytical and machine learning approaches, are implemented to reconstruct quasi point-like and track-like events, respectively. Track-like events mostly originate from cosmic muons. Their energy, direction and track length can be reconstructed with several reconstruction tools (for more details see e.g. [226–228]). In contrast to that, quasi point-like events deposit their energy in a smaller volume[8]. To reconstruct the energy and vertex of quasi point-like events, different reconstruction tools are implemented into JUNO's simulation and analysis framework (details in [229–232]).
One approach for vertex reconstruction is briefly introduced as example, since it is utilized in section 6. Interaction vertex and time of the event is reconstructed with a time likelihood algorithm using the scintillator response function, which mainly consists of the photon emission time profile of the scintillator, the TTS of the PMTs and their DCR [233]. By minimizing the negative log-likelihood function of the probability density function of this scintillator response, the best-fit values represent the reconstructed vertex and time of the event [233]. This results in a vertex resolution of the JUNO detector of around 10 cm at 1 MeV, including the effects of dark noise and TTS of the PMTs [233].

[8] Particles like e^+, e^-, p or α with visible energies $E_{vis} \lesssim 100$ MeV deposit their energy within a spherical volume with radius of around 0.5 m and are described as quasi point-like events.

4. Neutrinos from Dark Matter Annihilation in JUNO

The main subject of this thesis is a study of the sensitivity of the Jiangmen Underground Neutrino Observatory to neutrinos from dark matter self-annihilation.
A sensitivity study of JUNO for DM annihilation of WIMPs into neutrinos in the Sun has already been performed in [5] and [190] for DM masses from 4 GeV to 20 GeV as described in section 3.1.8. Though, JUNO's constraints from this search by measuring electron and muon (anti-)neutrinos with energies in the GeV range are less stringent than limits of comparable studies for the Super-Kamiokande water Cherenkov detector mainly due to JUNO's smaller fiducial mass (22.5 kt for Super-K and typically around 15 kt to 18 kt for JUNO [5]).
JUNO is designed to measure MeV neutrinos with high precision and is therefore an ideal detector to measure neutrinos from self-annihilation (or decay) of light DM particles with masses from few MeV to few hundred MeV. The most promising source for DM annihilation into neutrinos is the DM halo of the Milky Way, since the Sun and the Earth can be ruled out as source for this DM mass region (see section 2.4). Furthermore, most of the annihilation channels of light DM into SM particles are energetically forbidden. Especially for DM masses below the muon mass $m_\mu = 105.6$ MeV, only three annihilation channels are allowed, which limits the potential annihilation channels to channels producing monoenergetic fluxes: the direct annihilation into electron-positron pairs ($DM + DM \rightarrow e^- + e^+$), photons ($DM + DM \rightarrow \gamma + \gamma$) and neutrino-antineutrino pairs ($DM + DM \rightarrow \nu + \bar{\nu}$) [1].
In consequence of the arguments given above, JUNO's sensitivity for the self-annihilation of light DM particles with $m_{DM} \leq 100$ MeV into neutrinos in the Milky Way is studied within this thesis. The lower bound of JUNO's observable DM mass region is in the order of a few MeV. It is experimentally constrained on the one hand by the threshold of the inverse β decay reaction of $E_{thr.,IBD} \simeq 1.8$ MeV (see section 3.2) and on the other hand by the large background contribution of reactor electron antineutrinos below 10 MeV in JUNO (see section 5.1).
In this chapter the expected electron antineutrino flux from galactic dark matter annihi-

[1] For the annihilation channels into $e^- e^+$ and γ's, strong limits on the annihilation cross section and the corresponding branching ratios already exist for DM masses from few MeV to few hundred MeV as shown in figure 2.6. These limits are below the natural scale $\langle \sigma_A \, \mathrm{v} \rangle_{natural} \approx 3 \cdot 10^{-26} \, \mathrm{cm}^3/\mathrm{s}$ of a velocity-independent DM annihilation cross section and, therefore, velocity-independent DM self-annihilation into photons and positrons can be excluded at 90 % C.L. in this DM mass range as discussed in section 2.3.3.

lation (section 4.1), the resulting neutrino signal spectrum in the JUNO detector (section 4.2), JUNO's efficiency to detect IBD events (section 4.3) and the corresponding visible energy spectrum in JUNO (section 4.4) is determined and discussed.

4.1. Neutrino Flux from Galactic Dark Matter Annihilation

The expected neutrino (or antineutrino) flux per flavor on Earth from DM self-annihilation in the Milky Way is given by equation 2.2 in its general form. The study in this thesis is performed under the assumption that DM is a Majorana particle (i.e. $\kappa_1 = 2$) with non-vanishing DM self-interaction, which annihilates into neutrinos in the halo of the Milky Way. For the investigated DM masses of few MeV to 100 MeV, dominant annihilation directly into neutrinos with a branching ratio of 100 % is assumed, since annihilation into the other two possible channels is strongly constrained as discussed in section 2.3.3. The direct annihilation into neutrinos, $DM + DM \to \nu + \bar{\nu}$, yields a monoenergetic neutrino flux, where the neutrino energy E_ν is equal to the dark matter mass m_{DM}. Moreover, equal neutrino flavor composition of the expected flux at Earth (i.e. $\kappa_2 = 3$) is assumed similar to the discussion in section 2.4. These assumptions result in an expected (anti-)neutrino flux per flavor on Earth of

$$\frac{\mathrm{d}\phi_\nu^{DM}}{\mathrm{d}E_\nu} = \frac{\langle \sigma_A \, \mathrm{v} \rangle}{2\, m_{DM}^2} \, \frac{1}{3} \, \delta(E_\nu - m_{DM}) \, R_0 \, \rho_0^2 \, J_{avg}, \tag{4.1}$$

where $\langle \sigma_A \, \mathrm{v} \rangle$ describes the velocity-averaged DM self-annihilation cross section into all neutrino flavors, $R_0 = (8.5 \pm 1.0)$ kpc the distance from the solar system to the galactic center[2], $\rho_0 = 0.3$ GeV/cm^3 the local DM density [1] and J_{avg} the dimensionless angular-averaged J-factor introduced in equation 2.3.

The DM self-annihilation cross section $\langle \sigma_A \, \mathrm{v} \rangle$ is defined as product of the cross section and the relative velocity of dark matter particles in the halo of the Milky Way averaged over the velocity distribution. The natural scale of the velocity-independent thermally-averaged DM annihilation cross section is $\langle \sigma_A \, \mathrm{v} \rangle_{natural} \simeq 3 \cdot 10^{-26}$ cm^3/s [76] and describes the cross section needed to explain the observed abundance of DM in today's universe assuming thermal freeze-out[3].

The expected neutrino flux from DM annihilation further depends on the DM distribution in the halo of the Milky Way, which is represented by the J-factor J_{avg}. J_{avg} is the angular-averaged DM intensity over the whole Milky Way and is given by the angular-averaged line of sight integration of the square of the DM density profile ρ as already shortly discussed in section 2.4. The galactic dark matter density profile has been investigated in various studies, which led to several dark matter profile models proposed in literature [236]. The majority of these models are based on numerical N-body simulations of the structural evolution of the universe or on measurements of galactic rotation curves, and tend to agree at larger radii ($r \gtrsim 10$ kpc), but can considerably differ in the inner region of the galaxy [96]. Especially in this central region, the observations of the rotation curves favor a flat DM density profile, whereas N-body simulations of the universe's structural evolution prefer a cuspy (coreless) central density [237]. So, the chosen DM density profile model

[2] Latest measurements in 2019 presented in [234] determined the distance between solar system and galactic center to be $R_0 = (8.178 \pm 0.013\,(\mathrm{stat.}) \pm 0.022\,(\mathrm{sys.}))$ kpc. Nevertheless, $R_0 = (8.5 \pm 1.0)$ kpc, as suggested in [1] and [235], is used here for better comparison with studies of other experiments described in section 2.4.

[3] In case of suppression of the constant velocity-independent term, a velocity-dependent annihilation is dominant and the annihilation cross section can be expanded in powers of v/c, which results in a leading term of $\langle \sigma_A \, \mathrm{v} \rangle \propto ({}^{v(r)}/_{c})^2$ or $\langle \sigma_A \, \mathrm{v} \rangle \propto ({}^{v(r)}/_{c})^4$ in the non-relativistic limit [4]. To study of velocity-dependent DM annihilation into neutrinos, the galactic J-factor needs to be reevaluated, since the annihilation cross section depends on the distance r to the galactic center (for details see [4]).

Table 4.1.: Parametrization of the DM profile models NFW, Moore and Kravtsov and the resulting values of the angular-averaged J-factor J_{avg}. The best-fit values of ρ_0 of each model and the resulting dimensionless J-factor are taken from [238]. The limiting minimum and maximum values of ρ_0 are calculated in [239] satisfying observational constraints. The resulting minimum and maximum values of J_{avg} determined in [96] are also shown. To avoid numerical divergences by computing J_{avg}, a flat core for $r \leq 0.015$ kpc is assumed in [96] and [238].

	α	β	γ	r_s [kpc]	ρ_0 [GeV/cm^3]			J_{avg}		
					min.	best-fit	max.	min.	best-fit	max.
NFW	1.0	3.0	1.0	20	0.20	0.30	1.11	1.3	3.0	4.1
Moore	1.5	3.0	1.5	28	0.22	0.27	0.98	5.2	8.0	104
Kravtsov	2.0	3.0	0.4	10	0.32	0.37	1.37	1.9	2.6	8.5

strongly affects J_{avg} and the resulting neutrino flux. To quantify the impact of different profile models on J_{avg} and the neutrino flux, three of the most commonly used models for the galactic DM halo are investigated within this thesis. All of these models assume a spherically symmetric DM profile with isotropic velocity distribution and can be described by the general parametrization of [96] as function of the distance r to the galactic center:

$$\rho(r) = \rho_0 \left(\frac{R_0}{r}\right)^{\gamma} \left[\frac{1 + (R_0/r_s)^{\alpha}}{1 + (r/r_s)^{\alpha}}\right]^{\frac{\beta-\gamma}{\alpha}} \tag{4.2}$$

with the scale radius r_s, the inner cusp index γ, the slope β for $r \to \infty$ and the parameter α, which determines the shape of the profile in regions around r_s [4].
In the following, these three models are briefly described. Their corresponding parameters α, β, γ and r_s are compiled in table 4.1. Moreover, table 4.1 contains the best-fit values of ρ_0 and the resulting values of J_{avg} of each model, together with the minimum and maximum values of ρ_0 and J_{avg} that satisfy observational constraints (for details see [239]).
The NFW model [240] is a central cusp model determined by N-body simulations of the structural evolution in the cold DM scenario in the expanding universe and predicts an infinitely increasing central peak. It represents the most prominent model used in indirect DM searches. The model of Moore et al. [241] is based on high resolution N-body simulations of cold DM halos, which have been compared with observations of galactic rotation curves, and represents also a central cusp model. For the model of Kravtsov et al. [242], measurements of rotation curves of galaxies are studied to estimate the galactic radial DM density profile. The Kravtsov model predicts a flatter shape in the central region and therefore a smaller value of J_{avg}.
In figure 4.1, the DM density profiles of the Milky Way for the three different models are shown as function of the distance r to the galactic center using the parameters of table 4.1.

The entire DM halo of the Milky Way is taken as source for DM annihilation into neutrinos in this study, since the DM density profile differs significantly for $r \lesssim 1$ kpc depending on the chosen DM profile model as shown in figure 4.1. This minimizes the impact of differences of $\rho(r)$ for $r \lesssim 1$ kpc on the J-factor J_{avg} and on the resulting neutrino flux from DM self-annihilation. Moreover, the neutrino flux from DM self-annihilation is maximal by considering the whole DM halo as source. Nevertheless, this assumption accepts the

[4] In [236] and [238], a slightly different parametrization of the DM density profile is used, $\rho(r) \propto \frac{\rho_0}{\left(\frac{r}{r_s}\right)^{\gamma}\left[1+\left(\frac{r}{r_s}\right)^{\alpha}\right]^{\frac{\beta-\gamma}{\alpha}}}$, which however yields the similar values of J_{avg} for the corresponding DM density profile model.

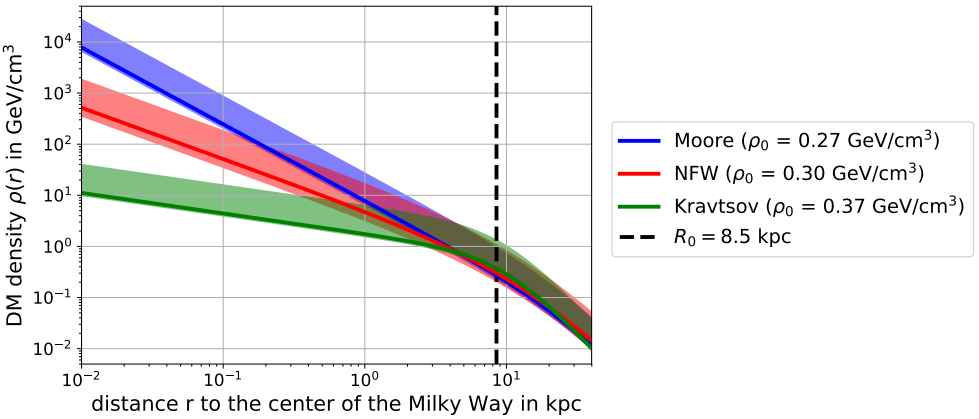

Figure 4.1.: Radial density profiles ρ of the dark matter halo of the Milky Way for the NFW, Moore and Kravtsov model as a function of the distance r to the galactic center. The density profiles are calculated according to the parametrization of equation 4.2 with the parameters of table 4.1 for radii r from 0.01 kpc to 40 kpc. The solid lines represent the density profiles using $\rho_{0,best-fit}$ of each model. The colored bands illustrate the valid region considering $\rho_{0,min}$ and $\rho_{0,max}$ of each model. The distance from the solar system to the galactic center $R_0 = 8.5$ kpc is shown as black dashed line.

loss of directional information about the incoming neutrinos[5]. Considering the best-fit values of ρ_0 of the three different DM profile models, the angular-averaged J-factor differs by a factor of around 3. The impact of the choice of different DM density profile models and corresponding values of J_{avg} on the expected neutrino flux and the DM annihilation cross section will be discussed in section 7.2. In the following, the canonical value of the angular-averaged DM intensity over the whole Milky Way of [238], $J_{avg} = 5$, is used for simplicity and to allow a reasonable comparison to results of other neutrino experiments. Considering the assumptions discussed above, the expected electron antineutrino flux on Earth from DM self-annihilation in the entire Milky Way ranges from $\phi^{DM}_{\bar{\nu}_e}(m_{DM} = 100\,\text{MeV}) \approx 0.0059\ \text{cm}^{-2}\text{s}^{-1}$ to $\phi^{DM}_{\bar{\nu}_e}(m_{DM} = 10\,\text{MeV}) \approx 0.59\ \text{cm}^{-2}\text{s}^{-1}$ for an assumed annihilation cross section of $\langle \sigma_A \text{v} \rangle = 3 \cdot 10^{-26}\ \text{cm}^3/\text{s}$.

4.2. Antineutrino Signal from Dark Matter Annihilation in JUNO

The main detection channel of the JUNO detector to measure neutrinos with energies below around 100 MeV is the inverse β decay (IBD), $\bar{\nu}_e + p \rightarrow e^+ + n$, because of its comparably large interaction cross section and the efficient background reduction due to the temporal and spatial coincidence of prompt and delayed signal. Therefore, the IBD reaction is used to measure the expected electron antineutrino flux from self-annihilation of light DM particles with $m_{DM} \leq 100$ MeV in the Milky Way.
The neutrino energy spectrum, i.e. the number of electron antineutrino events as function of the neutrino energy, from DM self-annihilation in the Milky Way detected via the IBD reaction in the JUNO detector is given by

[5] In contrast to considering the entire DM halo of the Milky Way as source for neutrinos from DM self-annihilation, also only the galactic center or a region around the galactic center can be observed to study DM annihilation into neutrinos. One advantage of this approach is to use the directional information of the incoming neutrinos to suppress isotropic background events. However, the J-factor and the resulting neutrino flux can strongly differ in the region around the galactic center depending on the chosen DM profile model and the expected neutrino flux is reduced compared to considering the entire DM halo. JUNO's ability to use the directional information to reduce background events and its sensitivity to neutrinos from DM annihilation near the galactic center will be shortly discussed in section 7.4.3.

$$\frac{\mathrm{d}N_S(E_{\bar{\nu}_e})}{\mathrm{d}E_{\bar{\nu}_e}} = \sigma_{IBD}(E_{\bar{\nu}_e}) \frac{\mathrm{d}\phi^{DM}_{\bar{\nu}_e}(E_{\bar{\nu}_e})}{\mathrm{d}E_{\bar{\nu}_e}} N_{target}\, t\, \epsilon_{IBD}\, \epsilon_{\mu\, veto} \tag{4.3}$$

with the IBD interaction cross section σ_{IBD}, the electron antineutrino flux from DM annihilation $\mathrm{d}\phi^{DM}_{\bar{\nu}_e}/\mathrm{d}E_{\bar{\nu}_e}$, the number of target protons N_{target}, the total exposure time t, the IBD detection efficiency ϵ_{IBD} and the efficiency $\epsilon_{\mu\, veto}$ due to the application of the muon veto.
The IBD interaction cross section is approximated with the parametrization performed in [192]:

$$\sigma_{IBD}(E_\nu) \approx 10^{-43}\,\mathrm{cm}^2\, p_e\, E_e^{(0)}\, E_\nu^{-0.07056+0.02018\,\ln E_\nu - 0.001953\,\ln^3 E_\nu}. \tag{4.4}$$

Here, all energies are expressed in MeV and $E_e^{(0)} = E_\nu - \Delta$ defines the positron energy of the IBD reaction at zeroth order of $1/M_p$ with $\Delta = M_n - M_p$. This parametrization agrees with the full analytical result of [192] within a few per mil for neutrino energies below 300 MeV.
The electron antineutrino flux on Earth is taken as in equation 4.1. To estimate the expected flux and the number of electron antineutrino events in JUNO, the assumptions presented in the previous section are used, e.g. the canonical value $J_{avg} = 5$ of the angular-averaged J-factor. The total number of free protons is $N_{target} = 1.45 \cdot 10^{33}$ for JUNO's central detector containing 20 kt of liquid scintillator. The total exposure time of JUNO is set to $t = 10$ years for this study. This is feasible for JUNO, which is expected to run for at least 20 years, and roughly similar to the exposure times of neutrino experiments described in section 2.4 and shown in figure 2.6.
The IBD detection efficiency ϵ_{IBD} strongly depends on the chosen IBD selection criteria and describes the fraction of detected IBD events in the JUNO detector based on the set selection criteria to the total number of IBD reactions inside the detector. The determination of the selection criteria, that provide the best signal to background ratio, and of the resulting IBD detection efficiency is one important part investigated within this thesis and is discussed in section 4.3 in detail.
The efficiency $\epsilon_{\mu\, veto}$ describes the loss of exposure of JUNO's central detector volume due to the application of the muon veto cut, which suppresses the background of cosmic muons and cosmogenic isotopes induced by cosmic muon spallation inside the detector. JUNO's efficiency due to the application of the muon veto for the studies of this thesis is determined to $\epsilon_{\mu\, veto} = 97.2$ % by simulations and described in detail in section 5.4.1.

4.3. IBD Selection Criteria and JUNO's Detection Efficiency

The IBD selection criteria contain a set of selection cuts that are applied to determine statistically whether a signal is caused by an inverse β decay reaction or not. The purpose of these selection criteria is to achieve the best signal to background ratio $N_S/\sqrt{N_S + N_B}$ with the number of signal and background events N_S and N_B, respectively. Due to the distinctive IBD signal signature of prompt and delayed signal coincident in time and space, the following selection cuts to specify IBD events can be employed:

A volume cut on the prompt signal is applied, where only a part of the total volume of JUNO's central detector acts as fiducial volume mainly to reduce external backgrounds at the outer region of the liquid scintillator volume. A cut on the energy of the prompt signal specifies the energy window that is observed. Additionally, a cut on the energy of the delayed signal ensures neutron captured on hydrogen specified by the emission of a

2.2 MeV gamma. The temporal coincidence between prompt and delayed signal is considered in a time difference cut. A cut on the number of delayed signals, the so-called multiplicity cut, is also applied. Since prompt and delayed signal are also correlated in space, a cut on the distance between them factors in the spatial coincidence of the IBD. Furthermore, a volume cut on the position of the delayed signal is applied.

A simulation of 20,000 IBD events with JUNO's detector simulation (section 3.4) is performed in this thesis to study JUNO's detector response to IBD events. Based on the simulation data, the cut parameters of the introduced selection criteria that result in the best signal to background ratio $N_S/\sqrt{N_S + N_B}$ and the corresponding IBD detection efficiency are determined.
Each simulated IBD event consists of one e^+-n pair specified by the kinetic energies of positron and neutron. The calculation of the positron and neutron energy of an IBD event as function of the neutrino energy is described in the following:
DM particles with masses between 10 MeV and 100 MeV are studied in this thesis and the energy of the electron antineutrinos produced by DM annihilation is equal to the DM mass, $E_{\bar{\nu}_e} = m_{DM}$. So, the electron antineutrino energy $E_{\bar{\nu}_e}$ is sampled from a uniform distribution between 10 MeV and 100 MeV. The total energy of the positron produced in an IBD interaction depends on $E_{\bar{\nu}_e}$ and the scattering angle θ between incoming neutrino and outgoing positron direction and is calculated with [243]

$$E_e^{(1)} = E_e^{(0)} \left[1 - \frac{E_{\bar{\nu}_e}}{M_p} \left(1 - \mathrm{v}_e^{(0)} \cos\theta\right)\right] - \frac{y^2}{M_p} \tag{4.5}$$

at first order of $1/M_p$ ($E_e^{(0)} = E_{\bar{\nu}_e} - \Delta$ is the positron's energy and $\mathrm{v}_e^{(0)} = p_e^{(0)}/E_e^{(0)}$ its velocity at zeroth order of $1/M_p$, $\Delta = M_n - M_p$ and $y^2 = (\Delta^2 - m_e^2)/2$). The cosine of the scattering angle θ is sampled from the differential IBD cross section at first order of $1/M_p$ [243]:

$$\left(\frac{\mathrm{d}\sigma}{\mathrm{d}\cos\theta}\right)^{(1)} = \frac{\sigma_0}{2}\left[\left(f^2 + 3g^2\right) + \left(f^2 - g^2\right)\mathrm{v}_e^{(1)}\cos\theta\right] E_e^{(1)} p_e^{(1)} - \frac{\sigma_0}{2}\left[\frac{\Gamma}{M_p}\right] E_e^{(0)} p_e^{(0)}. \tag{4.6}$$

The vector and axial-vector coupling constants are $f = 1$ and $g = 1.26$. $\mathrm{v}_e^{(1)}$ and $p_e^{(1)}$ are the positron's velocity and momentum at first order of $1/M_p$. The normalizing constant σ_0 and the function Γ, which depends on $E_e^{(0)}$, $\mathrm{v}_e^{(0)}$ and $\cos\theta$, are given in equation 8 and 13 of [243].
The corresponding kinetic energy of the neutron at first order of $1/M_p$ is calculated with

$$E_{n,kin} = \frac{E_{\bar{\nu}_e} E_e^{(0)}}{M_p}\left(1 - \mathrm{v}_e^{(0)}\cos\theta\right) + \frac{y^2}{M_p}. \tag{4.7}$$

MC truth data on position, photon hit times, number of photo-electrons (p.e.), quenched deposited energy etc. of the 20,000 simulated IBD events is used to analyze JUNO's detector response[6]. Since MC truth data represents the ideal detector response without taking into account effects of the electronics or applied reconstruction algorithms, MC truth data is smeared with the expected vertex and time resolution of JUNO to obtain a more realistic detector response.

[6] The events are randomly distributed in JUNO's central detector volume within a radius of $R_{total} = 17.7$ m and simulated with JUNO DetSim version J18v1r1-Pre1.

JUNO's vertex resolution of e^+, e^- and γ considering the TTS and DCR of the 20-inch PMTs and assuming point-like events is evaluated in [244] to $\sigma_{vertex} \approx 110\,\text{mm}/\sqrt{E_{vis}[\text{MeV}]}$ for visible energies below 8 MeV. For higher visible energies between 10 MeV and 100 MeV, the prompt energy deposition of e^+ of IBD events is not point-like. Analyzing the simulated IBD events, the mean track length $\langle L \rangle$ and the maximal track length L_{max} of positrons is $\langle L \rangle \approx 210$ mm and $L_{max} \approx 500$ mm. So, these quasi point-like events deposit their energy along a track of 210 mm on average. To take into account this spatial extend of the energy deposition, a vertex resolution of $\sigma_{vertex} = 250.0$ mm is assumed for events with visible energies between 10 MeV and 100 MeV. This assumed vertex resolution also agrees with the vertex resolution presented in section 6.1, which has been determined using the vertex reconstruction algorithm described in section 3.4.4.
The time resolution for p.e. at the PMTs of JUNO is defined by their TTS. It is considered by smearing the photon hit time t_{hit} with a Gaussian distribution with $\sigma = TTS/(2\sqrt{2\ln 2})$ by using the TTS parameters[7] shown in table 3.2.

The reconstructed position of the prompt signal is defined by the initial position of the positron from the MC truth data smeared with a Gaussian distribution with the vertex resolution $\sigma_{vertex} = 250.0$ mm introduced above.
The properties of energy and time of the prompt and delayed signal of the simulated event are specified by the pulse shape of the event. The pulse shape is the number of p.e. registered by the PMTs as function of the photon emission time t_{pe} and represents the temporal evolution of the signal independent of the position inside the central detector. Since MC truth data contains the number of p.e. as function of the hit time t_{hit} at the PMT and not as function of the photon emission time t_{pe}, the hit times must be corrected with the time-of-flight of the photons from their emission point to the absorption point at the PMT. The procedure for this correction is the following[8]:
For each registered photon hit, the ID number of the PMT and therefore its position is known. With the PMT position and the reconstructed position of the prompt signal described above, the distance $d = |\vec{r}_{reco} - \vec{r}_{PMT}|$ between the emission and absorption point can be calculated. Moreover, the time-of-flight $t_{tof} = d/c_{eff}$ can be calculated assuming an effective speed of light c_{eff}. This effective speed of light is tuned in [244] to reduce the bias of the vertex reconstruction. This bias occurs because of different effects like e.g. reflections on the acrylic sphere or PMT glass, scattering of the photons with the LS particles or the different refractive indices of water ($n_{\text{H}_2\text{O}} = 1.33$) and LS ($n_{LS} = 1.49$). In [244], the resulting effective speed of light is determined as $c_{eff} = 194.17$ mm/ns for the 20-inch dynode and 3-inch PMTs and $c_{eff} = 189.98$ mm/ns for the 20-inch MCP PMTs. It should be noted here, that the different values of c_{eff} for different PMT types are not physically motivated, but reduce the vertex bias best (for details see [244, 245]). The hit time t_{hit} of MC truth data is smeared with the corresponding TTS of the PMT and the time-of-flight t_{tof} is subtracted, resulting in the photon emission time $t_{pe} = t_{hit,smeared} - t_{tof}$. This defines the time of the photon emission in the liquid scintillator. The histogram of these photon emission times determines the pulse shape of the event and is divided into a prompt signal window from 0 ns to 1 µs and a delayed signal window from 1 µs to 2 ms. Less than 0.5 % of all delayed signals fall into the prompt signal window. The bin-width of the histogram is set to 5 ns.
The pulse shape of the prompt signal window is integrated over the photon emission time to get the total number of p.e. $N_{p.e.}$ of the prompt signal. For the conversion of total number of p.e. to visible energy in MeV, a linear conversion function $E_{vis} =$

[7] The TTS parameters of table 3.2 are given as FWHM of the transit time distribution.
[8] The described time-of-flight correction is only valid for quasi point-like events with typical track lengths below around 0.5 m. This is the case for positrons, electrons, protons or α particles with visible energies below around 100 MeV (see also section 3.4).

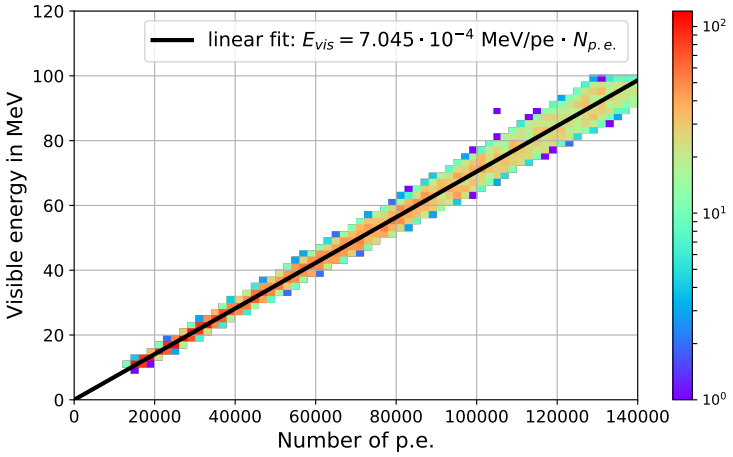

Figure 4.2.: Visible energy distribution of positrons simulated with JUNO's detector simulation as function of the detected number of p.e.. The visible energy E_{vis} is given by the quenched deposited energy in MeV. Positrons with kinetic energies between 10 MeV and 100 MeV are simulated. The plot contains data of 10,000 positron events. A linear fit $E_{vis} = A \cdot N_{p.e.}$ is performed on the data, which results in $A = 7.045 \cdot 10^{-4}$ MeV/p.e..

$7.045 \cdot 10^{-4}\,\mathrm{MeV/pe} \cdot N_{p.e.}$ is used. Positron events with kinetic energies between 10 MeV and 100 MeV are simulated with JUNO's detector simulation inside the central detector volume. Then, a linear fit of the quenched deposited energy, which is equal to the visible energy E_{vis}, as function of the corresponding number of p.e. is performed to determine the conversion function. The results of the simulation and the corresponding linear fit function are shown in figure 4.2.
The time window of the delayed signal of the pulse shape is analyzed to determine the number of delayed signals, the times, when the delayed signals begin and end, and the corresponding energies. The begin time of a delayed signal is given by the photon emission time, if the number of p.e. in a time window of 5 ns is above the threshold of 250 p.e., which is equivalent to a visible energy of around 0.2 MeV. The end time of a delayed signal is defined as the photon emission time, if each number of p.e. of three consecutive time windows of 5 ns is below the threshold of 250 p.e.. The energy of a delayed signal is calculated by integrating the pulse shape from begin to end time and converting the resulting number of p.e. into visible energy in MeV with the linear conversion function $E_{vis} = 7.045 \cdot 10^{-4}\,\mathrm{MeV/pe} \cdot N_{pe}$ of figure 4.2.
The position of the delayed signal, i.e. the position of the neutron capture, inside the detector is taken from the MC truth data and randomly smeared with the vertex resolution. Since a γ particle with $E = 2.2$ MeV is emitted in the neutron capture process on hydrogen, the vertex resolution $\sigma_{vertex} = 110\,\mathrm{mm}/\sqrt{E[\mathrm{MeV}]} \approx 74.0$ mm is assumed. The distance between prompt and delayed signal is therefore given as difference between the reconstructed position of the prompt signal and reconstructed position of the delayed signal, $d = |\vec{R}_{prompt} - \vec{R}_{del}|$. The distributions of the data of all 20,000 simulated IBD events after the analysis are displayed in section A.1 of the appendix.

Based on the analysis results described above, different cut parameters of the IBD selection criteria are tested. To be able to specify the efficiencies due to different cut parameters independently, the volume cut on the prompt signal, the energy cut on the prompt signal and the total delayed cut are applied separately to the simulated events. The total delayed cut combines all cuts related to the delayed signal and consists of the time difference cut, multiplicity cut, energy cut on the delayed signal, distance cut and volume cut on the

delayed signal. These cuts are applied consecutively in the above order.
The cut parameters that lead to the best selection criteria in terms of signal to background ratio are listed in table 4.2 and discussed in the following. The volume cut on the reconstructed position of the prompt signal, also called fiducial volume cut, is set to $R_{prompt} = \sqrt{X^2 + Y^2 + Z^2} < 16.0$ m, which reduces the fiducial mass of JUNO from 20 kt to 14.77 kt. The energy cut on the prompt signal is set to 10.0 MeV $\leq E_{prompt} \leq$ 100.0 MeV. To pass the time difference cut, begin and end time of at least one delayed signal must be within the delayed time window between 1.0 µs and 1.0 ms. The multiplicity cut of $N_{mult} = 1$ allows only one signal in the delayed time window between 1.0 µs and 1.0 ms as expected for IBD events and is only applied to events that pass the time difference cut. The energy cut on the delayed signal of 1.8 MeV $\leq E_{del} \leq$ 2.7 MeV is applied on all events that pass time and multiplicity cut. After these cuts, the cut on the distance between prompt and delayed signal of $d < 1.0$ m, and, subsequently, the volume cut on the position of the delayed signal of $R_{del} < 17.7$ m is applied.
The selection criteria with the cut parameters of table 4.2 are applied to all 20,000 simulated IBD events and cut efficiencies are defined as number of events that pass the cut divided by the total number of events the cut is applied to. The efficiency of each single cut with its statistical error, together with the total IBD detection efficiency, is compiled in table 4.2.
The volume cut on the prompt signal with cut efficiency of $\epsilon_{R_{prompt}} = (73.0 \pm 0.7)$ % reduces the IBD detection efficiency the most compared to the other cuts due to the strict cut criterion of $R_{prompt} < 16$ m, which is set to reduce fast neutron background events (details in section 5.4.2), the effect of total reflection at the acrylic sphere and background from external radioactivity. The efficiency of the total delayed cut of $\epsilon_{del} = (92.6 \pm 1.5)$ % is dominated by the time difference cut and the energy cut on the delayed signal, whereas the cuts on the multiplicity and the distance influence the cut efficiency only negligibly.

The total IBD detection efficiency averaged over the visible energy region is determined to $\epsilon_{IBD} = (67.0 \pm 0.7)$ % and displayed in figure 4.3 as function of the prompt visible energy. Above visible energies of 85 MeV, the IBD detection efficiency slightly decreases due to edge effects of the energy cut. For $E_{vis} < 85$ MeV, the efficiency doesn't depend on the energy within statistical fluctuations. Therefore, an energy-independent IBD detection efficiency of $\epsilon_{IBD} = 67.0$ % is assumed and used to calculate the neutrino energy spectrum in equation 4.3.

4.4. Visible Energy Spectrum in JUNO

The neutrino energy spectrum of equation 4.3 describes the number of IBD events from DM self-annihilation expected in JUNO as function of the neutrino energy and is proportional to the expected monoenergetic electron antineutrino flux. Thus, the neutrino energy spectrum is a monoenergetic spectrum at $E_\nu = m_{DM}$. Since JUNO will measure the visible energy E_{vis}, which represents the quenched deposited energy and is proportional to the number of p.e. (see figure 4.2), the neutrino energy spectrum needs to be converted into the visible energy spectrum. This is given by the number of IBD events as function of the visible energy taking into account the kinematics of the IBD detection channel. The resulting visible energy spectrum for a fixed DM mass is calculated numerically with the following procedure:
The electron antineutrino energy $E_{\bar{\nu}_e}$ is equal to the fixed DM mass m_{DM}. With $E_{\bar{\nu}_e}$, the differential IBD interaction cross section $\mathrm{d}\sigma/\mathrm{d}\cos\theta$ of equation 4.6 is calculated as function of the scattering angle θ and normalized that $\int_0^{2\pi} \mathrm{d}\sigma/\mathrm{d}\cos\theta\,\mathrm{d}\theta = 1$. Then, 100,000 values of $\cos\theta$ are randomly sampled from the differential cross section and the resulting total positron energies $E_e^{(1)}$ are calculated with equation 4.5 for $E_{\bar{\nu}_e}$ and each sampled

Table 4.2.: Selection criteria and cut parameters for IBD events, together with the resulting cut efficiencies ϵ and the total IBD detection efficiency ϵ_{IBD}. The cut efficiencies are determined by the analysis of IBD events simulated with JUNO's detector simulation. The consecutively applied cuts of the delayed cut are listed from (a) to (e) and their efficiencies are labeled as ϵ_j. The number of events N_{before} the cut is applied to, the number of events N_{after} that pass the applied cut and the statistical errors $\Delta\epsilon$ and $\Delta\epsilon_j$ of each cut efficiency are also shown.

selection criteria and cut parameters	N_{before}	N_{after}	$\epsilon \pm \Delta\epsilon$ in %	$\epsilon_j \pm \Delta\epsilon_j$ in %
Volume cut on prompt signal: $R_{prompt} < 16.0$ m	20,000	14,600	73.0 ± 0.8	
Energy cut on prompt signal: 10.0 MeV $\leq E_{prompt} \leq$ 100.0 MeV	20,000	19,236	96.2 ± 1.0	
Total delayed cut:	20,000	18,514	92.6 ± 0.9	
(a) Time difference cut: 1.0 µs $\leq \Delta t \leq$ 1.0 ms	20,000	19,130		95.7 ± 1.0
(b) Multiplicity cut: $N_{mult} = 1$	19,130	19,124		99.97 ± 1.0
(c) Energy cut on del. signal: 1.8 MeV $\leq E_{del} \leq$ 2.7 MeV	19,124	18,631		97.4 ± 1.0
(d) Distance cut: $d < 1.0$ m	18,613	18,569		99.7 ± 1.0
(e) Volume cut on del. signal: $R_{del} < 17.7$ m	18,569	18,514		99.7 ± 1.0
Total IBD detection efficiency	**20,000**	**13,390**	$\mathbf{67.0 \pm 0.7}$	

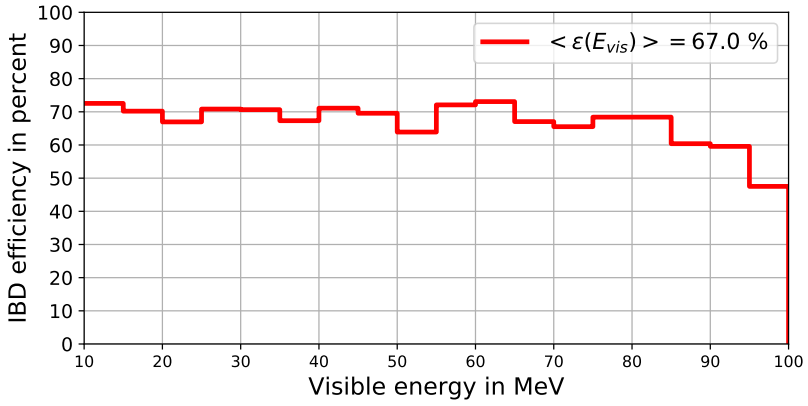

Figure 4.3.: Total IBD detection efficiency as function of the visible energy. The efficiency is determined by applying the prompt volume, prompt energy and total delayed cut described in section 4.3 and summarized in table 4.2. The efficiency average over the visible energy region $\langle \epsilon(E_{vis}) \rangle = 67.0$ % is also displayed.

value of $\cos\theta$. Afterwards, the visible energy of the prompt IBD signal is calculated for each value of the positron energy with $E_{vis} = E_e^{(1)} + m_e$. Here it is assumed, that the total prompt visible energy of an IBD event is only related to the positron energy deposition. As shown in equation 4.7, the kinetic energy of the neutron produced via IBD also depends on the incoming neutrino energy and the scattering angle and increases with increasing neutrino energies. Therefore, neutrons can have kinetic energies up to around 20 MeV for $E_{\bar{\nu}_e} \leq 100$ MeV. Such neutrons can deposit quenched energies up to 10 MeV in the prompt time window by scattering off protons and therefore contribute to the prompt energy. Nevertheless, more than 90 % of the prompt visible energy of IBD events with $E_{\bar{\nu}_e} \leq 100$ MeV is related to the positron energy deposition, which justifies the assumption of $E_{vis} = E_e^{(1)} + m_e$. The visible energy of the prompt signal is then randomly smeared with JUNO's energy resolution of equation 3.16. This yields 100,000 values for the smeared visible energy, which are display in a histogram with bin-width of 1 MeV and between visible energies of 10 MeV and 100 MeV. Finally, the histogram entries are scaled in such way, that the integral over the visible energies is equal to the expected number of signal events N_S of the assumed DM mass.
This represents the visible energy spectrum $\mathrm{d}N_S/\mathrm{d}E_{vis}$ of electron antineutrinos from DM self-annihilation in the Milky Way expected in the JUNO detector via IBD interactions for a fixed DM mass [9]. In figure 4.4, the visible energy spectra in JUNO after 10 years of data taking are shown exemplarily for different DM masses assumed and represent the expected spectrum in JUNO after applying the IBD selection cuts of table 4.2.
Since the DM annihilation cross section $\langle\sigma_A\,\mathrm{v}\rangle$ is not yet determined, the currently most stringent 90 % C.L. upper limits provided by neutrino experiments are utilized to estimate the electron antineutrino flux on Earth and the resulting number of events in JUNO. The strongest limitations of the DM annihilation cross section into neutrinos for DM masses between 15 MeV and 100 MeV are achieved by the Super-Kamiokande experiment in [4] and [75] ranging from $\langle\sigma_A\,\mathrm{v}\rangle_{90\%\,\mathrm{C.L.}}(m_{DM} = 30\,\mathrm{MeV}) = 1.94 \cdot 10^{-25}$ cm^3/s to $\langle\sigma_A\,\mathrm{v}\rangle_{90\%\,\mathrm{C.L.}}(m_{DM} = 100\,\mathrm{MeV}) = 1.91 \cdot 10^{-24}$ cm^3/s as discussed in section 2.4 and displayed in figure 2.6.
The resulting numbers N_S of IBD events from self-annihilation of DM particles with masses between 20 MeV and 100 MeV are also displayed in figure 4.4 ranging from $N_S = 8.0$ for $m_{DM} = 30.0$ MeV to $N_S = 50.2$ for $m_{DM} = 100.0$ MeV after 10 years of data taking. These numbers represent the largest expected numbers of signal events that are still allowed within the latest constraints. Assuming the natural scale of the DM annihilation cross section $\langle\sigma_A\,\mathrm{v}\rangle_{natural} \simeq 3 \cdot 10^{-26}$ cm^3/s, the expected numbers of events measured in JUNO are in the range of 1 event after 10 years of data taking.
The monoenergetic spectrum is broadened and the width of the visible energy spectra increase for larger DM masses, i.e. larger neutrino energies, as visible in figure 4.4. This is mainly due to the kinematics of the IBD reaction, where energy is also partly transferred to the neutron depending on the scattering angle θ. Moreover, the visible energy spectra are widened because of the smearing due to the considered energy resolution. However, this is just a small effect[10] because of JUNO's energy resolution of $\sigma_E/E \approx 3\,\%/\sqrt{E}$, which represents an advantage over water Cherenkov detectors.
To be able to detect electron antineutrinos from DM self-annihilation in the Milky Way,

[9] To prove the validity of the calculation of the visible energy spectrum described above, the visible energy spectrum is also predicted by simulating 10,000 IBD events with the JUNO detector simulation (version J18v1r1-Pre1) for an exemplary DM mass of $m_{DM} = 60.0$ MeV. The calculated spectrum for $m_{DM} = 60.0$ MeV and the simulated spectrum give similar results and agree very well with each other. Therefore, to avoid large simulation samples of each possible DM mass, the described calculation is used to predict the visible energy spectra of IBD events from DM annihilation in JUNO.

[10] As expected, the FWHM of the signal spectrum is broadened by the energy resolution by $\sigma_E = 3\,\% \cdot \sqrt{E_{vis}[\mathrm{MeV}]}$ compared to the spectrum, where only IBD kinematics are considered.

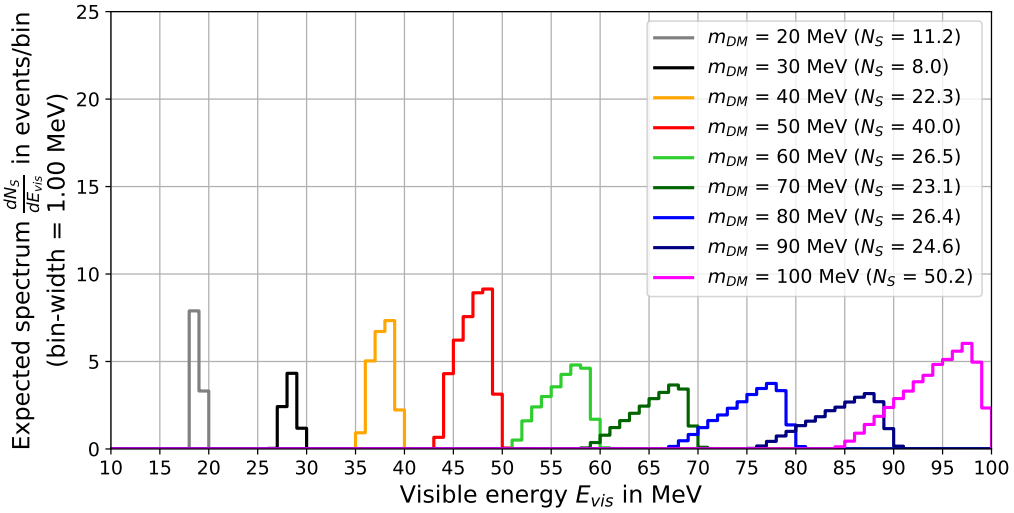

Figure 4.4.: Visible energy spectra $^{dN_S}/_{dE_{vis}}$ of electron antineutrinos produced by DM self-annihilation in the Milky Way and detected via IBD reactions in JUNO. As example, the visible energy spectra for DM masses of 20 MeV, 30 MeV, 40 MeV, 50 MeV, 60 MeV, 70 MeV, 80 MeV, 90 MeV and 100 MeV are shown following the description in section 4.4. All spectra are calculated for a total exposure time of 10 years considering an efficiency due to the application of the muon veto of $\epsilon_{\mu\,veto} = 97.2\,\%$ and a total IBD detection efficiency of $\epsilon_{IBD} = 67.0\,\%$, which leads to a fiducial mass of 14.77 kt. Moreover, an angular-averaged J-factor of $J_{avg} = 5.0$ and the currently most stringent limits of the annihilation cross section from Super-K [4, 75] for each DM mass are assumed. Furthermore, the expected number of signal events N_S for each assumed DM mass is displayed.

detailed knowledge about potential backgrounds in the JUNO detector is essential. Furthermore, if JUNO won't detect an IBD signal from DM annihilation, it could at least set an upper limit on the expected monoenergetic electron antineutrinos flux $\phi_{\bar{\nu}_e}^{DM}$ and on the DM self-annihilation cross section $\langle \sigma_A \, \mathrm{v} \rangle$.

5. Background Sources in JUNO

Detailed knowledge about potential background sources and their background spectra in the JUNO detector is essential to investigate JUNO's sensitivity for indirect DM search with neutrinos. In this chapter, all sources that lead to a background contribution in the JUNO detector with visible energies between few MeV and 100 MeV are discussed and their strength is determined. These backgrounds can be separated into two parts: IBD backgrounds and IBD-like backgrounds.
IBD backgrounds summarize all backgrounds produced in IBD interactions, $\bar{\nu}_e + p \rightarrow e^+ + n$, and therefore state irreducible backgrounds, since they cannot be distinguished from the IBD signals from DM self-annihilation described in the previous section. IBD backgrounds in JUNO are the reactor electron antineutrino background (see section 5.1), the diffuse supernova neutrino background (see section 5.2) and atmospheric electron antineutrinos interacting with free protons via charged current interaction (see section 5.3.2).
In contrast to that, IBD-like backgrounds contain all backgrounds that can mimic an IBD signal signature in JUNO's central detector. These background events can pass the IBD selection criteria defined in section 4.3 even if they are not produced in an IBD reaction. IBD-like backgrounds in JUNO are atmospheric electron neutrinos and antineutrinos interacting with ^{12}C via charged current interactions (see section 5.3.2), atmospheric muon neutrinos and antineutrinos interacting via charged current with free protons and ^{12}C (see section 5.3.2) and neutral current reactions of atmospheric neutrinos and antineutrinos with free protons and ^{12}C (see section 5.3.3). Moreover, also interactions induced by cosmic muons, like fast neutrons from the surrounding rock, cosmogenic isotopes and decaying muons, can cause IBD-like backgrounds in the JUNO detector (see section 5.4).
Additional background contributions from geo-neutrinos as well as non-neutrino backgrounds caused by natural radioactivity and accidental coincidences of non-correlated signals are discussed in section 5.5.

5.1. Reactor Electron Antineutrino Background

The largest background contribution for the indirect DM search with neutrinos in JUNO below energies of around 10 MeV is the reactor electron antineutrino background, since JUNO's detector design and its location has been chosen with the goal to measure electron antineutrinos produced in nuclear fission processes in nuclear power plants with high statistics. The visible energy spectrum of reactor electron antineutrinos in JUNO, especially the high energetic region of the reactor spectrum, is discussed in this section.

As described in section 3.1.2, reactor $\bar{\nu}_e$'s are emitted in β-decays of instable fission fragments, where the fission of the four fuel isotopes ^{235}U, ^{238}U, ^{239}Pu and ^{241}Pu constitutes more than 99.7 % of the thermal power and electron antineutrino production. The resulting reactor electron antineutrino flux $\phi_{\bar{\nu}_e}^{reactor}$ is defined in equation 3.7 and depends on the thermal power W_{th} of the nearby nuclear power plants, the fission rate R_f, the fission fraction F_i of each fission isotope and the antineutrino flux $\phi_{f,i}$ per fission of each isotope. The total thermal power of the Yangjiang and Taishan reactor cores will be $W_{th} = 35.8$ GW after completely finishing their construction, whereas at the beginning of JUNO's data taking the combined thermal power will be reduces to 26.6 GW. Nevertheless, $W_{th} = 35.8$ GW is used to estimate the expected reactor $\bar{\nu}_e$ flux, which will slightly overestimate the flux[1]. The fission rate, i.e. the number of fission per GW and second, is evaluated in [5] to $R_f = 3.125 \cdot 10^{19}$ fission/(GW s). The fission fractions F_i in the Yangjiang and Taishan reactor cores are adopted to be equal to the average values of the Daya Bay nuclear cores, because they are all pressurized water reactors [5]. Therefore, $F_{^{235}\mathrm{U}} = 0.577$, $F_{^{238}\mathrm{U}} = 0.076$, $F_{^{239}\mathrm{Pu}} = 0.295$ and $F_{^{241}\mathrm{Pu}} = 0.052$ is assumed here.
To predict the antineutrino flux and the spectrum $\phi_{f,i}$ per fission of each isotope, the summation method is used, which takes advantage of the available information on the β-decays of each fission fragment and sums over each nuclide's individual spectrum to obtain the total flux [165]. In contrast to that, the inversion method exploits the total spectrum by converting measured β-spectra of ^{235}U, ^{239}Pu and ^{241}Pu into the corresponding antineutrino flux. The inversion method provides the most precise results with uncertainties of 2-3 %, but predicts the antineutrino flux only up to $E_\nu = 8$ MeV, since the measurements were only performed up to this energy [162, 163]. Therefore, the reconstructed electron antineutrino spectra calculated in [164] with the summation method are used to determine the electron antineutrino flux of each isotope to be able to predict the flux also for energies above 8 MeV.
To determine the reactor $\bar{\nu}_e$ flux at JUNO site, three flavor neutrino vacuum oscillation as presented in section 3.1.1 is considered for normal and inverted neutrino mass ordering by using the electron antineutrino survival probability $P_{\bar{\nu}_e \to \bar{\nu}_e}$ defined in equation 3.9 with the distance between reactor cores and JUNO detector of $L = 52.5$ km and the oscillation parameters illustrated in table 3.1.
The neutrino energy spectrum of reactor neutrinos measured via the IBD in the JUNO detector is derived from the reactor electron antineutrino flux $\phi_{\bar{\nu}_e}^{reactor}$ after considering neutrino oscillation as described above:

$$\frac{\mathrm{d}N_{reactor}\left(E_{\bar{\nu}_e}\right)}{\mathrm{d}E_{\bar{\nu}_e}} = \frac{1}{4\,\pi\,L^2}\,\sigma_{IBD}\left(E_{\bar{\nu}_e}\right)\,\frac{\mathrm{d}\phi_{\bar{\nu}_e}^{reactor}\left(E_{\bar{\nu}_e}\right)}{\mathrm{d}E_{\bar{\nu}_e}}\,N_{target}\,t\,\epsilon_{IBD}\,\epsilon_{\mu\,veto}\,P_{\bar{\nu}_e \to \bar{\nu}_e}\left(E_{\bar{\nu}_e}, L\right). \tag{5.1}$$

The remaining parameters to determine the reactor neutrino energy spectrum are chosen equal to the values used to predict the neutrino energy spectrum from DM annihilation in equation 4.3. A total uncertainty of 10 % of the reactor electron antineutrino energy spectrum is conservatively assumed [246].
The resulting reactor neutrino energy spectrum of equation 5.1 expected to be measured via the IBD in JUNO after a runtime of 10 years and for a fiducial mass of 14.77 kt is shown in figure 5.1 for normal and inverted mass ordering. Figure 5.1 also displays the expected electron antineutrino energy spectrum from self-annihilation of DM particles with $m_{DM} = 15$ MeV calculated with equation 4.3 and assuming the currently best limit

[1] In addition to the Yangjiang and Taishan NPPs, the Daya Bay NPP and Huizhou NPP are located at distances to the detector of 215 km and 265 km, respectively, with 17.4 GW each. These reactors only contribute 0.5 % to the total thermal power [5] and are therefore neglected here.

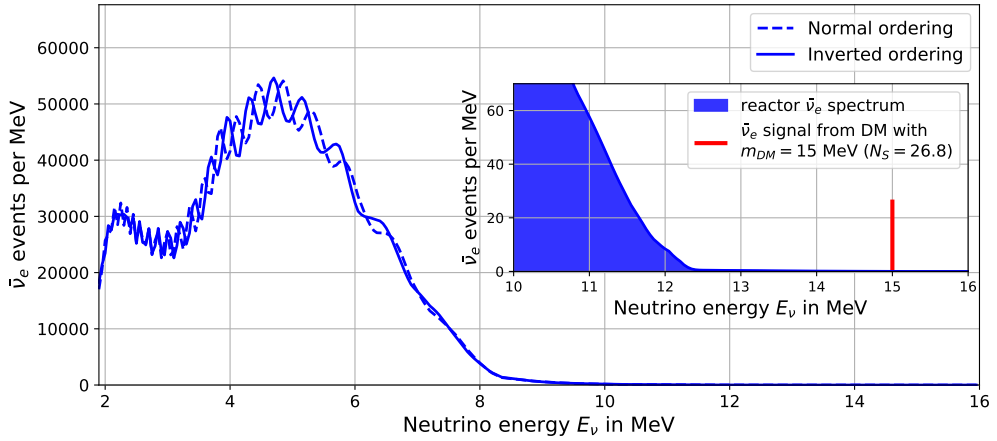

Figure 5.1.: Expected reactor electron antineutrino energy spectrum in JUNO after 10 years of data taking and for a fiducial mass of 14.77 kt for normal (dashed line) and inverted (solid line) neutrino mass ordering. The inset shows the reactor neutrino spectrum for $E_\nu \geq 10$ MeV together with the expected electron antineutrino peak from annihilation of DM particles with $m_{DM} = 15$ MeV described in section 4.2 and calculated with equation 4.3 assuming the currently best 90 % upper limit of $\langle \sigma_A \, \mathrm{v} \rangle \, (m_{DM} = 15\,\mathrm{MeV}) = 6.4 \cdot 10^{-25}$ cm^3/s.

of the annihilation cross section of $\langle \sigma_A \, \mathrm{v} \rangle = 6.4 \cdot 10^{-25}$ cm^3/s for $m_{DM} = 15$ MeV [4] for comparison. The reactor neutrino spectrum in JUNO overwhelms the neutrino signal spectrum from DM self-annihilation by orders of magnitudes for $E_\nu \lesssim 11$ MeV.

The visible energy spectrum $\mathrm{d}N_{reactor}/\mathrm{d}E_{vis}$ of the reactor $\bar{\nu}_e$ backgrounds is generated from the reactor neutrino energy spectrum of equation 5.1 considering the IBD kinematics defined in equation 4.5 and JUNO's energy resolution presented in section 3.3.2. The procedure is similar to the calculation of $\mathrm{d}N_S/\mathrm{d}E_{vis}$ depicted in section 4.4 and is described in the following:
One million values of $E_{\bar{\nu}_e}$ are randomly generated from the reactor neutrino energy spectrum of equation 5.1 for neutrino energies above 10 MeV [2]. Then, one thousand values of the positron energy E_e are calculated for each generated value of $E_{\bar{\nu}_e}$ taking into account the IBD kinematics of equation 4.5 similar to section 4.3. Afterwards the visible energy $E_{vis} = E_e + m_e$ is calculated for each generated value of E_e and smeared with the energy resolution of equation 3.16 using $a = 2.973$ %, $b = 0.768$ % and $c = 0.970$ % (as described in section 3.3.2). The values of E_{vis} are stored in a histogram with bin-width of 1 MeV to get the visible energy spectrum of the reactor $\bar{\nu}_e$ background.
The resulting visible energy spectrum of the reactor background expected to be measured via IBD reactions in the JUNO detector after 10 years of data taking and for a fiducial mass of 14.77 kt is shown in figure 5.2 for visible energies from 10 MeV to 100 MeV. In this energy region, $N_{reactor} = 38.2 \pm 3.8$ reactor $\bar{\nu}_e$ backgrounds events are expected. This yields an event rate of reactor background events of $R_{reactor} = (0.26 \pm 0.03)\,\mathrm{yr}^{-1}\,\mathrm{kt}^{-1}$. Moreover, the reactor electron antineutrino background sets the lower edge of the detection window for neutrinos from DM self-annihilation to $E_{vis,min} \approx 10.0$ MeV as shown in figure 5.1.

[2] For neutrino energies below 10 MeV, the reactor neutrino energy spectrum heavily overtops the expected neutrino spectrum from DM annihilation as illustrated in figure 5.1. Therefore only electron antineutrino energies above 10 MeV are considered here.

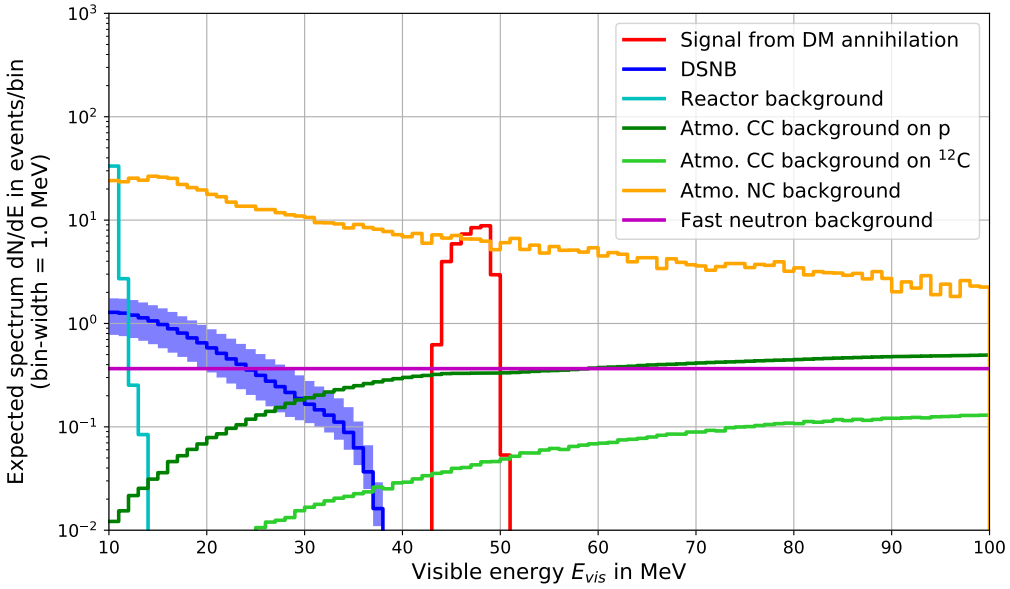

Figure 5.2.: Total expected visible energy spectrum of IBD events in JUNO after 10 years of data taking, for fiducial mass of 14.77 kt and for visible energies between 10 MeV and 100 MeV. All events pass the IBD selection criteria described in section 4.3. The reactor $\bar{\nu}_e$ background described in section 5.1 is display in cyan with $N_{reactor} = 38.2 \pm 3.8$. The diffuse supernova neutrino background (DSNB) discussed in section 5.2 is shown in blue, where the solid blue line represents the fiducial case with $N^{fid}_{DSNB} = 15.0 \pm 6.0$, while the blue region is bounded by the high and low case, respectively. The atmospheric CC background of electron antineutrinos interacting with free protons of section 5.3.2 is shown as dark green line ($N_{atmoCC,\bar{\nu}_e+p} = 30.5 \pm 7.6$), whereas the atmospheric CC background of $\bar{\nu}_e$'s interacting with ^{12}C nuclei is displayed as light green line ($N_{atmoCC,\bar{\nu}_e+^{12}\mathrm{C}} = 5.9 \pm 1.5$). The IBD-like atmospheric NC background studied in detail in section 5.3.3 is shown in orange with $N_{atmoNC} = 757 \pm 220$. The fast neutron background ($N_{FN} = 99.9 \pm 20.0$) is introduced in section 5.4.2 and shown in magenta. The electron antineutrino signal spectrum calculated in chapter 4 with the currently best limit of the DM annihilation cross section of $\langle \sigma_A \, \mathrm{v} \rangle_{Super-K} (m_{DM} = 50\,\mathrm{MeV}) = 1.1 \cdot 10^{-24}$ cm^3/s is shown in red exemplarily for $m_{DM} = 50$ MeV resulting in $N_S = 40.0$.

5.2. Diffuse Supernova Neutrino Background

The diffuse supernova neutrino background (DSNB) is caused by the diffuse flux of neutrinos and antineutrinos of all flavors produced in each supernova occurred in the universe. It is isotropic and constant over the lifetime of JUNO and, moreover, contains information about the cosmic star formation rate, the average core-collapse supernova neutrino spectrum and the rate of failed supernovae, i.e. stars that collapse directly into black holes without explosion [247]. The significant detection region of the DSNB lies between neutrino energies of around 5 MeV to 35 MeV [179]. Therefore, the $\bar{\nu}_e$ flux of the DSNB could cause an IBD background for the indirect DM search with JUNO.
Up to now, the DSNB was not measured by present neutrino detectors, but the Super-Kamiokande experiment sets the currently best limit, imposing an upper bound on the electron antineutrino flux of $\phi_{\bar{\nu}_e}^{DSNB} = (2.8 - 3.0)\ \mathrm{cm}^{-2}\mathrm{s}^{-1}$ for $E_{\bar{\nu}_e} \geq 17.3$ MeV at 90 % C.L.. The study of the DSNB performed within this thesis follows the work presented in [247], wherein the DSNB flux is modeled by using a set of simulation results for neutron star forming and black hole forming stellar collapses from the Garching group [248, 249].
The intensity and spectrum of the DSNB depend on the cosmological rate of core collapses $\dot{\rho}(z, M)$. This, so-called, supernova rate is differential in the progenitor mass M and proportional to the star formation rate $R_{SF}(z)$ at redshift z [247]:

$$\dot{\rho}(z, M) = R_{SF}(z)\, \frac{\phi(M)}{\int_{0.5\,M_\odot}^{125\,M_\odot} M\, \phi(M)\, \mathrm{d}M} \tag{5.2}$$

with the mass of the Sun $M_\odot = 1.99 \cdot 10^{30}$ kg and the initial mass function (IMF) $\phi(M)$ describing the mass distribution of stars at birth. To estimate the supernova rate, the Salpeter IMF $\phi(M) \propto M^{-2.35}$ of [250] is used here. The star formation rate is well described by the functional fit of [251]:

$$R_{SF}(z) = R_{SF}(0) \cdot \begin{cases} (1+z)^{\beta} & , \text{ for } 0 < z < 1, \\ 2^{\beta-\alpha}\ (1+z)^{\alpha} & , \text{ for } 1 < z < 4.5, \\ 2^{\beta-\alpha}\ 5.5^{\alpha-\gamma}\ (1+z)^{\gamma} & , \text{ for } 4.5 < z < 5, \end{cases} \tag{5.3}$$

where $\alpha = -0.26$, $\beta = 3.28$, $\gamma = -7.8$ and $R_{SF}(0) = \mathcal{O}(10^{-2})\, M_\odot\ \mathrm{Mpc}^{-3}\ \mathrm{yr}^{-1}$. Following [247], a total supernova rate normalization of $R_{cc}(0) = \int_{8\,M_\odot}^{125\,M_\odot} \dot{\rho}(0, M)\mathrm{d}M = (1.25 \pm 0.5)\ 10^{-4}\ \mathrm{Mpc}^{-3}\ \mathrm{yr}^{-1}$ is taken.
The outcome of the collapse, either explosion or direct black hole formation, depends on the interplay of several factors and leads to a complex pattern of the distribution of black hole forming collapses with M. Since the mechanism of a collapse into a black hole is still not fully understood, three different possibilities are investigated in [247] to account for this uncertainty labeled by the fraction f_{BH} of collapses that result in direct black hole formation[3]:

- $f_{BH} = 0.09$: all stars with $M \geq 40\, M_\odot$ result in failed supernovae, which represents the case, where direct black hole formation is rare and the DSNB is only slightly affected.
- $f_{BH} = 0.14$: stars with $M \geq 40\, M_\odot$ or with masses between 25 $M_\odot$ and 30 $M_\odot$ directly form black holes. Stars with $M \sim (25 - 30)\, M_\odot$ have high compactness, which is a characteristic of the density structure of the progenitor, and are more likely to form black holes than stars with $M \sim (30 - 40)\, M_\odot$ [252, 253].

[3] The fraction of direct black hole formation is defined as $f_{BH} = \int_\Sigma \phi(M)\mathrm{d}M\ /\ \int_{8\,M_\odot}^{125\,M_\odot} \phi(M)\mathrm{d}M$, where Σ is the region of values of M, where black hole formation is expected [247].

- $f_{BH} = 0.27$: all stars with $M \geq 20\,M_\odot$ collapse into a black hole.

For the neutrino flux from each supernova, the results of the spherically symmetric numerical simulation from the Garching group [248, 249] for four different progenitor models of solar metallicity are used. From these simulations the time-integrated flavor spectra $F^0_{\bar{\nu}_e}$ and $F^0_{\bar{\nu}_x}$ are calculated in [247] (x denotes the non-electron flavors μ and τ). The critical flavor component of the neutrino emission contributing to an IBD background in the JUNO detector is the $\bar{\nu}_e$ component. However, the $\bar{\nu}_e$ spectrum reaching the detector on Earth differs from the one at production because of neutrino oscillation. Considering neutrino oscillation inside the supernova envelope, the electron antineutrino spectrum on Earth is

$$F_{\bar{\nu}_e} = \bar{p}\, F^0_{\bar{\nu}_e} + (1 - \bar{p})\; F^0_{\bar{\nu}_x}, \tag{5.4}$$

where $\bar{p} \simeq 0.68$ is the energy-dependent probability describing the amount of flavor permutation [247].
The resulting diffuse $\bar{\nu}_e$ flux at JUNO site is

$$\phi^{DSNB}_{\bar{\nu}_e}(E_{\bar{\nu}_e}) = \frac{c}{H_0} \int_{8\,M_\odot}^{125\,M_\odot} \int_0^{z_{max}} \dot{\rho}(z, M)\, \frac{\mathrm{d}F_{\bar{\nu}_e}(E_{\bar{\nu}_e}(1+z), M)}{\mathrm{d}M}\, \frac{\mathrm{d}z}{\sqrt{\Omega_m (1+z)^3 + \Omega_\Lambda}}\, \mathrm{d}M \tag{5.5}$$

with the fractions of cosmic energy density in matter, $\Omega_m = 0.3$, and dark energy, $\Omega_\Lambda = 0.7$, the speed of light c and the Hubble constant H_0. $\mathrm{d}F_{\bar{\nu}_e}(E_{\bar{\nu}_e}(1+z), M)$ defines the number of $\bar{\nu}_e$ per unit energy after oscillation produced by an individual supernova with progenitor mass between M and $M + \mathrm{d}M$ [247, 254]. A maximum redshift of $z_{max} = 2$ is chosen in [247] to determine the diffuse $\bar{\nu}_e$ flux [4].
To consider the uncertainties of the astrophysical inputs, especially due to the uncertain supernova rate of equation 5.2, three different cases for the diffuse electron antineutrino flux in JUNO are investigated in the study of this thesis corresponding to the fractions of direct black hole formation f_{BH} described above. These cases are labeled *low case* with $f_{BH} = 0.09$, *fiducial case* with $f_{BH} = 0.14$ and *high case* with $f_{BH} = 0.27$ corresponding to the increasing intensity of the DSNB[5]. The resulting diffuse $\bar{\nu}_e$ flux of equation 5.5 for each case is illustrated in figure 5.3. Moreover, the electron antineutrino flux of the DSNB according to the current upper limit of Super-K of $\phi^{DSNB}_{\bar{\nu}_e} \approx 2.9\ \mathrm{cm}^{-2}\mathrm{s}^{-1}$ for $E_{\bar{\nu}_e} \geq 17.3$ MeV [180] is shown in figure 5.3 using the shape of the flux of the fiducial case normalized to reproduce the limit.

With the DSNB flux of equation 5.5, the neutrino energy spectrum of electron antineutrinos of the DSNB detected via IBD interactions in the JUNO detector is defined as

$$\frac{\mathrm{d}N_{DSNB}\,(E_{\bar{\nu}_e})}{\mathrm{d}E_{\bar{\nu}_e}} = \sigma_{IBD}\,(E_{\bar{\nu}_e})\; \frac{\mathrm{d}\phi^{DSNB}_{\bar{\nu}_e}\,(E_{\bar{\nu}_e})}{\mathrm{d}E_{\bar{\nu}_e}}\, N_{target}\, t\, \epsilon_{IBD}\, \epsilon_{\mu\,veto}. \tag{5.6}$$

Again, σ_{IBD}, N_{target}, t, ϵ_{IBD} and $\epsilon_{\mu\,veto}$ are set equal to section 4.2. The DSNB's visible energy spectrum $\mathrm{d}N_{DSNB}/\mathrm{d}E_{vis}$ in JUNO is generated following the same procedure as

[4] The interval $z > 2$ is excluded because the neutrino fluxes used in [247] are for solar metallicity, which becomes increasingly inaccurate for increasing z, since the metallicity of stars decreases for larger z. Therefore the DSNB is underestimated in the study of [247]. However, calculations in [247] show that the error is likely to be negligible for $E_\nu \gtrsim 11$ MeV.

[5] It is stressed in [247] that f_{BH} is not an input parameter of the calculation, but rather a useful label of the different cases considered. For each case, the DSNB is calculated in [247] including the progenitor-dependence of the neutrino fluxes.

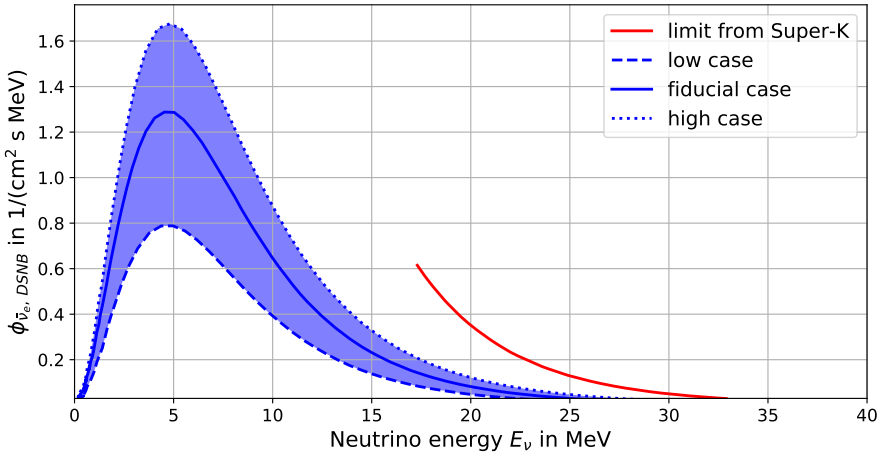

Figure 5.3.: The expected electron antineutrino flux of the DSNB in the JUNO detector as function of the neutrino energy for $\bar{p} = 0.68$ and $z_{max} = 2$. The predicted flux for the low (dashed line), fiducial (blue solid line) and high case (dotted line) is shown. The blue shaded area represents uncertainties of the flux due to astrophysical inputs. The flux that corresponds to the current Super-K upper limit of [180] is displayed as red line. Figure based on [247].

described in section 5.1.
The resulting visible energy spectrum of the DSNB in JUNO measured via IBD interactions after a total runtime of 10 years and for a fiducial mass of 14.77 kt is shown in figure 5.2 for visible energies between 10 MeV and 100 MeV. In figure 5.2, the DSNB spectrum for the fiducial case assumed in this study is displayed as line, whereas the blue shaded region is bounded by the low and high case, respectively. Assuming an overall uncertainty of the total DSNB detection rate of 40 % [255], $N_{DSNB} = 15.0 \pm 6.0$ events are expected for the fiducial case in JUNO after 10 years for visible energies from 10 MeV to 100 MeV, which yields an event rate of DSNB events of $R_{DSNB} = (0.10 \pm 0.04)\ \mathrm{yr}^{-1}\,\mathrm{kt}^{-1}$. Furthermore for the low case $N^{low}_{DSNB} = 8.9 \pm 3.6$ events and for the high case $N^{high}_{DSNB} = 22.2 \pm 8.9$ events are expected as IBD background from the DSNB. Therefore the DSNB causes a possible IBD background source for neutrinos from DM self-annihilation in the Milky Way, especially in the energy region from $E_{vis} \approx 12$ MeV to $E_{vis} \approx 30$ MeV, and must be considered in this sensitivity study, although it has not been measured until now. Nevertheless, the broad spectral shape of the DSNB differs from the peak-like DM signal spectrum, which still allows the observation of neutrinos from DM self-annihilation.

5.3. Atmospheric Neutrino Background

Atmospheric neutrinos are a potential background source for indirect DM searches with JUNO in a broad neutrino energy range dominating the spectrum for $E_\nu \gtrsim 30$ MeV. Several interaction channels will cause background events in JUNO's central detector, since the atmospheric neutrino flux at Earth contains neutrinos and antineutrinos of all flavors interacting with free protons and ^{12}C nuclei of the liquid scintillator. These interaction processes can be separated into two parts depending on the exchanged boson: charged current (CC) interaction events and neutral current (NC) interaction events.
First the expected atmospheric neutrino flux at JUNO site is introduced in section 5.3.1. Afterwards the atmospheric charged current neutrino background and the atmospheric neutral current neutrino background in JUNO is studied in detail in section 5.3.2 and 5.3.3, respectively.

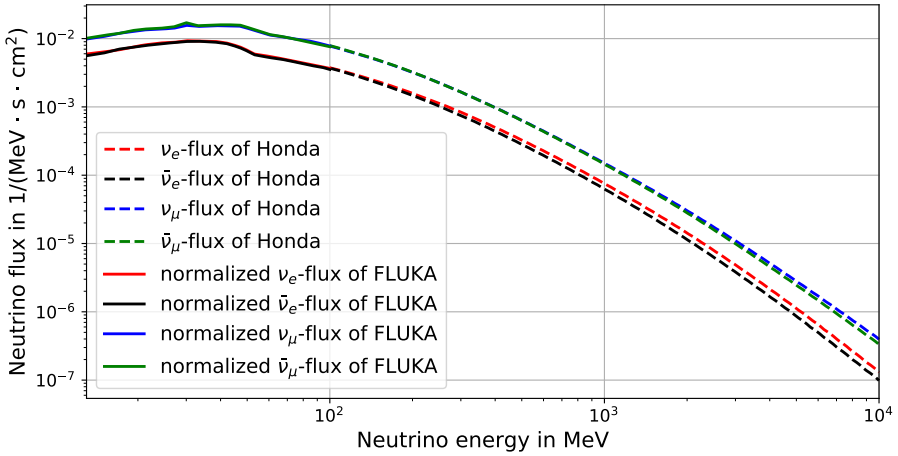

Figure 5.4.: Atmospheric neutrino flux of ν_e, $\bar{\nu}_e$, ν_μ and $\bar{\nu}_\mu$ at JUNO site for neutrino energies from 10 MeV to 10 GeV without considering neutrino oscillations. Dashed lines: atmospheric neutrino fluxes calculated with simulation results of Honda et al. [257]. Solid lines: atmospheric neutrino fluxes from FLUKA simulation results [260], normalized to match the flux of Honda in the overlapping energy region from 100 MeV to 944 MeV.

5.3.1. Atmospheric Neutrino Flux at JUNO site

The atmospheric neutrino flux at production consists of electron and muon (anti)neutrinos generated by cosmic ray interactions with the atmosphere's particles as described in section 3.1.7. Due to the relation to the cosmic ray flux, the atmospheric flux at Earth depends on the location on Earth's surface according to its magnetic field [181].
The atmospheric neutrino flux at JUNO site with its geographic location of 22°07′05″ N and 112°31′05″ E [5] is calculated using simulation results of Honda et al. [256, 257] for solar minimum and neutrino energies from 100 MeV to 10 TeV. The primary cosmic-ray flux at Earth is anti-correlated with the solar activity because the plasma from the Sun scatters the cosmic rays, and the cosmic ray flux and the corresponding atmospheric neutrino flux is reduced during periods of high solar activity [258, 259]. Therefore, minimal solar activity is assumed as conservative approach, which will slightly overestimate the total atmospheric neutrino flux [257].
For energies from 10 MeV to 944 MeV, the atmospheric neutrino flux is calculated in [260] from FLUKA simulation results, but for the location of the Super-Kamiokande detector (36°25′32.6″ N, 137°18′37.1″ E [110]). Since the effect of the local atmosphere accounts only for a few percent systematics and the difference in site is mainly due to the geomagnetic cutoff and therefore just a scaling factor [260], the atmospheric neutrino flux from FLUKA simulations is normalized to the flux from Honda in the overlapping energy region from 100 MeV to 944 MeV to predict the flux at JUNO site between neutrino energies from 10 MeV to 100 MeV. The normalization factors are $f_{\nu_e} = \int_{100\,\mathrm{MeV}}^{944\,\mathrm{MeV}} \phi_{\nu_e,Honda} \mathrm{d}E / \int_{100\,\mathrm{MeV}}^{944\,\mathrm{MeV}} \phi_{\nu_e,FLUKA} \mathrm{d}E = 0.85$, $f_{\bar{\nu}_e} = 0.88$, $f_{\nu_\mu} = 0.86$ and $f_{\bar{\nu}_\mu} = 0.87$. The normalized neutrino fluxes from FLUKA simulations between 10 MeV and 100 MeV, together with the fluxes from Honda between 100 MeV and 10 GeV, are used to specify the atmospheric neutrino fluxes of ν_e, $\bar{\nu}_e$, ν_μ and $\bar{\nu}_\mu$ at JUNO site and are shown in figure 5.4 without considering neutrino oscillation effects.

To predict the atmospheric neutrino flux at the location of the JUNO detector correctly, neutrino oscillation effects need to be taken into account. In [261], the neutrino oscillation probabilities are roughly estimated by considering three-flavor oscillation for atmospheric

neutrinos with a representative neutrino energy $E_\nu = 100$ MeV [6]. Assuming atmospheric neutrino fluxes produced 20 km above ground, a flavor ratio of $(\nu_\mu + \bar{\nu}_\mu)/(\nu_e + \bar{\nu}_e) = 2$ and a constant density approximation of the Earth to consider matter effects, the oscillation probabilities determined in [261] with oscillation parameters from [262] and for $E_\nu = 100$ MeV are: $P_{\nu_e \to \nu_e} = 0.67$, $P_{\nu_\mu \to \nu_\mu} = 0.41$, $P_{\nu_\mu \to \nu_e} = P_{\nu_e \to \nu_\mu} = 0.17$, $P_{\nu_\mu \to \nu_\tau} = 0.42$ and $P_{\nu_e \to \nu_\tau} = 0.16$ (the same oscillation probabilities are assumed for antineutrinos [5, 261]). With these oscillation probabilities, the atmospheric neutrino fluxes at JUNO site are calculated for neutrino energies from 10 MeV to 100 MeV. It is assumed that the probabilities calculated for $E_\nu = 100$ MeV are also valid for lower neutrino energies, which leads to an overall uncertainty of the flux of 25 % [260]. Considering neutrino oscillations, also a non-zero atmospheric ν_τ and $\bar{\nu}_\tau$ flux is present at JUNO site. Therefore, the atmospheric neutrino flux at JUNO site contains neutrinos and antineutrinos of all three flavors.

5.3.2. Atmospheric Charged Current Neutrino Background

Atmospheric neutrinos traversing JUNO's central detector volume can interact via charged current interactions with free protons and ^{12}C nuclei of the liquid scintillator[7] by the exchange of W^+/W^- bosons as described in section 3.2. This leads to several possible CC interaction channels that could cause background events in JUNO:

- atmospheric CC electron antineutrino background on free protons:
  $\bar{\nu}_e + p \to e^+ + n$
- atmospheric CC electron neutrino background on ^{12}C:
  $\nu_e + {}^{12}\mathrm{C} \to e^- + ...$
- atmospheric CC electron antineutrino background on ^{12}C:
  $\bar{\nu}_e + {}^{12}\mathrm{C} \to e^+ + ...$
- atmospheric CC muon antineutrino background on free protons:
  $\bar{\nu}_\mu + p \to \mu^+ + n.$
- atmospheric CC muon neutrino background on ^{12}C:
  $\nu_\mu + {}^{12}\mathrm{C} \to \mu^- + ...$
- atmospheric CC muon antineutrino background on ^{12}C:
  $\bar{\nu}_\mu + {}^{12}\mathrm{C} \to \mu^+ + ...$

These interaction channels will be discussed in the upcoming sections.
As mentioned in the previous section, the atmospheric neutrino flux at Earth also contains tau neutrinos and antineutrinos, which can interact via CC interactions with JUNO's liquid scintillator. These interactions of ν_τ and $\bar{\nu}_\tau$ on free protons and ^{12}C have been investigated in [5] resulting in a total number of atmospheric CC $\nu_\tau/\bar{\nu}_\tau$ events in JUNO of $N_{\nu_\tau + \bar{\nu}_\tau} = 134$ after 10 years, for 20 kt and distributed in the visible energy range from 0 GeV to 20 GeV (the total number of atmospheric CC $\nu_e/\bar{\nu}_e$ and $\nu_\mu/\bar{\nu}_\mu$ events in JUNO have been determined in [5] to $N_{\nu_e + \bar{\nu}_e} = 9773$ and $N_{\nu_\mu + \bar{\nu}_\mu} = 10883$, respectively). The fraction of $\nu_\tau/\bar{\nu}_\tau$ events to $\nu_e/\bar{\nu}_e$ and $\nu_\mu/\bar{\nu}_\mu$ events is 0.6 %. Therefore, the atmospheric CC

[6] The two-flavor neutrino oscillation, usually used for high energetic atmospheric neutrinos, is not valid for neutrinos in this low energy regime, since they are sensitive to the solar squared mass difference Δm^2_{21}.

[7] Atmospheric neutrinos and antineutrinos can also interact via CC on electrons of the target material: $\nu_e/\bar{\nu}_e + e^- \to e^- + \nu_e/\bar{\nu}_e$ and $\nu_\mu/\nu_\tau + e^- \to \nu_e + \mu^-/\tau^-$. Nevertheless, these interaction channels do not contribute to the atmospheric CC neutrino background in JUNO, since they do not mimic IBD events (no neutron capture) and the interaction cross sections for $E_\nu \geq 10$ MeV are comparably small as shown in figure 3.5 exemplarily for $\nu_e + e^- \to e^- + \nu_e$.

neutrino background is dominated by electron and muon neutrino (and antineutrino) interactions and CC interactions of atmospheric tau neutrinos and antineutrinos are neglected as potential background source in this study.

Charged Current Background of $\bar{\nu}_e$ on Protons

The most relevant atmospheric CC background source for the indirect DM search with JUNO are electron antineutrinos interacting with free protons since they also interact via the IBD reaction, $\bar{\nu}_e + p \rightarrow e^+ + n$, and are therefore indistinguishable from the signal signature of electron antineutrinos produced in DM self-annihilation. Moreover, the IBD interaction cross section is larger than CC interaction cross sections on ^{12}C as illustrated in figure 3.5.
The atmospheric $\bar{\nu}_e$ flux at JUNO site is given by the atmospheric antineutrino fluxes shown in figure 5.4 considering the oscillation probabilities introduced in section 5.3.1:

$$\begin{aligned}\phi_{\bar{\nu}_e}^{atmo} &= P_{\bar{\nu}_e \rightarrow \bar{\nu}_e}\, \phi_{\bar{\nu}_e} + P_{\bar{\nu}_\mu \rightarrow \bar{\nu}_e}\, \phi_{\bar{\nu}_\mu} \\ &\approx 0.67 \cdot \phi_{\bar{\nu}_e} + 0.17 \cdot \phi_{\bar{\nu}_\mu}. \end{aligned} \tag{5.7}$$

The atmospheric CC neutrino energy spectrum of electron antineutrinos interacting with free protons in the JUNO detector is then given by:

$$\frac{\mathrm{d}N_{atmoCC,\,\bar{\nu}_e+p}\,(E_{\bar{\nu}_e})}{\mathrm{d}E_{\bar{\nu}_e}} = \sigma_{IBD}\,(E_{\bar{\nu}_e})\, \frac{\mathrm{d}\phi_{\bar{\nu}_e}^{atmo}\,(E_{\bar{\nu}_e})}{\mathrm{d}E_{\bar{\nu}_e}}\, N_{target}\, t\, \epsilon_{IBD}\, \epsilon_{\mu\, veto}, \tag{5.8}$$

with the atmospheric $\bar{\nu}_e$ flux of equation 5.7. The remaining parameters are equal to section 4.2.
The visible energy spectrum $\mathrm{d}N_{atmoCC,\,\bar{\nu}_e+p}/\mathrm{d}E_{vis}$ of atmospheric electron antineutrinos interacting via CC with free protons in JUNO is calculated following the procedure described in section 5.1 with equation 5.8 considering IBD kinematics and JUNO's energy resolution.
The visible energy spectrum expected to be measured in JUNO after 10 years of data taking and for a fiducial volume of 14.77 kt is displayed in figure 5.2 for visible energy from 10 MeV to 100 MeV resulting in $N_{atmoCC,\,\bar{\nu}_e+p} = 30.5 \pm 7.6$ events. A total uncertainty of 25 % is assumed [260]. This yields an event rate of $R_{atmoCC,\,\bar{\nu}_e+p} = (0.21 \pm 0.05)\ \mathrm{yr}^{-1}\ \mathrm{kt}^{-1}$ and makes the atmospheric CC background of $\bar{\nu}_e$ interacting with free protons to one of the main backgrounds for indirect DM search with neutrinos in JUNO for energies above around 30 MeV.

Charged Current Background of $\nu_e/\bar{\nu}_e$ on ^{12}C

Atmospheric electron neutrinos and antineutrinos also interact with the ^{12}C nuclei of the organic liquid scintillator of JUNO's central detector through CC interaction producing electrons and positrons, respectively, and either ^{12}N or ^{12}B isotopes, that can be in ground state or excited states: $\nu_e + {}^{12}\mathrm{C} \rightarrow e^- + {}^{12}\mathrm{N}_{g.s.+e.s.}$ and $\bar{\nu}_e + {}^{12}\mathrm{C} \rightarrow e^+ + {}^{12}\mathrm{B}_{g.s.+e.s.}$.
These reaction channels differ from the IBD interaction channel with a positron and a neutron in the final state, but can cause so-called IBD-like background events in the JUNO detector depending on the de-excitation and potential decay of the produced isotopes. The IBD reaction is specified by the prompt energy deposition of the positron inside the detector volume and a temporally delayed capture of the thermalized neutron on hydrogen by emitting a 2.2 MeV gamma (details in section 3.2). In consequence of that, each event in JUNO's central detector with a similar signal signature (prompt energy deposition followed

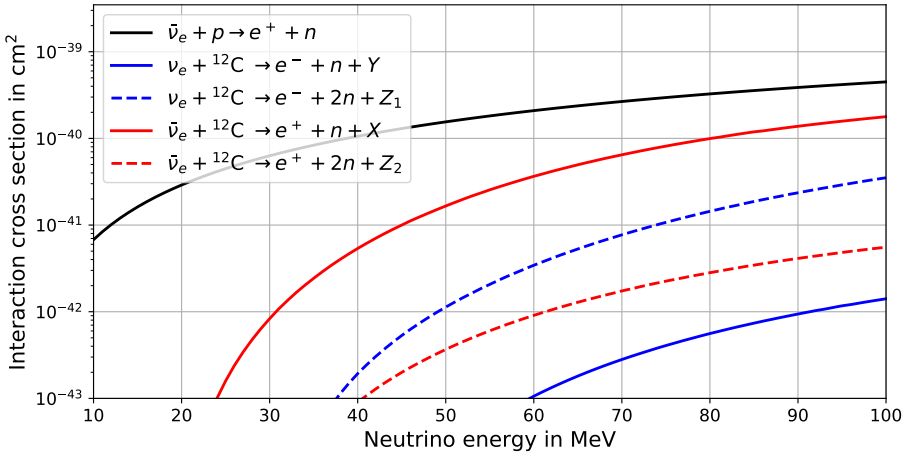

Figure 5.5.: Charged current neutrino interaction cross sections of ν_e and $\bar{\nu}_e$ interacting with ^{12}C for reaction channels with at least one neutron in the final state as calculated in [263]. The IBD interaction cross section of equation 4.4 is shown in black for comparison.

by a delayed emission of a 2.2 MeV gamma) can mimic an IBD signal and is an IBD-like background event.
The electrons and positrons produced in CC interactions of ν_e and $\bar{\nu}_e$ on ^{12}C deposit their energy directly in the scintillator volume, which leads to a prompt signal measured by the JUNO detector. A correlated delayed signal can only be caused by events with at least one neutron as final product of the interaction[8]. Therefore, only interaction channels with at least one neutron in the final state, either from de-excitation or decay of residual isotopes, can mimic an IBD signal signature.
To investigate the event rates of such $\nu_e/\bar{\nu}_e$ CC reactions on ^{12}C in JUNO, neutrino interaction cross sections are applied that have been calculated in [263] using new shell model Hamiltonians. The interaction channels with at least one neutron in the final state considering potential de-excitation and decay of residual isotopes are listed below, together with their total CC interaction cross sections calculated in [263] and integrated over neutrino energies from 10 MeV to 100 MeV:

- $\nu_e + {}^{12}\mathrm{C} \to e^- + {}^{12}\mathrm{N}_{e.s.} \to e^- + n + Y$: $\sigma = 2.6 \cdot 10^{-41}$ cm^2,
- $\nu_e + {}^{12}\mathrm{C} \to e^- + {}^{12}\mathrm{N}_{e.s.} \to e^- + 2n + Z_1$: $\sigma = 6.7 \cdot 10^{-40}$ cm^2,
- $\bar{\nu}_e + {}^{12}\mathrm{C} \to e^+ + {}^{12}\mathrm{B}_{e.s.} \to e^+ + n + X$: $\sigma = 4.5 \cdot 10^{-39}$ cm^2,
- $\bar{\nu}_e + {}^{12}\mathrm{C} \to e^+ + {}^{12}\mathrm{B}_{e.s.} \to e^+ + 2n + Z_2$: $\sigma = 1.3 \cdot 10^{-40}$ cm^2.

X, Y, Z_1 and Z_2 represent all products, except of neutrons, that are present in the final state. The interaction cross sections are also displayed in figure 5.5 for neutrino energies from 10 MeV to 100 MeV. The interaction cross section of $\bar{\nu}_e + {}^{12}\mathrm{C} \to e^+ + n + X$ is at least a factor of seven larger than the cross sections of the other channels listed above. So, only this interaction channel can cause a significant IBD-like background and is further investigated, while the other ones are neglected within this study.

The corresponding neutrino energy spectrum $\mathrm{d}N_{atmoCC,\bar{\nu}_e+{}^{12}\mathrm{C}}/\mathrm{d}E_{\bar{\nu}_e}$ is calculated with the atmospheric electron antineutrino flux introduced in equation 5.7 and the cross section of this channel displayed in figure 5.5:

[8] Interaction channels with more than one neutron as final product can also cause a single delayed signal, since neutrons can leave the central detector volume while thermalizing.

$$\frac{\mathrm{d}N_{atmoCC,\,\bar{\nu}_e+^{12}\mathrm{C}}\,(E_{\bar{\nu}_e})}{\mathrm{d}E_{\bar{\nu}_e}} = \sigma_{CC,\,\bar{\nu}_e+^{12}\mathrm{C}}\,(E_{\bar{\nu}_e})\;\frac{\mathrm{d}\phi^{atmo}_{\bar{\nu}_e}\,(E_{\bar{\nu}_e})}{\mathrm{d}E_{\bar{\nu}_e}}\,N_{target}\,t\,\epsilon_{IBD}\,\epsilon_{\mu\,veto}, \tag{5.9}$$

The number of targets is given by the number of ^{12}C nuclei in JUNO's central detector of $N_{target} = 8.82{\cdot}10^{32}$. To estimate the detection efficiency for this channel, the IBD detection efficiency of $\epsilon_{IBD} = 67.0\,\%$ is used, since additional particles represented by X (mainly ^{11}B) would, at most, reduce the detection efficiency. Therefore, the neutrino energy spectrum of equation 5.9 might be slightly overestimated. The remaining parameters are set equal to the previous sections.
The visible energy spectrum $\mathrm{d}N_{atmoCC,\,\bar{\nu}_e+^{12}\mathrm{C}}/\mathrm{d}E_{vis}$ of atmospheric electron antineutrino CC interactions on ^{12}C is generated considering the kinematics of the reaction $\bar{\nu}_e + {}^{12}\mathrm{C} \rightarrow e^+ + n + {}^{11}\mathrm{B}$, which is the most frequent one with 96.6 % [263]. With the simple assumptions that the neutron and ^{11}B isotope are at rest, the kinetic energy of the positron E_e is given by $E_e = E_{\bar{\nu}_e} + m_{^{12}\mathrm{C}} - m_e - m_n - m_{^{11}\mathrm{B}} \approx E_{\bar{\nu}_e} - 17.23$ MeV. The visible energy spectrum is generated considering these kinematics and JUNO's energy resolution of equation 3.16 following the same procedure as described in section 5.1.
The visible energy spectrum of $\bar{\nu}_e + {}^{12}\mathrm{C} \rightarrow e^+ + n + X$ in JUNO for 14.77 kt and after a lifetime of 10 years is shown in figure 5.2. A total uncertainty of 25 % [260] is assumed similar to the previous section. For visible energies between 10 MeV and 100 MeV, the number of expected background events that can mimic an IBD signature in JUNO is $N_{atmoCC,\,\bar{\nu}_e+^{12}\mathrm{C}} = 5.9 \pm 1.5$, which leads to a corresponding event rate of $R_{atmoCC,\,\bar{\nu}_e+^{12}\mathrm{C}} = (0.04 \pm 0.01)\ \mathrm{yr}^{-1}\ \mathrm{kt}^{-1}$. Despite the relatively small event rate, the CC background of electron neutrinos and antineutrinos interacting with ^{12}C needs to be considered to study the indirect DM search in JUNO, since it affects the visible energy spectrum especially in the higher energy region.

Charged Current Background of $\bar{\nu}_\mu$ on Protons and $\nu_\mu/\bar{\nu}_\mu$ on ^{12}C

Besides electron neutrinos and antineutrinos, also atmospheric muon neutrinos and antineutrinos interact with free protons and ^{12}C nuclei in the central detector of JUNO by the exchange of charged W^+/W^- bosons. In these reactions ($\bar{\nu}_\mu + p \rightarrow \mu^+ + n$, $\nu_\mu + {}^{12}\mathrm{C} \rightarrow \mu^- + {}^{12}\mathrm{N}_{g.s.+e.s.}$ and $\bar{\nu}_\mu + {}^{12}\mathrm{C} \rightarrow \mu^+ + {}^{12}\mathrm{B}_{g.s.+e.s.}$) muons are produced, which results in a larger energy threshold than for $\nu_e/\bar{\nu}_e$ CC interactions. So, these interaction channels only occur for higher energetic atmospheric neutrinos. Nevertheless, the produced muons can create visible energies between few MeV and 100 MeV inside the detector volume causing background events for the indirect DM search in this energy region. Moreover, these $\nu_\mu/\bar{\nu}_\mu$ CC interactions could mimic an IBD signal signature in JUNO's central detector and appear as IBD-like background. The muon (μ^+ or μ^-) deposits its energy promptly by ionizing the molecules of the liquid scintillator, whereas the neutron or neutrons emitted in the de-excitation processes of excited ^{12}N and ^{12}B isotopes thermalize and are captured by hydrogen temporally delayed and spatially correlated to the prompt energy deposition.
To estimate the background contribution of atmospheric muon (anti)neutrinos, the neutrino energy spectra of each channel introduced above is calculated with:

$$\frac{\mathrm{d}N_{atmoCC,\,\bar{\nu}_\mu+p}(E_{\bar{\nu}})}{\mathrm{d}E_{\bar{\nu}}} = \sigma_{CC,\,\bar{\nu}_\mu+p}(E_{\bar{\nu}})\;\frac{\mathrm{d}\phi^{atmo}_{\bar{\nu}_\mu}(E_{\bar{\nu}})}{\mathrm{d}E_{\bar{\nu}}}\;N_p\;t, \tag{5.10}$$

$$\frac{\mathrm{d}N_{atmoCC,\,\nu_\mu+^{12}\mathrm{C}}(E_\nu)}{\mathrm{d}E_\nu} = \sigma_{CC,\,\nu_\mu+^{12}\mathrm{C}}(E_\nu)\;\frac{\mathrm{d}\phi^{atmo}_{\nu_\mu}(E_\nu)}{\mathrm{d}E_\nu}\;N_{^{12}\mathrm{C}}\;t, \tag{5.11}$$

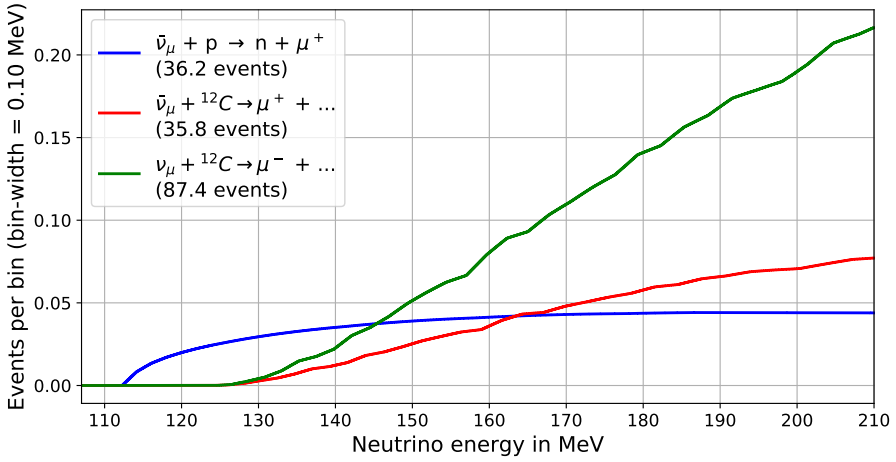

Figure 5.6.: Expected neutrino energy spectra of atmospheric ν_μ and $\bar{\nu}_\mu$ interacting via CC interactions with free protons and ^{12}C nuclei in JUNO for a fiducial mass of 14.77 kt and after 10 years of lifetime. The event numbers in the parentheses represent the number of events for 14.77 kt and 10 years of data taking in the energy range from 105 MeV to 210 MeV.

$$\frac{\mathrm{d}N_{atmoCC,\,\bar{\nu}_\mu+{}^{12}\mathrm{C}}(E_{\bar{\nu}})}{\mathrm{d}E_{\bar{\nu}}} = \sigma_{CC,\,\bar{\nu}_\mu+{}^{12}\mathrm{C}}(E_{\bar{\nu}})\,\frac{\mathrm{d}\phi^{atmo}_{\bar{\nu}_\mu}(E_{\bar{\nu}})}{\mathrm{d}E_{\bar{\nu}}}\,N_{^{12}\mathrm{C}}\,t, \tag{5.12}$$

where N_p and $N_{^{12}\mathrm{C}}$ are the number of free protons and ^{12}C nuclei in JUNO for 14.77 kt fiducial mass, respectively, and $t = 10$ years. The CC neutrino interaction cross sections $\sigma_{CC,\,\bar{\nu}_\mu+p}$, $\sigma_{CC,\,\nu_\mu+{}^{12}\mathrm{C}}$ and $\sigma_{CC,\,\bar{\nu}_\mu+{}^{12}\mathrm{C}}$ are taken from the GENIE event generator [264,265], where quasielastic CC scattering interactions [266] and CC resonance production [267] is considered. The atmospheric muon neutrino flux $\phi^{atmo}_{\nu_\mu}$ and muon antineutrino flux $\phi^{atmo}_{\bar{\nu}_\mu}$ at JUNO site after considering neutrino oscillations are given by the atmospheric fluxes and oscillation probabilities introduced in section 5.3.1:

$$\begin{aligned}\phi^{atmo}_{\nu_\mu}(E_\nu) &= P_{\nu_e\to\nu_\mu}\cdot\phi_{\nu_e}(E_\nu) + P_{\nu_\mu\to\nu_\mu}\cdot\phi_{\nu_\mu}(E_\nu)\\ &\approx 0.17\cdot\phi_{\nu_e}(E_\nu) + 0.41\cdot\phi_{\nu_\mu}(E_\nu),\end{aligned} \tag{5.13}$$

$$\begin{aligned}\phi^{atmo}_{\bar{\nu}_\mu}(E_{\bar{\nu}}) &= P_{\bar{\nu}_e\to\bar{\nu}_\mu}\cdot\phi_{\bar{\nu}_e}(E_{\bar{\nu}}) + P_{\bar{\nu}_\mu\to\bar{\nu}_\mu}\cdot\phi_{\bar{\nu}_\mu}(E_{\bar{\nu}})\\ &\approx 0.17\cdot\phi_{\bar{\nu}_e}(E_{\bar{\nu}}) + 0.41\cdot\phi_{\bar{\nu}_\mu}(E_{\bar{\nu}}).\end{aligned} \tag{5.14}$$

The resulting neutrino energy spectra of atmospheric muon neutrinos and antineutrinos interacting via CC with free protons and ^{12}C nuclei in JUNO are displayed in figure 5.6. After 10 years of data taking and for a fiducial mass of 14.77 kt, $N_{atmoCC,\,\bar{\nu}_\mu+p} \approx 36.2$, $N_{atmoCC,\,\nu_\mu+{}^{12}\mathrm{C}} \approx 87.4$ and $N_{atmoCC,\,\bar{\nu}_\mu+{}^{12}\mathrm{C}} \approx 35.8$ events are expected in JUNO for neutrino energies up to 210 MeV without considering any selection cuts[9].

To reduce the atmospheric CC ν_μ and $\bar{\nu}_\mu$ background, a cut on the standard deviation

[9] An event with $E_{\nu_\mu/\bar{\nu}_\mu} = 210$ MeV will produce a muon with maximal kinetic energy of around 103 MeV considering the kinematics of the described channels. This would correspond to a maximal visible energy in the JUNO detector of 103 MeV, if the muon deposits all its energy within the detector volume. So, the neutrino energy spectra and the event numbers are calculated up to $E_\nu = 210$ MeV, which corresponds to visible energies below around 103 MeV.

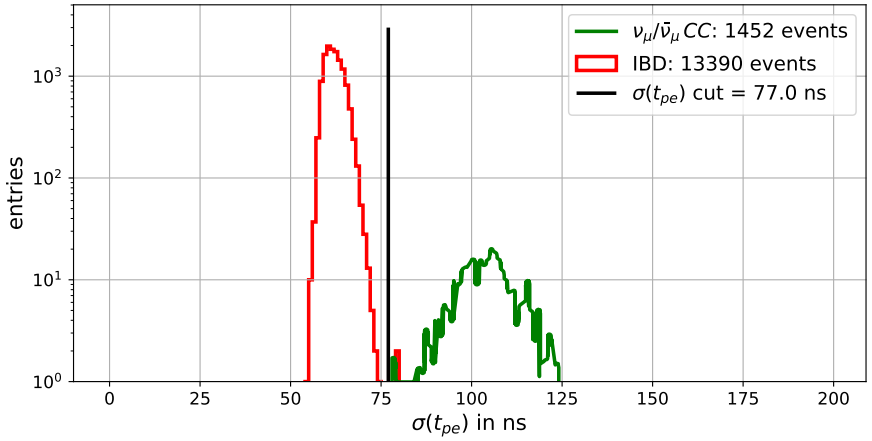

Figure 5.7.: Standard deviation $\sigma(t_{pe})$ of the photon emission times t_{pe} of simulated IBD events and simulated atmospheric CC ν_μ and $\bar{\nu}_\mu$ background events. 13390 IBD events and 1452 atmospheric ν_μ and $\bar{\nu}_\mu$ CC background events within $R < 16$ m are analyzed. The cut parameter $\sigma_{cut}(t_{pe}) = 77.0$ ns (black line) is also shown. The resulting survival efficiencies are $\epsilon^{IBD}_{\sigma(t_{pe})} = 99.98$ % and $\epsilon^{atmoCC}_{\sigma(t_{pe})} < 0.02$ %.

$\sigma(t_{pe})$ of the photon emission times t_{pe} of the pulse shapes, which is a measure of the temporal evolution of events inside the JUNO detector, can be applied. Since this temporal evolution of the pulse shapes and therefore the values of $\sigma(t_{pe})$ differ between IBD and atmospheric CC $\nu_\mu/\bar{\nu}_\mu$ events, $\sigma(t_{pe})$ is used to discriminate both event types.
The values for $\sigma(t_{pe})$ of IBD events are calculated from the pulse shapes of the prompt signals of the simulated IBD events described in section 4.3, that pass the IBD selection cuts. Atmospheric muon neutrinos and antineutrinos interacting via CC interactions with free protons and ^{12}C have been simulated in [268]. The events were generated with the GENIE event generator considering the neutrino fluxes of figure 5.4 and the interaction cross sections defined in equations 5.10, 5.11 and 5.12. The detector response of 1452 events was simulated with the JUNO detector simulation framework (version J18v1r1-Pre1) and $\sigma(t_{pe})$ of each event was calculated for events within $R < 16$ m and with deposited energy inside the central detector volume between 10^4 and 10^5 photo-electrons, which corresponds to visible energies from around 7 MeV to 70 MeV considering the conversion described in section 4.3. This sample of 1452 simulated events is equivalent to data of around 90 years in JUNO.
In figure 5.7, $\sigma(t_{pe})$ of 13390 IBD events, that pass all IBD selection cuts described in section 4.3, and $\sigma(t_{pe})$ of 1452 simulated atmospheric ν_μ and $\bar{\nu}_\mu$ CC background events from [268] are shown. A clear separation between both event types is visible. The cut parameter $\sigma_{cut}(t_{pe}) \leq 77.0$ ns leads to a survival efficiency of IBD events of $\epsilon^{IBD}_{\sigma(t_{pe})} = 99.98$ % for the analyzed dataset. None of the simulated atmospheric $\nu_\mu/\bar{\nu}_\mu$ events passes the cut and the survival efficiency of atmospheric CC muon neutrino background events is $\epsilon^{atmoCC}_{\sigma(t_{pe})} < 0.02$ % taking into account the statistical uncertainty.
Therefore, atmospheric muon neutrino and antineutrino background events produced via CC interactions on free protons and ^{12}C, respectively, can be reduced to a negligible level by a cut at $\sigma_{cut}(t_{pe}) = 77.0$ ns and are no background source for JUNO's measurement of neutrinos from DM self-annihilation in the Milky Way.

5.3.3. Atmospheric Neutral Current Neutrino Background

Besides the described atmospheric CC neutrino background, also neutral current interactions of atmospheric neutrinos and antineutrinos of all flavors with JUNO's liquid scintillator constitute a relevant background for the indirect DM search with neutrinos.
The atmospheric NC neutrino background was first measured as background in 2012 by the KamLAND experiment [195]. Interacting with JUNO's liquid scintillator, NC reactions of atmospheric neutrinos and antineutrinos of all flavors on free protons, electrons[10] and ^{12}C are present in JUNO:

- $\nu/\bar{\nu} + p \rightarrow \nu/\bar{\nu} + p$,
- $\nu/\bar{\nu} + e^- \rightarrow \nu/\bar{\nu} + e^-$,
- $\nu/\bar{\nu} + {}^{12}\mathrm{C} \rightarrow \nu/\bar{\nu} + ...$

Especially NC reactions on ^{12}C pose a critical background source for JUNO's sensitivity for indirect DM search because of the large variety of possible reaction channels. Depending on the energy of the incoming atmospheric neutrinos and antineutrinos, neutrons and protons can be knocked out of the ^{12}C nuclei, mesons like pions and kaons can be produced and additional particles like gammas, neutrons and protons can be emitted by the de-excitation of the residual isotopes. Several of these interaction channels can cause IBD-like background events in the JUNO detector, which makes the atmospheric NC neutrino background on ^{12}C to the main IBD-like background source for the search of neutrinos from DM annihilation in JUNO. In contrast to NC interactions on ^{12}C, NC reactions on free protons do not significantly contribute to the IBD-like background, which is shortly discussed at the end of the section.
In this section the investigation of the atmospheric NC neutrino background on ^{12}C in JUNO and the simulation and analysis to predict this background contribution performed within this thesis is presented in detail.

Event Rate of Atmospheric NC Neutrino Background in JUNO

The expected rate of atmospheric NC background events on ^{12}C in the JUNO central detector is:

$$\frac{\mathrm{d}N_{atmoNC}(E_\nu)}{\mathrm{d}t} = N_{^{12}\mathrm{C}} \sum_{i=0}^{5} \phi_{\nu_i}^{atmo,\,osc}(E_\nu)\ \sigma_{NC,\,\nu_i+^{12}\mathrm{C}}(E_\nu) \tag{5.15}$$

$$= N_{^{12}\mathrm{C}} \sum_{i=0}^{3} \phi_{\nu_i}^{atmo}(E_\nu)\ \sigma_{NC,\,\nu_i+^{12}\mathrm{C}}(E_\nu), \tag{5.16}$$

where $N_{^{12}\mathrm{C}} = 8.82 \cdot 10^{33}$ is the number of ^{12}C nuclei in the whole JUNO liquid scintillator and i specifies the neutrino flavor ($\nu_0 = \nu_e$, $\nu_1 = \bar{\nu}_e$, $\nu_2 = \nu_\mu$, $\nu_3 = \bar{\nu}_\mu$, $\nu_4 = \nu_\tau$, $\nu_5 = \bar{\nu}_\tau$). The atmospheric neutrino flux at JUNO site without considering neutrino oscillations $\phi_{\nu_i}^{atmo}$ and with oscillations $\phi_{\nu_i}^{atmo,\,osc}$ for each neutrino flavor is given by the flux shown in figure 5.4 and described in section 5.3.1, respectively. The NC neutrino interaction cross sections $\sigma_{NC,\,\nu_i+^{12}\mathrm{C}}$ on ^{12}C are taken from the GENIE event generator

[10] NC reactions on e^- cannot mimic IBD signals in JUNO, since no neutron is produced and a delayed signal is missing. Nevertheless, the electron could potentially knock out neutrons of the nuclei of the LS, which can be captured and produce delayed signals. However, the interaction cross section of neutrinos on electrons is comparably small for $E_\nu > 10$ MeV. Therefore, this channel is neglected as IBD-like background in this study.

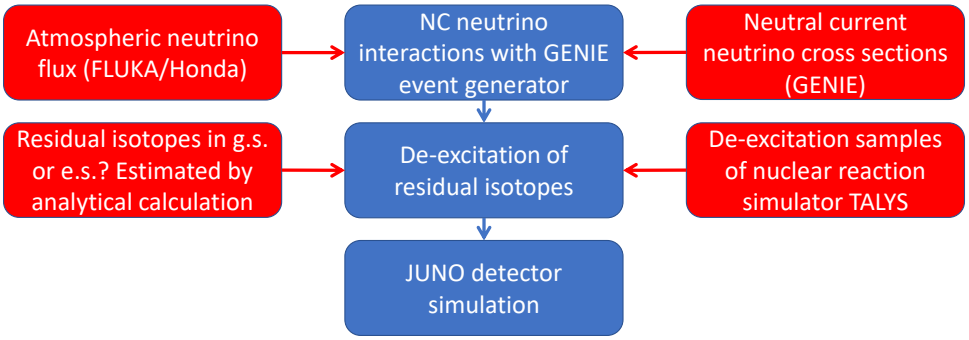

Figure 5.8.: Simulation procedure to predict the atmospheric NC neutrino background in JUNO. The simulation steps are illustrated in blue boxes; the corresponding inputs are shown in red boxes.

(*gxspl-FNALsmall.xml*, [267, 269, 270]).
Since the neutrino NC interaction cross sections are equal for the three neutrino and antineutrino flavors, respectively ($\sigma_{NC,\nu_e+^{12}\mathrm{C}} = \sigma_{NC,\nu_\mu+^{12}\mathrm{C}} = \sigma_{NC,\nu_\tau+^{12}\mathrm{C}}$), equation 5.15 is equal to equation 5.16 and the atmospheric neutrino fluxes without considering neutrino oscillations can be used to estimate the event rate.
The event rate of atmospheric NC neutrino interactions on ^{12}C in the whole JUNO detector for neutrino energies from 10 MeV to 10 GeV is then calculated with equation 5.16 resulting in

$$\frac{dN_{atmoNC}}{dt} = \int_{10\,\mathrm{MeV}}^{10\,\mathrm{GeV}} \frac{dN_{atmoNC}(E_\nu)}{dt}\, dE_\nu \approx 3.169 \cdot 10^{-5}\,\mathrm{s}^{-1}. \tag{5.17}$$

This leads to 10002 atmospheric NC interactions on ^{12}C in JUNO's central detector in a lifetime of 10 years.

Simulation of Atmospheric NC Neutrino Background in JUNO

To predict the IBD-like background caused by NC reactions of atmospheric neutrinos in JUNO, neutral current neutrino interactions with JUNO's liquid scintillator, potential de-excitation of residual isotopes and JUNO's detector response to the final interaction products are simulated in this study. The simulation procedure is illustrated in figure 5.8.

The NC interactions of atmospheric neutrinos with JUNO's liquid scintillator material are simulated with the GENIE event generator [264, 265]. The atmospheric neutrino fluxes of ν_e, $\bar{\nu}_e$, ν_μ and $\bar{\nu}_\mu$ at JUNO site for neutrino energies from 10 MeV to 10 GeV shown in figure 5.4 are used as input for GENIE. A composition of the LAB based liquid scintillator of JUNO (described in detail in section 3.3.1) of 12.01 % free protons, 87.92 % ^{12}C, 0.034 % ^{16}O, 0.027 % ^{14}N and 0.005 % ^{32}S characterizes the target material for the GENIE simulation. Around 1,500,000 NC interactions are simulated with GENIE (version: v2-12-0) for neutrino energies from 10 MeV to 10 GeV with the atmospheric neutrino fluxes and the target compositions described above. The NC neutrino interaction cross sections used in GENIE contain quasielastic scattering (QES), deep inelastic scattering (DIS) and resonance production by neutrinos (RES) and are based on [267, 269, 270].
86.1 % of all NC interaction simulated with GENIE are on ^{12}C and 13.8 % on free protons. The sum of the interaction fractions of the other LS components is only 0.07 % and, therefore, these NC interactions are neglected as background in the study performed in this thesis. The resulting NC reaction channels on ^{12}C simulated with GENIE for different residual isotopes and their fractions are shown in figure 5.9.

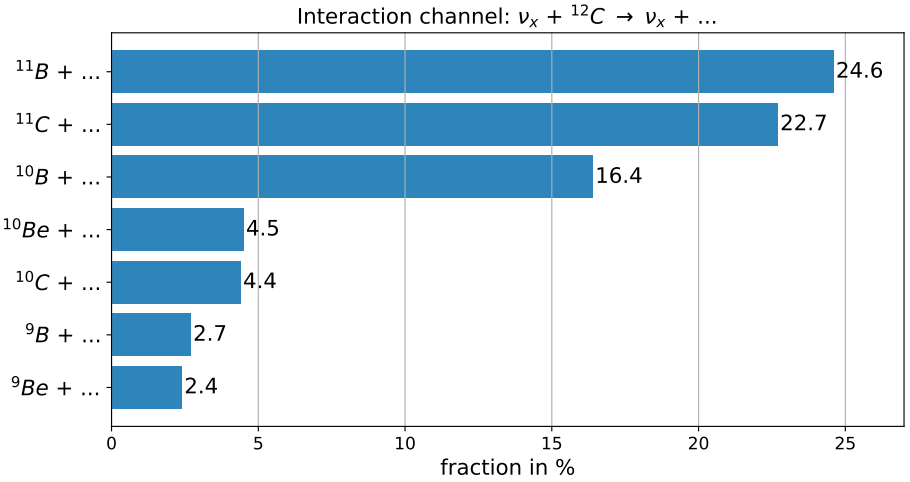

Figure 5.9.: Fractions of atmospheric NC neutrino interaction channels on ^{12}C from GENIE simulation before de-excitation (residual isotopes can be in ground and excited state). The seven most frequent isotopes (with an integrated fraction of 77.7 %) are displayed here.

In NC reactions, neutrons and/or protons can be knocked out of the ^{12}C nucleus and leave the residual isotope in ground or an excited state depending on the shell, where the nucleons are knocked out. Before NC interactions, ^{12}C nuclei of the LS are in ground state and two occupations of the energy levels, corresponding to a simple and a more sophisticated shell model, are possible due to correlations between the p-shells (especially pairing effects, for details see [271]). Both shell models and occupations are shown in figure 5.10 with the corresponding energy levels.
If the residual isotopes are in excited states, de-excitation processes of these isotopes must be considered. The procedure to estimate the probabilities, if a residual isotope is in an excited state, is described in detail for the example of ^{11}C. In channel $\nu_x/\bar{\nu}_x + {}^{12}\mathrm{C} \rightarrow \nu_x/\bar{\nu}_x + {}^{11}\mathrm{C} + n$, one neutron is knocked out from ^{12}C ground state and the following three states of ^{11}C are possible:

1. ^{11}C nuclei is in ground state with probability of $8/15 \approx 53$ % (neutron is knocked out from $P_{3/2}$ shell in simple shell model or from $P_{1/2}$ shell in advanced shell model, see case 1 of figure 5.10),
2. ^{11}C nuclei is in first excited state (emission of 2 MeV gamma [271]) with probability of $2/15 \approx 13$ % (only possible in advanced shell model, when the neutron is knocked out from $P_{3/2}$ shell, see case 2 of figure 5.10),
3. ^{11}C nuclei is in excited state with probability of $5/15 \approx 33$ % (neutron is knocked out from $S_{1/2}$ shell in both shell models, see case 3 of figure 5.10).

A similar approach is used to determine the probabilities for ^{11}B, when a proton is knocked out from ^{12}C nuclei.
For lighter isotopes like ^{10}C, ^{10}Be and ^{10}B, the probabilities of being in ground or excited state are calculated only by considering the simple shell model of figure 5.10 for simplicity and because the probabilities change only slightly, if the advanced shell model is also considered. This leads to the following probabilities P:

- for ^{10}C and ^{10}Be: ground state with $P = 6/15 = 40$ % and excited state with $P = 9/15 = 60$ %
- for ^{10}B: ground state with $P = 4/9 \approx 44$ % and excited state with $P = 5/9 \approx 56$ %.

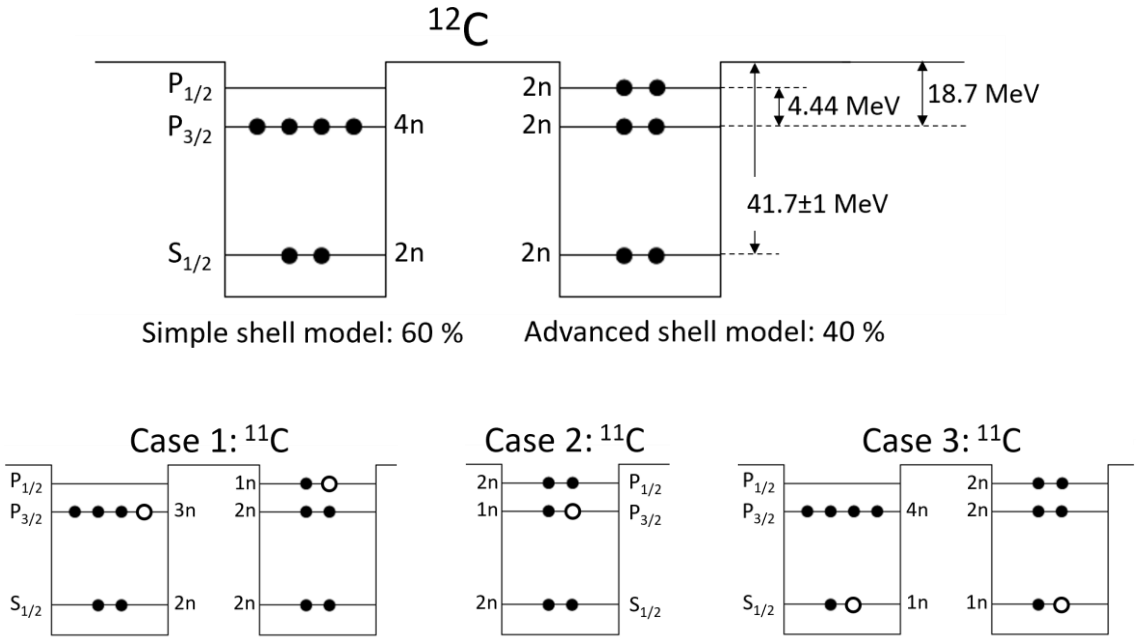

Figure 5.10.: Top: Occupation of energy levels by neutrons of the ^{12}C ground state. The probability for the occupation in the simple shell model is 60 % and in the advanced shell model 40 % [271]. The same occupations of energy levels are realized for protons in the ground state of ^{12}C [271]. Bottom: possible states of ^{11}C after neutron knock out. ^{11}C is in ground state in case 1, in the first excited state in case 2 and in excited state in case 3.

All lighter isotopes (^{9}C, ^{9}B, ^{9}Be, ^{9}Li, ...) are assumed to be in ground state, since a reasonable calculation of the probabilities and exact simulation of the de-excitation processes can not be achieved. This of course leads to an uncertainty of the atmospheric NC background on ^{12}C, but the fraction of these lighter isotopes to all NC interaction channels is only around 23.6 % and just a portion of that would be in excited states.
The described probabilities are used as input to specify if residual isotopes generated in NC interactions with GENIE are in ground or excited state. In case of excitation of the isotopes, simulation data of the de-excitation processes simulated with the nuclear reaction simulator TALYS [272] are used to consider the de-excitation of each residual isotope and its excited states. For more information about the implementation of these de-excitation simulation data see [273]. The most frequent de-excitation channels of ^{11}C* based on the de-excitation simulation of TALYS and the probabilities for different excited states described above are shown in figure 5.11 as an example.

All final particles, that are produced via NC interactions of atmospheric neutrinos and antineutrinos on ^{12}C and through potential de-excitation of residual isotopes, as well as their momenta are used as input for the JUNO detector simulation DetSim (version J18v1r1-Pre1) [11]. The most frequent final NC reaction channels on ^{12}C after potential

[11] Potential decay of residual isotopes is not considered here. Isotopes like ^{11}B, ^{10}B, ^{9}Be and ^{6}Li of the most frequent total interaction channels shown in figure 5.12 are stable. ^{11}C decays via β^{+}-decay into ^{11}B with $T_{1/2} \approx 20$ min [274], which is very long compared to the relevant delayed time window of 1 ms of IBD signals. ^{8}Be and ^{9}B decay with $T_{1/2} < 10^{-17}$ s into two α particles and $p + 2\alpha$ [274], respectively. These protons and α particles would slightly increase the visible energy of the prompt signal of atmospheric NC events of these channels. Nevertheless, since no additional neutrons are emitted in the decays, the detection efficiency and the number of IBD-like atmospheric NC events is affected negligibly. So, not considering potential decays of residual isotopes only leads to a small uncertainty, which is taking into account in the assumed total uncertainty of 29 %.

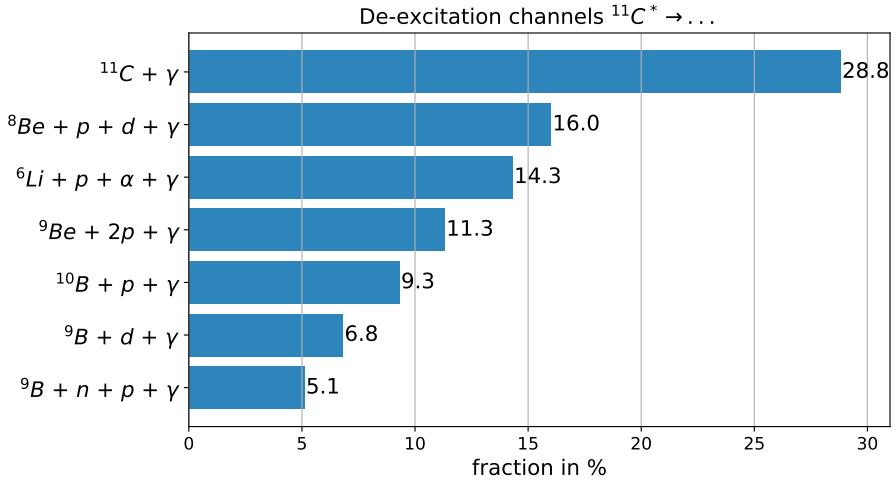

Figure 5.11.: Fractions of de-excitation channels of ^{11}C* based on the de-excitation processes of the nuclear reaction simulator TALYS and the described probabilities for the different excitation states of ^{11}C. The seven most frequent channels (with an integrated fraction of 91.6 %) are shown here.

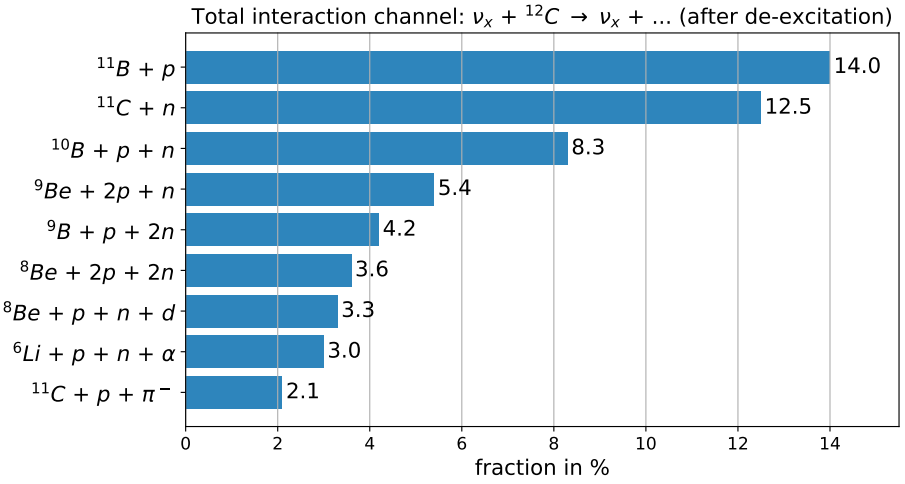

Figure 5.12.: Fractions of total atmospheric NC neutrino interaction channels on ^{12}C after considering potential de-excitation. The nine most frequent channels with an integrated fraction of 56.4 % are shown. Additional π^0's and γ's are not displayed here.

Table 5.1.: IBD selection criteria together with the resulting cut efficiencies and the total detection efficiency ϵ_{atmoNC} of atmospheric NC events on ^{12}C. The cut efficiencies are determined by the analysis of atmospheric NC events simulated with the JUNO detector simulation (middle column). The cuts of the delayed cut are listed from (a) to (e) and applied consecutively. For comparison, the cut efficiencies and the total IBD detection efficiency of IBD events from table 4.2 are shown (right column). The statistical errors $\Delta\epsilon$ of each cut efficiency are also listed.

	$\epsilon_{atmoNC} \pm \Delta\epsilon_{atmoNC}$ in %	$\epsilon_{IBD} \pm \Delta\epsilon_{IBD}$ in %
Volume cut on prompt signal	67.6 ± 0.2	73.0 ± 0.8
Energy cut on prompt signal	43.7 ± 0.1	96.2 ± 1.0
Total delayed cut:	25.2 ± 0.1	92.6 ± 0.9
(a) Time difference cut	69.0 ± 0.2	95.7 ± 1.0
(b) Multiplicity cut	45.7 ± 0.2	99.97 ± 1.0
(c) Energy cut on del. signal	91.2 ± 0.4	97.4 ± 1.0
(d) Distance cut	88.1 ± 0.4	99.7 ± 1.0
(e) Volume cut on del. signal	99.6 ± 0.5	99.7 ± 1.0
Total efficiency	$\mathbf{7.8 \pm 0.1}$	$\mathbf{67.0 \pm 0.7}$

de-excitations inputted into JUNO's detector simulation are displayed in figure 5.12. A large variety of different interaction channels containing neutrons, protons, deuterons, alpha, pions, gammas and various isotopes are present as figure 5.12 indicates.
JUNO's detector response of 400,000 atmospheric NC neutrino events on ^{12}C randomly distributed in the whole central detector volume have been simulated with JUNO DetSim within this thesis. This sample of 400,000 atmospheric NC events is equivalent to data of around 400 years taking into account the expected event rate of equation 5.17.

Analysis of Atmospheric NC Neutrino Background in JUNO

The simulation sample of 400,000 atmospheric NC neutrino events on ^{12}C in the JUNO detector is analyzed to estimate the number of NC background events that mimic an IBD signal. Therefore, the IBD selection criteria introduced and described in section 4.3 and summarized in table 4.2 are applied on the simulated atmospheric NC events in the exact same way like on the IBD events.
Hence, the MC truth data of the simulated atmospheric NC events is smeared with the expected vertex and time resolution of JUNO introduced in section 4.3. The pulse shapes, i.e. the number of p.e. as function of the photon emission time, of all simulated atmospheric NC events are calculated to specify the number of p.e. and the visible energy of prompt and delayed signals with the conversion function $E_{vis} = 7.045 \cdot 10^{-4}\text{MeV/p.e} \cdot N_{p.e.}$. Afterwards the IBD selection cuts described in section 4.3 are applied to each simulated atmospheric NC event. The volume cut on the prompt signal, energy cut on the prompt signal and the total delayed cut are applied on all 400,000 events separately to be able to specify their efficiencies due to different cut parameters independently. The distributions of the data of all simulated NC events are displayed in section A.2.
The resulting cut efficiencies of atmospheric NC neutrino background events on ^{12}C for the IBD selection cuts and their statistical errors are shown in table 5.1 together with the cut efficiencies of the simulated IBD events already presented in table 4.2 for comparison. Atmospheric NC background events that pass all described selection cuts mimic an IBD signal in JUNO's central detector and represent an IBD-like background for the indirect DM search with JUNO.

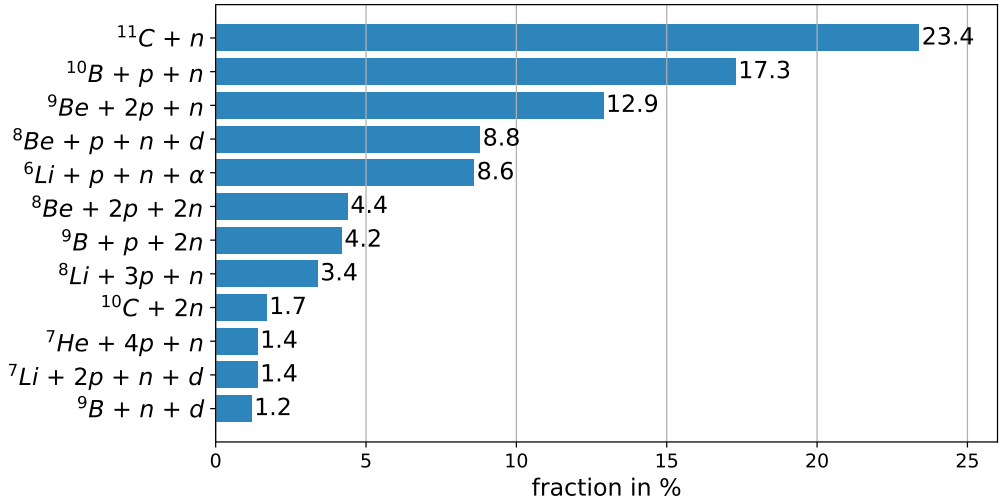

Figure 5.13.: Fractions of total atmospheric NC neutrino interaction channels on ^{12}C that mimic IBD signals in the JUNO detector. The twelve most frequent channels $\nu_x/\bar{\nu}_x + {}^{12}\mathrm{C} \rightarrow \nu_x/\bar{\nu}_x + ...$ producing IBD-like events in JUNO (with an integrated fraction of 88.7 %) are displayed. Additional π's and γ's are not shown.

The efficiency of the volume cut on the prompt signal is roughly similar for atmospheric NC events and IBD events, since both event types occur uniformly distributed within the central detector volume and the cut efficiency is dominated by the geometric reduction to a fiducial volume specified by $R_{prompt} < 16.0$ m. The energy cut on the prompt signal with a cut efficiency of $\epsilon_{E_{prompt}} = (43.7 \pm 0.1)$ % mainly depends on the choice of the observation window from 10 MeV to 100 MeV and reduces the atmospheric NC background by around two-thirds. The largest suppression of atmospheric NC events is provided by the total delayed cut with an efficiency of $\epsilon_{delayed} = (25.2 \pm 0.1)$ %. This great suppression ability relies on the strict selection criteria of IBD signals due to the temporal and spatial coincidence of prompt and delayed signal. Especially the multiplicity cut with an efficiency of $\epsilon_{mult} = (45.7 \pm 0.2)$ % reduces atmospheric NC background events very effectively compared to IBD events, since NC events often contain more than one neutron that can be captured on hydrogen and create a delayed signal.
In total, only 31,143 events of the 400,000 simulated atmospheric NC neutrino events mimic an IBD event signature. Therefore, the total cut efficiency of atmospheric NC neutrino background events on ^{12}C in the JUNO detector is $\epsilon_{atmoNC} = (7.8 \pm 0.1)$ %.
Considering the event rate of equation 5.17 and the efficiency due to the application of the muon veto $\epsilon_{\mu\,veto} = 97.2$ %, $N_{atmoNC} = 757 \pm 220$ atmospheric NC neutrino background events mimic an IBD event signature in the JUNO detector after 10 years of data taking, for a fiducial mass of 14.77 kt and for visible energies between 10 MeV and 100 MeV. A total uncertainty of the atmospheric NC background of 29 % is assumed according to [74]. An event rate of IBD-like atmospheric NC events of $R_{atmoNC} = (5.1 \pm 1.5)\,\mathrm{yr}^{-1}\,\mathrm{kt}^{-1}$ is given in the JUNO detector. The resulting visible energy spectrum of the IBD-like atmospheric NC neutrino background is shown in figure 5.2. It represents the dominant background source for the search for neutrinos from DM annihilation with the JUNO detector and overwhelms the expected signal and especially the other background contributions by at least one order of magnitude, but differs significantly in the spectral shape compared to the signal spectrum.
The fractions of the most frequent total atmospheric NC neutrino interaction channels on ^{12}C that mimic an IBD signal in JUNO's central detector are shown in figure 5.13.

The most crucial reaction channel is $\nu_x/\bar{\nu}_x + {}^{12}\mathrm{C} \rightarrow \nu_x/\bar{\nu}_x + {}^{11}\mathrm{C} + n$ with an expected frequency of 23.4 %. Nevertheless, many different NC interaction channels of atmospheric neutrinos on ^{12}C can create IBD-like signals in the detector, which makes the simulation and prediction of the atmospheric NC background to one of the main issues studied in this thesis.
84.5 % of the IBD-like events contain only one neutron (13.3 % contain two neutrons). In contrast to that, the fraction of IBD-like events without neutrons from NC interactions and potential de-excitation, i.e. the delayed signal is caused by a neutron produced in the LS by secondary particles, is just 1.0 %. So, atmospheric NC background events on free protons of the liquid scintillator ($\nu_x/\bar{\nu}_x + p \rightarrow \nu'_x/\bar{\nu}'_x + p'$) are neglected in this study, since no initial neutron is present.

5.4. Muon-induced Background

Cosmic muons and their spallation products are potential sources of background for the JUNO detector. These muons are generated in air showers in the atmosphere, can penetrate deep underground and produce secondary particles in the rock surrounding the JUNO detector as well as in JUNO's central detector itself.
Although the experimental hall is shielded with 650 m rock overburden to suppress the cosmic muon flux, the muon rate inside JUNO's central detector is still around 3.3 Hz with a mean muon energy of $\langle E_\mu \rangle \approx 207$ GeV [196]. The energy loss of such high energetic muons leads to nuclear break-up processes, where a variety of secondary particles like e.g. cosmogenic radioactive isotopes and neutrons can be produced. These secondary particles could cause IBD-like backgrounds in JUNO's central detector and are discussed within this section.

5.4.1. Background from Cosmogenic Isotopes

Energetic cosmic muons and subsequent particle showers can interact with ^{12}C in the liquid scintillator of the central detector and produce radioactive isotopes with proton numbers $Z < 6$ by electromagnetic or hadronic processes [5]. Several of these cosmogenic isotopes are β-neutron emitters and decay by emitting both a β^--particle, i.e. an electron, and a neutron. These β-neutron emitting isotopes could mimic an IBD signal in JUNO's central detector due to the prompt energy deposition of the β^- particle followed by the neutron capture on hydrogen. In the energy region accessible for JUNO to search for neutrinos from DM annihilation between 10 MeV and 100 MeV, only isotopes with Q value above 10 MeV could cause an IBD-like background.
In [5], the total decay rates of cosmogenic isotopes in JUNO's liquid scintillator are estimated by performing simulations with the FLUKA software. Following the results in [5], the decay rates of β-neutron emitting cosmogenic isotopes with $Q > 10$ MeV together with their corresponding decay modes, Q values and half-lives $T_{1/2}$ are summarized in table 5.2 for energies above 10 MeV.

^{9}Li dominates the cosmogenic background for energies below 12 MeV and its corresponding IBD-like background is orders of magnitudes higher than the expected neutrino signal from DM self-annihilation and prevents a measurement of neutrinos from DM annihilation for visible energies below 12 MeV. Therefore, the lower edge of the observation window for the indirect DM search with JUNO must be increased from $E_{vis} = 10$ MeV to $E_{vis} = 12$ MeV, which reduces the cosmogenic IBD-like background of ^{9}Li and ^{12}Be to a negligible level. The remaining cosmogenic IBD-like background is attributed to ^{11}Li and ^{14}B. The total rate for visible energies above 12 MeV is $R_{^{11}\mathrm{Li}+^{14}\mathrm{B}} = (57.3 \pm 5.7)\ (10\,\mathrm{yr} \cdot 14.77\,\mathrm{kt})^{-1}$ with an assumed uncertainty of 10 % and surpasses the expected number of neutrino signal events from DM annihilation at least by a factor of around 5 in the corresponding visible

Table 5.2.: Estimated decay rates of cosmogenic β-n emitting isotopes in JUNO's liquid scintillator for energies above 10 MeV and for 20 kt (based on the data of [5]). Only β-neutron emitting cosmogenic isotopes with Q value above 10 MeV and their corresponding decay rates per 10 years and 20 kt are listed. Information about decay modes, branching ratios of the specific decay mode, Q values and half-lives are taken from the TUNL Nuclear Data Group [274].

isotope	decay mode	branching ratio of decay mode	Q in MeV	half-life $T_{1/2}$	decay rate ($E > 10$ MeV)
^{9}Li	$e^- + n$	51 %	11.94	178.0 ms	28430.8
^{11}Li	$e^- + n$	83 %	20.55	8.8 ms	93.3
^{12}Be	$e^- + n$	0.5 %	11.71	21.5 ms	1.2
^{14}B	$e^- + n$	6.1 %	20.64	12.6 ms	2.4

energy region below $Q(^{11}\mathrm{B}) = 20.64$ MeV.
As consequence of that and to further suppress the cosmogenic background, a muon veto cut is introduced, since cosmogenic isotopes are directly correlated to cosmic muons traversing the detector volume. The muon veto criteria and cut strategy is described in the following and based on the muon veto cut introduced in [5] and [226]:

- If muons are tagged in the water pool only, the whole liquid scintillator volume is vetoed for 1.5 ms.
- If muons are tracked well in the central detector, the liquid scintillator volume is vetoed within a cylinder volume of radius $R_{cut} = 3.0$ m around the muon track for $T_{cut} = 0.2$ s.
- If muons are tagged in the central detector, but non-trackable, the whole liquid scintillator volume is vetoed for 0.2 s.

Due to the short half-lives of $T_{1/2,^{11}\mathrm{Li}} = 8.8$ ms and $T_{1/2,^{14}\mathrm{B}} = 12.6$ ms, 99.0 % of ^{11}Li and ^{14}B isotopes produced by well reconstructable muons can be cut away by a cylindrical volume with $R_{cut} = 3.0$ m and $T_{cut} = 0.2$ s around the reconstructed muon track. The inefficiency of the cosmogenic background reduction is only due to the radius cut of the cylinder R_{cut}, since few electrons and neutrons could leave the cylindrical veto volume and cause background events.
Under the assumption, that 99.0 % of all tagged muons have a good reconstructed track [5, 226], the efficiency due to the application of the muon veto is estimated to be $\epsilon_{\mu\,veto} =$ 97.2 %, which corresponds to an estimated dead time of the central detector in terms of exposure ratio of 2.8 %.
The total cosmogenic background rate of ^{11}Li and ^{14}B for 10 years of lifetime, 14.77 kt fiducial volume and $E_{vis} \geq 12$ MeV after considering the muon veto cut is $R^{\mu\,veto}_{^{11}\mathrm{Li}+^{14}\mathrm{B}} = (0.6 \pm 0.1)\,(10\,\mathrm{yr} \cdot 14.77\,\mathrm{kt})^{-1}$. Because of this small background rate and the fact, that this background only occurs for $E_{vis} \leq 20.64$ MeV, the IBD-like background of cosmogenic isotopes is neglected in this study.

5.4.2. Fast Neutron Background

Whereas cosmic muons traversing JUNO's central detector or large parts of the water pool are tagged by JUNO's veto systems (see section 3.3) and vetoed effectively by the muon veto cut introduced in the previous section, muons passing the surrounding rock of the detector and corner clipping muons in the water pool[12] can not be identified. These

[12] Muons with a track length smaller than 0.5 m inside the water pool are denoted as corner clipping muons.

muons produce fast neutrons[13] through spallation processes in the rock, which can enter the central detector unnoticed.
These fast neutrons can deposit energy inside the central detector and appear as background source. Furthermore, fast neutrons can mimic IBD events according to their signal signature: a prompt signal is produced by the energetic neutron scattering off protons and a delayed signal is given by the capture of the thermalized neutron on hydrogen [276]. So, fast neutrons also contribute to the IBD-like backgrounds for the indirect DM search with JUNO.
The fast neutron background in JUNO's central detector was simulated in [277]. In the cited work, only muons traveling through the rock or with a track length smaller than 0.5 m inside the water pool have been simulated. These muons are untaggable by JUNO's veto systems. The detector response of fast neutrons produced by these muons was simulated with the JUNO detector simulation DetSim and neutron events with prompt energy above 0.7 MeV and delayed signal within 1 ms after the prompt signal are labeled as IBD-like event. Around $1.56 \cdot 10^9$ muons (corresponding to about 1516 days of data taking) have been simulated in [277] which leads to a fast neutron IBD-like background rate inside the central detector of $R_{FN} = (0.077 \pm 0.015)\,(\text{kt yr MeV})^{-1}$ with an assumed uncertainty of 20 %. In [277], the fast neutron energy distribution decreases slightly for higher energies in the energy region from 10 MeV to 100 MeV, but the statistical fluctuations are large. In [276] and [278], the energy spectrum is assumed flat up to 50 MeV and decreases slightly for higher energies. For simplicity, the energy distribution of the fast neutron background in this study is assumed to be flat for visible energies between 10 MeV and 100 MeV. This conservative assumption might slightly overestimate the fast neutron background for energies above 50 MeV.
The resulting number of fast neutron background events in the whole central detector volume of JUNO for energies between 10 MeV and 100 MeV after 10 years of lifetime is $N_{FN,\,20\,\text{kt}} = 1374.0 \pm 275.0$ and therefore orders of magnitudes larger than the expected neutrino signal from DM self-annihilation. Nevertheless, the radial distribution of fast neutron events strongly decreases from the edge of the detector to its center as displayed in figure 5.14, since fast neutrons enter the detector volume from outside and lose energy by traveling through the water pool and central detector. Hence, a volume cut on the position of the prompt signal reduces the fast neutron background significantly.
The radial distribution is approximated by the function $f(R) = a \cdot \exp[(R-b)/c]$, that was fitted to the simulation data. With this function, the number of IBD-like fast neutron events for $R_{prompt} < 16.0$ m (corresponding to a fiducial mass of 14.77 kt) is calculated resulting in $N_{FN,\,14.77\,\text{kt}} = 102.8 \pm 20.6$ for visible energies between 10 MeV and 100 MeV. After considering the efficiency due to the application of the muon veto of $\epsilon_{\mu\,veto} = 97.2$ %, the total number of IBD-like fast neutron background events after 10 years of data taking is $N_{FN,\,14.77\,\text{kt}} = 99.9 \pm 20.0$. The resulting fast neutron energy spectrum is present in the interesting energy region from 10 MeV to 100 MeV and shown in figure 5.2.

5.4.3. Background from Decaying Muons

Another possible background source attributed to cosmic muons is the muon decay itself inside JUNO's central detector. Muons decay into a Michel electron/positron and neutrinos via $\mu^- \to e^- + \nu_\mu + \bar{\nu}_e$ and $\mu^+ \to e^+ + \nu_e + \bar{\nu}_\mu$, respectively, with a mean lifetime of $\tau = 2.2\,\mu\text{s}$ [5]. Therefore, if a muon is stopped inside the central detector volume and decays, the

[13] Free neutrons with kinetic energies above around 1 MeV are called fast neutrons. Fast neutron cannot only be produced by cosmic muons, but also by spontaneous fission of ^{238}U, ^{235}U and ^{232}Th in the rock, and by (α, n) reactions, where α particles emitted in the decay of uranium, thorium and their daughter products interact with lighter isotopes and produce neutrons [275]. Since these fast neutrons are negligible above visible energies of 10 MeV [275], this section only discusses muon-induced fast neutrons.

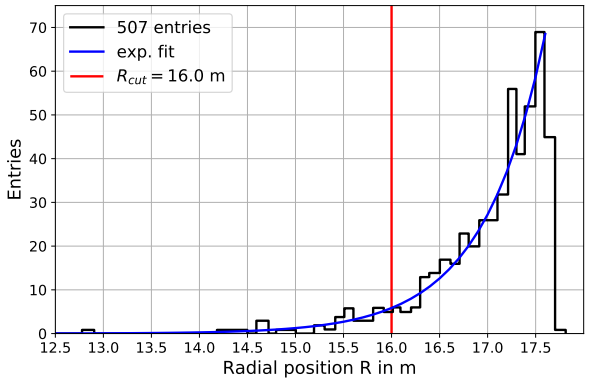

Figure 5.14.: Radial distribution of prompt signals of IBD-like fast neutron events in the JUNO central detector. The fast neutron events have been simulated in [277] and are shown in black. An exponential function $f(R) = a \cdot \exp[(R-b)/c]$ (blue line) is fitted to the simulation data resulting in best-fit parameters of $a = 79.9$, $b = 17.7$ and $c = 0.65$. The fiducial volume cut at $R_{cut} = 16.0$ m is shown as red line.

energy deposition of the Michel electron causes a prompt signal. A corresponding delayed signal could occur by the capture of a neutron, which is produced by the same muon before it decays. This signature of prompt energy deposition followed by a neutron capture on hydrogen would mimic an IBD signal and could act as background for the indirect DM search with JUNO.
By applying the muon veto cut introduced in section 5.4.1, a possible prompt signal of Michel electrons would be cut away due to the short muon lifetime of $\tau = 2.2\,\mu$s. Moreover, a possible delayed signal from the capture of a neutron produced by the muon is also cut away effectively.
So, decaying muons cause no IBD-like background for the study of indirect DM search with JUNO and are neglected within this thesis as consequence of the muon veto cut and its high efficiency.

5.5. Additional Background Sources

This section focuses on additional background sources and completes the chapter about backgrounds for the indirect DM search with JUNO via the IBD detection channel. Geo-neutrinos, accidental coincidences and backgrounds from natural radioactivity are briefly introduced and their potential to act as background is discussed.

Geo-neutrinos are antineutrinos and could interact via the IBD reaction channel. Nevertheless, the maximum antineutrino energy of geo-neutrinos of around 3.3 MeV (as shown in figure 3.3) is well below the lower edge of the observed energy window of 10 MeV, which makes geo-neutrinos to an insignificant background source for the study of this thesis.

Accidental coincidences of non-correlated backgrounds could produce IBD-like events in JUNO. The rate of accidental backgrounds can be calculated as $R_{acc} = R_p \cdot R_d \cdot \Delta T$, where R_p and R_d are the rate of prompt and delayed signals, respectively, and $\Delta T = 1$ ms is the time difference window [5]. Accidental backgrounds consist of a prompt and delayed signal and can be caused by random coincidences of *radioactivity + radioactivity*, *spallation neutrons + radioactivity* and *cosmogenic isotopes + radioactivity* [5].
For the JUNO detector, low radioactive materials are selected and passive shielding is designed to control the radioactive background. Nevertheless, ^{238}U, ^{232}Th, ^{222}Rn, ^{85}Kr, ^{60}Co

and ^{40}K in the rock, stainless steel, air, PMT glass, acrylic, liquid scintillator or dissolved in the water buffer produce radioactive background events with a rate of $R_{natural} = 7.63$ Hz in a fiducial volume within $R < 17.2$ m and for $E_{vis} > 0.7$ MeV [5]. Around 8 % of these events are neutron-like, i.e. mimic a delayed neutron capture signal, resulting in a rate of radioactive neutron-like background events of $R_{natural}^{neutron-like} = 0.61$ Hz. Therefore, around $R_{acc} = R_{natural} \cdot R_{natural}^{neutron-like} \cdot \Delta T \approx 402$ events per day are expected for $E_{vis} > 0.7$ MeV by random coincidences, where the prompt and delayed signals are caused by natural radioactivity (no cut on the prompt energy and distance is applied). However, the maximum decay energy of the listed radioactive isotopes and their corresponding decay chains is $E_{\alpha}^{max} \approx 8.8$ MeV for alpha particles and $E_{\beta}^{max} \approx 5.5$ MeV for β particles [279, 280]. Therefore, natural radioactivity cannot cause a prompt signal of an IBD event[14] specified by $E_{prompt} \geq 10$ MeV and random coincidences of *radioactivity + radioactivity* do not mimic IBD-like background events for the indirect DM search with JUNO.
Accidental coincidences of *spallation neutrons + radioactivity*, where the prompt signal is caused by spallation neutrons and the delayed signal by natural radioactivity, can also be neglected as IBD-like background for prompt energies above 10 MeV. Spallation neutrons are effectively suppressed by the muon veto cut introduced in section 5.4.1 to $R_n < 45$ events per day [5], which results in an accidental background rate of $R_{acc} = R_n \cdot R_{natural}^{neutron-like} \cdot \Delta T < 10\ \mathrm{yr}^{-1}$ for $E_{vis} > 0.7$ MeV. After applying the distance cut between prompt and delayed signal, the background rate of accidental coincidences of *spallation neutrons + radioactivity* is reduced to a negligible level of $R_{acc} < 0.02$ per 10 years.
Most of the cosmogenic isotopes produced through muon spallation in JUNO's central detector have Q-values below 10 MeV or are suppressed by the muon veto cut due to their small half-lives and cannot produce prompt signals in the relevant energy region [5]. However, cosmogenic isotopes like ^{8}Li, ^{8}B, ^{9}Li and ^{9}C could cause prompt signals by emitting β particles despite the muon veto cut due to their half-lives of few hundreds of ms [15]. The total event rate of these cosmogenic isotopes in the JUNO detector within 17.2 m for energies above 12 MeV and 0.2 s after the initial muon is $R_{cosmogenic} \approx 85648$ events per year. The event rate of random coincidences R_{acc} of cosmogenic isotopes as prompt signal and natural radioactivity as delayed signal, i.e. *cosmogenic isotopes + radioactivity*, within a time window of $\Delta t = 1.0$ ms and a distance between prompt and delayed signal of $d = 1.0$ m is given by

$$\begin{aligned} R_{accidental} &= R_{cosmogenic} \cdot R_{natural}^{neutron-like} \cdot \Delta t \cdot (d/17.7\,\mathrm{m})^3 \\ &\approx 85648\,\mathrm{yr}^{-1} \cdot 0.61\,\mathrm{s}^{-1} \cdot 1\,\mathrm{ms} \cdot (1.0\,\mathrm{m}/17.7\,\mathrm{m})^3 \\ &\approx 9.4 \cdot 10^{-3}\,\mathrm{yr}^{-1}. \end{aligned} \tag{5.18}$$

Only 0.094 IBD-like events after 10 years of data taking are expected according to the accidental coincidence of cosmogenic isotopes and natural radioactivity. Therefore the non-correlated background of random coincidences can be neglected in this study.

Another source of natural radioactivity inside the detector are alpha particles emitted in decay chains of the radioactive contaminants ^{238}U, ^{232}Th and ^{210}Po, which can induced $^{13}\mathrm{C}(\alpha, n)^{16}\mathrm{O}$ reactions in the liquid scintillator [177]. This reaction channel $\alpha + {}^{13}\mathrm{C} \rightarrow$

[14] Nevertheless natural radioactivity can produce potential delayed signals with a rate of $R_{natural}^{neutron-like} = 0.61$ Hz, when an energy between 1.8 MeV and 2.7 MeV is released.

[15] ^{8}Li: β^- decay with $Q = 16.0$ MeV and $T_{1/2} = 839$ ms. ^{8}B: β^+ decay with $Q = 16.6$ MeV and $T_{1/2} = 770$ ms. ^{9}Li: β^- decay (49 %) with $Q = 13.6$ MeV and $T_{1/2} = 178$ ms. ^{9}C: $\beta^+ n / \beta^+ \alpha$ decay with $Q = 15.5$ MeV and $T_{1/2} = 126$ ms. Data from [274].

$n + {}^{16}\mathrm{O}$ could mimic the IBD event signature. A prompt signal could be produced either by protons scattered off neutrons or by the de-excitation of ^{16}O. A delayed signal could be produced by the neutron captured on hydrogen. Since the maximum energy of alpha particles from these decay chains is $E_{\alpha}^{max} \approx 8.8$ MeV, the maximum kinetic energy, that could be transferred to the emitted neutron, is $E_{n}^{max} \lesssim 7.1$ MeV and the maximum de-excitation energy of ^{16}O is $E_{deex}^{max} \lesssim 7.1$ MeV [274]. Therefore neutrons scattering off protons as well as the de-excitation of ^{16}O cannot produce a prompt signal in the observed energy region between 10 MeV and 100 MeV and the α-n background do not affect the indirect DM search with JUNO.

In summary it can be stated, that none of the additional background sources discussed in this section contribute as relevant background to the study of this thesis.

5.6. Summary of Backgrounds in JUNO

In this chapter, all potential IBD and IBD-like backgrounds in JUNO for visible energies from 10 MeV to 100 MeV have been determined and discussed. The event numbers of all background contributions for the different cuts applied are summarized in table 5.3. The total expected visible energy spectra of IBD and IBD-like backgrounds in JUNO as well as the expected electron antineutrino signal from DM self-annihilation assuming DM particles with $m_{DM} = 50$ MeV are shown in figure 5.2.
The reactor $\bar{\nu}_e$ background overwhelms the $\bar{\nu}_e$ signal from DM annihilation for visible energies below 10 MeV, which sets the lower edge of the observable energy window to 10 MeV. Above visible energies of 10 MeV, $N_{reactor} = 38.2 \pm 3.8$ reactor electron antineutrino background events are expected in JUNO. The DSNB is present for 10 MeV$\leq E_{vis} \lesssim 35$ MeV and results in $N_{DSNB}^{fid} = 15.0 \pm 6.0$ background events assuming the fiducial case discussed in section 5.2. The dominant IBD background for visible energies above around 35 MeV are atmospheric $\bar{\nu}_e$ interacting via CC on protons with an expected event number of $N_{atmoCC,\bar{\nu}_e+p} = 30.5 \pm 7.6$. Moreover, the atmospheric $\nu_e/\bar{\nu}_e$ CC background on ^{12}C is present for $E_{vis} \gtrsim 40$ MeV with $N_{atmoCC,\bar{\nu}_e+{}^{12}\mathrm{C}} = 5.9 \pm 1.5$. Contrary to this, the CC background of atmospheric ν_μ and $\bar{\nu}_\mu$ is reduce to a negligible level of $N_{atmoCC,\nu_\mu/\bar{\nu}_\mu} < 0.03$ after applying a cut on the standard deviation of the photon emission time distribution $\sigma(t_{pe})$ discussed in section 5.3.2. Atmospheric NC background events represent the dominant background in the whole visible energy region from 10 MeV to 100 MeV, since $N_{atmoNC} = 757 \pm 220$ IBD-like background events are expected in JUNO after 10 years of data taking. The muon-induced background of cosmogenic isotopes due to the decay of ^{11}Li and ^{14}B only occurs for visible energies below 20.6 MeV and is reduced to a negligible level of $N_{^{11}\mathrm{Li}+^{14}\mathrm{B}} < 0.6$ after applying the muon veto cut presented in section 5.4.1. The fast neutron background in JUNO with $N_{FN} = 99.9 \pm 20.0$ is present in the whole visible energy region.
In contrast to the peak-like signal spectrum, the background contributions shown in figure 5.2 have a broad spectral shape. Due to this difference in the spectral shape, a sensitivity study with the JUNO detector for the indirect DM search is promising despite the comparably small signal event numbers.

Table 5.3.: Number of background events in JUNO for visible energies between 10 MeV and 100 MeV and after 10 years of data taking. The table summarizes all IBD backgrounds (reactor background, fiducial case of DSNB, atmo. CC of $\bar{\nu}_e$ on p) and IBD-like backgrounds (atmo. CC of $\nu_e/\bar{\nu}_e$ on ^{12}C, atmo. $\nu_\mu/\bar{\nu}_\mu$ CC, atmo. NC, cosmogenic isotopes, fast neutrons) discussed in chapter 5. The second column represents the event numbers before cuts are applied. The third column gives the event numbers after applying the cut on $\sigma(t_{pe})$. The fourth column contains the event numbers after the IBD cuts and the cut on $\sigma(t_{pe})$. The fifth column gives the event numbers and their uncertainties, which are also shown in figure 5.2, after the muon veto cut, the IBD cuts and the cut on $\sigma(t_{pe})$ (the cuts are applied consecutively from left to right in the table). The last column represents the visible energy region, where the background events occur.

	no cuts	after $\sigma(t_{pe})$ cut ($\epsilon_{\sigma(t_{pe})} = 99.98$ %)	after IBD cuts ($\epsilon_{IBD} = 67.0$ %)	after muon veto cut ($\epsilon_{\mu\,veto} = 97.2$ %)	typ. visible energies
Reactor background	58.7	58.7	39.3	38.2 ± 3.8	< 12 MeV
DSNB (fid.)	23.0	23.0	15.4	15.0 ± 6.0	10 MeV to 35 MeV
Atmo. CC ($\bar{\nu}_e + p$)	46.8	46.8	31.4	30.5 ± 7.6	15 MeV to 100 MeV
Atmo. CC ($\nu_e/\bar{\nu}_e + ^{12}$C)	9.1	9.1	6.1	5.9 ± 1.5	40 MeV to 100 MeV
Atmo. $\nu_\mu/\bar{\nu}_\mu$ CC	159.4	< 0.03	< 0.03	< 0.03	-
Atmo. NC	10002		779	757 ± 220	10 MeV to 100 MeV
Cosmogenic ^{11}Li and ^{14}B	77.6		57.3	0.6 ± 0.1	< 20.6 MeV
Fast neutron	1374.0	1374.0	102.8	99.9 ± 20.0	10 MeV to 100 MeV

6. Background Reduction by Pulse Shape Discrimination in JUNO

All IBD and IBD-like background contributions for the search for electron antineutrinos from DM self-annihilation in the Milky Way with the JUNO detector are extensively discussed in the previous chapter and selection cuts to reduce background events were introduced. IBD selection cuts suppress the atmospheric NC background by 92.2 % and the fiducial volume cut on the prompt signal reduces the fast neutron background by 92.5 %. Moreover, the muon veto cut suppresses background events from cosmogenic isotopes and decaying muons to a negligible level. The cut on $\sigma(t_{pe})$ reduces atmospheric CC muon neutrino and antineutrino events to a negligible level.
Nevertheless, the total expected visible energy spectrum of IBD events in JUNO displayed in figure 5.2 is still dominated by background contributions. Especially the IBD-like atmospheric NC background exceeds the expected neutrino signals from DM annihilation in the whole region of interest for the assumed limits of the DM annihilation cross section from Super-K. Therefore, an additional method, the *pulse shape discrimination (PSD)*, to further reduce background events was developed and studied in this thesis and will be presented in this chapter.

The pulse shape[1] of signals in liquid scintillator detectors depends on the particle type that excites the LS and can be parametrized by equation 3.14 with particle-specific time constants τ_i and corresponding weights ω_i as described in section 3.3.1 [201]. These time constants and weights differ for β-like particles (γ, e^- and e^+), nucleons (p and n) and α particles. In table 6.1, the time constants and weights of the different particle types for JUNO's LAB-based LS are summarized. The resulting pulse shapes of the three particle types calculated analytically with equation 3.14 are shown in figure 6.1. Pulse shapes for p/n are very similar to pulse shapes for α particles. Contrary to this, pulse shapes of lighter particles (γ's, e^- and e^+) decay faster in time than pulse shapes of heavier particles (p, n, α), which enables the discrimination between these particles types.
Prompt signals of IBD events are mainly caused by the prompt energy deposition of the positrons in the liquid scintillator volume. In contrast to that, prompt signals of IBD-like atmospheric NC events are given by the prompt energy deposition of protons, neutrons, alphas, gamma, etc. as shown in figure 5.13. In fast neutron events, the prompt signal

[1] The pulse shape, also called photon emission time profile, is defined as number of p.e. as function of the photon emission time and describes the temporal evolution of a signal in the LS independent of its position in the detector.

Table 6.1.: Decay time constants τ_i and corresponding weights ω_i of the photon emission of different particle types for the LAB-based liquid scintillator of JUNO. The light emission parameters for γ, e^- and e^+ particles are adopted from measurements [281, 282], while parameters for p, n and α particles are obtained from MC tuning in DayaBay [283]. The scintillation light emission is modeled with equation 3.14.

	τ_1 / ω_1	τ_2 / ω_2	τ_3 / ω_3
γ, e^-, e^+	4.93 ns / 79.9 %	20.6 ns / 17.1 %	190.0 ns / 3.0 %
p, n	4.93 ns / 65.0 %	34.0 ns / 23.1 %	220.0 ns / 11.9 %
α	4.93 ns / 65.0 %	35.0 ns / 22.8 %	220.0 ns / 12.2 %

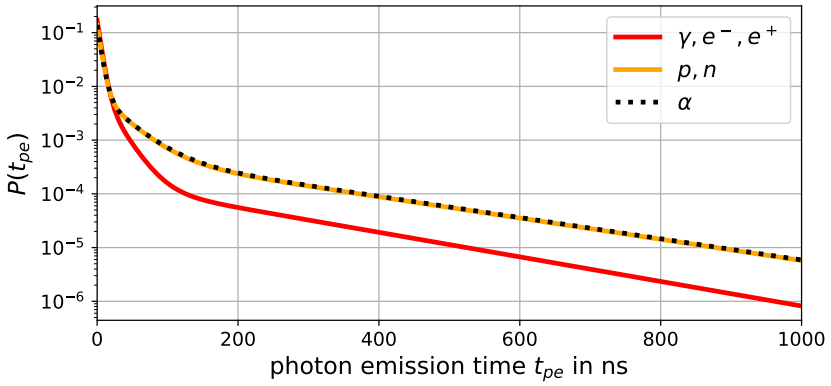

Figure 6.1.: Pulse shapes of different particle types calculated analytically with equation 3.14 using the corresponding time constants and weights listed in table 6.1 for JUNO's LS.

is caused by neutrons scattering off protons. Therefore, pulse shapes of IBD events differ from pulse shapes of IBD-like atmospheric NC and fast neutron events in JUNO and can be discriminated against these IBD-like backgrounds, which is studied in this chapter in detail.
Section 6.1 describes the simulation and analysis to generate realistic pulse shapes of IBD, IBD-like atmospheric NC and fast neutron events in JUNO. Afterwards, the method to discriminate the pulse shapes of different event types and the resulting pulse shape discrimination cut efficiencies are presented in section 6.2. The resulting total visible energy spectrum in JUNO after applying the PSD cut is given in section 6.3.

6.1. Pulse Shape Analysis

In order to analyze pulse shapes of different particle types, IBD, atmospheric NC and fast neutron events that mimic IBD signals in the JUNO detector are simulated within JUNO's simulation and analysis framework presented in section 3.4.
The whole simulation and reconstruction chain of the JUNO simulation and analysis framework (version J20v2r0) with detector and electronics simulation and reconstruction of waveforms, energies and vertices is used to generate realistic pulse shapes.
For pulse shape analysis, only events that pass the IBD selection criteria of table 4.2 are used as input for the simulation. IBD and IBD-like atmospheric NC events are simulated uniformly inside the fiducial volume specified by $R < 16.0$ m. Moreover, neutrons are generated within the simulation framework representing fast neutron events. These neutrons with kinetic energies between 10 MeV and 250 MeV are simulated in a spherical shell in the LS volume defined by $14.0\,\text{m} < R < 16.0$ m to take into account the radial distribution

of fast neutron events displayed in figure 5.14.

The first step of the simulation chain is the simulation of the detector response with JUNO DetSim (see section 3.4.1), where the decay time constants τ_i and corresponding weights ω_i of the photon emission of the LAB-based liquid scintillator of table 6.1 have been implemented. In DetSim, the scintillation light emission is modeled by equation 3.14 assuming three fluorescence components.
The second step is the electronics simulation ElecSim described in section 3.4.2. The MC truth data of DetSim is translated into PMT waveforms taking into account the characteristics of the PMTs and the electronics: PDE, DCR and TTS, listed in table 3.2, as well as pre- and after-pulses, overshoot, saturation effects, electronic noise and FADC properties are implemented in ElecSim (for details see [222]).
After the electronics simulation, the calibration and waveform reconstruction introduced in section 3.4.3 is performed, where the digitized PMT waveforms are reconstructed with the deconvolution method to get the charge and time information of each photon hit at each PMT.
The last step of the simulation chain is the energy and vertex reconstruction. Using the time likelihood algorithm described in section 3.4.4, the energy and vertex of each event is reconstructed assuming quasi point-like events. The energy and vertex reconstruction reproduces the MC truth data of DetSim well resulting in a resolution of the vertex reconstruction in x-direction of $\sigma_{IBD} = 259$ mm, $\sigma_{atmoNC} = 257$ mm and $\sigma_{neutron} = 413$ mm for events with reconstructed energies between 10 MeV and 100 MeV and with reconstructed radii of $R_{reco} < 16.0$ m [2].

After the described full simulation chain, the pulse shapes of each simulated event are calculated from the charge and time information of the waveform reconstruction and the reconstructed vertex $\vec{r}_{reco}$ of the event. Each reconstructed hit time t_{reco} is corrected with the time-of-flight t_{tof} to get the photon emission time t_{pe} ($\vec{r}_{PMT}$ is the position of the hit PMT and c_{eff} describes the effective speed of light for the JUNO detector introduced in section 4.3):

$$t_{pe} = t_{reco} - t_{tof} = t_{reco} - \frac{|\vec{r}_{reco} - \vec{r}_{PMT}|}{c_{eff}}. \tag{6.1}$$

With the photon emission times and the corresponding charges, the pulse shape is calculated as number of p.e. $N_{p.e.}$ as function of t_{pe} and given in a histogram with bin-width of 5 ns.
Afterwards, each pulse shape is shifted such that the global maximum of the pulse shape in a bin of 5 ns is located at $t_{pe} = 0.0$ ns. This allows a reasonable comparison of the temporal decay of the pulse shapes. Moreover, only events with a reconstructed energy E_{reco} between 10 MeV and 100 MeV and with a reconstructed radial position $R_{reco} < 16.0$ m are considered, which yields 10,945 IBD, 22,309 atmospheric NC and 3,880 neutron events.

The resulting average pulse shapes of IBD events, atmospheric NC events and fast neutron events are displayed in figure 6.2. On average, the pulse shapes of prompt signals of IBD events decay faster in time because of dominant energy deposition by the positron. In contrast to that, pulse shapes of atmospheric NC events and pure neutron events decay slower in time and, on average, overlap for photon emission times above around 100 ns

[2] The reconstruction performance in y- and z-direction is similar as expected for a radially symmetric detector. The vertex resolution of IBD and atmospheric NC events agrees well with the vertex resolution $\sigma_{vertex} = 250.0$ mm assumed in section 4.3. The vertex resolution of neutron events is larger due to the larger mean track length $\langle L \rangle \approx 720$ mm of neutrons.

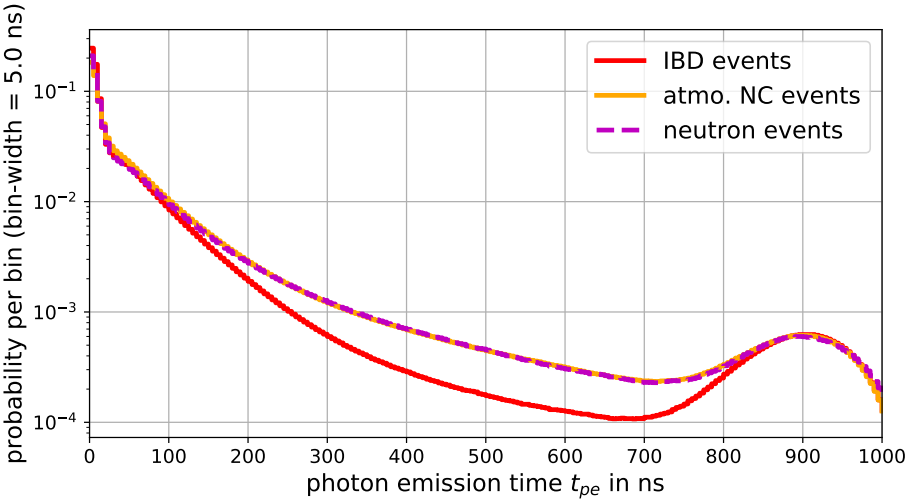

Figure 6.2.: Average pulse shapes of prompt signals of IBD events (red), atmospheric NC events (orange) and neutron events (magenta) with $R_{reco} < 16.0$ m and for reconstructed visible energies from 10 MeV to 100 MeV. The pulse shapes are normalized to $\int_{0\,\mathrm{ns}}^{1\,\mu\mathrm{s}} P(t)\mathrm{d}t = 1$. Pulse shapes of atmospheric NC events and neutron events overlap for photon emission times larger than around 100 ns.

due to the prevailing energy deposition of neutrons and protons. Figure 6.2 also shows one component of the after-pulse model of MCP PMTs implemented into the electronics simulation as a peak at around 900 ns (for more details about the implemented after-pulse model see [222, 284]).

6.2. JUNO's Pulse Shape Discrimination Performance

The differences of the simulated pulse shapes of different event types allow the discrimination of IBD signal events from atmospheric NC and fast neutron background events and, therefore, further suppression of IBD-like backgrounds for the indirect DM search with the JUNO detector. The concept of pulse shape discrimination (PSD) to distinguish between signal and background events is well established in liquid scintillator experiments [285–287] and several methods have been developed over the last decade.
The method of PSD used in this study is the tail-to-total ratio (TTR) method. The ratio between the charge in a specific time window of the tail of the pulse shape and the charge of the total pulse shape is the parameter to distinguish between different event types:

$$TTR = \frac{\int_{t_{start}}^{t_{end}} P(t_{pe})\mathrm{d}t_{pe}}{\int_{0\,\mathrm{ns}}^{700\,\mathrm{ns}} P(t_{pe})\mathrm{d}t_{pe}}. \tag{6.2}$$

The time window of the total pulse shape is set from 0 ns to 700 ns, whereas the tail window is defined from t_{start} to t_{end} [3].
An advantage of the TTR method for PSD is its fast and straightforward implementation. Furthermore, neither knowledge about average pulse shapes nor large computational power

[3] The prompt time window of pulse shapes is set from 0 ns to 1000 ns. Some pulse shapes contain an after-pulse at around 900 ns as shown in figure 6.2. This after-pulse increases the charge of the pulse shape in the total prompt time window. To prevent this, the total time window is set up to 700 ns, where no after-pulse occurs.

is required. However, a disadvantage is that only integrated values of pulse shapes are used and additional information of the pulse shapes might be unexploited. Other methods like e.g. the Gatti method [288] or methods using neural networks [289] could provide better PSD performances, but are not discussed within the sensitivity study of this work.

The PSD performance of JUNO investigated within this thesis is determined by the tail window (defined by t_{start} and t_{end}) and event selection criteria that maximize the signal to background ratio $S/\sqrt{S+B}$.
The number of signal events S is the number of IBD signal events from DM self-annihilation after applying an energy-dependent PSD cut efficiency $\epsilon_{PSD,IBD}(E)$ on the expected signal spectra $N_S(E)$ described in chapter 4 [4]:

$$S = \int_{E_1}^{E_2} \epsilon_{PSD,IBD}(E)\, N_S(E)\, \mathrm{d}E. \tag{6.3}$$

E_1 and E_2 depend on the assumed DM mass and are set according to the energy window, where the signal spectrum is above a threshold of 10^{-4} events per 1 MeV.
The total number of background events B is defined in a similar way after applying energy-dependent PSD cut efficiencies to the corresponding expected background spectra displayed in figure 5.2 and described in chapter 5:

$$\begin{aligned} B = \int_{E_1}^{E_2} \Big[& \epsilon_{PSD,IBD}(E) \big[N_{reactor}(E) + N_{DSNB}(E) + N_{atmoCC,\bar{\nu}_e+p}(E) \\ & + N_{atmoCC,\bar{\nu}_e+{}^{12}\mathrm{C}}(E) \big] + \epsilon_{PSD,atmoNC}(E) N_{atmoNC}(E) \\ & + \epsilon_{PSD,FN}(E) N_{FN}(E) \Big] \, \mathrm{d}E. \end{aligned} \tag{6.4}$$

The PSD cut efficiencies ϵ_{PSD} are determined by the tail window and the event selection criteria that are introduced in the following. To calculate the signal to background ratio, all background contributions (IBD-like backgrounds like atmospheric NC and fast neutron events as well as IBD backgrounds such as reactor, DSNB and atmospheric CC events) are taken into account and B is integrated between E_1 and E_2.
The signal to background ratio depends on the assumed DM mass. In the study presented here, DM masses from 15 MeV to 100 MeV in 5 MeV steps are assumed to determine the expected energy spectrum in JUNO and JUNO's sensitivity. Therefore, the signal to background ratio averaged over all assumed DM masses quantifies the efficiency of PSD in terms of an effective background reduction and is used as parameter that should be maximal.

The TTR of each simulated pulse shape of IBD, atmospheric NC and neutron events is calculated with equation 6.2 for a variety of different tail windows defined by tail start times of t_{start} =100 ns, 150 ns, ..., 450 ns and tail end times of t_{end} = 600 ns and t_{end} = 700 ns. As an example, the resulting TTR distributions of IBD, atmospheric NC and neutron events as function of the reconstructed radial position R^3 and as function of the reconstructed energy, i.e. the visible energy E_{vis}, are displayed in figure 6.3 for a tail window from 200 ns to 600 ns.

[4] To determine S, the expected signal spectra $N_S(E)$ assuming the currently best 90 % C.L. limit of the annihilation cross section from Super-K are used. The tail window and the event selection criteria that maximize the signal to background ratio change, if another DM annihilation cross section is assumed. However, the resulting PSD performance is only slightly (within 3 %) affected by this.

On average, TTR values of atmospheric NC events are larger than the TTR values of IBD events, since more charge lies in the tail window for atmospheric NC events due to the slower decay of the pulse shapes as expected from figure 6.2. Moreover, the TTR distribution of neutron events clearly differ from the distribution of IBD events because of the different pulse shapes for positrons and neutrons in liquid scintillators.
Figure 6.3 indicates that TTR values of all events slightly decrease with increasing radial position R^3. The reason for this behavior is that photons emitted near the center are scattered more frequently and, thus, might travel longer until being absorbed by the PMTs than photons released at the edge of the detector. A fraction of these scattered photons can be detected that late that they appear in the tail window of the pulse shape. Therefore, TTR values at the center are larger compared to the ones at the edge of the detector. Especially for smaller tail start times $t_{start} \leq 200$ ns, this effect is sizable, while TTR values follow an almost flat distribution as function of the radial position R^3 for $t_{start} \geq 300$ ns.
The discrimination of IBD events and IBD-like atmospheric NC events based on their TTR strongly depends on the events' visible energy (see figure 6.3). For energies above around 40 MeV, the TTR distributions of IBD and atmospheric NC events are clearly separated. In contrast to that, the TTR distribution of a large part of atmospheric NC events significantly overlaps with the IBD TTR distribution for lower energies, especially below around 25 MeV. The main reason for this feature is that the prompt energy deposition of IBD-like atmospheric NC events is driven by different particles (n, p, γ, α etc.) and their contribution to the total energy deposition depends on the total energy of the event. For energies below 25 MeV, more than 10 % of the total visible energy of the event is caused by the energy deposition of gamma particles. Since the decay time constants and weights defining the scintillation time profile are identical for gammas and positrons, the pulse shapes of IBD and these "gamma-dominated" atmospheric NC events are not separable and the TTR distributions overlap. Another minor reason is the smaller photon statistics of these low energetic events, which decreases the discrimination power of different event types. Above approximately 40 MeV, the energy deposition of IBD-like atmospheric NC events is dominated by neutrons and protons and, therefore, the resulting TTR values clearly differ from IBD events. Furthermore, TTR distributions of atmospheric NC events, where the energy deposition is mainly caused by neutrons and protons, agree with the ones of neutron events as expected.

Since the TTR values depend on the visible energy E_{vis} as well as on the radial position R of the events as discussed above, two linear TTR cut functions are defined to determine the PSD cut efficiency (B_1 in MeV^{-1}, B_2 in m^{-3}):

$$TTR_{cut}(E_{vis}) = A_1 + B_1 \cdot E_{vis}, \tag{6.5}$$

$$TTR_{cut}(R^3) = A_2 + B_2 \cdot R^3. \tag{6.6}$$

Only events with TTR values smaller than $TTR_{cut}(E_{vis})$ and $TTR_{cut}(R^3)$ pass the PSD cut. The procedure to determine the PSD cut efficiencies based on the introduced cut functions is described in the following:
The PSD survival efficiency of atmospheric NC events is fixed to $\epsilon_{PSD,atmoNC} = 1$ %. Then, the TTR values of IBD, atmospheric NC and neutron events are calculated for a tail window from 100 ns to 600 ns. Based on these TTR distributions, the parameter space of the cut parameters A_1, B_1, A_2 and B_2 is scanned and the PSD survival efficiencies of IBD events $\epsilon_{PSD,IBD}$ and neutron events $\epsilon_{PSD,neutron}$ as well as the resulting signal to background ratio is calculated for each set of A_1, B_1, A_2 and B_2. Therefore, you get the cut parameters that maximize the signal to background ratio for the specific tail window

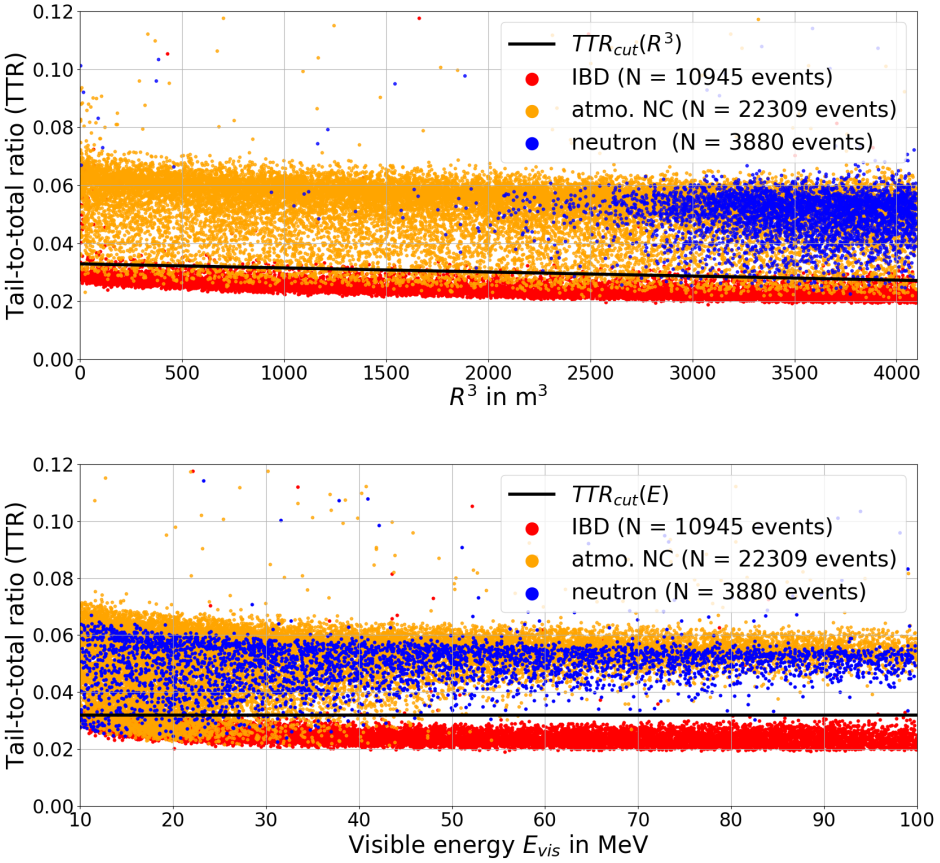

Figure 6.3.: Tail-to-total ratio distributions of prompt signals of simulated IBD, IBD-like atmospheric NC and neutron events for a tail window from 200 ns to 600 ns together with the TTR cut functions that result in the best signal to background ratio. Only events with TTR values smaller than $TTR_{cut}(E_{vis})$ and $TTR_{cut}(R^3)$ pass the PSD cut. Top: TTR values as function of the reconstructed radial position R^3 with the TTR cut function $TTR_{cut}(R^3) = 0.0329 - 1.4 \cdot 10^{-6}\,\mathrm{m}^{-3} \cdot R^3$ (black line). Bottom: TTR values as function of the visible energy E_{vis} with the TTR cut function $TTR_{cut}(E_{vis}) = 0.0320$, $B_1 = 0.0$ MeV^{-1} (black line).

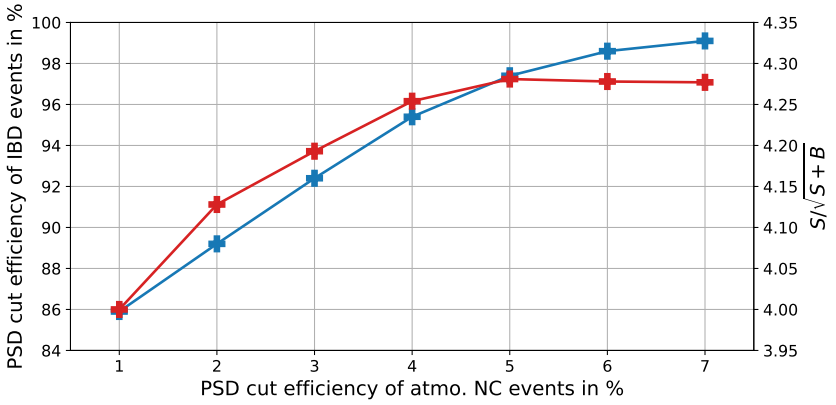

Figure 6.4.: PSD cut efficiencies of IBD events and corresponding signal to background ratios $S/\sqrt{S+B}$ as function of the PSD cut efficiency of IBD-like atmospheric NC events. The PSD cut efficiencies of IBD events correspond to the left y-axis and are shown in blue. The signal to background ratios corresponding to the right y-axis are shown in red. Data is taken from table 6.2.

Table 6.2.: Survival efficiencies of the PSD cut of IBD-like atmospheric NC, IBD and fast neutron events and the corresponding tail windows that lead to the best signal to background ratio $S/\sqrt{S+B}$. The signal to background ratio is defined as average of the signal to background ratios of all assumed DM masses (m_{DM} = 15 MeV, 20 MeV, ..., 100 MeV). The best signal to background ratio with the corresponding tail window and efficiencies is displayed in bold.

$\epsilon_{PSD,atmoNC}$	$\epsilon_{PSD,IBD}$	$\epsilon_{PSD,FN}$	optimized tail window	$S/\sqrt{S+B}$
1.0 %	85.9 %	0.1 %	250 ns to 600 ns	4.000
2.0 %	89.2 %	0.1 %	200 ns to 600 ns	4.128
3.0 %	92.4 %	0.2 %	250 ns to 600 ns	4.193
4.0 %	95.4 %	0.4 %	200 ns to 600 ns	4.254
5.0 %	**97.4 %**	**0.6 %**	**200 ns to 600 ns**	**4.281**
6.0 %	98.6 %	1.0 %	150 ns to 600 ns	4.278
7.0 %	99.1 %	1.2 %	200 ns to 600 ns	4.277

from 100 ns to 600n ns and the fixed PSD cut efficiency $\epsilon_{PSD,atmoNC} = 1$ %. This is done for different tail windows defined by the tail start times t_{start} =100 ns, 150 ns, ..., 450 ns and tail end times $t_{end} = 600$ ns and $t_{end} = 700$ ns, again for the fixed PSD cut efficiency $\epsilon_{PSD,atmoNC} = 1$ %. The largest signal to background ratio of $S/\sqrt{S+B} = 4.000$ for a fixed PSD cut efficiency of $\epsilon_{PSD,atmoNC} = 1$ % is achieved for a tail window from 250 ns to 600 ns and with the cut parameters $A_1 = 0.0053$, $B_1 = 5.72 \cdot 10^{-4}$ MeV^{-1}, $A_2 = 0.0185$ and $B_2 = -6.0 \cdot 10^{-7}$ m^{-3}.
This whole procedure is also done for fixed efficiencies of $\epsilon_{PSD,atmoNC} = 2$ %, 3 %, 4 %, 5 %, 6 % and 7 %. The resulting PSD cut efficiencies of atmospheric NC, IBD and fast neutron events and the corresponding tail windows, which lead to the largest signal to background ratio $S/\sqrt{S+B}$, are summarized in table 6.2. Figure 6.4 shows the PSD cut efficiencies of IBD events and the corresponding signal to background ratios $S/\sqrt{S+B}$ listed in table 6.2 as function of the PSD cut efficiency of atmospheric NC events.

As a result, the largest signal to background ratio and therefore the most efficient pulse shape discrimination based on the TTR method can be achieved with a tail window from 200 ns to 600 ns. The corresponding TTR cut functions to reach this signal to background ratio of $S/\sqrt{S+B} = 4.281$ are $TTR_{cut}(E_{vis}) = 0.0320$ (independent of E_{vis}, since $B_1 = 0.0$ MeV^{-1}) and $TTR_{cut}(R^3) = 0.0329 - 1.4 \cdot 10^{-6}\,\text{m}^{-3} \cdot R^3$. These cut functions are also shown in figure 6.3. The resulting PSD survival efficiencies are $\epsilon_{PSD,atmoNC} = 5.0$ %, $\epsilon_{PSD,IBD} = 97.4$ % and $\epsilon_{PSD,FN} = 0.6$ % and are shown in figure 6.5 as function of the visible energy. Pulse shape discrimination based on the TTR method is very efficient for energies above around 40 MeV, where IBD events can be nearly perfectly separated from atmospheric NC and neutron events as indicated in figure 6.5. For lower energies, especially below around 25 MeV, the discrimination power decreases, since the TTR values of IBD and "gamma-dominated" atmospheric NC events resemble (as discussed above).

6.3. Final Visible Energy Spectrum in JUNO

For simulated IBD events, the total PSD survival efficiency for visible energies between 10 MeV and 100 MeV is $\epsilon_{PSD,IBD} = 97.4$ % with a statistical error of $\Delta\epsilon_{PSD,IBD} = 1.3$ %. To consider the PSD cut, the energy-dependent IBD PSD cut efficiency displayed in figure 6.5 is applied to the IBD signal spectra of electron antineutrons originated from DM self-annihilation for each assumed DM mass described in chapter 4 and to all IBD background spectra shown in figure 5.2 and discussed in chapter 5 (reactor neutrino background,

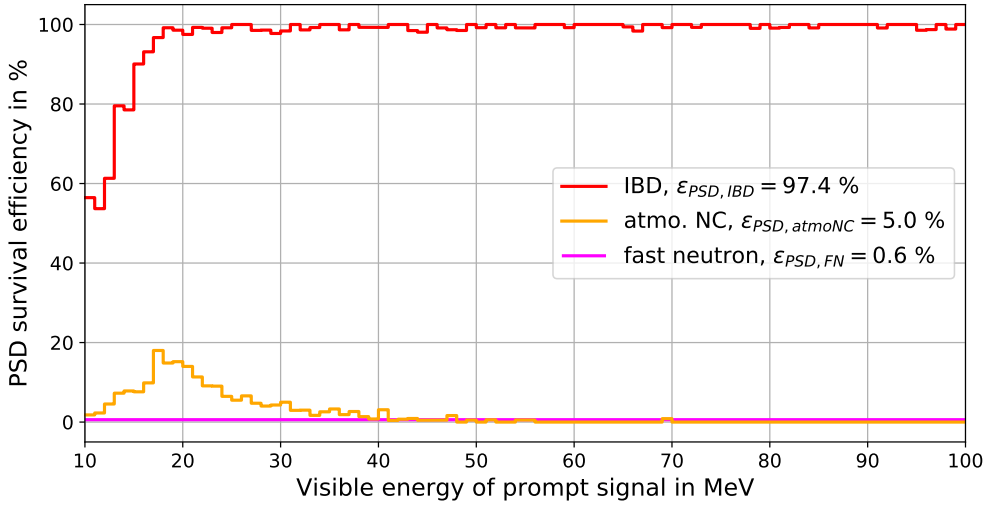

Figure 6.5.: Pulse shape discrimination cut efficiencies of IBD, IBD-like atmospheric NC and fast neutron events as function of the visible energy E_{vis}. The PSD efficiencies are determined with the TTR method for a tail window from 200 ns to 600 ns and the TTR cut functions shown in figure 6.3 and lead to the best signal to background ratio. The PSD efficiencies are displayed in bins of 1 MeV width.

DSNB and atmospheric CC neutrino background on free protons).
The IBD PSD survival efficiency $\epsilon_{PSD,IBD}(E_{vis})$ is also applied to the atmospheric CC neutrino background on ^{12}C shown in figure 5.2, since the prompt signals of atmospheric $\bar{\nu}_e$'s interacting via CC on ^{12}C are mainly caused by the energy deposition of positrons, similar to IBD signals. This conservative assumption might slightly overestimate the atmospheric CC background on ^{12}C.
With the TTR method introduced in this section, a total PSD survival efficiency of IBD-like atmospheric NC events of $\epsilon_{PSD,atmoNC} = (5.0 \pm 0.2)$ % can be achieved. The energy spectrum of atmospheric NC events after applying the PSD cut is calculated with the energy-dependent PSD cut efficiency illustrated in figure 6.5 and the atmospheric NC background spectrum of figure 5.2. After applying this energy-dependent PSD cut, the number of atmospheric NC neutrino background events that mimic an IBD signal in JUNO for a lifetime of 10 years is reduced to $N^{PSD}_{atmoNC} = 37.1 \pm 10.8$.
The resulting total PSD survival efficiency of fast neutron events is $\epsilon_{PSD,FN} = 0.6$ %, which reduces the expected number of fast neutron background events in JUNO after 10 years of data taking and for visible energies from 10 MeV to 100 MeV to $N^{PSD}_{FN} = 0.6 \pm 0.1$. Therefore, the fast neutron background is neglected in the following.

The total visible energy spectrum expected in the JUNO detector for 10 years of data taking and a fiducial mass of 14.77 kt is shown in figure 6.6 after considering the PSD cut introduced in this section. A summary of the number of background events in JUNO after applying the PSD cut is given in table 6.3.
The signal spectrum is displayed exemplarily for DM particles with $m_{DM} = 50.0$ MeV and assuming the currently best 90 % C.L. upper limit on the DM annihilation cross section of $\langle \sigma_A \, \mathrm{v} \rangle_{Super-K} = 1.1 \cdot 10^{-24}$ cm^3/s for $m_{DM} = 50$ MeV provided by Super-K. The total visible energy spectra for more assumed DM masses (15 MeV, 20 MeV, ..., 100 MeV) are displayed in section B of the appendix.
The atmospheric NC background is suppressed very effectively by PSD to $N^{PSD}_{atmoNC} = 37.1 \pm 10.8$. Especially for energies above 50 MeV, the background of IBD-like atmo-

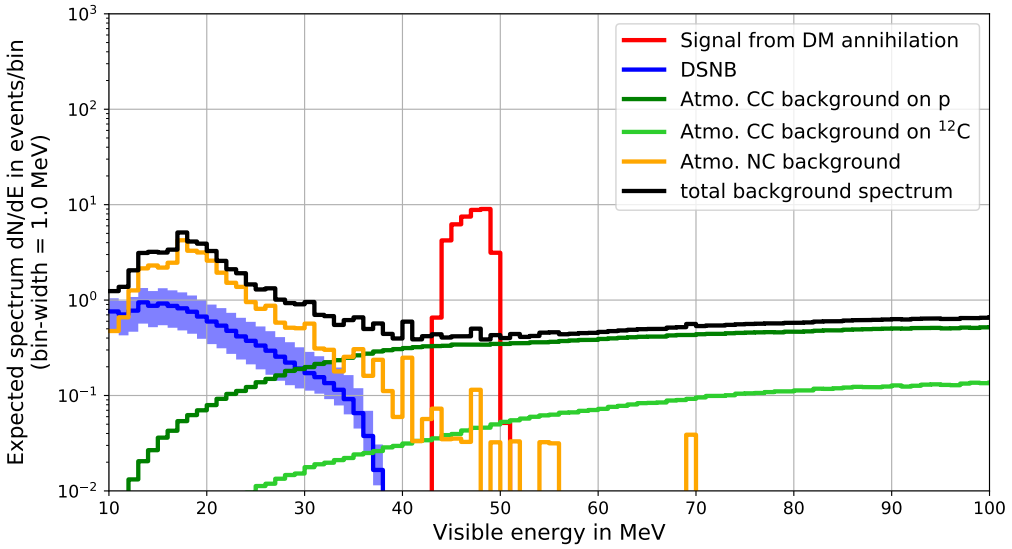

Figure 6.6.: Total expected visible energy spectrum of IBD events after PSD in JUNO for 10 years of data taking, a fiducial mass of 14.77 kt and visible energies between 10 MeV and 100 MeV. All events pass the IBD cuts, the muon veto cut, the cut on $\sigma(t_{pe})$ and the PSD cut. The total PSD survival efficiencies are $\epsilon_{PSD,IBD} = 97.4$ %, $\epsilon_{PSD,atmoNC} = 5.0$ % and $\epsilon_{PSD,FN} = 0.6$ %. The DSNB is shown in blue, where the solid blue line represents the fiducial case with $N^{fid,PSD}_{DSNB} = 12.6 \pm 5.0$, while the blue region is bounded by the high and low case, respectively. The atmospheric CC background of electron antineutrinos interacting with free protons is shown as dark green line ($N^{PSD}_{atmoCC,\bar{\nu}_e+p} = 30.3 \pm 7.6$), whereas the atmospheric CC background of $\bar{\nu}_e$'s interacting with ^{12}C nuclei is displayed as light green line ($N^{PSD}_{atmoCC,\bar{\nu}_e+^{12}\mathrm{C}} = 5.9 \pm 1.5$). The IBD-like atmospheric NC background is shown in orange with $N^{PSD}_{atmoNC} = 37.1 \pm 10.8$. The resulting total background spectrum is given as black line with a total number of background events after PSD of $N^{PSD}_{B} = 85.9 \pm 24.9$. The electron antineutrino signal spectrum calculated with the currently best 90 % C.L. limit on the DM annihilation cross section of $\langle \sigma_A \mathrm{v} \rangle_{Super-K}$ ($m_{DM} = 50\,\mathrm{MeV}$) = $1.1{\cdot}10^{-24}$ cm^3/s is shown in red exemplarily for $m_{DM} = 50$ MeV resulting in $N^{PSD}_{S} = 39.6$.

spheric NC events is reduced to a negligible level.
In the low energy region from 10 MeV to around 35 MeV, the DSNB and the atmospheric NC background dominate the spectrum. The DSNB is reduced to $N^{fid,PSD}_{DSNB} = 12.6 \pm 5.0$ for the fiducial case, $N^{low,PSD}_{DSNB} = 7.5 \pm 3.0$ for the low case and $N^{high,PSD}_{DSNB} = 18.8 \pm 7.5$ for the high case. Moreover, the reactor electron antineutrino background is suppressed to $N^{PSD}_{reactor} = 21.5 \pm 2.2$ events for visible energies above 10 MeV. For $E_{vis} \geq 12$ MeV, only 0.2 reactor background events are expected. Due to this small event number, the reactor electron antineutrino background is neglected in the following.
The atmospheric CC neutrino background dominates the spectrum for higher visible energies. Above around 50 MeV, the atmospheric CC neutrino background is the only background source for the search of neutrinos from DM annihilation in JUNO ($N^{PSD}_{atmoCC,\bar{\nu}_e+p} = 30.3 \pm 7.6$ and $N^{PSD}_{atmoCC,\bar{\nu}_e+^{12}\mathrm{C}} = 5.9 \pm 1.5$).

Table 6.3.: Number of background events in JUNO for visible energies between 10 MeV and 100 MeV, a fiducial mass of 14.77 kt and after 10 years of data taking. The table summarizes IBD backgrounds (reactor background, fiducial case of the DSNB, atmo. CC of $\bar{\nu}_e + p$) and IBD-like backgrounds (atmo. CC of $\bar{\nu}_e + {}^{12}\mathrm{C}$, atmo. NC, fast neutron) that pass the IBD selection cuts, the muon veto cut and the cut on $\sigma(t_{pe})$. The corresponding event numbers are listed in the second column. In the third column, the event numbers after applying the PSD cut are listed. The last column represents the visible energy region, where the background events occur.

	before PSD cut	after PSD cut	typ. visible energies
Reactor background	38.2 ± 3.8	21.5 ± 2.2	< 12 MeV
DSNB (fid.)	15.0 ± 6.0	12.6 ± 5.0	10 MeV $\leq E_{vis} \lesssim$ 35 MeV
Atmo. CC ($\bar{\nu}_e + p$)	30.5 ± 7.6	30.3 ± 7.6	20 MeV $\lesssim E_{vis} \leq$ 100 MeV
Atmo. CC ($\bar{\nu}_e + {}^{12}\mathrm{C}$)	5.9 ± 1.5	5.9 ± 1.5	40 MeV $\lesssim E_{vis} \leq$ 100 MeV
Atmo. NC	757 ± 220	37.1 ± 10.8	10 MeV $\leq E_{vis} \lesssim$ 50 MeV
Fast neutron	99.9 ± 20.0	0.6 ± 0.1	

7. JUNO's Sensitivity for Indirect Dark Matter Search

The main goal of this thesis is the determination of JUNO's sensitivity to measure electron antineutrinos from DM self-annihilation in the Milky Way as an excess over backgrounds via the IBD detection channel.
To specify the sensitivity, the contribution of the signal process to the expected spectrum is investigated and the upper limit that can be set on the signal contribution is determined. This upper limit on the number of signal events can then be translated into an upper limit on a monoenergetic electron antineutrino flux and, furthermore, into an upper limit on the DM self-annihilation cross section $\langle \sigma_A \mathrm{v} \rangle$.
In section 7.1, the analysis method to determine the upper limit on the number of signal events employed in this thesis is introduced. The resulting sensitivity of JUNO, its limit on the DM self-annihilation cross section and its discovery potential is presented in section 7.2. A comparison with limits from other neutrino detectors is given in section 7.3. Possible improvements for the indirect DM search with JUNO are presented in section 7.4.

7.1. Analysis Method

In order to calculate the upper limit on the number of signal events from DM self-annihilation in JUNO, a Bayesian analysis based on [290] is performed. In [290], a Bayesian analysis of the probability of a signal in presence of background has been developed for sparsely populated spectra and criteria for claiming evidence for a signal have been proposed.
The principle of the Bayesian analysis of [290] is introduced in section 7.1.1 and the application to the indirect DM search with JUNO is described in section 7.1.2.

7.1.1. Principle of Bayesian Analysis

The analysis method introduced in [290] and used here is based on Bayes' theorem[1].
The observed number of events in the i-th bin of the spectrum is denoted n_i. The probability to observe the measured spectrum, given by the set of the number of signal events

[1] The assumptions for the analysis are: the spectrum is confined to a certain region of interest; the spectral shapes of a possible signal and of the backgrounds are known; the spectrum is divided into bins and the event numbers in the bins follow Poisson distributions [290]. All assumptions are valid for the expected spectra in JUNO and in THEIA.

S and the number of background events B, is the product of the probabilities to observe the N values under the assumption that the fluctuations in the bins of the spectrum are uncorrelated [290]. The expected number of events λ_i in the i-th bin can be expressed in terms of S and B:

$$\lambda_i(S,B) = S \cdot f_{S,i} + B \cdot f_{B,i}. \tag{7.1}$$

$f_{S,i}$ and $f_{B,i}$ are the normalized shapes of the known signal and background spectra, respectively, for each energy bin i. The number of observed events n_i in each bin can fluctuate around λ_i according to Poisson distribution. This yields the conditional probability to obtain the measured spectrum

$$p\left(\text{spectrum}|S,B\right) = \prod_{i=1}^{N} \frac{\lambda_i(S,B)^{n_i}}{n_i!} e^{-\lambda_i(S,B)}. \tag{7.2}$$

Following Bayes' Theorem, the posterior probability, i.e. the probability that the observed spectrum can be explained by the set of parameters S and B, is:

$$p\left(S,B|\text{spectrum}\right) = \frac{p\left(\text{spectrum}|S,B\right) \cdot p_0(S) \cdot p_0(B)}{\int p\left(\text{spectrum}|S,B\right) \cdot p_0(S) \cdot p_0(B)\, \mathrm{d}S\, \mathrm{d}B} \tag{7.3}$$

with the conditional probability of equation 7.2 and the prior probabilities for the number of signal $p_0(S)$ and background events $p_0(B)$. These prior probabilities are chosen depending on the knowledge from previous experiments, measurements and models, and are assumed to be uncorrelated.
In order to estimate the signal contribution, the posterior probability $p\left(S,B|\text{spectrum}\right)$ is marginalized with respect to the number of background events B [290]:

$$p\left(S|\text{spectrum}\right) = \int p\left(S,B|\text{spectrum}\right)\, \mathrm{d}B. \tag{7.4}$$

A 90 % probability upper limit S_{90} on the number of signal events is then calculated by integrating equation 7.4 up to 90 % probability:

$$\int_0^{S_{90}} p\left(S|\text{spectrum}\right)\, \mathrm{d}S = 0.90. \tag{7.5}$$

To evaluate the sensitivity of an experiment, possible spectra are numerically generated from Monte Carlo simulations of signal and background events. These datasets (or ensembles) are produced according to Poisson distributions and subsequently analyzed with the analysis from above. The output parameters, e.g. the 90 % upper limit S_{90}, are histogrammed and the frequency distribution is interpreted as the probability density for the parameter under study [290]. From these distributions, the mean value and, for example, the 68 % probability interval can be deduced and used to determine the sensitivity of an experiment [290].

7.1.2. Bayesian Analysis for JUNO

JUNO's sensitivity is determined using the Bayesian analysis described above for a set of assumed DM masses of m_{DM} = 15 MeV, 20 MeV, 25 MeV, ..., 95 MeV and 100 MeV and

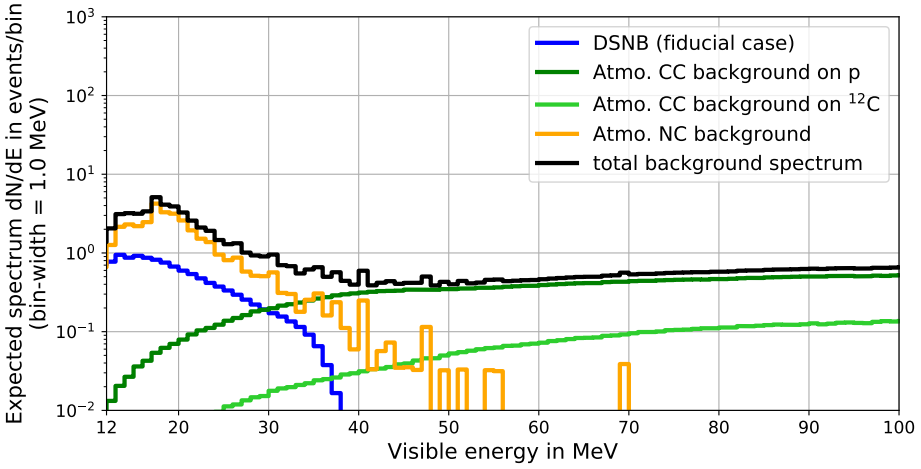

Figure 7.1.: Expected background-only spectrum in JUNO after PSD for a lifetime of 10 years, a fiducial mass of 14.77 kt and visible energies between 12 MeV and 100 MeV. The background spectra are equal to the spectra shown in figure 6.6 (the fiducial case is displayed for the DSNB). The total PSD survival efficiencies are $\epsilon_{PSD,IBD} = 97.4$ %, $\epsilon_{PSD,atmoNC} = 5.0$ % and $\epsilon_{PSD,FN} = 0.6$ %.

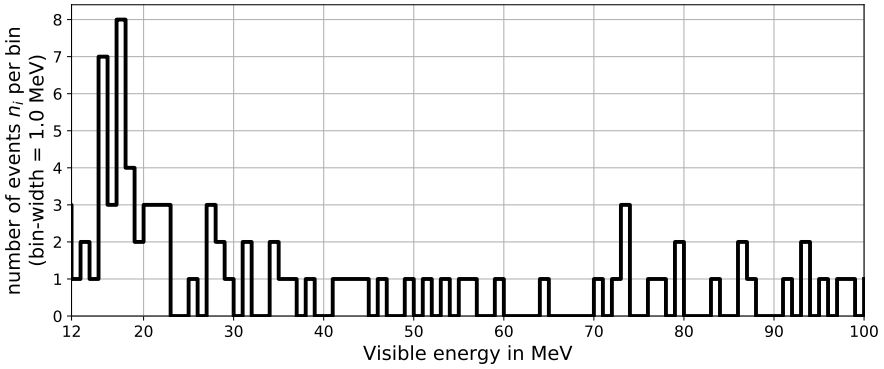

Figure 7.2.: Example of a dataset generated from the background-only spectrum of JUNO shown in figure 7.1. The dataset represents the observed number of events n_i per energy bin i. The bin size is 1 MeV.

for a visible energy region from 12 MeV to 100 MeV [2].
Since JUNO is still under construction, the outcome of the experiment, i.e. the observed number of events n_i per energy bin, is predicted by datasets generated from the background-only spectrum of JUNO shown in figure 7.1. In total, 1,000 datasets are generated by Poisson distributed random numbers for each energy bin i with the total number of background events $B_i = B_{DSNB_i} + B_{atmoCC+p,i} + B_{atmoCC+^{12}C,i} + B_{atmoNC,i}$ as mean value. One dataset is shown as example in figure 7.2. For each of these 1,000 datasets, the Bayesian analysis of section 7.1.1 is applied. This is repeated for each assumed value of the DM mass.

[2]The lower edge of the visible energy window is increased from 10 MeV to 12 MeV (compared to the previous chapters) due to the following reasons: on the one hand, the reactor electron antineutrino background can be neglected for $E_{vis} \geq 12$ MeV and, on the other hand, the number of signal events for the lightest assumed DM mass of $m_{DM} = 15$ MeV is $N_S(m_{DM} = 15 \text{ MeV}) = 0.0$ for $E_{vis} < 12$ MeV. Therefore, the reactor background is suppressed to a negligible level without reducing the signal efficiency.

The expected number of events λ_i in JUNO is

$$\begin{aligned}\lambda_i(S,B) =& S \cdot f_{S,i} + B_{DSNB} \cdot f_{DSNB,i} + B_{atmoCC+p} \cdot f_{atmoCC+p,i} \\ &+ B_{atmoCC+^{12}\mathrm{C}} \cdot f_{atmoCC+^{12}\mathrm{C},i} + B_{atmoNC} \cdot f_{atmoNC,i},\end{aligned} \tag{7.6}$$

where S, B_{DSNB} , $B_{atmoCC+p}$, $B_{atmoCC+^{12}\mathrm{C}}$ and B_{atmoNC} are the total number of signal and background events, respectively, and $f_{S,i}$, $f_{DSNB,i}$, $f_{atmoCC+p,i}$, $f_{atmoCC+^{12}\mathrm{C},i}$ and $f_{atmoNC,i}$ are the normalized spectral shapes of the signal and background spectra[3] after the PSD cut described in chapter 6. Therefore, the conditional probability defined in equation 7.2 is a function of S and the four background contributions in JUNO and the posterior probability for JUNO is

$$\begin{aligned}p\left(S, B_{DSNB}, ..., B_{atmoNC}|\text{spectrum}\right) \propto\ & p\left(\text{spectrum}|S, B_{DSNB}, ..., B_{atmoNC}\right) \\ & \cdot p_0(S) \cdot p_0(B_{DSNB}) \cdot p_0(B_{atmoCC+p}) \\ & \cdot p_0(B_{atmoCC+^{12}\mathrm{C}}) \cdot p_0(B_{atmoNC}).\end{aligned} \tag{7.7}$$

The prior probability $p_0(S)$ for the number of signal events is set flat up to the maximum value $S_{max} = 60.0$, consistent with the existing limit of Super-K [75] ($S_{max} = 60$ for $\langle \sigma_A \, \mathrm{v} \rangle_{Super-K} = 2.2 \cdot 10^{-24}$ cm^3/s at $m_{DM} = 100$ MeV):

$$p_0(S) = \begin{cases} 1/S_{max} & \text{, for } 0 \leq S \leq S_{max}, \\ 0 & \text{, otherwise.} \end{cases} \tag{7.8}$$

The prior probabilities for the number of background events is given by a Gaussian distribution with mean value μ_B equal to the total expected number of background events of the corresponding background and width σ_B:

$$p_0(B) = \begin{cases} \dfrac{\exp\left(-\frac{(B-\mu_B)^2}{2\sigma_B^2}\right)}{\int_0^\infty \exp\left(-\frac{(B-\mu_B)^2}{2\sigma_B^2}\right) \mathrm{d}B} & \text{, for } B \geq 0, \\ 0 & \text{, for } B < 0. \end{cases} \tag{7.9}$$

So, the background contributions are assumed to be known within some uncertainty that is represented by σ_B (recall that the shape of each background spectrum is however fixed). Here, a very conservative approach for the uncertainty of the background contributions of $\sigma_B = 2 \cdot \mu_B$ is assumed[4].
The marginalization of the posterior probability of equation 7.7, which is a function of the free parameters S, B_{DSNB}, $B_{atmoCC+p}$, $B_{atmoCC+^{12}\mathrm{C}}$ and B_{atmoNC}, is done with Markov Chain Monte Carlo (MCMC) sampling with the python package *emcee* [291]. This package is based on [292]. The start values of S, B_{DSNB}, $B_{atmoCC+p}$, $B_{atmoCC+^{12}\mathrm{C}}$ and B_{atmoNC} for the MCMC sampling are given by minimizing the negative logarithm of the conditional probability $\ln\left[p\left(\text{spectrum}|S, B_{DSNB}, ..., B_{atmoNC}\right)\right]$. Then the logarithm of the

[3] The spectral shapes of the signal spectra after PSD for the different assumed DM masses are shown in figure B.5 and B.6. The spectral shapes of the backgrounds are shown in figure 7.1. For the DSNB, the normalized spectral shape of the fiducial case is considered here. The other cases will be discussed in section 7.2.

[4] The analysis is also done for more stringent prior probabilities for the number of background events defined by equation 7.9 with $\sigma_B = \mu_B/2$, which will be discussed in section 7.2.

posterior probability $\ln\left[p\left(S, B_{DSNB}, ..., B_{atmoNC}|\text{spectrum}\right)\right]$ is marginalized with respect to S, B_{DSNB}, $B_{atmoCC+p}$, $B_{atmoCC+^{12}\text{C}}$ and B_{atmoNC} with the given start values. The results of the marginalization are shown in figure 7.3 exemplarily for the dataset of figure 7.2 and for an assumed DM mass of $m_{DM} = 50$ MeV. The only relevant (anti)correlation is observed between the parameters B_{DSNB} and B_{atmoNC} and between the parameters $B_{atmoCC+p}$ and $B_{atmoCC+^{12}\text{C}}$. This is due to the similar spectral shapes in the same energy region of the DSNB and atmospheric NC background, and of the atmospheric CC background on protons and ^{12}C. All other parameters are uncorrelated.
After the marginalization of the posterior probability, the 90 % upper limit S_{90} of the number of signal events as well as the estimators for the number of background events (B^*_{DSNB}, $B^*_{atmoCC+p}$, $B^*_{atmoCC+^{12}\text{C}}$, B^*_{atmoNC}) are calculated.
This marginalization is done for each dataset. The mean of all 1,000 values of the 90 % upper limit on the number of signal events represents the average 90 % upper limit $\tilde{S}_{90}$. Moreover, the 68 % and 95 % probability intervals are calculated from the distribution of S_{90}.
This analysis is performed for different DM masses (15 MeV, 20 MeV, ..., 100 MeV), which results in 90 % upper limits $\tilde{S}_{90}(m_{DM})$ on the number of signal events as function of the DM mass. Because of the monoenergetic electron antineutrino flux at Earth, the DM mass is equal to the electron antineutrino energy $E_{\bar{\nu}_e}$. Therefore, the 90 % upper limits on the number of signal events can also be interpreted as function of the electron antineutrino energy $\tilde{S}_{90}(m_{DM}) = \tilde{S}_{90}(E_{\bar{\nu}_e})$. The resulting 90 % upper limit $\tilde{S}_{90}(E_{\bar{\nu}_e})$ on the number of signal events in JUNO after 10 years of data taking and for the PSD efficiencies determined in section 6.2 ($\epsilon_{PSD,IBD} = 97.4$ %, $\epsilon_{PSD,atmoNC} = 5.0$ %) is shown in figure 7.4 together with the 68 % and 95 % probability interval, respectively.

7.2. Sensitivity of JUNO

The 90 % upper limit $\tilde{S}_{90}(E_{\bar{\nu}_e})$ on the number of signal events can be translated into a 90 % upper limit on a monoenergetic $\bar{\nu}_e$ flux $\phi_{\bar{\nu}_e,90\%}(E_{\bar{\nu}_e})$ in JUNO with equation 4.3 and by considering the PSD efficiency $\epsilon_{PSD,IBD}$ determined in section 6.2:

$$\phi_{\bar{\nu}_e,90\%}(E_{\bar{\nu}_e}) = \frac{\tilde{S}_{90}(E_{\bar{\nu}_e})}{\sigma_{IBD}(E_{\bar{\nu}_e})\ N_p\ t\ \epsilon_{IBD}\ \epsilon_{\mu\,veto}\ \epsilon_{PSD,IBD}(E_{\bar{\nu}_e})}, \tag{7.10}$$

where σ_{IBD} is the IBD interaction cross section of equation 4.4, $N_p = 1.45 \cdot 10^{33}$ the number of free protons in JUNO, $t = 10$ years the total exposure time, $\epsilon_{IBD} = 67.0$ % the IBD detection efficiency and $\epsilon_{\mu\,veto} = 97.2$ % the efficiency due to the application of the muon veto. The PSD efficiency $\epsilon_{PSD,IBD}$ of IBD events is a function of the electron antineutrino energy and is defined as

$$\epsilon_{PSD,IBD}(E_{\bar{\nu}_e}) = \frac{\int_{12\,\text{MeV}}^{100\,\text{MeV}} N_S^{PSD}(E_{\bar{\nu}_e}, E_{vis})\text{d}E_{vis}}{\int_{12\,\text{MeV}}^{100\,\text{MeV}} N_S(E_{\bar{\nu}_e}, E_{vis})\text{d}E_{vis}} \tag{7.11}$$

with $N_S^{PSD}(E_{\bar{\nu}_e})$ and $N_S(E_{\bar{\nu}_e})$ as number of signal events after and before the PSD cut, respectively, determined in section 6.2 (total $\epsilon_{PSD,IBD} = 97.4$ %, total $\epsilon_{PSD,atmoNC} = 5.0$ %).
The resulting 90 % upper limit on the $\bar{\nu}_e$ flux for JUNO is shown in figure 7.5 with the 68 % and 95 % probability intervals. It should be noted here that the upper limit $\phi_{\bar{\nu}_e,90\%}$ represents a model-independent 90 % upper limit on a monoenergetic electron antineutrino flux at Earth (independent of its origin) and does not depend on the assumptions and assumed properties of DM self-annihilation in the Milky Way made in section 4.1. For

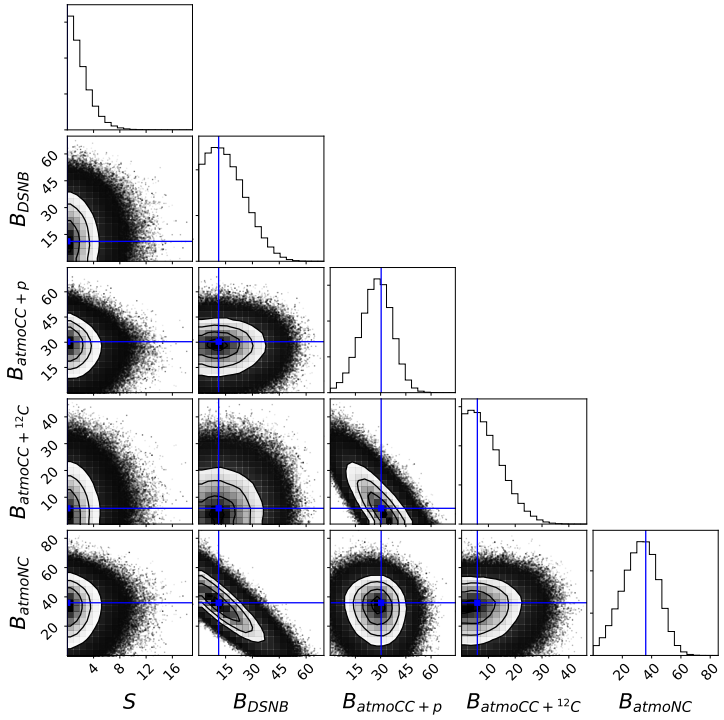

Figure 7.3.: Results of MCMC sampling of the posterior probability of equation 7.7 exemplarily for an assumed DM mass of $m_{DM} = 50$ MeV and for the analyzed dataset shown in figure 7.2. Each 2D contour plot represents the posterior probability as function of two free parameters marginalized with respect to the other parameters. The 1D plots show the posterior probability of one free parameter marginalized with respect to the others, e.g. the top left plot represents the posterior probability $p\,(S|\text{spectrum})$ marginalized with respect to B_{DSNB}, $B_{atmoCC+p}$, $B_{atmoCC+^{12}\text{C}}$ and B_{atmoNC} as function of S. The blue lines are the number of expected background events from the spectrum shown in figure 7.1. The figure is generated with [293].

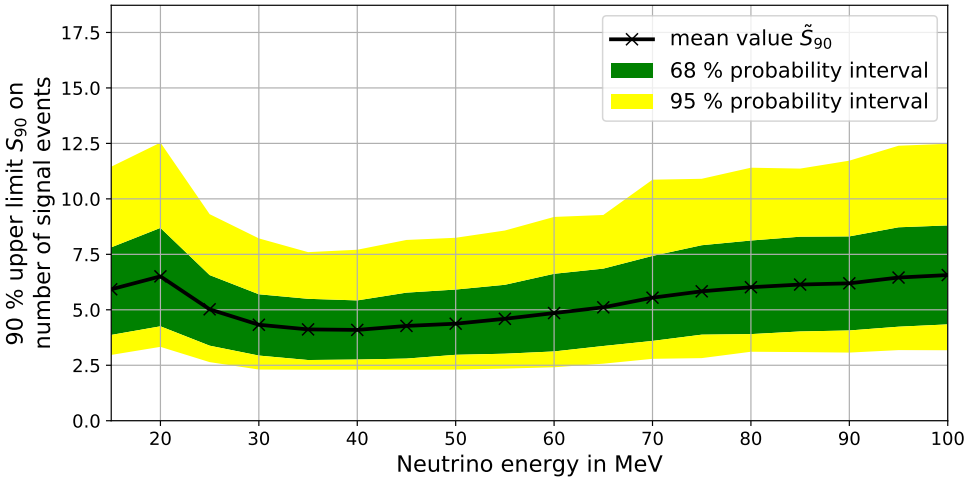

Figure 7.4.: Mean value of the 90 % upper limit on the number of signal events $\tilde{S}_{90}$ in JUNO as well as the 68 % and 95 % probability interval as function of the neutrino energy. The mean values and probability intervals are analyzed for DM masses and neutrino energies, respectively, from 15 MeV to 100 MeV in 5 MeV steps.

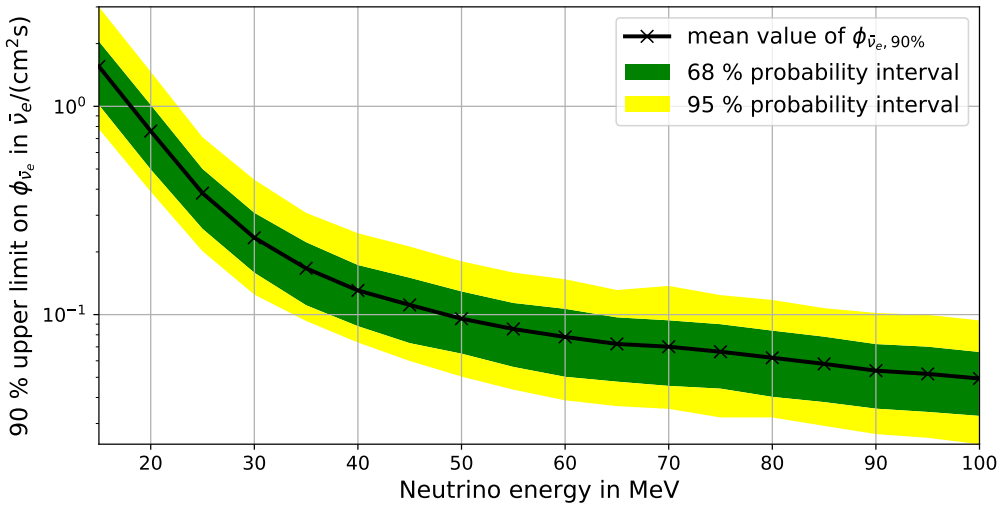

Figure 7.5.: 90 % probability upper limit on a monoenergetic electron antineutrino flux in JUNO as function of the neutrino energy. The mean values of $\phi_{\bar{\nu}_e,90\%}$ are displayed in black, the 68 % probability interval is shown in green and the 95 % probability interval in yellow. The mean values and probability intervals are analyzed for neutrino energies from 15 MeV to 100 MeV with steps of 5 MeV.

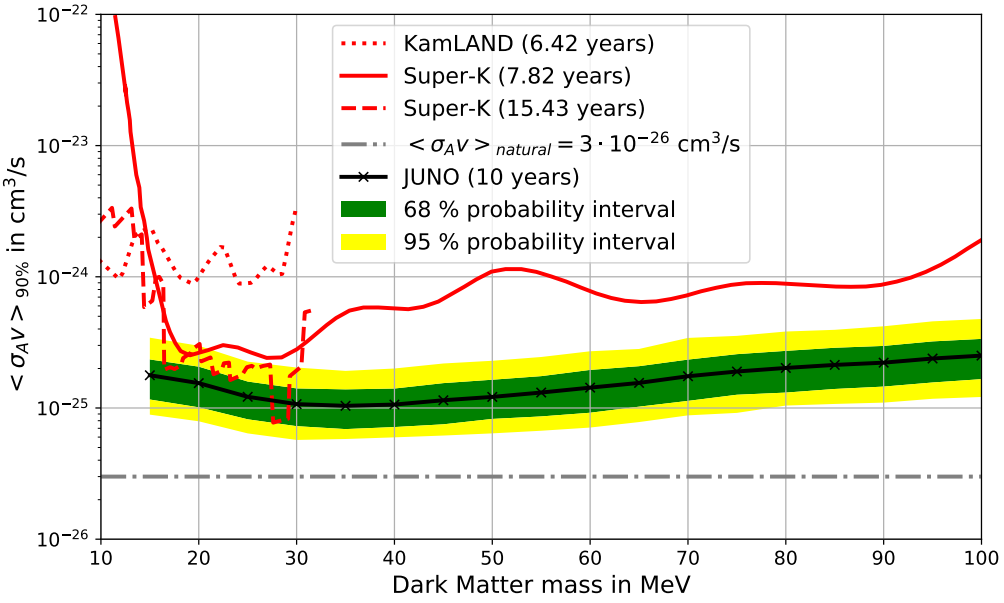

Figure 7.6.: 90 % probability upper limit on the DM self-annihilation cross section $\langle \sigma_A \, \mathrm{v} \rangle$ for the JUNO experiment. $\langle \sigma_A \, \mathrm{v} \rangle_{90\%}$ for JUNO after 10 years of data taking is displayed in black and analyzed for DM masses from 15 MeV to 100 MeV with steps of 5 MeV. The 68 % probability interval is shown in green and the 95 % probability interval in yellow. The best currently existing 90 % C.L. upper limits of KamLAND and Super-K discussed in section 2.4.2 are shown in red. The natural scale of the DM self-annihilation cross section $\langle \sigma_A \, \mathrm{v} \rangle_{natural} = 3 \cdot 10^{-26}$ cm^3/s is displayed as gray line.

example, it could also be interpreted as the upper limit on a monoenergetic electron antineutrino flux originated from the potential two body decay of a DM particle into a neutrino-antineutrino pair, $DM \rightarrow \nu + \bar{\nu}$. In this case, the 90 % upper limit $\phi_{\bar{\nu}_e,90\%}$ of figure 7.5 could be translated into a 90 % upper limit on the DM lifetime τ_{DM}.
With the 90 % upper limit $\phi_{\bar{\nu}_e,90\%}$, the 90 % probability upper limit on the DM self-annihilation cross section $\langle\sigma_A\,\mathrm{v}\rangle$ for JUNO is calculated with

$$\langle\sigma_A\,\mathrm{v}\rangle_{90\%}\,(m_{DM}) = \phi_{\bar{\nu}_e,90\%}(E_{\bar{\nu}_e})\;\frac{6\cdot m_{DM}^2}{\delta(E_{\bar{\nu}_e}-m_{DM})\;R_0\;\rho_0^2\;J_{avg}} \tag{7.12}$$

following equation 4.1. As discussed in section 4.1, Majorana DM particles annihilating directly into neutrino-antineutrino pairs in the entire Milky Way, equal neutrino flavor composition at Earth and the canonical value $J_{avg} = 5$ of the angular-averaged J-factor are assumed. The resulting 90 % upper limit on the DM self-annihilation cross section determined with the JUNO detector is shown in figure 7.6 with the 68 % and 95 % probability intervals, respectively (the best currently existing 90 % C.L. upper limits of KamLAND and Super-K presented in section 2.4.2 are also displayed for comparison). Moreover, the natural scale of the DM self-annihilation cross section $\langle\sigma_A\,\mathrm{v}\rangle_{natural} = 3{\cdot}10^{-26}\ \mathrm{cm}^3/\mathrm{s}$ is also displayed in figure 7.6 (in the following figures of chapter 7, the natural scale $\langle\sigma_A\,\mathrm{v}\rangle_{natural}$ is always displayed as gray line).
The 90 % upper limit on the DM self-annihilation cross section for JUNO ranges from $\langle\sigma_A\,\mathrm{v}\rangle_{90\%}(m_{DM} = 35\,\mathrm{MeV}) = 1.0\cdot10^{-25}\ \mathrm{cm}^3/\mathrm{s}$ to $\langle\sigma_A\,\mathrm{v}\rangle_{90\%}\,(m_{DM} = 100\,\mathrm{MeV}) = 2.5\cdot10^{-25}\ \mathrm{cm}^3/\mathrm{s}$. The limit of the self-annihilation cross section averaged over the DM mass region from 15 MeV to 100 MeV is $\langle\sigma_A\,\mathrm{v}\rangle_{90\%}^{average} = 1.633\cdot10^{-25}\ \mathrm{cm}^3/\mathrm{s}$. Annihilation cross sections greater than the limit shown in figure 7.6 are excluded at 90 % C.L.. The currently best limits of Super-K can be improved by JUNO in the whole DM mass region from 15 MeV to 100 MeV, except of 27.5 MeV $\leq m_{DM} \leq$ 29.2 MeV (more details about the comparison of limits between neutrino experiment is given in section 7.3).
The same analysis as described in section 7.1.2 is also performed assuming prior probabilities of the number of background events defined by equation 7.9 with $\sigma_B = \mu_B/2$. So, it is assumed that the different background contributions are more confined. The 90 % upper limits averaged over the DM mass region from 15 MeV to 100 MeV of both cases agree with each other within less than 0.5 %. Therefore, the choice of σ_B doesn't affect the sensitivity of JUNO.
To validate the calculation and analysis described in section 7.1.2 and applied in this thesis, the 90 % upper limit on the DM self-annihilation cross section is also determined using the Bayesian Analysis Toolkit (BAT), which is a similar data analysis toolkit based on Bayes' Theorem and realized with the use of MCMC (see [294]). The results of the limits of the DM self-annihilation cross section match within 0.2 % for the two used analysis packages.

JUNO's Sensitivity for Different DM Properties

The 90 % upper limit on $\langle\sigma_A\,\mathrm{v}\rangle$ shown in figure 7.6 is calculated under the assumptions that the angular-averaged J-factor is $J_{avg} = 5$ and DM is a Majorana particle.
As discussed in section 4.1, the angular-averaged J-factor strongly depends on the DM density profile $\rho(r)$ in the Milky Way. Three DM profile models (Kravtsov, NFW, Moore) were introduced, which result in J-factors of $J_{avg}^{Kravtsov} = 2.6$, $J_{avg}^{NFW} = 3.0$ and $J_{avg}^{Moore} = 8.0$ (see table 4.1). In figure 7.7, the 90 % upper limit on the DM self-annihilation cross section calculated with equation 7.12 assuming different J-factors is shown. Depending on the chosen DM profile model, $\langle\sigma_A\,\mathrm{v}\rangle_{90\%}$ differs by a factor of around three.
The 90 % upper limit on the DM self-annihilation cross section is moreover calculated

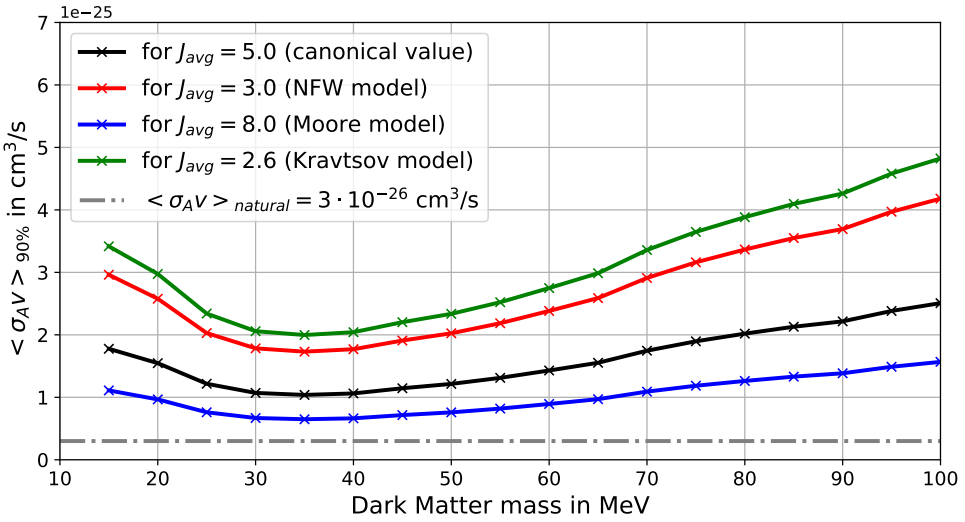

Figure 7.7.: 90 % probability upper limit on the DM self-annihilation cross section $\langle \sigma_A \, \mathrm{v} \rangle$ for the JUNO experiment for different assumed DM profile models of the Milky Way. $\langle \sigma_A \, \mathrm{v} \rangle_{90\%}$ after 10 years of data taking is displayed assuming $J_{avg}^{Kravtsov} = 2.6$ (green), $J_{avg}^{NFW} = 3.0$ (red) and $J_{avg}^{Moore} = 8.0$ (blue), respectively. The 90 % upper limit shown in figure 7.6, where $J_{avg} = 5$ is assumed, is shown in black for comparison.

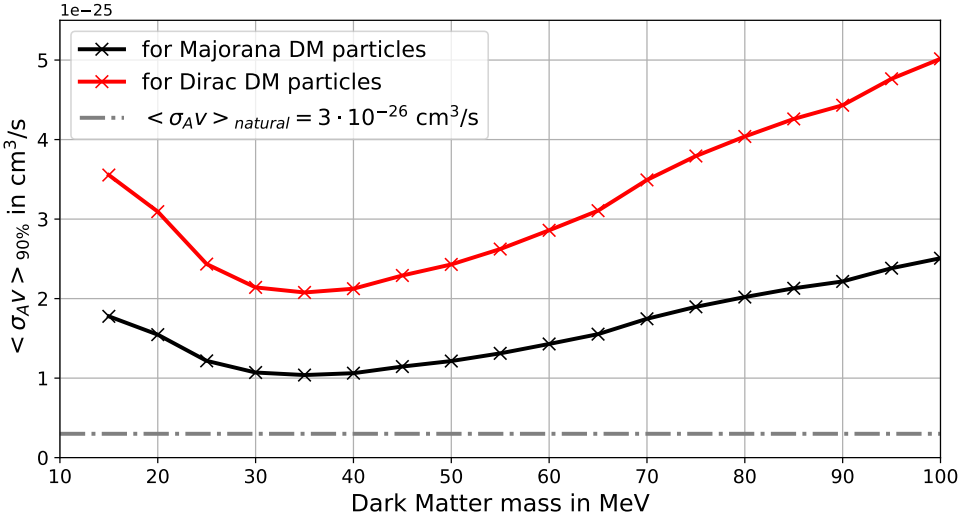

Figure 7.8.: 90 % probability upper limit on the DM self-annihilation cross section $\langle \sigma_A \, \mathrm{v} \rangle$ for the JUNO experiment assuming Dirac (red) and Majorana (black) DM particles, respectively. The 90 % upper limit for Majorana particles is also shown in figure 7.6.

under the assumption that DM particles are Dirac particles instead of Majorana particles ($\kappa_1 = 4$ in equation 2.2 for Dirac DM). The resulting limit assuming Dirac DM particles as well as the limit for Majorana DM particles is shown in figure 7.8 (in both cases $J_{avg} = 5$ is assumed). If DM particles are Majorana particles, the limit on the self-annihilation cross section is more stringent by a factor of around two as expected.

JUNO's Sensitivity for Different PSD Efficiencies

The upper limit on the DM self-annihilation cross section shown in figure 7.6 is analyzed using the signal and background spectra after the PSD cut specified by the total survival efficiencies of $\epsilon_{PSD,IBD} = 97.4$ % and $\epsilon_{PSD,atmoNC} = 5.0$ %. These PSD efficiencies yield the best signal to background ratio $S/\sqrt{S+B}$ as described in section 6.2.
To determined the impact of the PSD cut on the resulting 90 % upper limit on the DM self-annihilation cross section, the analysis described in section 7.1.2 was performed for each PSD efficiency listed in table 6.2 [5]. The resulting 90 % upper limits on the DM self-annihilation cross section for different PSD efficiencies are shown in figure 7.9 together with $\langle \sigma_A \, \mathrm{v} \rangle_{90\%}$ averaged over the DM mass range from 15 MeV to 100 MeV.
The upper limits agree with each other for DM masses above around 35 MeV within statistical uncertainties. For smaller DM masses, the upper limits vary depending on the PSD efficiencies. Especially for $m_{DM} = 15$ MeV, the upper limits differ up to a factor of 3.3, which represents the largest influence of PSD.
The best averaged 90 % upper limit on the DM self-annihilation cross section is achieved considering the PSD cut specified by the total survival efficiencies of $\epsilon_{PSD,IBD} = 97.4$ % and $\epsilon_{PSD,atmoNC} = 5.0$ %. So, the PSD efficiencies that result in the largest signal to background ratio yield the most stringent upper limit on the DM annihilation cross section. Nevertheless, JUNO's sensitivity is only slightly decreased (< 0.9 %), if a PSD cut specified by $\epsilon_{PSD,atmoNC} = 4.0$ %, $\epsilon_{PSD,atmoNC} = 6.0$ % or $\epsilon_{PSD,atmoNC} = 7.0$ % is applied.

JUNO's Sensitivity for Different DSNB Models

The analysis described in section 7.1.2 is also performed assuming the low and high case of the DSNB of section 5.2 (all other spectra and parameters, e.g. total PSD efficiencies of $\epsilon_{PSD,IBD} = 97.4$ % and $\epsilon_{PSD,atmoNC} = 5.0$ %, remain unchanged). The resulting 90 % upper limits on the DM self-annihilation cross section are shown in figure 7.10 for the low and high case, respectively.
The differences of the 90 % upper limit on the DM self-annihilation cross section due to the assumed DSNB cases is clearly visible in the DM mass region below around 35 MeV. For the low case, the number of DSNB events is smaller, which results in a better limit on the DM annihilation cross section. In contrast to that, the number of DSNB events for the high case is larger resulting in a worse upper limit. Above DM masses of around 75 MeV, the upper limits for the three cases (low, fiducial, high) slightly differ, which is due to statistical uncertainties and not because of physical effects.

JUNO's Sensitivity for Different Exposure Times

All limits for JUNO presented above are determined for a total exposure time of $t = 10$ years. To investigate the dependence of JUNO's sensitivity on the exposure time, the

[5] For the PSD cut with total efficiencies of $\epsilon_{PSD,IBD} = 85.9$ % and $\epsilon_{PSD,atmoNC} = 1.0$ %, $\langle \sigma_A \, \mathrm{v} \rangle$ was not determined, since the PSD cut suppresses the expected signal for $m_{DM} = 15$ MeV to a negligible level ($N_S(m_{DM} = 15 \text{ MeV}) = 0.0$). For each of the other PSD efficiencies listed in table 6.2, 1,000 datasets were generated according to the specific background-only spectrum, the analysis of section 7.1.2 was applied and $\tilde{S}_{90}(E_{\bar{\nu}_e})$ was determined. With $\tilde{S}_{90}(E_{\bar{\nu}_e})$, $\phi_{\bar{\nu}_e,90\%}(E_{\bar{\nu}_e})$ and $\langle \sigma_A \, \mathrm{v} \rangle_{90\%}(m_{DM})$ was calculated for each assumed PSD efficiency.

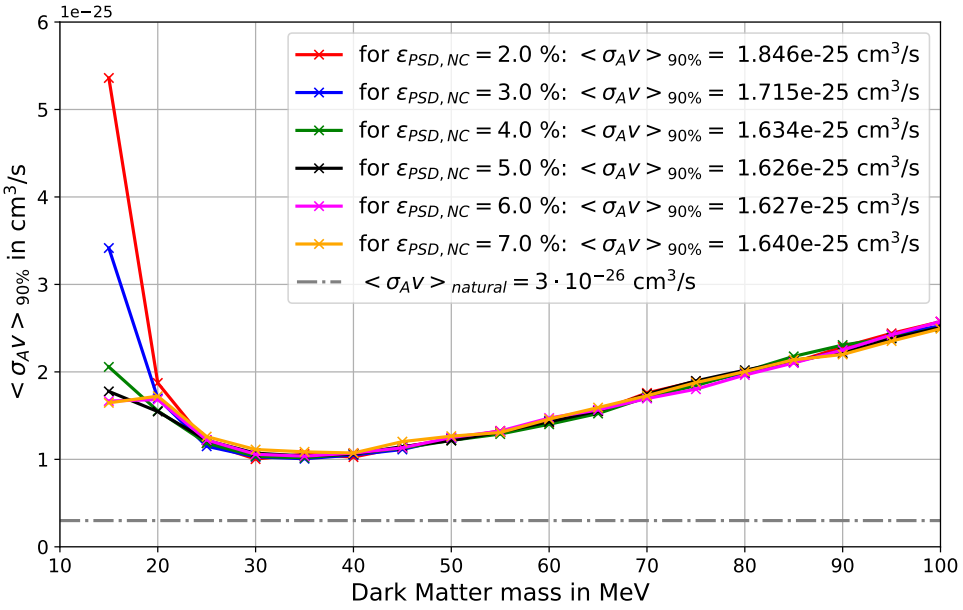

Figure 7.9.: 90 % probability upper limit on the DM self-annihilation cross section $\langle \sigma_A \, \mathrm{v} \rangle$ for the JUNO experiment after 10 years of data taking for different PSD efficiencies. The upper limits are displayed for $\epsilon_{PSD,IBD} = 89.2$ % and $\epsilon_{PSD,atmoNC} = 2.0$ %, $\epsilon_{PSD,IBD} = 92.4$ % and $\epsilon_{PSD,atmoNC} = 3.0$ %, $\epsilon_{PSD,IBD} = 95.4$ % and $\epsilon_{PSD,atmoNC} = 4.0$ %, $\epsilon_{PSD,IBD} = 97.4$ % and $\epsilon_{PSD,atmoNC} = 5.0$ %, $\epsilon_{PSD,IBD} = 98.6$ % and $\epsilon_{PSD,atmoNC} = 6.0$ %, and $\epsilon_{PSD,IBD} = 99.1$ % and $\epsilon_{PSD,atmoNC} = 7.0$ %. Moreover, $\langle \sigma_A \, \mathrm{v} \rangle_{90\%}$ averaged over DM masses from 15 MeV to 100 MeV is given for each case.

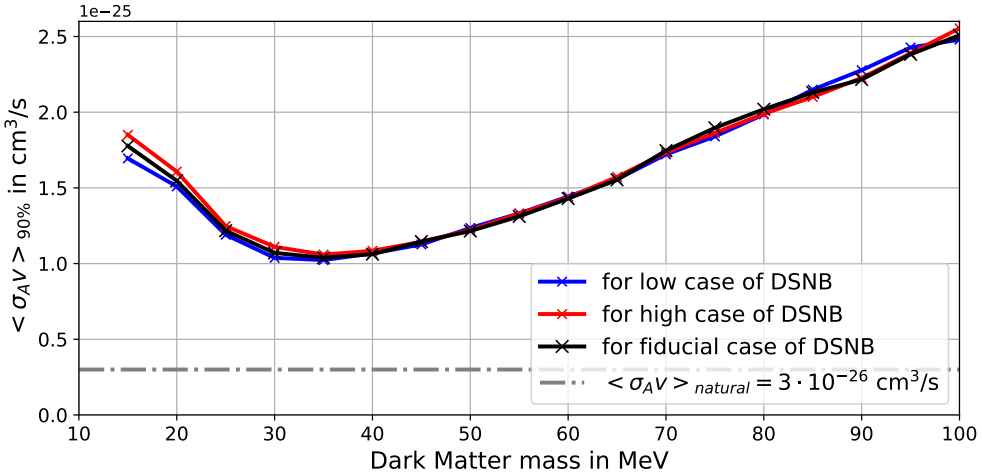

Figure 7.10.: 90 % probability upper limit on the DM self-annihilation cross section $\langle \sigma_A \, \mathrm{v} \rangle$ for the JUNO experiment for the low (blue) and high (red) case of the DSNB. The 90 % upper limit for the fiducial case (black) of figure 7.6 is also shown.

analysis presented in section 7.1.2 is also done for total exposure times of $t = 1$ year, $t = 5$ years and $t = 20$ years, respectively. For each exposure time, the signal and background spectra are calculated and 1,000 datasets generated from the corresponding background-only spectrum are analyzed for each assumed DM mass (15 MeV, 20 MeV, ..., 100 MeV). The resulting 90 % upper limit on the DM self-annihilation determined with JUNO for the different exposure times is presented in figure 7.11. Moreover, figure 7.11 shows the 90 % upper limits averaged over DM masses from 15 MeV to 100 MeV for the different exposure times.
JUNO's sensitivity increases, i.e. the 90 % upper limit decreases, for longer exposure times as expected. Especially by increasing the exposure time, i.e. the lifetime of the detector, from $t = 1$ year to $t = 5$ years, the sensitivity can be significantly improved by a factor of around 3.3. Above total exposure times of $t = 10$ years, only a slight improvement of the sensitivity can be gained.

JUNO's Discovery Potential

JUNO's potential to claim the discovery of (or the evidence for) an electron antineutrino signal from DM self-annihilation in the Milky Way as an excess over backgrounds is estimated here to finalize the section about the sensitivity of JUNO. JUNO's discovery potential is estimated based on the signal to background ratio $S/\sqrt{S+B}$, which can be related to a significance and interpreted as criterion for claiming the discovery of a signal in a simplified approach (no detailed analysis to determine the discovery potential was performed).
The signal to background ratio $S/\sqrt{S+B}$ in JUNO is calculated for an annihilation cross section that corresponds to the best currently existing 90 % C.L. upper limit on the DM self-annihilation cross section. For all DM masses in the range from 15 MeV to 100 MeV, Super-K gives the best limit as shown e.g. in figure 7.13. All previously discussed cuts are applied to get the number of signal and background events after 10 years. The result is shown in figure 7.12 together with the 3σ and 5σ significance levels.
JUNO's discovery potential will be between 3σ and 5σ for most DM masses from 15 MeV to 100 MeV assuming the upper limit on the annihilation cross section of Super-K. For $20\,\text{MeV} \leq m_{DM} \leq 30$ MeV, the discovery potential will be below 3σ, whereas for $m_{DM} =$ 50, 55 and 100 MeV a discovery of DM self-annihilation into neutrinos could be claimed with more than 5σ considering the assumptions made here.

7.3. Discussion and Comparison with Limits from other Experiments

Figure 7.13 shows the 90 % upper limits on the DM self-annihilation cross section of JUNO together with the limits of the neutrino experiments KamLAND, Super-K and Hyper-K. The upper limit of JUNO was determined in the previous section and is already shown in figure 7.6. To determine $\langle \sigma_A \, \mathrm{v} \rangle_{90\%}$ of JUNO, the signal and background spectra (fiducial case of DSNB, atmospheric $\bar{\nu}_e$ CC background on p and ^{12}C, atmospheric NC background) of IBD events after all described cuts (IBD cut, muon veto cut and PSD cut with $\epsilon_{PSD,IBD} = 97.4$ %, $\epsilon_{PSD,atmoNC} = 5.0$ % and $\epsilon_{PSD,FN} = 0.6$ %) are analyzed for a fiducial mass of 14.77 kt and after a total exposure time of 10 years. Moreover, Majorana DM particles are assumed and the parameters of equation 7.12 are set to $J_{avg} = 5$, $R_0 = 8.5$ kpc and $\rho_0 = 0.3$ GeV/cm^3. The currently existing 90 % upper limits for DM masses between 10 MeV and 100 MeV of KamLAND [74] and Super-K [4, 75] introduced in section 2.4.2 are shown in figure 7.13. The prospective upper limits of Hyper-K and of Hyper-K doped with gadolinium [121] discussed in section 2.4.2 are also displayed in figure 7.13 for a lifetime of 10 years[6].

[6] The limits of Hyper-K of [121] are determined for a lifetime of 20 years, but scaled here to a lifetime of 10 years for better comparison.

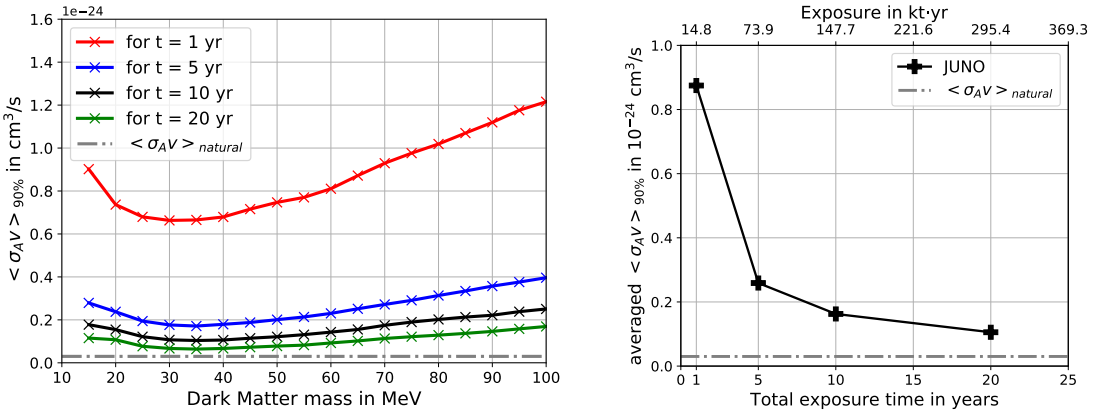

Figure 7.11.: Left: 90 % probability upper limit on the DM self-annihilation cross section $\langle \sigma_A \, \mathrm{v} \rangle$ as function of the DM mass for the JUNO experiment for different total exposure times t. The upper limits are calculated and shown for $t = 1$ year (red), $t = 5$ years (blue) and $t = 20$ years (green), respectively. For comparison, $\langle \sigma_A \, \mathrm{v} \rangle_{90\%}$ for $t = 10$ years of figure 7.6 is shown in black. Right: 90 % upper limit on the DM self-annihilation cross section of JUNO averaged over DM masses from 15 MeV to 100 MeV as function of the total exposure time (and total exposure, respectively).

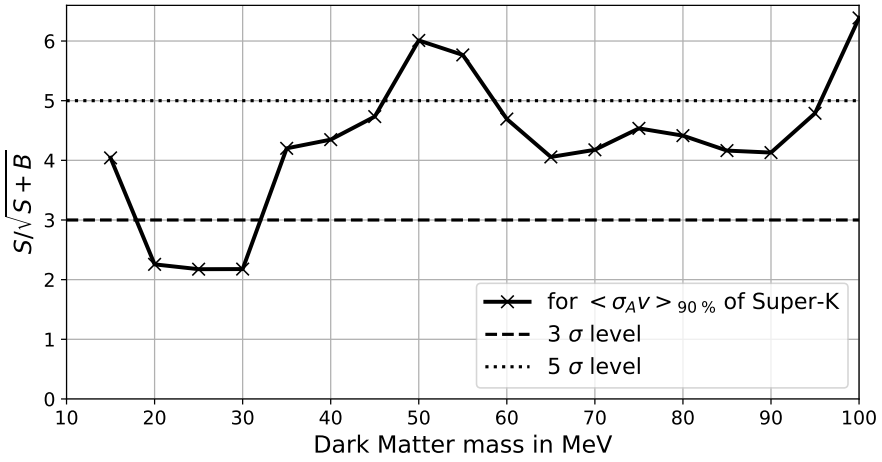

Figure 7.12.: Signal to background ratio $S/\sqrt{S+B}$ in JUNO as function of the DM mass. The signal to background ratio assuming the best currently existing 90 % C.L. upper limits on the DM self-annihilation cross section of Super-K is shown as black solid line. The 3σ (5σ) significance level is displayed as dashed (dotted) black line.

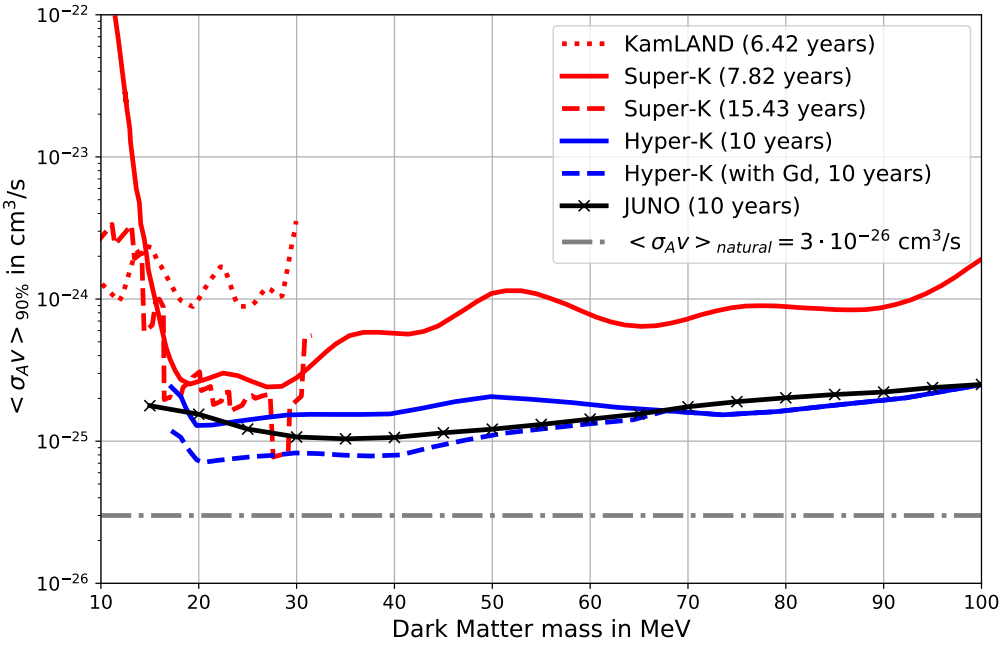

Figure 7.13.: 90 % probability upper limit on the DM self-annihilation cross section $\langle \sigma_A \, \mathrm{v} \rangle$ for the JUNO experiment compared to limits of KamLAND, Super-K and Hyper-K. $\langle \sigma_A \, \mathrm{v} \rangle_{90\%}$ for JUNO after a lifetime of 10 years is displayed in black and analyzed for DM masses from 15 MeV to 100 MeV with steps of 5 MeV. The 90 % upper limits of KamLAND (dotted) and Super-K (dashed and solid) discussed in section 2.4.2 are shown in red. The predicted 90 % upper limit of Hyper-K for a lifetime of 10 years of [121] is displayed as solid blue line. The upper limit of Hyper-K doped with gadolinium is shown as dashed blue line.

By comparing the upper limits on the DM self-annihilation cross section of the two liquid scintillator detectors, JUNO will improve the upper limit of KamLAND by a factor of 7 to 33 for DM masses between 15 MeV and 30 MeV. This is mainly due to the larger exposure of JUNO (147.7 kt yr exposure in JUNO, 4.5 kt yr exposure in KamLAND). It should be noted here that the DSNB is not considered in the determination of the upper limit of KamLAND in [74]. Therefore, the upper limit of KamLAND shown in figure 7.13 is slightly overestimated[7].

The 90 % upper limit of JUNO will be a factor of 2 to 9 better in the whole DM mass region from 15 MeV to 100 MeV than the upper limit of Super-K for data of 7.82 years, although the exposure of Super-K ($22.5\,\mathrm{kt} \cdot 7.82\,\mathrm{yr} = 176.0\,\mathrm{kt\,yr}$) is slightly larger than the exposure of JUNO (147.7 kt yr). Furthermore, JUNO will also improve the 90 % upper limit of Super-K after 15.43 years of data taking, which corresponds to an exposure of 347 kt yr, by a factor of 2 to 3.5, except of the DM mass region between 27.5 MeV and 29.2 MeV.
The main reason is that non-IBD backgrounds in the LS detector JUNO are reduced very effectively because of the IBD signal signature. In the water Cherenkov detector Super-K, the neutron capture signal of the IBD is below the detection threshold and cannot be measured. Moreover, muons with kinetic energies below 54 MeV produced by atmospheric neutrinos are invisible in Super-K. Therefore, Michel electrons/positrons from the decay of invisible muons cause the main background below energies of 50 MeV (details are given in section 2.4.2). In JUNO, this background can be suppressed to a negligible level, on the one hand due to the coincident measurement of prompt and delayed signal of the IBD and, on the other hand, because of the muon veto cut, which identifies such "invisible" muons. Another non-IBD background, the atmospheric NC background, can be reduced more effectively in JUNO because of the ability to measure the coincident prompt and delayed signal and the strict IBD selection criteria. Furthermore, non-IBD background events are reduced with the PSD cut in JUNO, which was not applied in the analysis of Super-K in [75] and [4]. So, backgrounds are reduced more efficiently in JUNO than in Super-K, which results in a better 90 % upper limit on the DM self-annihilation cross section. Another minor reason for the worse sensitivity of Super-K is the worse energy resolution compared to JUNO ($\sigma_E^{Super-K} = 14.2$ % at 10 MeV, $\sigma_E^{JUNO} = 0.9$ % at 10 MeV), since the peak-like signal spectra are smeared more.
For $27.5\,\mathrm{MeV} \leq m_{DM} \leq 29.2\,\mathrm{MeV}$, the 90 % upper limit of Super-K is better than the limit of JUNO determined within this thesis because of statistical uncertainties of the Super-K limit. The limit of Super-K of [4] is derived from the energy spectrum determined in [117] for neutrino energies between 11 MeV and 31 MeV. In [117], 29 events are observed in this energy region (in good agreement with the expectations of 33.7 ± 4.6 background events). Above energies of 25 MeV, the statistics of the energy spectrum is poor with 0 to 2 events per 1 MeV bin. Therefore, the statistical uncertainty of the upper limit on the DM self-annihilation cross section presented in [4] derived from this spectrum is large in this energy and DM mass range, respectively.

The sensitivity of JUNO to measure neutrinos from DM self-annihilation in the Milky Way will be comparable to the prospective sensitivity of Hyper-K. By only comparing the exposure of both detectors (1870 kt yr for Hyper-K to 147.7 kt yr for JUNO), the upper limit of Hyper-K might be expected to be significantly better than the limit of JUNO. However, due to the same reasons as discussed above for Super-K, backgrounds in JUNO can be reduced and suppressed better and more effectively than in Hyper-K, which com-

[7] All other assumptions, like e.g. $J_{avg} = 5$, are equal for the study of JUNO and KamLAND and the same background contributions are considered.

pensates the smaller exposure and yields similar sensitivities. Especially for DM masses below around 65 MeV, where the sensitivity of Hyper-K is reduced because of background events caused by invisible muons, JUNO provides the best sensitivity to measure neutrinos from DM self-annihilation in the Milky Way. As discussed in section 2.4.2, gadolinium could be added to the target volume in a second future phase of Hyper-K. This would reduce the background from invisible muons by around 70 % and increase the sensitivity of Hyper-K for $m_{DM} \leq 65$ MeV. However, it has not been decided yet, if gadolinium will be added to Hyper-K in the future, since it poses a significant technological challenge.

All in all, the JUNO experiment will improve the currently existing 90 % upper limits on the DM self-annihilation cross section for DM masses from 15 MeV to 100 MeV by a factor of around 2 to 9, except for DM masses between 27.5 MeV and 29.2 MeV. Moreover, JUNO's sensitivity will be comparable with the predicted sensitivity of Hyper-K and provide the best sensitivity to measure electron antineutrinos from DM self-annihilation in the Milky Way for DM masses below around 65 MeV among neutrino detectors built in the next few years. Furthermore, JUNO's potential to claim the discovery of an electron antineutrino signal from DM self-annihilation in the Milky Way as an exess over backgrounds will be between 3σ and 5σ for most DM masses from 15 MeV to 100 MeV.

7.4. Possible Improvements for Indirect Dark Matter Search with JUNO

To conclude the chapter about JUNO's sensitivity for indirect DM search, an outlook for possible further enhancement of JUNO's sensitivity is given. Potential changes and additional studies to improve the sensitivity further are given in the following.

7.4.1. Optimization of Detector Properties

Possible improvements according to changes of the detector's location, design and setup, respectively, are:

- The fiducial volume of JUNO, which is defined by $R < 16.0$ m corresponding to 14.77 kt, could be increased to $R < 16.5$ m ($R < 17.0$ m). This would increase the fiducial mass, and therefore the total exposure, of JUNO by around 10 % to 16.2 kt (by ~ 20 % to 17.7 kt). However, the background of fast neutrons would also be increased by a factor of about 2 (4.5). Moreover, total reflection at the acrylic sphere becomes more likely for $R > 16$ m and would affect the time-of-flight correction to determine the pulse shapes, which would slightly decrease the PSD performance. For $R > 16$ m, also non-linearity effects of the detector response increase. Nevertheless, an increase of the fiducial volume could slightly improve JUNO's sensitivity.
- The change of the location of the detector would enhance the sensitivity, but is not feasible for JUNO. A change of the location to a location at smaller latitude, e.g. to INO site at 10° N [186], would reduce the atmospheric neutrino flux and, therefore, the atmospheric CC and NC background (reduction by around 5 % at INO site). This would slightly improve the sensitivity, especially for $m_{DM} \gtrsim 50$ MeV, where the atmospheric CC background limits the sensitivity.

7.4.2. Additional Detection Channels and Background Reduction Methods

Additional analyses and studies that could be investigated to improve JUNO's sensitivity are:

- In addition to the IBD detection channel considered in this study, the interaction channel $\bar{\nu}_e + {}^{12}\mathrm{C} \rightarrow e^+ + n + {}^{11}\mathrm{B}$ could be investigated additionally, since it provides an IBD-like signal signature (as discussed in section 5.3.2). Considering the interaction cross section of $\bar{\nu}_e + {}^{12}\mathrm{C} \rightarrow e^+ + n + {}^{11}\mathrm{B}$ of [263] and the electron antineutrino flux from DM self-annihilation in the Milky Way of equation 4.1, the number of signal events in JUNO would be increased by less than 10 % for $m_{DM} \lesssim 60$ MeV and by 10 % to around 20 % for $60\,\mathrm{MeV} \leq m_{DM} \leq 100$ MeV. However, the visible energy spectra would be broader and shifted to lower visible energies compared to the IBD spectra due to the kinematics of the detection channel. The backgrounds in JUNO, except of the DSNB (the atmospheric $\bar{\nu}_e$ CC background on ${}^{12}\mathrm{C}$ is already considered), would not be affected. The DSNB would only be slightly increased for visible energies below around 15 MeV due to the kinematics of the interaction. Therefore, by considering $\bar{\nu}_e + {}^{12}\mathrm{C} \rightarrow e^+ + n + {}^{11}\mathrm{B}$ as second detection channel, JUNO's sensitivity could be improved by few percent, especially in the higher DM mass region.

- Other PSD methods, e.g. based on machine learning algorithms, could be applied to further improve the PSD performance of IBD events against atmospheric NC and fast neutron background events. This could increase JUNO's sensitivity by few percent, especially for $m_{DM} \lesssim 40$ MeV, where the atmospheric NC background dominates the visible energy spectrum. To estimate JUNO's sensitivity according to a further improved PSD performance, perfect PSD, i.e. $\epsilon_{PSD,IBD} = 100$ %, $\epsilon_{PSD,atmoNC} = 0$ % and $\epsilon_{PSD,FN} = 0$ %, is assumed. This would lead to a signal to background ratio of $S/\sqrt{S+B} = 4.450$ (compared to $S/\sqrt{S+B} = 4.281$ of the PSD cut applied in this study in chapter 6). So, the signal to background ratio would be increased by 4 %. This can be translated to an improvement of the upper limit on the DM self-annihilation cross section by approximately 4 % assuming perfect PSD.

- An additional suppression method, besides PSD, of the atmospheric NC background is to search for the coincidence of atmospheric NC events with the subsequent decay of corresponding residual isotopes [179]. Since some of the resulting final isotopes of IBD-like atmospheric NC events are not stable (e.g. ${}^{11}\mathrm{C}$, see figure 5.13 for the most-frequent channels), they could decay temporally delayed to the neutron capture. This would cause a triple coincidence signature in the detector of prompt signal, delayed signal from neutron capture and further delayed decay of the residual isotope [295]. This triple coincidence signature can be used to discriminate atmospheric NC events and IBD events. In [179], it was determined that atmospheric NC events of reaction $\nu_i + {}^{12}\mathrm{C} \rightarrow \nu_i + n + {}^{11}\mathrm{C}$ can be reduced by 77 % by applying a triple coincidence cut. This would reduce the total atmospheric NC background by 18 %. IBD events, signal and background, would be reduced by around 6 % [179]. The resulting signal to background ratio after the PSD cut of section 6.2 and the described triple coincidence cut would be reduced by 2.6 % to $S/\sqrt{S+B} = 4.169$ (compared to the signal to background ratio after PSD without applying the triple coincidence cut), since the signal inefficiency decreases the signal to background ratio. Therefore, a triple coincidence cut would not improve JUNO's sensitivity.

7.4.3. Directional Information in JUNO

In the sensitivity study presented so far, the whole Milky Way is considered as source for neutrinos from DM self-annihilation. In contrast to that, also only neutrinos originating from a specific region at the sky can be studied. The basic idea is to use the directional information of the incoming $\bar{\nu}_e$'s to determine signal events and reduce isotropic background events. This might lead to an increased signal to background ratio and could improve the

sensitivity.
Since the DM density increases towards the galactic center and, therefore, DM annihilation is more likely in a region around the galactic center, electron antineutrinos produced in DM self-annihilation in a region around the galactic center are studied here and the effect on the sensitivity by restricting the acceptance to a region around the galactic center is estimated. The study aims to evaluate JUNO's ability to benefit from the directional information and to improve its sensitivity compared to the sensitivity considering the whole Milky Way.
To roughly estimate JUNO's potential, the following assumptions are made[8]: The model of Moore represents the most cuspy model of the models introduced in section 4.1. Therefore, it is used to parameterize the DM density profile $\rho(r)$ of the Milky Way. Moreover, it is assumed that the direction of the positron produced in the IBD reaction can be reconstructed perfectly in JUNO resulting in a perfect angular resolution ($\sigma_\theta = 0°$) of the JUNO detector.
The $\bar{\nu}_e$ flux from DM self-annihilation (given in equation 4.1 for the entire Milky Way) can be expressed as function of the angle ψ between the galactic center and the direction of the incoming electron antineutrino by:

$$\frac{\mathrm{d}\phi_\nu^{DM}}{\mathrm{d}E_\nu} = \frac{\langle \sigma_A \, \mathrm{v} \rangle}{2\, m_{DM}^2} \, \frac{1}{3} \, \delta(E_\nu - m_{DM}) \, R_0 \, \rho_0^2 \, J_\psi \tag{7.13}$$

with the J-factor J_ψ depending on ψ:

$$J_\psi = \int_{\cos\psi}^{+1} J(\psi') \, \mathrm{d}(\cos\psi') = \frac{1}{2\, R_0 \, \rho_0^2} \int_{\cos\psi}^{+1} \int_0^{l_{max}} \rho^2(r) \, \mathrm{d}l \, \mathrm{d}(\cos\psi'). \tag{7.14}$$

$J(\psi)$ for the DM density profile model of Moore is shown in figure 7.14. More than 99 % of all neutrinos from DM self-annihilation are produced within an zenith angle of $\psi < 10°$ assuming the Moore profile model. The angular distribution of the incoming electron antineutrinos in JUNO is defined by $J(\psi)$ and their directions, i.e. the zenith angle ψ between galactic center and neutrino, are sampled from $J(\psi)$. Due to the cuspy Moore model and the resulting shape of $J(\psi)$ shown in figure 7.14, the $\bar{\nu}_e$ direction with respect to the galactic center is very well confined.

The direction of the incoming $\bar{\nu}_e$ in JUNO cannot be directly measured, but it is correlated to the direction of the positron produced in IBD interaction by the angle θ, which is defined as angle between $\bar{\nu}_e$ and e^+. This correlation is determined by the kinematics of the IBD reaction and given by the differential IBD interaction cross section $\mathrm{d}\sigma/\mathrm{d}\cos(\theta)$ of equation 4.6. The differential IBD interaction cross section depends on the neutrino energy $E_{\bar{\nu}_e}$ and is shown in figure 7.14 as function of θ exemplarily for $E_{\bar{\nu}_e} = 20$ MeV, 60 MeV and 100 MeV. The correlation between $\bar{\nu}_e$ and e^+ direction in IBD interactions and, therefore, the directional information about the incoming $\bar{\nu}_e$ strongly depends on the neutrino energy and increases for increasing energies as indicated in figure 7.14. Especially for $E_{\bar{\nu}_e} \lesssim 30$ MeV, the directional information is very poor.
The convolution of $J(\psi)$ and $\mathrm{d}\sigma(\theta, E_{\bar{\nu}_e})/\mathrm{d}\cos(\theta)$ results in a distribution $f(\eta, E_{\bar{\nu}_e})$, where η is defined as zenith angle of the positron direction with respect to the galactic center. The procedure to determine $f(\eta, E_{\bar{\nu}_e})$ is described in the following:
1,000 values of ψ are generated from $J(\psi)$ defined in equation 7.14 and shown in figure 7.14. For each value of ψ and for a set electron antineutrino energy, for example $E_{\bar{\nu}_e} = 15$ MeV,

[8] All assumptions made in this section are optimistic and will overestimate JUNO's sensitivity. So, this study yields the best possible sensitivity of JUNO considering neutrinos from DM annihilation in a region around the galactic center.

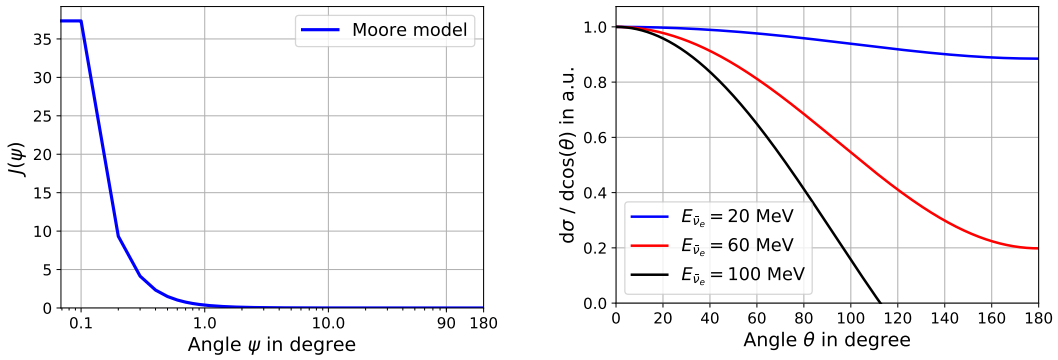

Figure 7.14.: Left: Galactic $J(\psi)$ as function of the angle ψ to the galactic center for the DM density profile model of Moore. For $\psi < 0.1°$, a flat core is assumed to avoid divergences by integrating $J(\psi)$. Right: Differential interaction cross section $\mathrm{d}\sigma/\mathrm{d}\cos(\theta)$ of IBD as function of the angle θ between positron and neutrino direction. The differential cross section is shown exemplarily for $E_{\bar{\nu}_e} = 20$ MeV, 60 MeV and 100 MeV. The cross sections are scaled to 1 for $\theta = 0°$ for better comparison.

10,000 values of θ are generated from $\mathrm{d}\sigma(\theta, E_{\bar{\nu}_e})/\mathrm{d}\cos(\theta)$ and 10,000 values of the azimuth angle φ are generated uniformly distributed between 0° and 360°. For each (θ, φ)-pair and angle ψ, the angle η is calculated resulting in a distribution $f(\eta, E_{\bar{\nu}_e})$ for the set electron antineutrino energy[9]. With $f(\eta, E_{\bar{\nu}_e})$, the survival efficiency $\epsilon_{S,dir}$ of signal events to a direction cut according to a maximal angle η_{max} is calculated:

$$\epsilon_{S,dir}(\eta_{max}, E_{\bar{\nu}_e}) = \frac{\int_0^{2\pi}\int_0^{\eta_{max}} f(\eta, E_{\bar{\nu}_e})\,\sin\eta\,\mathrm{d}\eta\,\mathrm{d}\varphi}{\int_0^{2\pi}\int_0^{\pi} f(\eta, E_{\bar{\nu}_e})\,\sin\eta\,\mathrm{d}\eta\,\mathrm{d}\varphi}. \tag{7.15}$$

This survival efficiency describes the ratio of number of IBD signal events with $\eta < \eta_{max}$ with respect to the direction to the galactic center to the total number of signal events. Averaged over the lifetime of JUNO, all background contributions in JUNO (DSNB and atmospheric CC and NC background) are isotropic. Therefore, the survival efficiency $\epsilon_{B,dir}$ of background events to a direction cut according to η_{max} is

$$\epsilon_{B,dir}(\eta_{max}) = \frac{\int_0^{2\pi}\int_0^{\eta_{max}} \sin\eta\,\mathrm{d}\eta\,\mathrm{d}\varphi}{\int_0^{2\pi}\int_0^{\pi} \sin\eta\,\mathrm{d}\eta\,\mathrm{d}\varphi} = \frac{1-\cos\eta_{max}}{2}. \tag{7.16}$$

The resulting number of signal and background events expected in JUNO after 10 years of data taking are defined as $N_S^{dir} = \epsilon_{S,dir}(\eta_{max}, E_{\bar{\nu}_e}) \cdot N_S^{PSD}(E_{\bar{\nu}_e})$ and $N_B^{dir} = \epsilon_{B,dir}(\eta_{max}) \cdot \left[N_{DSNB}^{fid,PSD} + N_{atmoCC,\bar{\nu}_e+p}^{PSD} + N_{atmoCC,\bar{\nu}_e+{}^{12}\mathrm{C}}^{PSD} + N_{atmoNC}^{PSD}\right]$ considering the number of signal and background events after the PSD cut presented in section 6.3. The survival efficiencies of signal and background events, respectively, are calculated for the set electron antineutrino energy and for different values of $\eta_{max} = 10°$, 30°, 50°, 70°, 90°, 100°, 110°, 120°, 130°, 150°.
The described procedure is performed for $m_{DM} = E_{\bar{\nu}_e} = 15, 20, ..., 100$ MeV. So, the survival efficiencies of signal and background events to a direction cut are calculated for a set of $E_{\bar{\nu}_e}$ and a set of η_{max}.

[9]Since ψ is well confined by $J(\psi)$ assuming the DM density profile model of Moore, η and the angular distribution $f(\eta, E_{\bar{\nu}_e})$ is mainly dominated by the distribution of θ and strongly depends on $E_{\bar{\nu}_e}$.

The best signal to background ratio of $S/\sqrt{S+B} = 5.372$ (averaged over DM masses from 15 MeV to 100 MeV) is achieved for $\eta_{max} = 120°$. Following the Bayesian analysis of section 7.1, the 90 % upper limit $\tilde{S}_{90}(m_{DM})$ on the number of signal events is calculated for the signal and background spectra after considering the direction cut with $\eta_{max} = 120°$ described above. The 90 % upper limit on the electron antineutrino flux is given by

$$\phi_{\bar{\nu}_e,90\%}(E_{\bar{\nu}_e}) = \frac{\tilde{S}_{90}(E_{\bar{\nu}_e})}{\sigma_{IBD}(E_{\bar{\nu}_e})\ N_p\ t\ \epsilon_{IBD}\ \epsilon_{\mu\,veto}\ \epsilon_{PSD,IBD}(E_{\bar{\nu}_e})\ \epsilon_{S,dir}(E_{\bar{\nu}_e})} \tag{7.17}$$

similar to equation 7.10. Following equation 7.13, the resulting 90 % probability upper limit on the DM self-annihilation cross section $\langle \sigma_A \, \mathrm{v} \rangle$ for JUNO is

$$\langle \sigma_A \, \mathrm{v} \rangle_{90\%} (m_{DM}) = \phi_{\bar{\nu}_e,90\%}(E_{\bar{\nu}_e})\ \frac{6 \cdot m_{DM}^2}{\delta(E_{\bar{\nu}_e} - m_{DM})\ R_0\ \rho_0^2\ J_\psi}. \tag{7.18}$$

In figure 7.15, the 90 % upper limit on the DM self-annihilation cross section for JUNO after a lifetime of 10 years and taking into account the directional information of the electron antineutrino signal is shown for $\eta_{max} = 120°$. $\langle \sigma_A \, \mathrm{v} \rangle_{90\%}$ considering DM annihilation in the whole Milky Way ($\eta_{max} = 180°$ and $J_{avg}^{Moore} = 8$, see figure 7.7) is shown for comparison. The same analysis as described above was also performed assuming $\eta_{max} = 30°$ and $\eta_{max} = 90°$. The resulting upper limit on $\langle \sigma_A \, \mathrm{v} \rangle$ for $\eta_{max} = 90°$ is also shown in figure 7.15.

The best 90 % upper limit on the DM self-annihilation cross section taking into account the directionality of the neutrino signal is achieved for $\eta_{max} = 120°$ for DM masses from 15 MeV to 90 MeV. For $\eta_{max} = 90°$, where the hemisphere with respect to the galactic center is considered as region of interest, the sensitivity is slightly decreased by around 15 % compared to the sensitivity for $\eta_{max} = 120°$ (except for $m_{DM} > 90$ MeV, where a direction cut with $\eta_{max} = 90°$ yields the best sensitivity). For angles of $\eta_{max} \lesssim 60°$, the sensitivity of JUNO decreases significantly (e.g. by a factor of 5 comparing the sensitivities for $\eta_{max} = 30°$ and $\eta_{max} = 120°$), since directional information of $\mathrm{d}\sigma/\mathrm{d}\cos\theta$ and therefore of $f(\eta)$ is poor. So, too many signal events are cut away for $\eta_{max} \lesssim 60°$, which strongly reduces the signal to background ratio $S/\sqrt{S+B}$ compared to larger angles of η_{max}.

However, considering the whole Milky Way as potential source for neutrinos from DM self-annihilation yields the most stringent limit on the DM self-annihilation cross section for $m_{DM} = E_{\bar{\nu}_e} \leq 65$ MeV (see figure 7.15). In this energy region, the directional information about incoming neutrinos is poor due to the kinematics of the IBD reaction shown in figure 7.14 and JUNO's sensitivity cannot be improved by using the directionality. In contrast to that, the directional information about the neutrino signal could be used to improve JUNO's sensitivity for $m_{DM} = E_{\bar{\nu}_e} > 65$ MeV. As shown in figure 7.15, $\langle \sigma_A \, \mathrm{v} \rangle_{90\%}$ could be improve by around 10 % compared to the upper limit considering the whole Milky Way. So, JUNO could benefit from the directional information for these higher energies and DM masses, respectively.

Nevertheless, the reconstruction of the positron direction in JUNO is assumed to be perfect for the presented study (i.e. $\theta_{reco} = \theta_{real}$ and $\varphi_{reco} = \varphi_{real}$). In reality, the angular resolution of JUNO for positron events with 10 MeV $\leq E_e \leq$ 100 MeV is up to around 80° (at 1σ) [296]. So, the sensitivity of JUNO presented in this section would be decreased considering the angular resolution. Moreover, the sensitivity would be decreased, if the NFW or Kravtsov model of the galactic DM density profile is assumed, since the angular distribution $J(\psi)$ for these models is broader than for the Moore model.

The limitation of JUNO to use the directional information of the neutrino signal is dominated by the angular distribution of the IBD. So far, only the direction of the positron is

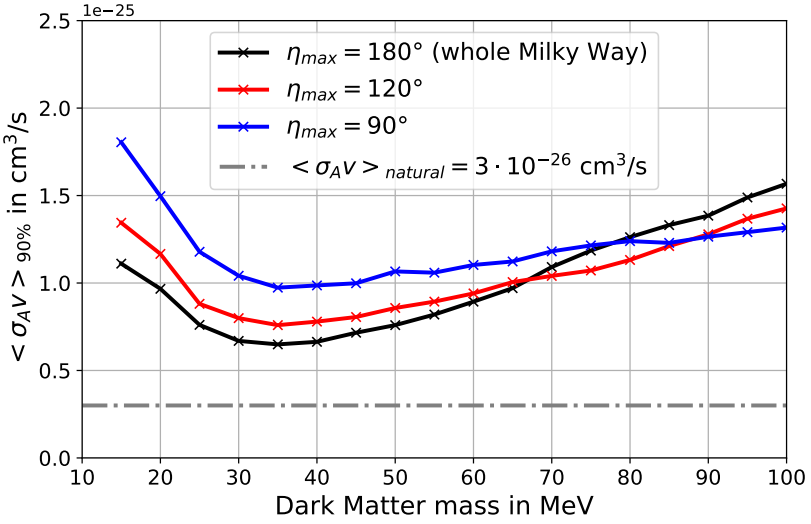

Figure 7.15.: 90 % probability upper limit on the DM self-annihilation cross section $\langle \sigma_A \, \mathrm{v} \rangle$ for the JUNO experiment including a cut on the direction of the antineutrinos for $\eta_{max} = 90°$ (blue) and $\eta_{max} = 120°$ (red), respectively. For comparison, the limit considering annihilation in the whole Milky Way (i.e. $\eta_{max} = 180°$ and $J_{avg}^{Moore} = 8$) of figure 7.7 is shown in black. All limits are determined assuming the DM density profile of Moore.

utilized to get information about the direction of the incoming neutrino. In [297, 298], the angular distribution between the $\bar{\nu}_e$ direction and the vector $\vec{X}_{e^+,n} = \vec{X}_{e^+} - \vec{X}_n$ between the position of the positron's energy deposition and the neutron capture is studied for reactor electron antineutrinos with $E_{\bar{\nu}_e} \lesssim 12$ MeV. The resulting angular distribution is shown in figure 7.16. Compared to the angular distribution of the IBD given by $\mathrm{d}\sigma/\mathrm{d}\cos(\theta)$ for a comparable energy $E_{\bar{\nu}_e} = 15$ MeV, the angle between neutrino and $\vec{X}_{e^+,n}$ is more confined. Using this approach and the angular distribution of [297, 298], the 90 % upper limit on the DM self-annihilation cross section in JUNO for $m_{DM} = 15$ MeV assuming $\eta_{max} = 90°$ and $\eta_{max} = 120°$ is calculated similar to the description above[10]. The results are displayed in figure 7.16 for $\eta_{max} = 90°$, $\eta_{max} = 120°$ and assuming the whole Milky Way ($\eta_{max} = 180°$). For $\eta_{max} = 120°$ ($\eta_{max} = 90°$), the upper limit on the DM self-annihilation cross section is improved by around 3 % (6 %) using the approach of [298] compared to limits shown in figure 7.15, since the angular distribution between neutrino direction and $\vec{X}_{e^+,n}$ is more confined. Therefore, JUNO's sensitivity for $m_{DM} = 15$ MeV could be slightly improved by using the approach of [298].

[10] A reasonable comparison of the two approaches is only valid for $m_{DM} = E_{\bar{\nu}_e} = 15$ MeV, since the approach of [298] was only investigated for $E_{\bar{\nu}_e} \lesssim 12$ MeV.

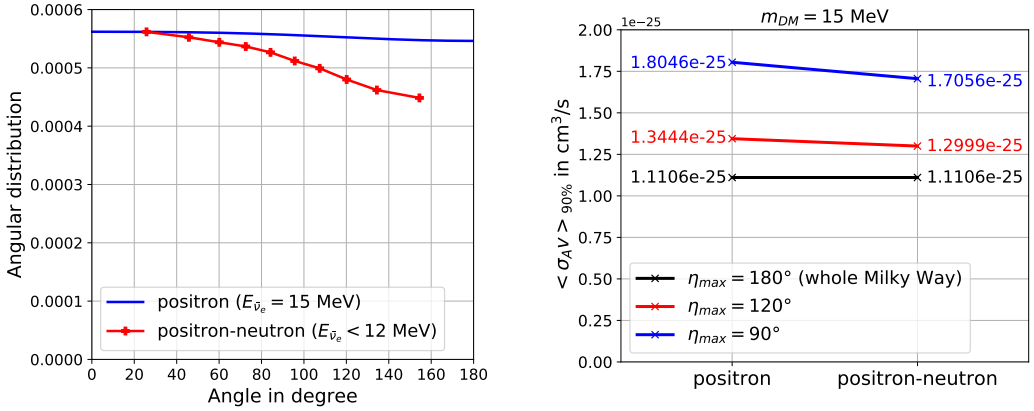

Figure 7.16.: Left: Angular distributions of the IBD as function of the angle between incoming neutrino and positron and of the angle between incoming neutrino and vector $\vec{X}_{e^+,n}$. The angular distribution of the angle between neutrino and vector $\vec{X}_{e^+,n}$ between positron and neutron of [298] is labeled as "positron-neutron" and shown in red. The angular distribution of the angle between neutrino and positron given by the differential interaction cross section of equation 4.6 is labeled as "positron" and shown in blue for $E_{\bar{\nu}_e} = 15$ MeV. Right: 90 % upper limit on the DM self-annihilation cross section of the two described approaches (again labeled as "positron" and "positron-neutron") for $\eta_{max} = 90°$, $\eta_{max} = 120°$ and $\eta_{max} = 180°$ (i.e. the whole Milky Way) and assuming $m_{DM} = 15$ MeV.

8. Indirect Dark Matter Search with THEIA

The general approach for the design of neutrino detectors, which house a light-producing target in a large-scale photon detector, has achieved exceptional success in the field of neutrino physics [299]. Up to now, mainly two detector concepts characterized by their target materials provide the best ability to detect neutrinos and measure their properties: water Cherenkov detectors and liquid scintillator detectors.
Large water Cherenkov detectors such as Super-Kamiokande and the proposed Hyper-Kamiokande experiment benefit from the long attenuation length and relatively low cost of ultra-pure water, which allows to realize large-scale detection volumes. Moreover, water Cherenkov detectors provide a good directional resolution and particle identification power by measuring the emitted Cherenkov light. Disadvantages of water Cherenkov detectors are the low photon light yields, which result in a worse energy resolution, and the inability to detect particles with energies below a comparably high threshold ($E_{th.} \approx 4.5$ MeV for Super-K, for details see section 2.4.2). Therefore, for example, neutron capture on hydrogen releasing $E_\gamma = 2.2$ MeV cannot be tagged, which reduces the IBD detection efficiency and prevents the suppression of invisible muons as background for indirect DM or DSNB searches [6].
In contrast to that, liquid scintillator detectors such as KamLAND, Borexino, SNO+ and JUNO have low energy thresholds, which allows the detection of neutron capture on hydrogen, and provide very good energy resolutions due to the large light yield of the scintillator. Moreover, pulse shape discrimination can be used to reduce background events (see chapter 6). Disadvantages compared to water Cherenkov detectors are the poor directional information due to nearly isotropic light emission and the limitation of the detector size because of light attenuation (for details see section 2.4.2 and chapter 3). The use of organic liquid scintillators also introduces issues of cost and undesirable environmental and safety problems [6].

The development of new technologies, especially in the area of novel scintillating liquids, opens up the possibility to combine different features of water Cherenkov and liquid scintillator detectors into a new kind of large-scale neutrino detectors, the so-called *water-based liquid scintillator detectors* [6, 300].
By introducing a small amount, typically 1 % to 10 %, of liquid scintillator into water[1], the light yield can be adjusted and increased compared to water Cherenkov detectors to improve the energy resolution and to allow the detection of particles below Cherenkov

[1] For details about the chemistry of WbLS and the technology to produce WbLS, see [300].

threshold, while not sacrificing directional resolution [6]. The cost of such water-based liquid scintillators is still relatively low and environmental and safety problems can be significantly reduced compared to pure liquid scintillators, since only a small amount of LS is added to the water volume.
Furthermore, the properties of water-based liquid scintillators (WbLS) together with the development of new advanced photodetection and reconstruction capabilities enable the possibility to discriminate between scintillation and Cherenkov photons [114] based on three approaches:

- The emission of Cherenkov light is faster than the excitation and de-excitation of LS molecules responsible for the scintillation light emission [6]. Therefore, fast light sensors that are able to resolve this temporal difference permit the identification of Cherenkov photons arriving nanoseconds before the scintillation photons [301]. This can be realized by fast, high QE PMTs [302] and additionally be improved by using Large Area Picosecond Photo-Detectors (LAPPDs), which are newly developed 20 cm x 20 cm imaging photosensors with single photo-electron time resolution below 100 picoseconds and sub-cm spatial resolution (for details about LAPPDs see [303, 304]).
- Scintillation light is emitted in a narrow wavelength band in the near-UV region (typically between ≈ 350 nm and ≈ 500 nm), whereas the Cherenkov photon emission spectrum spans a broad wavelength region [305]. Wavelength-sensitive photosensors, e.g. dichroic filters or dichroicons [306], could distinguish scintillation photons from the blue-green lower end of the Cherenkov spectrum and discriminate these two types [307].
- The characteristic angular dependency of Cherenkov light emission causes a ring-shaped pattern on top of the isotropic scintillation light emission [301]. Advanced reconstruction techniques aim to resolve these underlying patterns to discriminate Cherenkov from scintillation photons. Two complementary approaches to reconstruction in WbLS detectors are a likelihood ansatz like e.g. developed in Super-K and a three-dimensional topological reconstruction, which is e.g. implemented in JUNO (for details see [6, 308, 309]).

The ability to discriminate scintillation and Cherenkov light allows to reconstruct the direction of the particle and to distinguish between e-like and μ-like particles by measuring its Cherenkov ring pattern. Moreover, the ratio between Cherenkov and scintillation light of an event represents a unique parameter to separate different event types.

All new technologies introduced above, i.e. a water-based liquid scintillator target, fast, high QE and wavelength-sensitive photo-sensors and new advanced reconstruction techniques, could be realized in the proposed THEIA detector (for detailed information about THEIA see [6]).

This chapter aims to study THEIA's sensitivity for neutrinos from dark matter self-annihilation and extends the indirect DM search with neutrinos to the newly developed water-based liquid scintillator detectors. Section 8.1 introduces the general detector concept of THEIA and the proposed detector configuration used to predict THEIA's sensitivity for the indirect DM search within this thesis. The expected neutrino signal from DM self-annihilation in THEIA is presented in section 8.2, followed by the description and determination of background sources in THEIA in section 8.3. Techniques to reduce background events in THEIA are presented in section 8.4. Finally, THEIA's sensitivity to measure neutrinos from DM annihilation as an excess over backgrounds is elaborated in section 8.5.

8.1. The THEIA Detector

THEIA would be the first large-volume WbLS detector that has been suggested as part of the Advanced Scintillator Detection Concept [299]. The proposed detector would combine a large WbLS target volume with fast, high QE PMTs, newly developed LAPPDs and dichromatic photosensors and could separate between Cherenkov and scintillation light at a certain level as described above. Two distinct detector configurations are proposed in [6]: THEIA25 and THEIA100. THEIA25 would contain 25 kt WbLS as target and could potentially be located at SURF at a depth of 1,490 m. The large scale follow-up detector of THEIA25 might be realized in THEIA100 with 100 kt WbLS target volume. Both detector configurations would house WbLSs with 1 % to 10 % LAB-based LS and ultra-pure water. Due to the novel detector technologies, the large size and location deep underground, THEIA25 and THEIA100 could cover a broad neutrino physics and astrophysics program that will be shortly listed here (for an exhaustive description see [6]):

- Long baseline neutrino program with high sensitivity to measure neutrino oscillation parameters, neutrino mass ordering and CP violation by operating in an on-axis beam;
- atmospheric neutrino measurements;
- search for nucleon decay, especially for $p \rightarrow K^+ + \bar{\nu}$ and $N \rightarrow 3\nu$;
- solar neutrinos: detection of CNO neutrinos as well as providing high statistics and low threshold ($\sim$ 3 MeV) measurements of the shape of ^{8}B solar neutrinos;
- geo-neutrinos from the Earth's crust and mantle;
- supernova neutrinos;
- world-leading sensitivity to detect the DSNB $\bar{\nu}_e$-flux [301];
- search for neutrino-less double beta decay in future phases.

Since THEIA is just in its early design stages[2], the exact specifications of the detector including the concrete geometry, the mixture of the WbLS and the different used photosensors are not finally decided. Therefore, one potential detector configuration of THEIA based on reliable and validated measurements is used for the study within this thesis to predict THEIA's detector response and described in the following.

Detector Configuration of THEIA25

The determination of THEIA's sensitivity is based on the detector configuration of THEIA25. The detector simulation is realized with the RAT-PAC simulation and analysis tool [315] built with Geant4 [219], ROOT [119] and C++. Within the RAT-PAC framework, MC simulations of the THEIA25 detector including its geometry, characteristics of WbLS target and properties of the used photosensors as well as its response to particles interacting in the target volume are performed.
For the simulation, THEIA25 is assumed as right cylindrical volume with height and diameter of 31.8 m containing 25 kt WbLS. The total target volume of 25 kt is defined by the volume enclosed by the photosensors and no veto or buffer volume is considered.
To provide an assumed photocathode coverage of 25 %, the detector is equipped with

[2]There is an active R&D effort for all technologies used in THEIA, for example WbLS development at BNL [310], characterization and optimization with the CheSS detector at UC Berkeley and LBNL [311], fast photon sensor development [303] and development of reconstruction algorithms [6]. There is also a strong connection with other, already existing, experiments like ANNIE [312], SNO+ [313] and WATCHMAN [314].

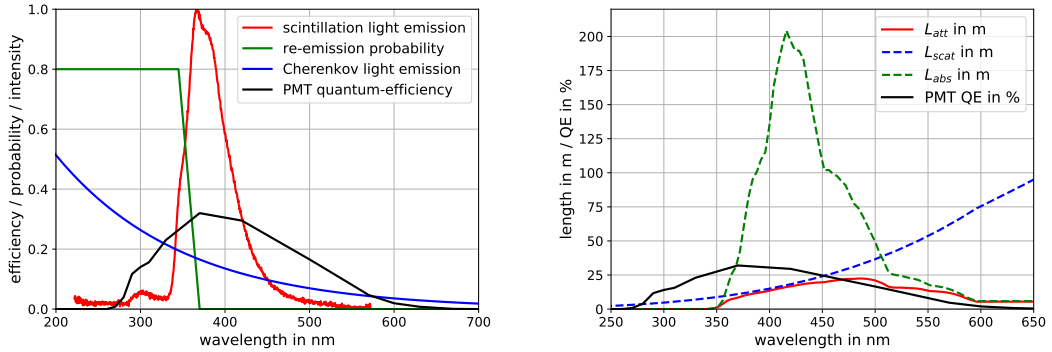

Figure 8.1.: Properties of the 3 % WbLS model implemented into the RAT-PAC simulation for THEIA25. Left: Scintillation and Cherenkov light emission spectra in red and blue, respectively, with the re-emission probability in green as function of the photon wavelength. The quantum efficiency of the implemented Hamamatsu R11780 HQE PMTs is shown in black. Right: Rayleigh scattering length L_{scat} and absorption length L_{abs} as dashed blue and dashed green line, respectively. The resulting attenuation length L_{att} defined as $L_{att}^{-1} = L_{scat}^{-1} + L_{abs}^{-1}$ is displayed in red. The QE of the implemented PMTs is shown in black.

19,773 12-inch Hamamatsu R11780 HQE PMTs characterized in [302]. These fast and high QE PMTs reach a maximum QE of 32 % at a wavelength of $\lambda = 370$ nm (see figure 8.1) and have TTS of 1.29 ± 0.14 ns defined as σ of the transit time distribution. Moreover, the single p.e. spectrum measured in [302] is implemented into the simulation to consider the charge response of the PMTs. In this detector configuration of THEIA25, no LAPPDs and no wavelength-sensitive photosensors are implemented.

The WbLS model used in the simulation consists of 3 % liquid scintillator (LAB + PPO) and 97 % ultra-pure water, which is a much studied mixture validated by measurements (see [316]) and results in an expected scintillation photon light yield of $LY_{scin.} \approx 500$ photons per MeV [3]. Scintillation light generation, photon absorption and re-emission of the LS is implemented based on [316] and [317]. Cherenkov light production is integrated by the G4Cerenkov class of Geant4. The scintillation and Cherenkov emission spectra as well as the re-emission probability implemented into the simulation are displayed in figure 8.1. Most of the emitted short-wavelength ($\lambda \lesssim 340$ nm) Cherenkov light is absorbed and re-emitted by the LS as figure 8.1 illustrates.
The time profile of scintillation light emission is parametrized by equation 3.14 similar to JUNO, but with one set of time constants and corresponding weights for all particles [316] ($\tau_1 = 2.005$ ns, $\omega_1 = 98.7$ %, $\tau_2 = 12.5$ ns, $\omega_2 = 1.2$ %, $\tau_3 = 127.66$ ns, $\omega_3 = 0.1$ %), since no validated measurements of time profiles of different particles in WbLS exist up to now. This is also the case for quenching effects in WbLS targets. Therefore, values of the Birks constants of pure LAB are assumed.
The absorption length is determined by a combination of the absorption length of LAB + PPO measured at BNL and of the absorption length of water of [318, 319]. Moreover, Rayleigh scattering of 3 % WbLS is implemented based on internal THEIA collaboration communication with BNL. The absorption length and Rayleigh scattering length, together with the resulting attenuation length is shown in figure 8.1.

[3] WbLS with LS fraction less than 3 % provide a lower light yield and are more suitable for high energy neutrino measurements [6]

8.2. Antineutrino Signal from Galactic Dark Matter Annihilation in THEIA

To determine THEIA's sensitivity for neutrinos from DM self-annihilation in the DM halo of the Milky Way, the same assumptions are made as presented in chapter 4. Therefore, electron antineutrinos from direct DM self-annihilation, $DM + DM \rightarrow \nu + \bar{\nu}$, of light DM particles with masses from 10 MeV to 100 MeV detected via the inverse β decay are studied within this section.
The expected monoenergetic electron antineutrino energy spectrum measured via IBD in the described THEIA25 detector configuration is based on equation 4.3 using the $\bar{\nu}_e$ flux at Earth of equation 4.1 with the same assumptions as in section 4.1:

$$\frac{\mathrm{d}N_S(E_{\bar{\nu}_e})}{\mathrm{d}E_{\bar{\nu}_e}} = \sigma_{IBD}(E_{\bar{\nu}_e}) \frac{\mathrm{d}\phi^{DM}_{\bar{\nu}_e}(E_{\bar{\nu}_e})}{\mathrm{d}E_{\bar{\nu}_e}} \, N_{target} \, t \, \epsilon_{IBD} \, \epsilon_{\mu\,veto} \, \epsilon_{e-like}. \tag{8.1}$$

The IBD interaction cross section σ_{IBD} is given in equation 4.4. The number of target protons N_{target} per kt of a WbLS with 3 % LAB-based LS is $N_{target}/M = 6.7 \cdot 10^{31}\,\mathrm{kt}^{-1}$ resulting in $N_{target} = 1.68 \cdot 10^{33}$ free protons for the 25 kt target mass of THEIA25. A total exposure time of $t = 10$ years is assumed. The efficiency due to the application of the muon veto is $\epsilon_{\mu\,veto} = 99.0$ % (for details see section 8.3.5) and the efficiency of the discrimination between e-like and μ-like events is $\epsilon_{e-like} = 99.4$ %, which is discussed explicitly in section 8.3.3. The total IBD detection efficiency of THEIA25 is $\epsilon_{IBD} = 69.7$ % determined by simulations with the introduced RAT-PAC simulation framework. These parameters are always used in this chapter, if not stated otherwise.

In the following, the simulation, analysis and IBD selection cuts to determine the IBD detection efficiency ϵ_{IBD} of THEIA25 are presented. THEIA25's detector response for 20,000 IBD events is simulated with the RAT-PAC simulation framework. The electron antineutrino energy is sampled from a uniform distribution from 10 MeV to 100 MeV and the kinetic energies of positron and neutron are calculated according to equations 4.5, 4.6 and 4.7 similar to section 4.3.
The light yield of the THEIA25 detector configuration with a 3 % WbLS target is elaborated from the simulation data[4]. The total light yield defined by the total measured charge Q by the PMTs in p.e. per MeV for the THEIA25 detector is $LY = 74$ p.e./MeV. The light yield LY sets the energy resolution of THEIA25 to $\sigma_E/E = 1/\sqrt{LY \cdot E} \approx 11.6\,\%/\sqrt{E[\mathrm{MeV}]}$ and, moreover, allows to convert the total measured charge in p.e. into visible energy in MeV with $E_{vis} = {}^1/_{LY} \cdot Q$ due to the linear correlation between charge and visible energy. The individual light yields of IBD events for scintillation, Cherenkov and re-emission light are $LY_{scin} = 41$ p.e./MeV, $LY_{Cheren} = 9$ p.e./MeV and $LY_{reem} = 24$ p.e./MeV, respectively. Cherenkov light measured at the PMTs is strongly reduced compared to initially produced Cherenkov photons, since most short-wavelength Cherenkov photons are absorbed and re-emitted by the LS as indicated in figure 8.1.
The MC truth data of the detector simulation is analyzed based on the IBD selection criteria listed in table 8.1. These cut parameters lead to the best signal to background ratio $N_S/\sqrt{N_S + N_B}$. The distributions of the simulation data as well as the IBD selection cut acceptance windows of table 8.1 are shown in section C.1 of the appendix. The volume cut on the prompt signal position, the energy cut on the prompt signal and the total delayed cut (containing a time difference cut, multiplicity cut, delayed energy cut, distance cut and volume cut on the delayed signal position) are applied independently on all 20,000

[4]The expected scintillation photon light yield of around 500 produced scintillation photons per MeV of section 8.1 agrees well the scintillation light yield of 530 photons per MeV given from the simulation data.

Table 8.1.: Selection criteria and cut parameters for IBD events, together with the resulting cut efficiencies ϵ and the total IBD detection efficiency ϵ_{IBD} of THEIA25. The cut efficiencies are determined by the analysis of IBD events simulated with the RAT-PAC simulation framework for THEIA25. The consecutively applied cuts of the delayed cut are listed from (a) to (e) and their efficiencies are labeled as ϵ_j. The number of events N_{before} the cut is applied to, the number of events N_{after} that pass the applied cut and the statistical errors $\Delta\epsilon$ and $\Delta\epsilon_j$ of each cut efficiency are also shown.

selection criteria and cut parameters	N_{before}	N_{after}	$\epsilon \pm \Delta\epsilon$ in %	$\epsilon_j \pm \Delta\epsilon_j$ in %
Volume cut on prompt signal: $\rho_{prompt} < 14.4$ m, $\lvert z_{prompt}\rvert < 14.4$ m	20,000	14,904	74.5 ± 0.8	
Energy cut on prompt signal: 740 p.e. $\leq Q_{prompt} \leq 7400$ p.e.	20,000	19,408	97.0 ± 1.0	
Total delayed cut:	20,000	19,028	95.1 ± 1.0	
(a) Time difference cut: 1.0 µs $\leq \Delta t \leq 1.0$ ms	20,000	19,463		97.3 ± 1.0
(b) Multiplicity cut: $N_{mult} = 1$	19,463	19,439		99.9 ± 1.0
(c) Energy cut on del. signal: 1.7 MeV $\leq E_{del} \leq 2.8$ MeV	19,439	19,377		99.7 ± 1.0
(d) Distance cut: $d < 1.0$ m	19,377	19,297		99.6 ± 1.0
(e) Volume cut on del. signal: $\rho_{del} < 15.9$ m, $\lvert z_{del}\rvert < 15.9$ m	19,297	19,028		98.6 ± 1.0
Total IBD detection efficiency	**20,000**	**13,948**	$\mathbf{69.7 \pm 0.8}$	

simulated events similar to section 4.3.
The reconstructed position of the prompt signal is defined by the initial position of the event from MC truth data smeared with the expected vertex resolution for THEIA25. In [305], the vertex resolution of THEIA-like detectors with different target masses, LS fractions, PMT coverages and TTS are investigated. The most conservative result of [305] is a vertex resolution of $\sigma_{vertex} = \sqrt{\sigma_x^2 + \sigma_y^2 + \sigma_z^2} \approx 17.5$ cm, which is assumed for the THEIA25 detector considered here. The volume cut on the position of the prompt signal is $\rho_{prompt} = \sqrt{x_{smeared}^2 + y_{smeared}^2} < 14.4$ m and $|z_{prompt}| < 14.4$ m and reduces the fiducial volume of THEIA25 to 18.7 kt. This corresponds to an outer layer between PMT surface and fiducial volume of 1.5 m width that is rejected and reduces surface backgrounds, border effects and the background imposed by fast neutrons (see section 8.3.5).
For the energy cut on the prompt signal, the registered charge of all PMTs in the prompt time window between 0 ns and 1.0 µs is summed up. This represents the total measured charge Q_{prompt} of the prompt signal, which can be converted into a visible energy of the prompt signal by considering the light yield of THEIA25 of $LY = 74$ p.e./MeV as discussed above. The accepted prompt energy region is set from 10 MeV to 100 MeV, which corresponds to a charge region between 740 p.e. and 7400 p.e..
The total delayed cut describes the consecutive application of the time difference, multiplicity, delayed energy, distance and delayed volume cut. The time Δt between prompt and delayed signal is defined by the neutron capture time of the MC truth data and only events with 1.0 µs $\leq \Delta t \leq$ 1.0 ms pass the time difference cut. The number of delayed signals within this time window represents the multiplicity of the event and, since only one delayed signal is expected for IBD events, a multiplicity cut of $N_{mult} = 1$ is set. The energy of the delayed signal is given by the energy emitted in the neutron capture process smeared with THEIA25's energy resolution of 11.6 % at 1 MeV. Only delayed signals with energies between 1.7 MeV and 2.8 MeV, i.e. neutrons being captured on hydrogen, pass the cut. Due to the spatial correlation of IBD events, the distance between reconstructed position of the prompt signal and reconstructed position of the delayed signal must be smaller than 1.0 m. The reconstructed position of the delayed signal is given by the position of neutron capture from MC truth data smeared with the vertex resolution of THEIA25 introduced above. To pass the volume cut on the delayed signal, the reconstructed position of the delayed signal needs to lie inside the total detector volume specified by $\rho_{del} =< 15.9$ m and $|z_{del}| < 15.9$ m.
These IBD selection criteria are applied to all 20,000 simulated IBD events and result in individual cut efficiencies defined as $\epsilon = N_{after}/N_{before}$. N_{before} represents the number of events the cut is applied to, while N_{after} are the number of events that pass the applied cut. The efficiencies of each single cut with their statistical errors are compiled in table 8.1. The volume cut on the prompt signal reduces the detection efficiency the most due to the strict cut criterion, which is set to decrease fast neutron and external background events (see section 8.3.5). The efficiency of the total delayed cut of $\epsilon_{del} = (95.1 \pm 1.0)$ % is very high despite the stringent selection cuts and only significantly reduced by the time difference cut. The cuts on the multiplicity, delayed energy and distance between prompt and delayed signal all provide survival efficiencies close to 100 %. The total IBD detection efficiency[5] in THEIA25 is determined to $\epsilon_{IBD} = (69.7 \pm 0.8)$ % and used to calculate the neutrino energy spectrum of equation 8.1.

The visible energy spectrum of electron antineutrinos from DM self-annihilation in the Milky Way expected in THEIA25 is calculated with equation 8.1 considering the IBD kinematics of equation 4.5 and the energy resolution of THEIA25 following the same

[5]The determined IBD detection efficiency in THEIA25 doesn't depend on the visible energy of the prompt signal. Therefore, an energy-independent IBD detection efficiency is used in this study.

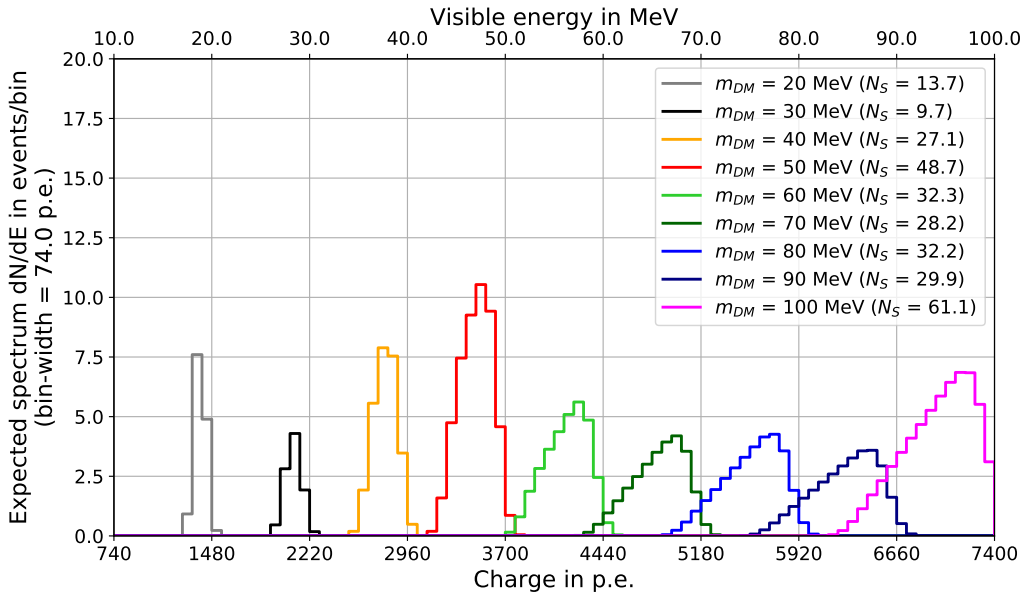

Figure 8.2.: Visible energy spectra $^{dN_S}/_{dE_{vis}}$ of electron antineutrinos produced by DM self-annihilation in the Milky Way and detected via IBD reactions in THEIA25. As example, DM masses of 20 MeV, 30 MeV, 40 MeV, 50 MeV, 60 MeV, 70 MeV, 80 MeV, 90 MeV and 100 MeV are assumed. All spectra are calculated for a total exposure time of 10 years considering an efficiency due to the application of the muon veto of $\epsilon_{\mu\,veto} = 99.0$ %, a discrimination efficiency between e-like and μ-like events of $\epsilon_{e-like} = 99.4$ % and a total IBD detection efficiency of $\epsilon_{IBD} = 69.7$ %. Moreover, an angular-averaged J-factor of $J_{avg} = 5.0$ and the currently most stringent 90 % C.L. upper limits of the annihilation cross section from Super-K [4, 75] for each DM mass are assumed. Furthermore, the expected number of signal events N_S for each assumed DM mass is displayed.

procedure as introduced in section 4.4 [6]. In figure 8.2, the resulting visible energy spectra as well as the expected number of signal events N_S in THEIA25 after a lifetime of 10 years and for a fiducial mass of 18.7 kt are shown exemplarily for different assumed DM masses. The number of signal events ranging from $N_S(m_{DM} = 30\,\text{MeV}) = 9.7$ to $N_S(m_{DM} = 100\,\text{MeV}) = 61.1$ considering the currently most stringent 90 % C.L. upper limits of the annihilation cross section from Super-K. Therefore, these numbers of signal events represent the largest event numbers expected in THEIA25 that are still allowed within the latest constraints discussed in section 2.4.2.

Compared to JUNO, the number of signal events expected in THEIA25 is increased by around 20 %. The main reason is the larger number of free protons in the fiducial volume of THEIA25 due to the larger fiducial mass of 18.7 kt compared to the fiducial mass of JUNO of 14.77 kt. This increases the number of signal events by around 17 %. The slightly larger efficiencies of THEIA25 according to the IBD detection, application of the muon veto and discrimination between e-like and μ-like events account for the remaining 3 % increase.
The shapes of the signal spectra in THEIA25 for $m_{DM} \lesssim 30$ MeV are broader than in JUNO because of the worse energy resolution of THEIA25 (the FWHM of these spectra are increased up to around 30 % compared to JUNO). Nevertheless, this effect becomes negligible for larger DM masses, where the widths of the spectra are dominated by the IBD kinematics.

[6] As expected, the FWHM of a signal spectrum is broadened by the energy resolution by $\sigma_E = 11.6\,\% \cdot \sqrt{E_{vis}[\text{MeV}]}$ compared to the spectrum, where only IBD kinematics are considered.

8.3. Background Sources in THEIA

The maximal expected number of signal events in THEIA25 determined in section 8.2 are around 1 to 6 events per year depending on the DM mass. Therefore, THEIA's sensitivity to measure these electron antineutrino signal events as an excess over backgrounds strongly depends on the knowledge, precise prediction and reduction of all background events occurring in the region of interest between neutrino energies of 10 MeV and 100 MeV.
This section covers the determination of all potential background sources for the indirect DM search with THEIA, which can be separated into indistinguishable IBD backgrounds, like the reactor neutrino background (see section 8.3.1), the DSNB (see section 8.3.2) and atmospheric $\bar{\nu}_e$'s interacting via CC on free protons (see section 8.3.3), and into IBD-like backgrounds, such as atmospheric neutrino CC interactions on ^{12}C and ^{16}O (see section 8.3.3), atmospheric NC background events (see section 8.3.4) and muon-induced backgrounds (see section 8.3.5).

8.3.1. Reactor Neutrino Background

Reactor electron antineutrinos constitute the dominant artificial background source for neutrino detectors and limit THEIA's detection potential for energies below 10 MeV (detailed information about reactor neutrinos is given in section 3.1.2 and 5.1).
The total reactor neutrino background rate $R = 32.0$ NIU [7] at the location of THEIA25 at SURF is calculated in [320] for $E_{\bar{\nu}_e} < 10$ MeV assuming the IBD interaction cross section of equation 4.4. This results in an estimated background rate for THEIA25 with a 3 % WbLS target of

$$R_{reactor} = R \cdot N_{target} = 32.0\,\text{NIU} \cdot 6.7 \cdot 10^{31}\,\frac{\text{protons}}{\text{yr}} = 21.4\,\frac{\text{evts}}{\text{kt yr}}. \tag{8.2}$$

Around $N_{reactor} = 4,000$ reactor background events measured via IBD below 10 MeV are expected for THEIA25 after 10 years of data taking and for a fiducial mass of 18.7 kt, which is factor of 30 smaller than the expected event number for the JUNO detector ($N_{reactor,JUNO} \approx 120,000$ events below 10 MeV after 10 years). Translating this ratio to visible energies above 10 MeV, the expected number of reactor background events in THEIA25 is $N_{reactor,THEIA25}(E_{vis} > 10\,\text{MeV}) \approx 1.7$. This number is comparably small and around 99 % of the reactor background events are below visible energies of 10 MeV. Therefore, the reactor electron antineutrino background is neglected for THEIA25. Nevertheless, the reactor neutrino background sets the lower edge of the observational energy window to 10 MeV.

8.3.2. Diffuse Supernova Neutrino Background

The expected electron antineutrino flux $\phi^{DSNB}_{\bar{\nu}_e}$ of the diffuse supernova neutrino background (DSNB) at Earth is presented and discussed in detail in section 5.2. THEIA would have an excellent sensitivity to measure diffuse supernova neutrinos [179, 301]. Therefore, the DSNB will cause an IBD background for the indirect DM search with THEIA25.
The electron antineutrino flux $\phi^{DSNB}_{\bar{\nu}_e}$ of the DSNB at THEIA's location is given by equation 5.5 following section 5.2. Again three different cases of the flux (low, fiducial and high case) are assumed to take into account the large uncertainties of the astrophysical inputs. The neutrino energy spectrum of the DSNB in THEIA25 measured via IBD reactions is

$$\frac{\mathrm{d}N_{DSNB}\,(E_{\bar{\nu}_e})}{\mathrm{d}E_{\bar{\nu}_e}} = \sigma_{IBD}\,(E_{\bar{\nu}_e})\,\frac{\mathrm{d}\phi^{DSNB}_{\bar{\nu}_e}\,(E_{\bar{\nu}_e})}{\mathrm{d}E_{\bar{\nu}_e}}\,N_{target}\,t\,\epsilon_{IBD}\,\epsilon_{\mu\,veto}\,\epsilon_{e-like}. \tag{8.3}$$

[7] The neutrino interaction unit NIU is defined as 1 NIU $= \frac{1\,\text{event}}{10^{32}\,\text{protons}\cdot\text{yr}}$.

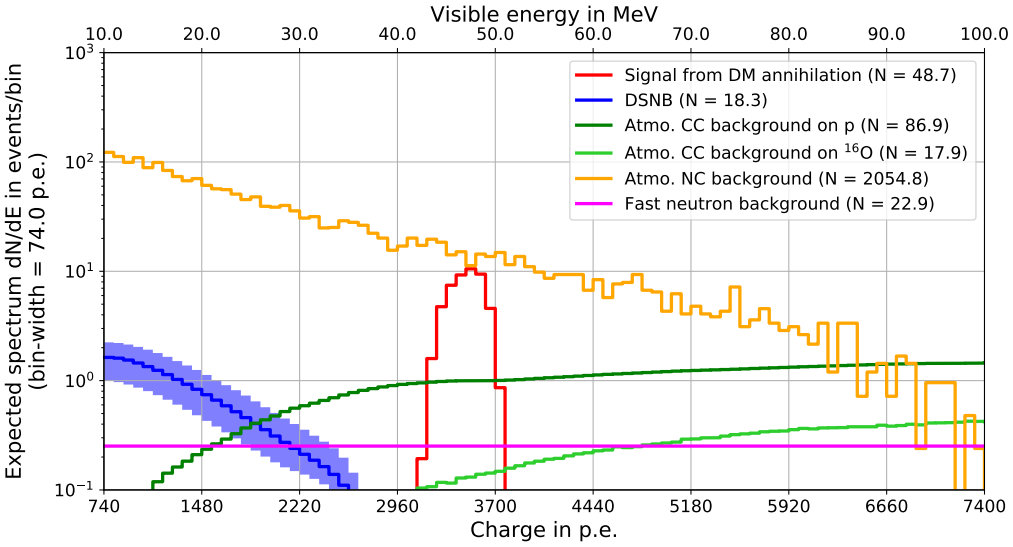

Figure 8.3.: Total expected visible energy spectrum of IBD events in THEIA25 after 10 years of data taking, for fiducial mass of 18.7 kt and for visible energies between 10 MeV and 100 MeV. All events pass the IBD selection criteria listed in table 8.1. The diffuse supernova neutrino background (DSNB) discussed in section 8.3.2 is shown in blue, where the solid blue line represents the fiducial case with $N^{fid}_{DSNB} = 18.3 \pm 7.3$, while the blue region is confined by the high and low case, respectively. The atmospheric CC background of $\bar{\nu}_e$'s interacting with free protons of section 8.3.3 is shown as dark green line ($N_{atmoCC,\bar{\nu}_e+p} = 86.9 \pm 21.7$), whereas the atmospheric CC background of $\bar{\nu}_e$'s interacting with ^{16}O nuclei is displayed as light green line ($N_{atmoCC,\bar{\nu}_e+^{16}\mathrm{O}} = 17.9 \pm 4.5$). The IBD-like atmospheric NC background studied in section 8.3.4 is shown in orange with $N_{atmoNC} = 2054.8 \pm 595.9$. The fast neutron background ($N_{FN} = 22.9 \pm 4.5$) is introduced in section 8.3.5 and shown in magenta. The electron antineutrino signal spectrum calculated in section 8.2 with the currently best 90 % C.L. upper limit of the DM annihilation cross section of $\langle \sigma_A \, \mathrm{v} \rangle_{Super-K} \, (m_{DM} = 50\,\mathrm{MeV}) = 1.1 \cdot 10^{-24}$ cm^3/s is shown in red exemplarily for $m_{DM} = 50$ MeV resulting in $N_S = 48.7$.

The visible energy spectrum of the DSNB in THEIA25 for a total runtime of 10 years and a fiducial mass of 18.7 kt is shown in figure 8.3 for energies between 10 MeV and 100 MeV. It is generated with equation 8.3 considering the IBD kinematics and the energy resolution of THEIA25 following the similar procedure as introduced in section 5.1.
In the presented energy region and assuming a total uncertainty of 40 %, $N^{low}_{DSNB} = 10.9 \pm 4.4$ events, $N^{fid}_{DSNB} = 18.3 \pm 7.3$ events and $N^{high}_{DSNB} = 27.0 \pm 10.8$ events are expected in THEIA25 for the low, fiducial and high case, respectively. This yields an expected event rate in THEIA25 for the fiducial case of $R^{fid}_{DSNB} = (0.10 \pm 0.04)$ yr^{-1} kt^{-1}.

8.3.3. Atmospheric Charged Current Background

Charge current interactions of atmospheric neutrinos and antineutrinos with nucleons and nuclei of the WbLS target constitute backgrounds in THEIA. Atmospheric neutrinos and antineutrinos of all three flavors are interacting via the exchange of a charged W^+/W^- boson with free protons, ^{12}C and ^{16}O nuclei resulting in various interaction channels present in the detector[8]:

[8] Atmospheric neutrinos and antineutrinos can also interact via CC on electrons of the target material: $\nu_e/\bar{\nu}_e + e^- \rightarrow e^- + \nu_e/\bar{\nu}_e$ and $\nu_\mu/\nu_\tau + e^- \rightarrow \nu_e + \mu^-/\tau^-$. Nevertheless, these interaction channels do not contribute to the atmospheric CC neutrino background, since they do not mimic IBD events and

- $\bar{\nu}_e + p \rightarrow e^+ + n$,
- $\nu_e/\bar{\nu}_e + {}^{12}\mathrm{C} \rightarrow e^-/e^+ + {}^{12}\mathrm{N}^*/{}^{12}\mathrm{B}^*$,
- $\nu_e/\bar{\nu}_e + {}^{16}\mathrm{O} \rightarrow e^-/e^+ + {}^{16}\mathrm{F}^*/{}^{16}\mathrm{N}^*$,
- $\bar{\nu}_\mu + p \rightarrow \mu^+ + n$,
- $\nu_\mu/\bar{\nu}_\mu + {}^{12}\mathrm{C} \rightarrow \mu^-/\mu^+ + {}^{12}\mathrm{N}^*/{}^{12}\mathrm{B}^*$,
- $\nu_\mu/\bar{\nu}_\mu + {}^{16}\mathrm{O} \rightarrow \mu^-/\mu^+ + {}^{16}\mathrm{F}^*/{}^{16}\mathrm{N}^*$,
- $\bar{\nu}_\tau + p \rightarrow \tau^+ + n$,
- $\nu_\tau/\bar{\nu}_\tau + {}^{12}\mathrm{C} \rightarrow \tau^-/\tau^+ + {}^{12}\mathrm{N}^*/{}^{12}\mathrm{B}^*$,
- $\nu_\tau/\bar{\nu}_\tau + {}^{16}\mathrm{O} \rightarrow \tau^-/\tau^+ + {}^{16}\mathrm{F}^*/{}^{16}\mathrm{N}^*$.

The atmospheric flux at the location of the THEIA25 detector as well as each of these interaction channels are shortly introduced and discussed in this section and the resulting atmospheric CC background for the indirect DM search with THEIA25 is estimated.
At production, atmospheric neutrinos are mostly electron and muon (anti)neutrinos, but also tau (anti)neutrinos are expected at THEIA site due to neutrino oscillations. Nevertheless, the CC tau neutrino cross section is strongly suppressed at low neutrino energies because of the large mass of the tau lepton relative to the electron and muon [321]. Therefore, and following the estimations presented in section 5.3.2, the atmospheric $\nu_\tau/\bar{\nu}_\tau$ CC interaction background is neglected in this study.

Atmospheric Neutrino Flux at SURF

THEIA25 would be most likely located at SURF at 44.35°N and 103.75°W [322]. The atmospheric neutrino flux of ν_e, $\bar{\nu}_e$, ν_μ and $\bar{\nu}_\mu$ without considering neutrino oscillations is simulated by Honda et al. for the location of SURF for neutrino energies from 100 MeV to 10 TeV [256]. For lower neutrino energies, i.e. from 10 MeV to 944 MeV, the atmospheric neutrino flux of ν_e, $\bar{\nu}_e$, ν_μ and $\bar{\nu}_\mu$ is predicted by FLUKA simulations, but for the location of Gran Sasso at 42.5°N, 13.0°O [260]. Since the atmospheric flux increases with larger geographic (geomagnetic) latitude, the FLUKA fluxes are scaled in a similar way like described in section 5.3.1 to agree with the fluxes of Honda in the overlapping energy region from 100 MeV to 944 MeV. This results in scaling factors of $f_{\nu_e} \approx f_{\bar{\nu}_e} \approx f_{\nu_\mu} \approx f_{\bar{\nu}_\mu} \approx 1.4$. Therefore, the expected atmospheric neutrino fluxes (for $\nu_i = \nu_e, \bar{\nu}_e, \nu_\mu, \bar{\nu}_\mu$) at SURF without considering neutrino oscillations are approximated with

$$\phi_{\nu_i,\mathrm{THEIA}}(E_{\nu_i}) = \begin{cases} 1.4 \cdot \phi_{\nu_i,\text{Gran Sasso, FLUKA}} & \text{, for } E_{\nu_i} < 100\,\mathrm{MeV}, \\ \phi_{\nu_i,\text{SURF, Honda}} & \text{, for } E_{\nu_i} \geq 100\,\mathrm{MeV}. \end{cases} \tag{8.4}$$

The resulting atmospheric neutrino fluxes at SURF are shown in figure 8.4 for neutrino energies from 10 MeV to 10 GeV.
In order to take into account neutrino oscillations, the oscillation probabilities introduced in section 5.3.1 are considered to predict the atmospheric neutrino and antineutrino fluxes of all three flavors at SURF. It should be noted here that, due to the larger geomagnetic latitude, the atmospheric flux at SURF is about a factor of 2 larger than at JUNO site (22.0°N) and around a factor of 1.7 larger than at the location of Super-K (36.4°N) for neutrino energies between 10 MeV and 10 GeV.

the interaction cross sections for $E_\nu \geq 10$ MeV are comparably small as shown in figure 3.5 exemplarily for $\nu_e + e^- \rightarrow e^- + \nu_e$.

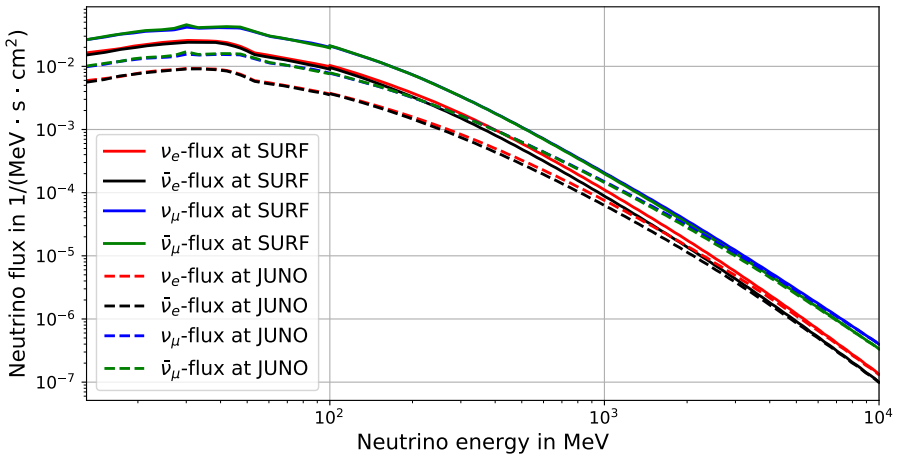

Figure 8.4.: Atmospheric neutrino flux of ν_e, $\bar{\nu}_e$, ν_μ and $\bar{\nu}_\mu$ at SURF and at JUNO site for neutrino energies from 10 MeV to 10 GeV without considering neutrino oscillations. The fluxes at SURF are displayed as solid lines. The atmospheric neutrino fluxes at JUNO site are shown for comparison and displayed as dashed lines.

Atmospheric Charged Current $\nu_e/\bar{\nu}_e$ Background

Atmospheric electron neutrinos and antineutrinos can interact via charged current with free protons, ^{12}C and ^{16}O nuclei of the WbLS target of THEIA25.

Electron antineutrinos interacting with free protons $\bar{\nu}_e + p \rightarrow e^+ + n$ pose the most dangerous reaction channels and represent an indistinguishable IBD background. The expected neutrino energy spectrum of this channel in THEIA25 is

$$\frac{\mathrm{d}N_{atmoCC,\bar{\nu}_e+p}\left(E_{\bar{\nu}_e}\right)}{\mathrm{d}E_{\bar{\nu}_e}} = \sigma_{IBD}\left(E_{\bar{\nu}_e}\right) \frac{\mathrm{d}\phi^{atmo}_{\bar{\nu}_e}\left(E_{\bar{\nu}_e}\right)}{\mathrm{d}E_{\bar{\nu}_e}} N_{target}\, t\, \epsilon_{IBD}\, \epsilon_{\mu\, veto}\, \epsilon_{e-like} \tag{8.5}$$

with the atmospheric electron antineutrino flux $\phi^{atmo}_{\bar{\nu}_e} \approx 0.67 \cdot \phi_{\bar{\nu}_e} + 0.17 \cdot \phi_{\bar{\nu}_\mu}$ considering neutrinos oscillations.
The visible energy spectrum of the atmospheric CC $\bar{\nu}_e$ background on free protons in THEIA25 is given by equation 8.5 considering the IBD kinematics and THEIA25's energy resolution and displayed in figure 8.3 as dark green line. Assuming a total uncertainty of 25 % [260], $N_{atmoCC,\bar{\nu}_e+p} = 86.9 \pm 21.7$ events are expected for visible energies between 10 MeV and 100 MeV, which results in an event rate of $R_{atmoCC,\bar{\nu}_e+p} = (0.46 \pm 0.12)$ yr^{-1} kt^{-1}. Therefore, the atmospheric CC $\bar{\nu}_e$ background on free protons is one of the main backgrounds for indirect DM search with neutrinos in THEIA25 for energies above around 35 MeV.

Furthermore, CC interactions of electron neutrinos and antineutrinos on the nuclei of the WbLS can be background sources of IBD-like events.
To estimate the background contribution of atmospheric $\nu_e/\bar{\nu}_e$ interacting with ^{12}C, only reaction channels with exactly one neutron in the final state are considered to ensure their IBD-like signal signature[9]: $\nu_e + {}^{12}\mathrm{C} \rightarrow e^- + n + X$ and $\bar{\nu}_e + {}^{12}\mathrm{C} \rightarrow e^+ + n + X$ (X represents

[9] In principle, channels with two (or more) neutrons in the final state could also cause IBD-like background events, if one (or more) neutrons leave the detector without being captured. However, the probability for this to happen and, moreover, the interaction cross section for such channels is small. Therefore, these channels are neglected in this study.

^{11}N, ^{11}B or lighter isotopes with additional p, α, etc.). The event numbers of these channels for visible energies between 10 MeV and 100 MeV are estimated with $N = \sigma \cdot \phi \cdot N_{^{12}\mathrm{C}} \cdot t$, where σ is the interaction cross section from [263], ϕ the atmospheric ν_e and $\bar{\nu}_e$ flux, respectively, considering neutrino oscillation as described above, $N_{^{12}\mathrm{C}} = 3.25 \cdot 10^{31}$ the number of ^{12}C nuclei in the 25 kt WbLS target with 3 % LS of THEIA25 and t the exposure time of 10 years. In total, only $N \approx 0.8$ events are expected in THEIA25 after 10 years and for energies from 10 MeV to 100 MeV due to the lower interaction cross sections compared to the IBD cross section (see figure 5.5) and the comparably small number of ^{12}C nuclei because of the small LS fraction in the studied WbLS. The number of events mimicking an IBD signal is even less than 0.8 events, since no IBD detection efficiency is considered in this background estimation. So, this background can be neglected.

A similar approach is applied to estimate the background of atmospheric $\nu_e/\bar{\nu}_e$ interacting via CC on ^{16}O nuclei. In [323], interaction cross sections of $\nu_e/\bar{\nu}_e$ on ^{16}O with one neutron in the final state are calculated, which are used to predict the number of background events in THEIA25. The only reaction channel with significant event rate is $\bar{\nu}_e + {}^{16}\mathrm{O} \rightarrow e^+ + n + {}^{15}\mathrm{N}$. The neutrino energy spectrum of this channel in THEIA25 is

$$\frac{\mathrm{d}N_{atmoCC,\bar{\nu}_e+^{16}\mathrm{O}}(E_{\bar{\nu}_e})}{\mathrm{d}E_{\bar{\nu}_e}} = \sigma_{CC,\bar{\nu}_e+^{16}\mathrm{O}}(E_{\bar{\nu}_e}) \, \frac{\mathrm{d}\phi^{atmo}_{\bar{\nu}_e}(E_{\bar{\nu}_e})}{\mathrm{d}E_{\bar{\nu}_e}} \, N_{target} \, t \, \epsilon_{IBD} \, \epsilon_{\mu\, veto} \, \epsilon_{e-like} \quad (8.6)$$

with the interaction cross section $\sigma_{CC,\bar{\nu}_e+^{16}\mathrm{O}}$ of [323], the atmospheric $\bar{\nu}_e$ flux $\phi^{atmo}_{\bar{\nu}_e}$ at SURF and the number of ^{16}O nuclei in the 25 kt WbLS target $N_{target} = 8.0 \cdot 10^{32}$. To estimate the detection efficiency of this channel, the IBD detection efficiency of $\epsilon_{IBD} = 69.7$ % is taken as conservative assumption, since the ^{15}N isotope only slightly affects the event signature. The number of events as function of the visible energy is generated using equation 8.6 and considering THEIA25's energy resolution and a simple assumption of the kinematics of the reaction $\bar{\nu}_e + {}^{16}\mathrm{O} \rightarrow e^+ + n + {}^{15}\mathrm{N}$. It is assumed that the emitted neutron and ^{15}N isotope are at rest[10].
The resulting visible energy spectrum of $\bar{\nu}_e + {}^{16}\mathrm{O} \rightarrow e^+ + n + {}^{15}\mathrm{N}$ in THEIA25 for energies between 10 MeV and 100 MeV is shown in figure 8.3 as light green line. $N_{atmoCC,\bar{\nu}_e+^{16}\mathrm{O}} = 17.9 \pm 4.5$ events are expected in THEIA25 that mimic an IBD signal assuming an overall uncertainty of 25 %. The event rate is $R_{atmoCC,\bar{\nu}_e+^{16}\mathrm{O}} = (0.10 \pm 0.02)$ yr^{-1} kt^{-1}. So, the atmospheric CC electron neutrino and antineutrino background on ^{16}O needs to be considered in the search for neutrinos from DM self-annihilation with THEIA25, since it affects the visible energy spectrum especially in the higher energy region.

Atmospheric Charged Current $\nu_\mu/\bar{\nu}_\mu$ Background

Atmospheric muon neutrinos and antineutrinos also interact via CC interactions with free protons, ^{12}C and ^{16}O nuclei inside the THEIA25 detector by producing muons. Such μ-like events are also a background source and could cause IBD-like background events for the indirect DM search with THEIA.
To estimate the total number of μ-like events in THEIA25 for visible energies between 10 MeV and 100 MeV, interaction cross sections of $\bar{\nu}_\mu + p \rightarrow \mu^+ + n$, $\nu_\mu/\bar{\nu}_\mu + {}^{12}\mathrm{C} \rightarrow \mu^-/\mu^+ + ...$ and $\nu_\mu/\bar{\nu}_\mu + {}^{16}\mathrm{O} \rightarrow \mu^-/\mu^+ + ...$ provided by GENIE [266] and the atmospheric $\nu_\mu/\bar{\nu}_\mu$ flux at SURF considering neutrino oscillations, $\phi^{atmo}_{\nu_\mu/\bar{\nu}_\mu} \approx 0.41 \cdot \phi_{\nu_\mu/\bar{\nu}_\mu} + 0.17 \cdot \phi_{\nu_e/\bar{\nu}_e}$, are used. The total number of μ-like events of all presented channels is then given by $N_{\mu-like} = \sum_i \sigma_i \cdot \phi^{atmo}_{\nu_\mu/\bar{\nu}_\mu} \cdot N_{target} \cdot t$ with the respective number of free protons $N_p = 1.68 \cdot 10^{33}$,

[10] Therefore, the kinetic energy of the positron is $E_{e,kin} = E_{\bar{\nu}_e} + m_{^{16}\mathrm{O}} - m_n - m_e - m_{^{15}\mathrm{N}} \approx E_{\bar{\nu}_e} - 14$ MeV.

^{12}C nuclei $N_{^{12}\mathrm{C}} = 3.25 \cdot 10^{31}$ and ^{16}O nuclei $N_{^{16}\mathrm{O}} = 8.0 \cdot 10^{32}$ in the 25 kt target volume of THEIA25 and for $t = 10$ years. The visible energy spectrum is generated according to the kinematics of the reaction channel assuming that the produced neutron and residual isotopes are at rest. Moreover, it is assumed that the kinetic muon energy is completely visible inside the detector. These assumptions result in $N_{\mu-like} \approx 750$ events for visible energies from 10 MeV to 100 MeV. It must be noted here that no IBD selection cuts are applied on the μ-like events. Therefore, only a fraction of these events act as IBD-like background in THEIA25. Nevertheless, the number of μ-like events must be suppressed further.

To reduce this background, e-like events, i.e. events with energy deposition of electrons and positrons, need to be discriminated from μ-like events. In LS detectors such as JUNO, this is realized with the cut parameter $\sigma(t_{pe})$ as discussed in section 5.3.2, whereas in water Cherenkov detectors like Super-K, e-like and μ-like events are separated due to different ring pattern[11] inside the detector [113].
Both discrimination approaches are possible for THEIA25, since it combines the characteristics of LS and water Cherenkov detectors. However, the separation based on the scintillation light is challenging because of the small light yield and small scintillation photon statistics. Therefore, the very effective discrimination based on the differences in the ring pattern investigated in Super-K (see [113]) is translated to THEIA25 to estimate the efficiency of the discrimination of e-like and μ-like events. In [113], likelihood methods are used to separate μ^+/μ^- and $e^+/e^-/\gamma$ by algorithms based on the diffuseness of the edge of the Cherenkov rings. This results in a mis-identification probability between μ-like and e-like events of 0.6 % ± 0.1 % for events with visible energies between 30 MeV and 1.33 GeV [113]. This means that only 0.6 % of all μ-like events are mis-identified as e-like events and are a potential background, while $\epsilon_{e-like} = 99.4$ % of all e-like events are correctly identified as e-like events and survive this discrimination cut.
This discrimination efficiency can be translated to THEIA25, since the fiducial mass, photocathode coverage and detection efficiency is similar to Super-K, resulting in a total number of μ-like events of $N_{\mu-like} \approx 4.5$ events in THEIA25. Taking into account the strict IBD selection criteria presented in section 8.2, the number of IBD-like μ-like events is even less and therefore negligible for the study performed within this thesis.

One of the main backgrounds of water Cherenkov detectors are invisible muons produced by atmospheric muon neutrinos and antineutrinos (see section 2.4.2). Muons with kinetic energies below the Cherenkov threshold, e.g. $E_{\mu,thr.} = 54$ MeV for Super-K, are invisible in water Cherenkov detectors. They can decay at rest by emitting Michel electron/positrons, which cannot be distinguished from the prompt positron signal of the IBD reaction. However, this background source is completely suppressed in THEIA, since such muons can be detected due to the scintillation light component and are no longer invisible to the detector.

8.3.4. Atmospheric Neutral Current Background

In this section, neutral current (NC) interactions of atmospheric neutrinos and antineutrinos with the WbLS target of THEIA25 are studied. Neutrinos and antineutrinos of all flavors can interact via exchange of a Z^0 boson with protons, ^{12}C nuclei, ^{16}O nuclei and electrons of the WbLS. The corresponding reaction channels are ($\nu_i = \nu_e, \bar{\nu}_e, \nu_\mu, \bar{\nu}_\mu, \nu_\tau, \bar{\nu}_\tau$):

- $\nu_i + e^- \rightarrow \nu_i + e^-$,
- $\nu_i + p \rightarrow \nu_i + p$,

[11] μ-like events are identified by a sharp Cherenkov ring, while e-like events produce a more diffuse Cherenkov ring pattern.

- $\nu_i + {}^{12}\mathrm{C} \rightarrow \nu_i + ...$,
- $\nu_i + {}^{16}\mathrm{O} \rightarrow \nu_i + ...$

NC reactions on electrons cannot mimic IBD signals in THEIA25, since no neutron is produced and a delayed signal is missing. Nevertheless, the electron could potentially knock out neutrons of the nuclei of the WbLS, which can be captured and produce delayed signals. However, the interaction cross section of neutrinos on electrons is comparably small above neutrino energies of 10 MeV (as shown in figure 3.5). Therefore, atmospheric neutrinos interacting via NC on electrons is neglected as IBD-like background in this study.
In contrast to that, NC interactions on ^{12}C can pose IBD-like background events as discussed in section 5.3.3. The fraction of NC interactions on ^{12}C to the total number of NC interactions in a WbLS target with 3 % LS is calculated assuming the atmospheric neutrino flux at SURF of section 8.3.3 and NC interaction cross sections of GENIE. Only 2.5 % of all NC reactions in THEIA25 are on ^{12}C nuclei mainly due to the small LS fraction of the WbLS. So, NC interactions on ^{12}C are neglected in the following and only atmospheric NC events produced in interactions with water (free protons and ^{16}O) are further studied in detail.

Event Rate of Atmospheric NC Background in THEIA25

The expected event rate of atmospheric NC background events on protons and ^{16}O in THEIA25 is calculated assuming the atmospheric neutrino fluxes $\phi^{atmo}_{\nu_i}$ at SURF (see figure 8.4) and the NC interaction cross sections on protons, σ_{NC,ν_i+p}, and ^{16}O, $\sigma_{NC,\nu_i+{}^{16}\mathrm{O}}$, from GENIE (*gxspl-FNALsmall.xml*, [267, 269, 270]):

$$\frac{\mathrm{d}N_{atmoNC}(E_\nu)}{\mathrm{d}t} = N_p \left(\sum_{i=0}^{3} \phi^{atmo}_{\nu_i}(E_\nu)\sigma_{NC,\nu_i+p} \right) + N_{^{16}\mathrm{O}} \left(\sum_{i=0}^{3} \phi^{atmo}_{\nu_i}(E_\nu)\sigma_{NC,\nu_i+{}^{16}\mathrm{O}} \right). \tag{8.7}$$

$N_p = 1.6 \cdot 10^{33}$ is the number of free protons and $N_{^{16}\mathrm{O}} = 8.0 \cdot 10^{32}$ the number of ^{16}O nuclei in the water component of the 25 kt target of THEIA25. The neutrino flavor is specified by i ($\nu_0 = \nu_e, \nu_1 = \bar{\nu}_e, \nu_2 = \nu_\mu, \nu_3 = \bar{\nu}_\mu$). The non-oscillated atmospheric neutrino fluxes can be used to calculate the event rate similar to equation 5.16.
The event rate of atmospheric NC neutrino interactions on water in THEIA25 for neutrino energies from 10 MeV to 10 GeV is $8.05 \cdot 10^{-5}\,\mathrm{s}^{-1}$, resulting in 25398.0 events in a lifetime of 10 years.

Simulation of Atmospheric NC Background in THEIA25

To estimate the IBD-like background caused by NC interactions of atmospheric neutrinos in THEIA25, NC reactions on water, possible de-excitations of residual isotopes and the detector response of THEIA25 to the final reaction products are simulated in this study.
The NC interactions of atmospheric neutrinos and antineutrinos with water, i.e. protons and ^{16}O nuclei, of the WbLS of THEIA25 are simulated with GENIE (version: 3.0.6) for neutrinos energies from 10 MeV to 10 GeV. The LS component of the WbLS is neglected due to its small fraction as discussed above. The atmospheric neutrino fluxes of $\nu_e, \bar{\nu}_e, \nu_\mu$ and $\bar{\nu}_\mu$ at SURF without considering neutrino oscillations described in section 8.3.3 are used as input for the simulation. The NC interaction cross sections in GENIE contain QES, DIS and RES [267, 269, 270].
In NC interactions on ^{16}O nuclei, neutrons and/or protons can be knocked out and leave the residual isotopes in ground or an excited state. The de-excitation probability and

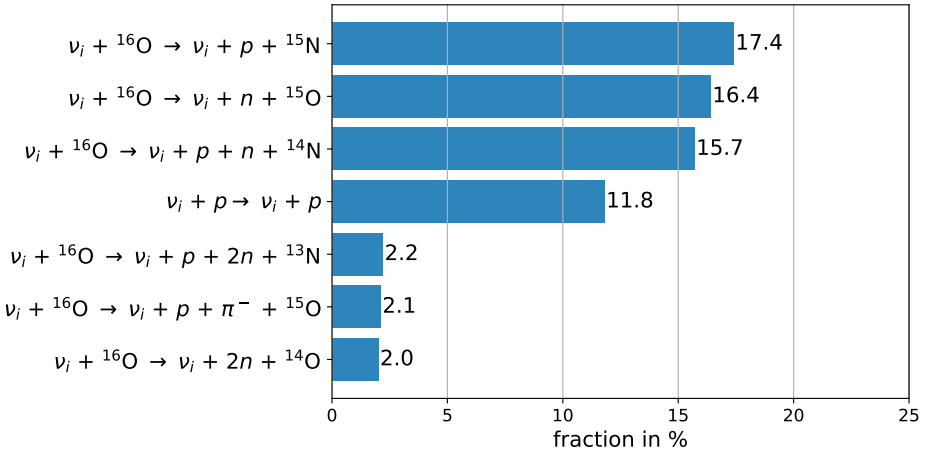

Figure 8.5.: Fractions of atmospheric NC interaction channels on free protons and ^{16}O nuclei. The interactions are simulated with GENIE considering potential de-excitations of the residual isotopes. The seven most frequent channels with an integrated fraction of 67.5 % are shown. Additional γ's and π^0's are not listed here.

the corresponding de-excitation processes for QE NC events[12] are considered according to calculations and measurements of [324–326]. The probability that a nucleon is knocked out of the $s_{1/2}$, $p_{3/2}$ or $p_{1/2}$ shell of the ^{16}O nuclei is assumed as $P(s_{1/2}) = 25$ %, $P(p_{3/2}) = 50$ % and $P(p_{1/2}) = 25$ % (for details see [324]). If the nucleon is knocked out from the $p_{1/2}$ shell, the residual isotope is in ground state and no de-excitation needs to be considered. If the nucleon is knocked out from the $p_{3/2}$ shell, the residual isotope de-excites via γ emission [324, 325]. The de-excitation γ energy (and the corresponding branching ratio) is 6.32 MeV (87.2 %) or 9.93 MeV (6.4 %) in case of proton knock-out, and 6.18 MeV (100 %) in case of neutron knock-out [326]. If the nucleon is knocked out from the $s_{1/2}$ shell, several de-excitation channels with gamma and nucleon emission are possible. The corresponding de-excitation channels and branching ratios considered here are based on the measurement of [325]. The same model is assumed for proton and neutron knock-out. All final particles that are produced via NC interactions of atmospheric neutrinos and antineutrinos on free protons and ^{16}O and through potential de-excitation of residual isotopes are used as input for the THEIA25 detector simulation with the described RAT-PAC simulation tool. The most frequent final NC reaction channels are displayed in figure 8.5. The detector response of THEIA25 of 104,940 atmospheric NC events have been simulated, which is equivalent to data of more than 40 years taking into account the expected event rate from above.

Analysis of Atmospheric NC Background in THEIA25

The simulation sample of 104,940 atmospheric NC events on free protons and ^{16}O in THEIA25 is analyzed to estimate the number of NC background events that mimic an IBD signal. Therefore, the IBD selection cuts described in section 8.2 and summarized in table 8.1 are applied on the simulated NC events in the exact same way like on the simulated IBD events. The distribution of the simulation data as well as the IBD selection

[12] Potential de-excitations for NC events from DIS or RES interactions are not considered in this study, since no validated measurements of the de-excitation probabilities and de-excitation channels exist. Therefore, a reliable prediction of the de-excitation is not possible. Moreover, only 29 % of all simulated NC events are from DIS and RES interactions and just a portion of that would further de-excite. So, not considering de-excitation for DIS and RES interactions only leads to a minor uncertainty.

Table 8.2.: IBD selection criteria together with the resulting cut efficiencies and the total detection efficiency ϵ_{atmoNC} of atmospheric NC events on free protons and ^{16}O. The cut efficiencies are determined by the analysis of atmospheric NC events simulated with the RAT-PAC simulation tool for THEIA25 (middle column). The cuts of the delayed cut are listed from (a) to (e) and applied consecutively. For comparison, the cut efficiencies and the total IBD detection efficiency of IBD events from table 8.1 are shown (right column). The statistical errors $\Delta\epsilon$ of each cut efficiency are also listed.

	$\epsilon_{atmoNC} \pm \Delta\epsilon_{atmoNC}$ in %	$\epsilon_{IBD} \pm \Delta\epsilon_{IBD}$ in %
Volume cut on prompt signal	74.1 ± 0.5	74.5 ± 0.8
Energy cut on prompt signal	43.7 ± 0.2	97.0 ± 1.0
Total delayed cut:	30.9 ± 0.3	95.1 ± 1.0
(a) Time difference cut	58.2 ± 0.4	97.3 ± 1.0
(b) Multiplicity cut	61.6 ± 0.5	99.9 ± 1.0
(c) Energy cut on del. signal	99.8 ± 1.0	99.7 ± 1.0
(d) Distance cut	88.2 ± 0.9	99.6 ± 1.0
(e) Volume cut on del. signal	98.2 ± 1.0	98.6 ± 1.0
Total efficiency	$\mathbf{8.2 \pm 0.1}$	$\mathbf{69.7 \pm 0.8}$

cut acceptance windows are shown in section C.2 of the appendix. The volume cut on the position of the prompt signal, the energy cut on the prompt signal and the total delayed cut are applied independently on all 104,940 atmospheric NC events. The total delayed cut contains the time difference cut, multiplicity cut, delayed energy cut, distance cut and volume cut on the delayed signal, which are applied sequentially.

The resulting cut efficiencies of atmospheric NC background events for the IBD selection cuts and their statistical errors are shown in table 8.2 together with the cut efficiencies of the simulated IBD events already presented in table 8.1 for comparison. Atmospheric NC events that pass all IBD cuts mimic an IBD signal in THEIA25 and are an IBD-like background for the indirect DM search with THEIA.
The efficiency of the volume cut on the position of the prompt signal is similar for atmospheric NC and IBD events, since both are simulated uniformly distributed within the detector volume and the cut efficiency is dominated by the geometric reduction of the detector volume. The largest suppression of the atmospheric NC background is given by the total delayed cut with a survival efficiency of $\epsilon_{delayed} = (30.9 \pm 0.3)$ % due to strict selection criteria of IBD signals because of the temporal and spatial coincidence of prompt and delayed signal. Moreover, the multiplicity cut with an efficiency of $\epsilon_{mult} = (61.6 \pm 0.5)$ % reduces atmospheric NC events very efficiently compared to IBD events, since NC events often contain more than one neutron being captured and, therefore, more than one delayed signal.
In total, only 8,576 atmospheric NC events of the 104,940 simulated events mimic an IBD event signature in THEIA25 resulting in a total cut efficiency of $\epsilon_{atmoNC} = (8.2 \pm 0.1)$ %. The most frequent NC interaction channels that mimic an IBD signal in THEIA25 are shown in figure 8.6. The most crucial reaction channels is $\nu_i + {}^{16}\mathrm{O} \rightarrow \nu_i + p + n + {}^{14}\mathrm{N}$ with an expected frequency of 52.5 %, followed by the channel $\nu_i + {}^{16}\mathrm{O} \rightarrow \nu_i + + n + {}^{15}\mathrm{O}$ with 27.8 %. Only 0.9 % of all IBD-like NC events are associated with interactions on free protons. Nevertheless, many different interaction channels can create IBD-like signals in the THEIA25 detector, which makes the simulation of the atmospheric NC background essential to study THEIA's sensitivity for indirect DM search.
Considering the event rate of atmospheric NC events calculated above, the efficiency due to the application of the muon veto $\epsilon_{\mu\,veto} = 99.0$ % and an assumed total uncertainty

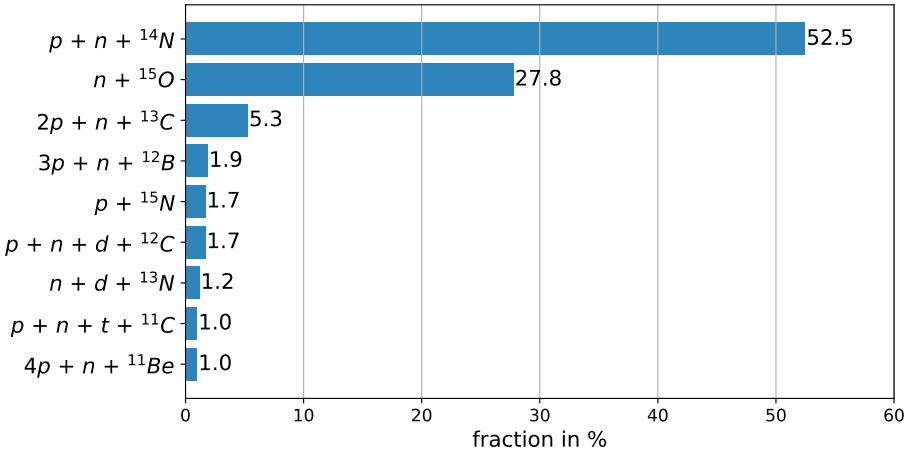

Figure 8.6.: Fractions of atmospheric NC interaction channels on protons and ^{16}O that mimic IBD signals in the THEIA25 detector. The nine most frequent channels producing IBD-like events (with an integrated fraction of 94.0 %) are NC interactions on ^{16}O ($\nu_i + {}^{16}\mathrm{O} \rightarrow \nu_i + ...$) and displayed here. Additional γ's and π^0's are not shown.

of 29 % [74], $N_{atmoNC} = 2054.8 \pm 595.9$ atmospheric NC background events mimic an IBD signal in THEIA25 for visible energies from 10 MeV to 100 MeV. The event rate of IBD-like atmospheric NC events in THEIA25 is $R_{atmoNC} = (11.0 \pm 3.2)$ yr^{-1} kt^{-1}. The resulting visible energy spectrum of the IBD-like atmospheric NC background is shown in figure 8.3 and represents the dominant background spectrum for the search for neutrinos from DM self-annihilation with THEIA25. It overwhelms the expected DM signal by at least one order of magnitude, but differs significantly in the spectral shape.

8.3.5. Muon-induced Background

Cosmic muons and their spallation products can induce background events in the THEIA25 detector by producing secondary particles in the rock surrounding the detector as well as in the detector itself.
The preferred location of THEIA25 would be SURF at a depth of 4,300 m.w.e. [6], where the cosmic muon flux is $\phi_\mu = 4.2 \cdot 10^{-9}$ cm^{-2} s^{-1} with a mean muon energy of $\langle E_\mu \rangle = 293$ GeV [6]. The muon-induced backgrounds from cosmogenic isotopes and fast neutrons in THEIA25 will be discussed in the following.

Background from Cosmogenic Isotopes

Cosmogenic isotopes are produced by muon spallation on ^{16}O and ^{12}C nuclei of the WbLS target of THEIA. These isotopes can decay by emitting a β particle (i.e. electron or positron) and a neutron, and can therefore mimic an IBD signal signature in the THEIA25 detector.
The only isotope produced at a relevant cross section with a Q value above 10 MeV is ^{9}Li (see [179, 301]). ^{9}Li decays with a half-life of $T_{1/2} = 178.0$ ms via the decay channels $^9\mathrm{Li} \rightarrow \bar{\nu}_e + e^- + {}^9\mathrm{Be}$ (with branching ratio of 49.2 %) and $^9\mathrm{Li} \rightarrow \bar{\nu}_e + e^- + n + 2\alpha$ (with branching ratio of 50.8 %) [274]. The Q value of the β-neutron emission of ^{9}Li is $Q = 11.9$ MeV [274]. So, ^{9}Li isotopes decaying via the emission of an electron and neutron could mimic IBD signals in THEIA25 in the visible energy region above 10 MeV and represent an IBD-like background.
To estimate the expected event rate in THEIA25, ^{9}Li production yields measured in

the liquid scintillator detector Borexino, $Y_{^9\mathrm{Li},LS} = (2.9 \pm 0.3) \cdot 10^{-7} \left(\mu\,\mathrm{g/cm^2}\right)^{-1}$ with $\langle E_{\mu,Borexino}\rangle = 283$ GeV [327], and in the water Cherenkov detector Super-K, $Y_{^9\mathrm{Li},H_2O} = (5.1 \pm 1.6) \cdot 10^{-8} \left(\mu\,\mathrm{g/cm^2}\right)^{-1}$ with $\langle E_{\mu,SuperK}\rangle = 270$ GeV [328], are adopted.
Since the production cross section of cosmogenic isotopes scales with the muon energy $\sigma \propto E_\mu^{0.75}$ [329, 330], the total ^{9}Li yield for THEIA25 is estimated to

$$\begin{aligned} Y_{^9\mathrm{Li},THEIA25} &= 0.03 \cdot \frac{\langle E_{\mu,THEIA}\rangle^{0.75}}{\langle E_{\mu,Borexino}\rangle^{0.75}} Y_{^9\mathrm{Li},LS} + 0.97 \cdot \frac{\langle E_{\mu,THEIA}\rangle^{0.75}}{\langle E_{\mu,SuperK}\rangle^{0.75}} Y_{^9\mathrm{Li},H_2O} \\ &\approx 0.03 \cdot 1.03 \cdot Y_{^9\mathrm{Li},LS} + 0.97 \cdot 1.06 \cdot Y_{^9\mathrm{Li},H_2O} \\ &\approx 6.2 \cdot 10^{-8} \left(\mu\,\mathrm{g/cm^2}\right)^{-1} \end{aligned} \tag{8.8}$$

considering a WbLS target with 3 % LS and 97 % water. So, the total ^{9}Li production rate in the THEIA25 detector is $R_{^9\mathrm{Li},THEIA25} = Y_{^9\mathrm{Li},THEIA25} \cdot \phi_\mu \approx (8.1 \pm 2.1)$ kt^{-1} yr^{-1}. Taking into account the branching ratio of β-neutron emission of ^{9}Li of 50.8 %, the ^{9}Li background rate reduces to $R_{^9\mathrm{Li},THEIA25} \approx (4.1 \pm 1.1)$ kt^{-1} yr^{-1}.
The resulting number of β-neutron emitting ^{9}Li isotopes in THEIA25 with a target mass of 25 kt measured after 10 years of data taking and for visible energies above 10 MeV is $N_{^9\mathrm{Li}} \leq 162.3 \pm 43.5$ [13].

To suppress the background of cosmogenic ^{9}Li isotopes, a muon veto cut is introduced for THEIA25 similar to the considerations for JUNO discussed in section 5.4.1. So, a cylindrical volume with radius $R_{cut} = 5$ m around the muon track is vetoed for a time of $T_{cut} = 2$ s. This provides an excellent veto efficiency of more than 99 % due to the short half-life of ^{9}Li of 178.0 ms compared to $T_{cut} = 2$ s and the expected lateral production profile (for details see [331]). Therefore, the cosmogenic ^{9}Li background can be reduced to $N_{^9\mathrm{Li}}^{\mu\,veto} \leq 1.6 \pm 0.4$ and neglected in this study.
The loss of exposure for THEIA25 of such a muon veto with $R_{cut} = 5$ m and $T_{cut} = 2$ s is less than 1 %. Therefore, an efficiency (in terms of exposure) due to the application of the muon veto of $\epsilon_{\mu\,veto} = 99.0$ % is conservatively assumed for THEIA25.

Fast Neutron Background

Fast neutrons that are produced through spallation processes of cosmic muons[14] in the rock around the THEIA25 detector can enter the detector unnoticed and, furthermore, can mimic IBD events (details about the fast neutron background are given in section 5.4.2). The IBD-like background of fast neutrons in THEIA25 is discussed in the following.
The estimation of the fast neutron background in THEIA25 uses simulation results from a similar study performed for LENA [332] and follows the work of [179].
In [332], a simulation of the fast neutron background is performed in limestone rock ($CaCO_3$, $\rho = 2.74$ g/cm^3), for a mean muon energy of $\langle E_\mu\rangle = 300$ GeV and a muon flux of $\phi_{\mu,LENA} = 5.6 \cdot 10^{-9}$ cm^{-2} s^{-1} at depth of 4,000 m.w.e.. It is assumed that all muon tracks are vertically due to the large and homogeneous rock overburden. Only neutrons in a 4 m thick cylinder around the detector volume has been simulated in [332], since

[13] To conservatively calculate $N_{^9\mathrm{Li}}$ for visible energies above 10 MeV, a rectangular β-spectrum is assumed. This overestimates the number of β-neutron emitting ^{9}Li isotopes in THEIA25, for what reason $N_{^9\mathrm{Li}} \leq 162.3 \pm 43.5$ is given as upper limit.

[14] Fast neutrons can also be produced by spontaneous fission of ^{238}U, ^{235}U and ^{232}Th in the rock, and by (α, n) reactions, where α particles emitted in the decay of uranium, thorium and their daughter products interact with lighter isotopes and produce neutrons [275]. Since these fast neutrons are negligible above visible energies of 10 MeV, this section only discusses muon-induced fast neutrons.

the mean free path length of fast neutrons in the rock is below 1 m. The simulation results in a neutron yield for energies above 10 MeV of

$$Y_{n,LENA}(E > 10 \text{ MeV}) = 2.8 \cdot 10^{-4} \ (\mu \text{ g/cm}^2)^{-1}. \tag{8.9}$$

Assuming the cylindrical detector geometry of THEIA25 with $d = h = 31.8$ m, it can be approximated that $R_{\mu,THEIA25} \approx 6 \cdot 10^5$ muons per year traverse a 4 m thick cylinder volume around the detector volume. Since the neutron production rate $R^{\mu}_{n,THEIA25}$ per muon scales with the mean muon energy (and the average rock density at SURF is similar to ρ_{CaCO_3} [333]), it is given by [179]

$$R^{\mu}_{n,THEIA25} = Y_{n,LENA}(E > 10 \text{ MeV}) \cdot \rho_{\text{CaCO}_3} \cdot 31.8 \text{ m} \cdot \left(\frac{293 \text{ GeV}}{300 \text{ GeV}}\right)^{0.75} \approx 2.4 \text{ n}/\mu. \tag{8.10}$$

So, in total, $R_{n,THEIA25} = R^{\mu}_{n,THEIA25} \cdot R_{\mu,THEIA25} \approx 1.4 \cdot 10^6$ neutrons per year with energies above 10 MeV are produced by cosmic muons in a 4 m thick surrounding volume of THEIA25.
This results in $N_{FN,THEIA25} \approx 347 \pm 69$ fast neutron events in the THEIA25 detector for visible energies from 10 MeV to 100 MeV and after 10 years of data taking following the calculations of [179]. Here, a total uncertainty of 20 % and a flat energy distribution for fast neutron events is assumed.
To reduce the fast neutron background in THEIA25, a volume cut on the position of the prompt signal of fast neutron events of $\rho = \sqrt{x^2 + y^2} < 14.4$ m and $|z| < 14.4$ m is applied. This reduces the fast neutron IBD-like background[15] between 10 MeV and 100 MeV to $N_{FN,18.7 \text{ kt}} = 22.9 \pm 4.5$ (for details see [179]). The corresponding fast neutron background spectrum is shown in figure 8.3.

8.3.6. Summary of Backgrounds in THEIA

A summary of all IBD and IBD-like backgrounds in THEIA25 for visible energies between 10 MeV and 100 MeV is given in this section. Table 8.3 summarizes the event numbers of all background contributions before and after the different applied cuts. In figure 8.3, the total expected visible energy spectra of IBD and IBD-like backgrounds in THEIA25 as well as the expected $\bar{\nu}_e$ signal from DM annihilation assuming $m_{DM} = 50$ MeV are shown.
The reactor electron antineutrino background is neglected above $E_{vis} > 10$ MeV due to the small event number of $N_{reactor} < 1.2$, but sets the lower edge of the visible energy window to 10 MeV. The DSNB is present for visible energies from 10 MeV to around 35 MeV and results in $N^{fid}_{DSNB} = 18.3 \pm 7.3$ background events for the fiducial case. Atmospheric $\bar{\nu}_e$ interacting via CC on protons are the dominant IBD background for $E_{vis} \gtrsim 30$ MeV with an expected event number of $N_{atmoCC,\bar{\nu}_e+p} = 86.9 \pm 21.7$. The atmospheric $\nu_e/\bar{\nu}_e$ CC background on ^{16}O with $N_{atmoCC,\bar{\nu}_e+^{16}\text{O}} = 17.9 \pm 4.5$ occurs for $E_{vis} \gtrsim 45$ MeV. In contrast to that, atmospheric $\nu_e/\bar{\nu}_e$ interacting through CC on ^{12}C with $N_{atmoCC,\nu_e/\bar{\nu}_e+^{12}\text{C}} \ll 0.6$ are negligible in THEIA25. The CC background of atmospheric $\nu_\mu/\bar{\nu}_\mu$ can be neglected is this study after applying the discrimination cut between e-like and μ-like events. Atmospheric NC events represent the dominant background in the whole visible energy region from 10 MeV to 100 MeV. $N_{atmoNC} = 2054.8 \pm 595.9$ IBD-like background events are expected in THEIA25. The muon-induced background of cosmogenic isotopes due to ^{9}Li

[15] The efficiency due to the application of the muon veto $\epsilon_{\mu \, veto} = 99.0$ % and the discrimination efficiency between e-like and μ-like events $\epsilon_{e-like} = 99.4$ % is also considered.

Table 8.3.: Number of background events in THEIA25 for visible energies between 10 MeV and 100 MeV and after 10 years of data taking. The table summarizes all IBD backgrounds (reactor background, fiducial case of DSNB, atmo. CC of $\bar{\nu}_e$ on p) and IBD-like backgrounds (atmo. CC of $\nu_e/\bar{\nu}_e$ on ^{12}C/^{16}O, atmo. $\nu_\mu/\bar{\nu}_\mu$ CC, atmo. NC, cosmogenic isotopes, fast neutrons) discussed in section 8.3. The second column represents the event numbers before cuts are applied. The third column gives the event numbers after applying the discrimination cut between e-like and μ-like events. The fourth column contains the event numbers after the IBD cuts. The fifth column gives the event numbers and their uncertainties after the cut due to the application of the muon veto, which are also shown in figure 8.3. The cuts are applied consecutively from left to right in the table. The last column represents the visible energy region, where the background events occur.

	no cuts	after disc. cut ($\epsilon_{e-like} = 99.4$ %)	after IBD cuts ($\epsilon_{IBD} = 69.7$ %)	after cut due to muon veto ($\epsilon_{\mu\,veto} = 99.0$ %)	typ. visible energies
Reactor background	1.7	1.7	1.2	< 1.2	< 12 MeV
DSNB (fid.)	26.7	26.5	18.5	18.3 ± 7.3	10 MeV to 35 MeV
Atmo. CC ($\bar{\nu}_e + p$)	126.7	126.0	87.8	86.9 ± 21.7	15 MeV to 100 MeV
Atmo. CC ($\nu_e/\bar{\nu}_e + {}^{12}$C)	0.8	$\ll 0.6$	$\ll 0.6$	$\ll 0.6$	-
Atmo. CC ($\nu_e/\bar{\nu}_e + {}^{16}$O)	26.1	25.9	18.1	17.9 ± 4.5	45 MeV to 100 MeV
Atmo. $\nu_\mu/\bar{\nu}_\mu$ CC	750	4.5	$\ll 3.1$	$\ll 3.1$	-
Atmo. NC	25398		2075.6	2054.8 ± 595.9	10 MeV to 100 MeV
Cosmogenic ^{9}Li	319.5		162.3	< 1.6	< 12 MeV
Fast neutron	347	345	23.1	22.9 ± 4.5	10 MeV to 100 MeV

only occurs for $E_{vis} < 12$ MeV and is reduced to a negligible level of $N_{^9\mathrm{Li}} < 1.6$ events after applying the muon veto cut introduced in section 8.3.5. The fast neutron background with $N_{FN} = 22.9 \pm 4.5$ events is present in the whole visible energy region.

The number of background events in THEIA25, except of the fast neutron background, is increased by a factor of 1.2 to 3 compared to JUNO mainly because of two reason: the fiducial volume and the atmospheric neutrino flux. Due to the larger number of free protons in the larger fiducial volume of THEIA25, the number of DSNB and atmospheric CC and NC background events is increased by around 20 %. The atmospheric CC and NC background is furthermore enhanced because of the two times larger atmospheric neutrino flux at SURF compared to the location of JUNO. The detection efficiencies of IBD and atmospheric NC events are very similar for THEIA25 and JUNO and don't yield larger background contributions. The fast neutron background in THEIA25 is smaller than in JUNO, since the muon flux is smaller because of the larger rock overburden at SURF.

8.4. Background Reduction in THEIA

Backgrounds still dominate the visible energy spectrum of THEIA25 despite the reduction due to the application of IBD selection cuts, the discrimination cut between e-like and μ-like events, and the muon veto cut. Therefore, additional methods to further reduce background events were studied in this thesis. These additional background reduction methods could suppress non-IBD backgrounds by around 99 %, while the survival efficiency of IBD events would exceed 97 %.
The basic approach is to use THEIA's capability to separate Cherenkov from scintillation light to discriminate between IBD and IBD-like events, especially between the IBD signal and IBD-like atmospheric NC and fast neutron events. This allows on the one hand the reconstruction of the Cherenkov ring pattern, which will be discussed in detail in section 8.4.1, and on the other hand the evaluation of the ratio of reconstructed Cherenkov to scintillation photons, which will be presented in section 8.4.2.

In a WbLS detector such as THEIA, there are three different properties that can be used to effectively and precisely separate Cherenkov and scintillation light as introduced in the beginning of the chapter: the time difference between Cherenkov and scintillation photons at the photosensor[16], the wavelength difference of a fraction of Cherenkov photons to scintillation photons, and the difference between the Cherenkov ring pattern and the isotropic scintillation light emission. A combination of these three properties and suitable fast and wavelength-sensitive photosensors provide an excellent separation power [6]. Therefore, perfect separation between Cherenkov and scintillation photons is assumed for THEIA's sensitivity estimation in this work.

8.4.1. Cherenkov Ring Counting

The number of Cherenkov rings created by the prompt signal of an event can be used to discriminate IBD against IBD-like background events. For an IBD event, one Cherenkov ring is expected. In contrast to that, no Cherenkov rings are expected for atmospheric NC and fast neutron events [301]. A Cherenkov ring produced by a simulated IBD event in THEIA25 is shown in figure D.11 of the appendix as example.
In IBD events, a single Cherenkov ring is created due to the energy deposition of the charged positron.
In contrast to that, an uncharged fast neutron doesn't create Cherenkov photons itself.

[16] The separation performance due to the time difference strongly depends on the TTS of the photosensors, which smears the hit times of Cherenkov and scintillation photons.

Nevertheless, a proton that is scattered off a fast neutron in the detector could create Cherenkov photons and a Cherenkov ring, if its kinetic energy is above the Cherenkov threshold of $E_{p,th.} \approx 460$ MeV for protons in THEIA[17]. Moreover, neutrons can scatter on ^{16}O nuclei and excite the oxygen nuclei. Gammas with around 6 MeV emitted in the de-excitation of ^{16}O (more details are given in section 8.3.4) can scatter on free electrons due to the Compton effect. These electrons can have kinetic energies to exceed the Cherenkov threshold for electrons of $E_{e,th.} \approx 0.25$ MeV in THEIA25 and produced Cherenkov photons. Since most of the recoiling protons of fast neutron events are below the Cherenkov threshold and the number of Cherenkov photons produced by electrons is usually too small to reconstruct a Cherenkov ring, no Cherenkov rings are expected in general per fast neutron event.
IBD-like atmospheric NC events can contain multiple final products, mainly neutrons, protons and gammas (see section 8.3.4), that deposit energy in the prompt time window. Protons (and protons being scattered off neutrons) must have kinetic energies above the Cherenkov threshold of around 460 MeV to create Cherenkov rings in THEIA. Gammas can scatter on free electrons due to the Compton effect, which create Cherenkov photons as discussed above. However, the number of produced Cherenkov photons is usually too small to create a Cherenkov ring.

The efficiency of a cut on the number of Cherenkov rings per event to reduce non-IBD backgrounds in THEIA25 is determined in the following. Therefore, IBD and atmospheric NC events that passed the IBD selection cuts described in section 8.2 and 8.3.4 are analyzed further. Additionally, 5,000 neutron events representing the fast neutron background have been simulated with the RAT-PAC simulation tool for the THEIA25 detector configuration. This results in around 2,700 neutron events with visible energies (quenched deposited energies) from 10 MeV to 100 MeV and within a fiducial volume defined by $\rho < 14.4$ m and $|z| < 14.4$ m.
A simple approach to determine the number of Cherenkov rings per event is used here, since a detailed reconstruction of the event topology goes beyond the possibilities of this study. So, the number of p.e. from Cherenkov light $N_{pe,cheren}$ in the prompt time window for each initial particle of an event is calculated from the simulation data. The condition that a Cherenkov ring is discernible in THEIA25 is set to $N_{pe,cheren} > 90$ p.e.. It is assumed that a positron with $E_{vis} = 10$ MeV creates a sufficiently bright Cherenkov ring. Such positron produces on average 90 p.e. from Cherenkov light due to the Cherenkov light yield of $LY_{cheren} = 9$ p.e./MeV in THEIA25.

The number of Cherenkov rings per event is calculated for IBD, atmospheric NC and fast neutron events based on the condition defined above and listed in table 8.4.
Only events with exactly one Cherenkov ring pass the Cherenkov ring counting cut. This results in total survival efficiencies of $\epsilon_{IBD,ring} = 98.7$ % for IBD events, $\epsilon_{atmoNC,ring} = 2.9$ % for atmospheric NC events and $\epsilon_{FN,ring} = 10.0$ % for fast neutron events and agrees well with the expectations. The cut efficiencies as function of the visible energy are shown in figure 8.7.
The survival efficiency of IBD events due to Cherenkov ring counting cut is only reduced from 100 % for events with $E_{vis} \lesssim 15$ MeV, since some of these lower energetic events don't fulfill the Cherenkov ring condition. Fast neutron and especially atmospheric NC background events are strongly suppressed by the Cherenkov ring counting cut in the

[17] The criterion for the emission of Cherenkov photons in a medium is $v > c/n$ with the velocity of the particle in this medium v, the speed of light in vacuum c and the refractive index of the medium n [334]. Due to the refractive index of the WbLS in THEIA25 of $n = 1.347$ at wavelength of 380 nm, the threshold velocity is $v_{th.} \approx 2.22 \cdot 10^8$ m/s. The threshold for the kinetic energy of a particle to produce Cherenkov light is then $E_{kin,th.} = \left[(1 - (v_{th.}/c)^2)^{-1/2}\right] m_0 c^2$, which results in a Cherenkov threshold for the kinetic energy of a proton of $E_{p,th.} \approx 460$ MeV.

Table 8.4.: Number of IBD, atmospheric NC and fast neutron events depending on the number of Cherenkov rings N_{ring} per event. The condition that a Cherenkov ring is discernible in THEIA25 is set to $N_{pe,cheren} > 90$ p.e.. In total, 13948 IBD, 8576 atmospheric NC and 2701 fast neutron events were analyzed.

	events with $N_{ring} = 0$	events with $N_{ring} = 1$	events with $N_{ring} \geq 2$
IBD	179	13769	0
Atmo. NC	8324	252	0
Fast neutron	2430	271	0

whole visible energy region from 10 MeV to 100 MeV.

With the energy-dependent cut efficiencies $\epsilon_{ring}(E_{vis})$ shown in figure 8.7, the resulting signal and background spectra after the Cherenkov ring counting cut are calculated with the spectra shown in figure 8.3. The cut efficiency $\epsilon_{IBD,ring}$ for IBD events is applied to the signal spectra and the IBD backgrounds (DSNB and atmospheric CC background of $\bar{\nu}_e + p$). Moreover, it is also applied to the atmospheric CC background of $\bar{\nu}_e$ on ^{16}O, since the prompt signal is mainly caused by the energy deposition of the positron similar to IBD events. This conservative assumption might slightly overestimate the atmospheric CC background on ^{16}O. The cut efficiency $\epsilon_{atmoNC,ring}$ is applied to the atmospheric NC background spectrum, whereas $\epsilon_{FN,ring}$ is applied to the fast neutron background spectrum. The total spectrum in THEIA25 after the Cherenkov ring counting cut is shown in figure 8.8.
The resulting event numbers are $N_{DSNB}^{fid,ring} = 16.7 \pm 6.7$ events for the fiducial case of the DSNB (low case: $N_{DSNB}^{low,ring} = 9.9 \pm 4.0$, high case: $N_{DSNB}^{high,ring} = 24.8 \pm 9.9$), $N_{atmoCC,\bar{\nu}_e+p}^{ring} = 86.8 \pm 21.7$ for the atmospheric CC background of $\bar{\nu}_e + p$, $N_{atmoCC,\bar{\nu}_e+^{16}\mathrm{O}}^{ring} = 17.9 \pm 4.5$ for the atmospheric CC background of $\bar{\nu}_e + ^{16}$O, $N_{atmoNC}^{ring} = 60.4 \pm 17.5$ for the atmospheric NC background and $N_{FN}^{ring} = 1.5 \pm 0.3$ for the fast neutron background.

As a result, atmospheric NC and fast neutron events can be significantly reduced by the discussed Cherenkov ring counting cut without any relevant loss (only 1.3 %) in IBD signal efficiency. Even if Cherenkov and scintillation photons could not be perfectly separated, advanced reconstruction methods should be able to resolve the ring pattern and the number of Cherenkov rings per event. Nevertheless, since no reconstruction of the event topology is performed in this study, the condition for a Cherenkov ring of $N_{pe,cheren} > 90$ p.e. might be optimistic and the cut efficiencies overestimated. More robust cut efficiencies of the Cherenkov ring counting cut in THEIA25 can only be determined after reconstructing the ring pattern.

8.4.2. Cherenkov to Scintillation Ratio

Besides the Cherenkov ring counting cut, WbLS detectors like THEIA provide a unique discrimination technique based on the C/S ratio. It is defined as the ratio of the total number of p.e. from Cherenkov light in the prompt time window to the total number of p.e. from scintillation light in the prompt time window and depends on the particle type. The prompt positron of IBD events features a comparably high C/S ratio. In contrast to that, the final products of atmospheric NC events are mostly hadronic and emit no or comparably few Cherenkov photons like discussed in the previous section. This is also the case for fast neutron events. So, comparably small C/S ratios are expected in general for atmospheric NC and fast neutron events, which allows to discriminate them against IBD events.

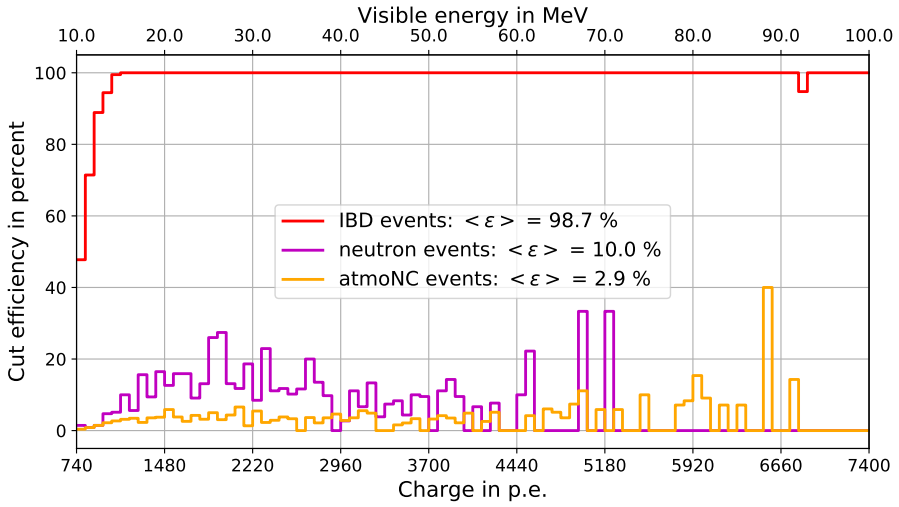

Figure 8.7.: Cherenkov ring counting cut efficiencies in THEIA25 of IBD, IBD-like atmospheric NC and fast neutron events as function of the charge and visible energy, respectively. Only events with one single Cherenkov ring pass the cut. The total efficiency averaged over the visible energy region $\langle\epsilon\rangle$ is shown for each event type. The efficiencies are displayed in bins of 74 p.e. corresponding to 1 MeV.

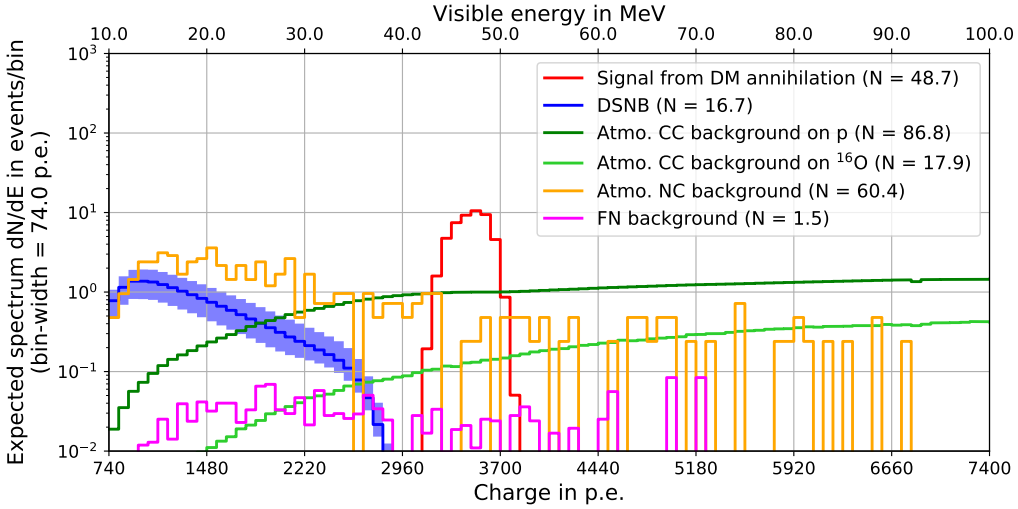

Figure 8.8.: Total expected visible energy spectrum after the Cherenkov ring counting cut in THEIA25 for 10 years of data taking, a fiducial volume of 18.7 kt and visible energies from 10 MeV to 100 MeV. All events pass the Cherenkov ring counting cut and the IBD selection cuts. The DSNB is shown in blue (solid line represents fiducial case, blue region is confined by low and high case), atmospheric CC background of $\bar{\nu}_e + p$ is displayed in dark green and atmospheric CC background of $\nu_e/\bar{\nu}_e + {}^{16}\mathrm{O}$ is shown in light green. The atmospheric NC background and the fast neutron background are shown in orange and magenta, respectively. The signal spectrum assuming the currently best 90 % C.L. upper limit of the DM annihilation cross section of Super-K is displayed in red exemplarily for $m_{DM} = 50$ MeV.

To determine the discrimination power of THEIA25 due to the C/S ratio, two independent studies have been performed. In the first study, the C/S ratio of IBD, atmospheric NC and fast neutron events that pass the IBD selection cuts are studied. The Cherenkov ring counting cut is not taken into account to evaluate the discrimination efficiencies of the C/S ratio independently. In the second study, only events that pass both cuts, the IBD selection cuts as well as the Cherenkov ring counting cut, are considered.

C/S Ratio Cut only

Here, the C/S ratio is calculated from the simulation data for each IBD, atmospheric NC and fast neutron event that passes the IBD selection cuts of section 8.2. The C/S ratios of IBD and IBD-like atmospheric NC events[18] are displayed as function of the charge/visible energy in figure 8.9. For visible energies above around 23 MeV ($\widehat{=}$1700 p.e.), the C/S ratios show the expected behavior and IBD events with larger C/S ratios can be clearly separated from atmospheric NC events with smaller C/S ratios. Below around 23 MeV ($\widehat{=}$1700 p.e.), most of the atmospheric NC events can also be clearly discriminated from IBD events, but some atmospheric NC events have C/S ratios similar to IBD events. In these events, the energy deposition in the prompt time window is dominated by gammas emitted in the de-excitation processes of ^{16}O described in section 8.3.4. These gammas can scatter on free electrons due to the Compton effect, which produce Cherenkov photons. This leads to a C/S ratio comparable to IBD events.

To specify the discrimination power of THEIA25, event selection criteria based on the C/S ratio distributions of figure 8.9 are determined with the goal to maximize the signal to background ratio $S/\sqrt{S+B}$ [19]. Due to the C/S ratio distributions shown in figure 8.9, a cut function $f(Q)$ is defined as function of the charge Q to discriminate between IBD and atmospheric NC events:

$$f(Q) = \begin{cases} a + b \cdot Q & \text{, for } Q < Q_1, \\ c & \text{, for } Q \geq Q_1. \end{cases} \tag{8.11}$$

A constant cut function $f(Q) = c$ is assumed for $Q \geq Q_1$, since C/S ratios of IBD and atmospheric NC events clearly differ above charges of around 1700 p.e.. For $Q < Q_1$, a linear cut function specified by the cut parameters a and b is assumed. The cut parameter b is given as $b = (c-a)/Q_1$ to ensure that $f(Q_1) = a + b \cdot Q_1 = c$.
The parameter c is set to $c = 0.101$. Then, six different values of $Q_1 = 1500$ p.e., 1600 p.e., 1700 p.e., 1800 p.e., 1900 p.e., 2000 p.e. are tested. For each value of Q_1, the cut parameter a is scanned from 0.101 to 0.3 in steps of 0.001 to find the value of a that maximizes $S/\sqrt{S+B}$.
As a result, the best signal to background ratio of $S/\sqrt{S+B} = 2.291$ and therefore the most efficient discrimination based on the C/S ratio cut can be achieved with $Q_1 = 1,700$ p.e., $a = 0.196$ and $c = 0.101$ (b is then given by $b = -5.59 \cdot 10^{-5}$ p.e.$^{-1}$). The resulting cut function $f(Q)$ is also displayed in figure 8.9. All events with C/S ratios above this cut function pass the C/S ratio cut. The survival efficiencies corresponding to the determined cut function are shown in figure 8.9 as function of the charge/visible energy. Here, also the cut efficiency of fast neutron events is displayed. The total cut efficiencies of the C/S ratio cut are $\epsilon_{IBD,C/S} = 12995/13948 = 93.2$ % for IBD events, $\epsilon_{atmoNC,C/S} = 26/8576 = 0.3$ % for IBD-like atmospheric NC events and $\epsilon_{FN,C/S} = 5/2701 = 0.2$ % for fast neutron events.

[18] The C/S ratios of neutron events are distributed similar to C/S ratios of atmospheric NC events and are not shown in figure 8.9 for reasons of clarity.
[19] S and B represent the number of signal and background events after applying the C/S ratio cut.

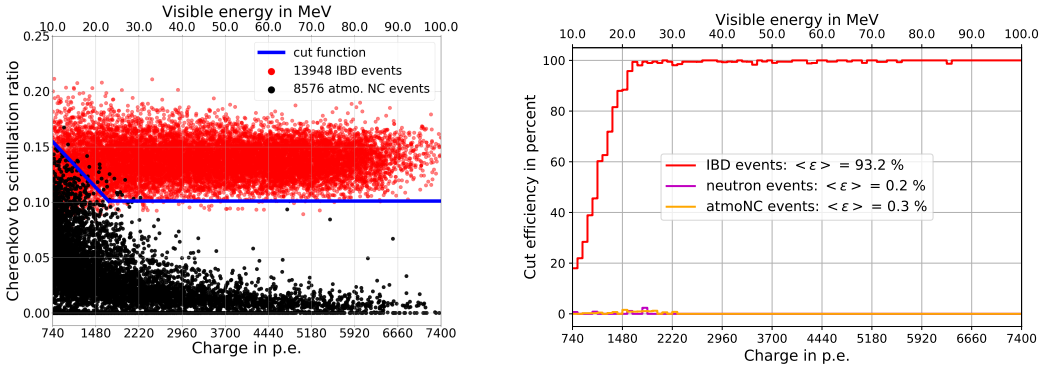

Figure 8.9.: Left: C/S ratio of IBD and atmospheric NC events as function of the charge and visible energy, respectively. IBD events are shown as red dots, atmospheric NC events as black dots. The cut function $f(Q) = 0.196 - 5.59 \cdot 10^{-5} \cdot Q[\text{p.e.}]$ for $Q < 1700$ p.e. and $f(Q) = 0.101$ for $Q \geq 1700$ p.e. is displayed as blue line. Right: C/S ratio cut efficiencies in THEIA25 of IBD, IBD-like atmospheric NC and fast neutron events as function of the charge and visible energy, respectively. The cut efficiencies are determined with the cut function from above. The total efficiency averaged over the visible energy region $\langle\epsilon\rangle$ is shown for each event type. The efficiencies are displayed in bins of 74 p.e. corresponding to 1 MeV.

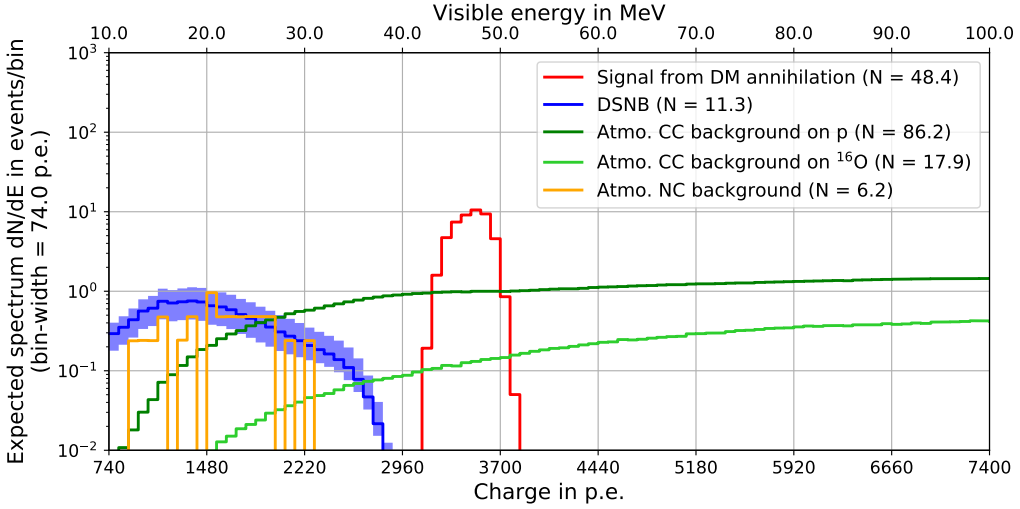

Figure 8.10.: Total expected visible energy spectrum after the C/S ratio cut in THEIA25 for 10 years of data taking, a fiducial volume of 18.7 kt and visible energies from 10 MeV to 100 MeV. All events pass the C/S ratio cut and the IBD selection cuts. The DSNB is shown in blue (solid line represents fiducial case, blue region is confined by low and high case), atmospheric CC background of $\bar{\nu}_e + p$ is displayed in dark green and atmospheric CC background of $\nu_e/\bar{\nu}_e + {}^{16}\text{O}$ is shown in light green. The atmospheric NC background is shown in orange. The signal spectrum assuming the currently best 90 % C.L. upper limit of the DM annihilation cross section of Super-K is displayed in red exemplarily for $m_{DM} = 50$ MeV.

The background of fast neutron and atmospheric NC events can be efficiently reduced by the C/S ratio cut in the whole visible energy region between 10 MeV and 100 MeV. Especially above visible energies of around 23 MeV ($\widehat{=}$1700 p.e.), IBD events and IBD-like background events can be nearly perfectly separated as figure 8.9 indicates. For $E_{vis} \lesssim 23$ MeV, the discrimination power decreases, since C/S ratios of IBD and atmospheric NC events overlap. Therefore, the survival efficiency of IBD events decreases from 23 MeV to 10 MeV.

The energy-dependent cut efficiencies $\epsilon_{C/S}(E_{vis})$ of figure 8.9 and the spectra shown in figure 8.3 are used to calculate the signal and background spectra after the C/S ratio cut (similar to section 8.4.1). The resulting spectra in THEIA25 after 10 years of data taking are shown in figure 8.10.
The numbers of background events are $N_{DSNB}^{fid,C/S} = 11.3 \pm 4.5$ events for the fiducial case of the DSNB (low case: $N_{DSNB}^{low,C/S} = 6.7 \pm 2.7$, high case: $N_{DSNB}^{high,C/S} = 17.2 \pm 6.9$), $N_{atmoCC,\bar{\nu}_e+p}^{C/S} = 86.2 \pm 21.5$ for the atmospheric CC background of $\bar{\nu}_e + p$, $N_{atmoCC,\bar{\nu}_e+^{16}\mathrm{O}}^{C/S} = 17.9 \pm 4.5$ for the atmospheric CC background of $\bar{\nu}_e + {}^{16}\mathrm{O}$, $N_{atmoNC}^{C/S} = 6.2 \pm 1.8$ for the atmospheric NC background and $N_{FN}^{C/S} < 0.1$ for the fast neutron background.
IBD-like atmospheric NC backgrounds events can be reduced very effectively with the C/S ratio cut. The background spectrum after the C/S ratio cut only appears at visible energies below around 30 MeV. Furthermore, the fast neutron background is suppressed to a negligible level by the C/S ratio cut. So, the C/S ratio cut of THEIA25 provides an excellent discrimination power of IBD events against atmospheric NC and fast neutron events. In this study, the C/S ratio cut is applied solely without taking into account the Cherenkov ring counting cut, which shows THEIA's ability to reduce background events even without reconstructing the Cherenkov ring pattern.

Cherenkov Ring Counting and C/S Ratio Cut

Here, the C/S ratios of events that have passed the Cherenkov ring counting cut, i.e. events with one single Cherenkov ring specified by $N_{p.e.,cheren} \geq 90$ p.e. as described in section 8.4.1, are analyzed. The C/S ratios of these IBD, atmospheric NC and fast neutron events are calculated and displayed in figure 8.11 as function of the charge and visible energy, respectively. By comparing the C/S ratios of figure 8.9 and 8.11, the reduction due to the Cherenkov ring counting cut is clearly visible. Atmospheric NC events with C/S ratios smaller than 0.02 as well as events with visible energies below around 30 MeV and comparably small C/S ratios (about 0.05 to 0.1) are cut away by the Cherenkov ring counting cut, since too few Cherenkov photons are produced to create a Cherenkov ring.
To specify the discrimination power of THEIA25 due to the C/S ratios of figure 8.11, an event selection condition is determine to maximize the signal to background ratio $S/\sqrt{S+B}$. Therefore, a constant cut function $g(Q) = c$ is defined to discriminate IBD against atmospheric NC and fast neutron events. To determine the cut parameter c that maximizes the signal to background ratio, c is scanned from 0.05 to 0.20 with steps of 0.001. A maximal signal to background ratio of $S/\sqrt{S+B} = 2.293$ is achieved with the cut function $g(Q) = 0.104$, which is also shown in figure 8.11. Only events with C/S ratio above the cut function pass the C/S ratio cut. The total cut efficiencies of the C/S ratio cut introduced here and the Cherenkov ring counting cut of section 8.4.1 are displayed in figure 8.11 as function of the charge and visible energy, respectively. Most of atmospheric NC and fast neutron background events are cut away, especially above visible energies of 30 MeV. The cut efficiency of IBD events is nearly 100 % in the whole visible energy region, only slightly decreasing for $E_{vis} \lesssim 20$ MeV. Particularly below 30 MeV, the combined Cherenkov ring counting and C/S ratio cut provides a much better IBD cut

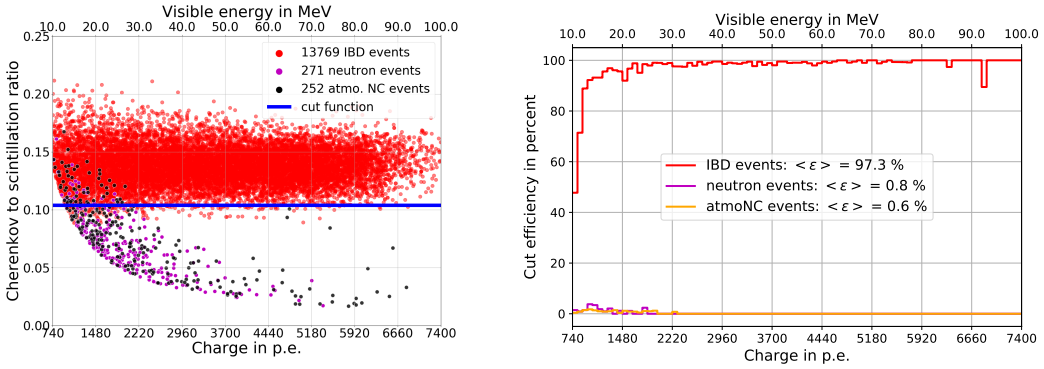

Figure 8.11.: Left: C/S ratio of IBD, atmospheric NC and fast neutron events as function of the charge and visible energy, respectively. All events have passed the IBD selection cuts described in section 8.2 and the Cherenkov ring counting cut introduced in section 8.4.1. IBD events are shown as red dots, atmospheric NC events as black dots and fast neutron events as magenta dots. The cut function $g(Q) = 0.104$ is displayed as blue line. Right: Total cut efficiencies of Cherenkov ring counting and C/S ratio cut in THEIA25 of IBD, IBD-like atmospheric NC and fast neutron events as function of the charge and visible energy, respectively. The total efficiency averaged over the visible energy region $\langle\epsilon\rangle$ is shown for each event type. The efficiencies are displayed in bins of 74 p.e. corresponding to 1 MeV.

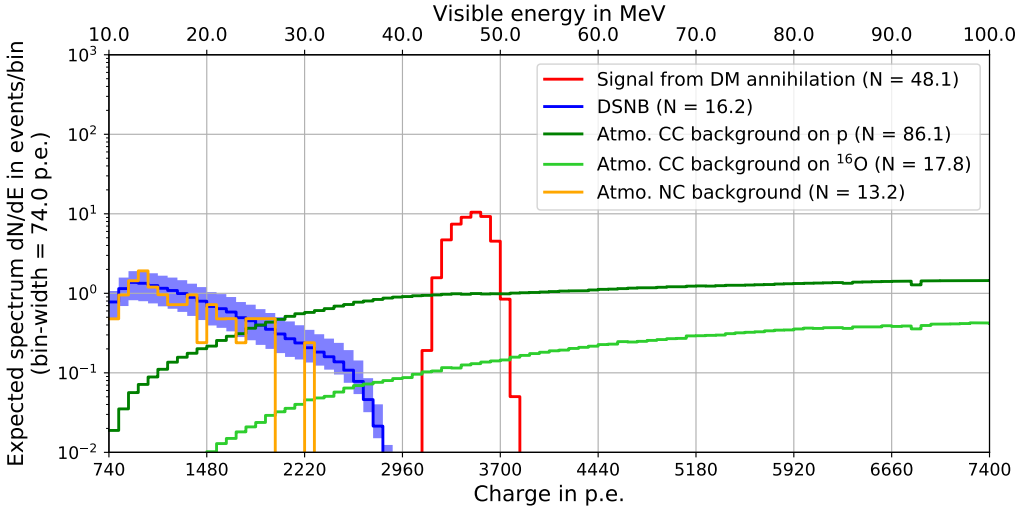

Figure 8.12.: Total expected visible energy spectrum after the Cherenkov ring counting and C/S ratio cut in THEIA25 for 10 years of data taking, a fiducial volume of 18.7 kt and visible energies from 10 MeV to 100 MeV. All events pass the Cherenkov ring counting cut, C/S ratio cut and the IBD selection cuts. The DSNB is shown in blue (solid line represents fiducial case, blue region is confined by low and high case), atmospheric CC background of $\bar{\nu}_e + p$ is displayed in dark green and atmospheric CC background of $\nu_e/\bar{\nu}_e + {}^{16}\mathrm{O}$ is shown in light green. The atmospheric NC background is shown in orange. The signal spectrum assuming the currently best 90 % C.L. upper limit of the DM annihilation cross section of Super-K is displayed in red exemplarily for $m_{DM} = 50$ MeV.

efficiency than the C/S ratio cut only. The total cut efficiencies averaged over the visible energy region from 10 MeV to 100 MeV are $\epsilon_{IBD,ring+C/S} = 13570/13948 = 97.3$ % for IBD events, $\epsilon_{atmoNC,ring+C/S} = 55/8576 = 0.6$ % for IBD-like atmospheric NC events and $\epsilon_{FN,ring+C/S} = 22/2701 = 0.8$ % for fast neutron events.

The energy-dependent total cut efficiencies $\epsilon_{ring+C/S}$ and the spectra after the IBD selection cuts of figure 8.3 are used to calculate the signal and background spectra after the Cherenkov ring counting and C/S ratio cut (similar to section 8.4.1 and the first study of section 8.4.2). The resulting spectra represent the signal and background spectra for THEIA25 after applying all discussed cuts and are shown in figure 8.12 (the signal spectrum is shown exemplarily for a DM mass of 50 MeV. In section E of the appendix, the total expected spectra in THEIA25 for DM masses from 15 MeV to 100 MeV are displayed.) The numbers of background events are $N_{DSNB}^{fid,ring+C/S} = 16.1 \pm 6.4$ events for the fiducial case of the DSNB (low case: $N_{DSNB}^{low,ring+C/S} = 9.6 \pm 3.9$, high case: $N_{DSNB}^{high,ring+C/S} = 24.0 \pm 9.6$), $N_{atmoCC,\bar{\nu}_e+p}^{ring+C/S} = 86.1 \pm 21.5$ for the atmospheric CC background of $\bar{\nu}_e + p$, $N_{atmoCC,\bar{\nu}_e+^{16}\mathrm{O}}^{ring+C/S} = 17.8 \pm 4.5$ for the atmospheric CC background of $\bar{\nu}_e + {}^{16}\mathrm{O}$, $N_{atmoNC}^{ring+C/S} = 13.2 \pm 3.8$ for the atmospheric NC background and $N_{FN}^{ring+C/S} < 0.2$ for the fast neutron background. So, IBD-like atmospheric NC background events can be efficiently reduced by the described cut, especially for $E_{vis} \gtrsim 30$ MeV. Moreover, the fast neutron background is reduced to a negligible level without any relevant loss (only 2.7 %) in IBD signal efficiency. So, non-IBD backgrounds in THEIA25 can be reduced very efficiently by combining the Cherenkov ring counting and C/S ratio cut. It must be mentioned here, that the discrimination power of THEIA25 due to presented C/S ratio cut might slightly decrease, if Cherenkov and scintillation photons are not separated perfectly. However, the discrimination efficiencies could be further improved by using not a simple linear, but more complex, cut function.

As a summary, the numbers of background events in THEIA25 before and after applying the described cuts are listed in table 8.5 for visible energies between 10 MeV and 100 MeV and after 10 years of data taking. Non-IBD backgrounds in THEIA25 can be reduced with excellent efficiency by applying the Cherenkov ring counting and C/S ratio cut. Moreover, the signal to background ratios $S/\sqrt{S+B}$ of each cut are presented. By combining the Cherenkov ring counting cut and the C/S ratio cut, the signal to background ratio can be increased by a factor of 3.6 compared to the signal to background ratio after IBD, muon veto and discrimination cut between e-like and μ-like events. So, THEIA25 strongly profits from its novel technologies like the WbLS target and the fast and wavelength-sensitive photo-sensors, which allows the separation between Cherenkov and scintillation light and the application of selection cuts on the C/S ratio and the number of Cherenkov rings.
Non-IBD backgrounds, especially the atmospheric NC background, could be reduced even more effectively than by PSD in the LS detector JUNO presented in chapter 6. However, it must be noted that perfect separation between Cherenkov and scintillation light is assumed and only the detector simulation of THEIA25 is performed in contrast to JUNO, where also electronics simulation and waveform, vertex and energy reconstruction is considered. The signal to background ratio of THEIA25 is by a factor of around 2 smaller than the signal to background ratio of JUNO mainly because of the comparably larger atmospheric neutrino flux at SURF, which yields the larger irreducible atmospheric CC background in THEIA25. Nevertheless, the WbLS detector THEIA25 would be an excellent detector for indirect DM search with neutrinos because of its exceptional background reduction capability.

Table 8.5.: Number of background events in THEIA25 for visible energies between 10 MeV and 100 MeV, a fiducial mass of 18.7 kt and after 10 years of data taking. The table summarizes IBD backgrounds (fiducial case of the DSNB, atmo. CC of $\bar{\nu}_e + p$) and IBD-like backgrounds (atmo. CC of $\bar{\nu}_e + {}^{16}\mathrm{O}$, atmo. NC, fast neutron) that pass the IBD selection cuts, the muon veto cut and the discrimination cut between e-like and μ-like events. The corresponding event numbers are listed in the second column. In the third column, the event numbers after applying the Cherenkov ring counting cut are listed. The fourth column represents the event numbers after applying the C/S ratio cut (without taking into account the Cherenkov ring cut). In the fifth column, the event numbers after applying all cuts, including Cherenkov ring counting and C/S ratio cut, are shown. The last column represents the visible energy region, where the background events occur.

	before ring and C/S cut	ring cut	C/S cut	all cuts	typ. visible energies
DSNB (fid.)	18.3	16.7	11.3	16.1	$10\ \mathrm{MeV} \leq E_{vis} \lesssim 35\ \mathrm{MeV}$
Atmo. CC $(\bar{\nu}_e + p)$	86.9	86.8	86.2	86.1	$15\ \mathrm{MeV} \lesssim E_{vis} \leq 100\ \mathrm{MeV}$
Atmo. CC $(\nu_e/\bar{\nu}_e + {}^{16}\mathrm{O})$	17.9	17.9	17.9	17.8	$45\ \mathrm{MeV} \lesssim E_{vis} \leq 100\ \mathrm{MeV}$
Atmo. NC	2054.8	60.4	6.2	13.2	$10\ \mathrm{MeV} \leq E_{vis} \lesssim 30\ \mathrm{MeV}$
Fast neutron	22.9	1.5	< 0.1	< 0.2	
$S/\sqrt{S+B}$	0.635	2.029	2.291	2.293	

8.5. THEIA's Sensitivity for Indirect Dark Matter Search

In this section, the sensitivity of THEIA25 to measure electron antineutrinos from DM self-annihilation in the Milky Way via the IBD detection channel as an excess over backgrounds is presented.
The upper limit on the number of signal events from DM self-annihilation in THEIA25 is calculated in section 8.5.1 based on the Bayesian analysis of section 7.1. Section 8.5.2 presents the resulting upper limits on the electron antineutrino flux and on the DM self-annihilation cross section for THEIA25. A comparison of the limit on the DM self-annihilation cross section of THEIA25 with limits of other neutrino experiments is given in section 8.5.3

8.5.1. Bayesian Analysis for THEIA

In order to calculate the upper limit on the number of signal events in THEIA25, the Bayesian analysis introduced in section 7.1 is applied. The sensitivity of THEIA25 is determined for a set of DM masses ranging from $m_{DM} = 15$ MeV to $m_{DM} = 100$ MeV (in steps of 5 MeV) and for visible energies from 12 MeV to 100 MeV [20]. The procedure to calculate the upper limit in THEIA25 is similar to the determination of the upper limits in JUNO. Therefore, only the differences to section 7.1 are described here.
The background-only spectrum of THEIA25 after the Cherenkov ring counting and C/S ratio cut (see section 8.4.2), for the fiducial case of the DSNB and after 10 years of data

[20] This visible energy region corresponds to a charge region from 888 p.e. to 7400 p.e.. The lower edge of the visible energy window is increased from 10 MeV to 12 MeV which suppresses the reactor background to a negligible level without reducing the signal efficiency.

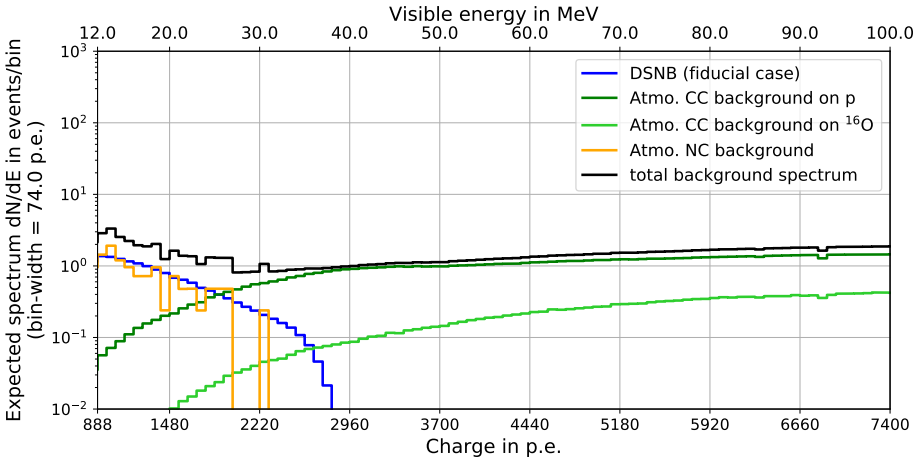

Figure 8.13.: Expected background-only spectrum in THEIA25 after Cherenkov ring counting and C/S ratio cut for a lifetime of 10 years, a fiducial mass of 18.7 kt and visible energies between 12 MeV and 100 MeV. The background spectra are equal to the spectra shown in figure 8.12 (the fiducial case of the DSNB is displayed). The total survival efficiencies of the Cherenkov ring counting and C/S ratio cut are $\epsilon_{IBD,ring+C/S} = 97.3$ %, $\epsilon_{atmoNC,ring+C/S} = 0.6$ % and $\epsilon_{FN,ring+C/S} = 0.8$ %.

taking is shown in figure 8.13 and used to generate datasets of THEIA25. In contrast to JUNO, where CC interactions of atmospheric $\bar{\nu}_e$'s on ^{12}C cause background events, the atmospheric CC background on ^{16}O is considered for THEIA25. So, the expected number of events per bin λ_i and the posterior probability $p\,(S, B|\text{spectrum})$ for THEIA25 depend on the total number of signal and background events S, B_{DSNB} , $B_{atmoCC+p}$, $B_{atmoCC+^{16}\text{O}}$ and B_{atmoNC}. The marginalization of the posterior probability for the set of DM masses given above results in an upper limit on the number of signal events $\tilde{S}_{90}(m_{DM}) = \tilde{S}_{90}(E_{\bar{\nu}_e})$ as function of the DM mass and electron antineutrino energy, respectively. This 90 % upper limit $\tilde{S}_{90}(E_{\bar{\nu}_e})$ is shown in figure 8.14 together with the 68 % and 95 % probability intervals.

8.5.2. Sensitivity of THEIA25

The 90 % upper limit on the monoenergetic $\bar{\nu}_e$ flux $\phi_{\bar{\nu}_e,90\%}(E_{\bar{\nu}_e})$ in THEIA25 is calculated with the 90 % upper limit $\tilde{S}_{90}$ using equation 8.1 and considering the survival efficiency $\epsilon_{IBD,ring+C/S}$ of IBD events due to the application of the Cherenkov ring counting and C/S ratio cut shown in figure 8.11:

$$\phi_{\bar{\nu}_e,90\%}(E_{\bar{\nu}_e}) = \frac{\tilde{S}_{90}(E_{\bar{\nu}_e})}{\sigma_{IBD}(E_{\bar{\nu}_e})\ N_p\ t\ \epsilon_{IBD}\ \epsilon_{\mu\,veto}\ \epsilon_{e-like}\ \epsilon_{IBD,ring+C/S}(E_{\bar{\nu}_e})}. \tag{8.12}$$

The resulting 90 % upper limit on the electron antineutrino flux for THEIA25 is shown in figure 8.15 together with the 68 % and 95 % probability intervals. It represents a model-independent upper limit on a monoenergetic $\bar{\nu}_e$ flux at Earth.

The 90 % upper limit $\langle\sigma_A\,\text{v}\rangle_{90\%}(m_{DM})$ on the DM self-annihilation cross section for THEIA25 can then be calculated with equation 7.12. It is shown in figure 8.16 together with the best currently existing 90 % upper limits of KamLAND and Super-K and with the natural scale of the annihilation cross section $\langle\sigma_A\,\text{v}\rangle_{natural} = 3 \cdot 10^{-26}$ cm^3/s ($\langle\sigma_A\,\text{v}\rangle_{natural}$ is always shown as gray line in following figures).
The 90 % upper limit on the DM self-annihilation cross section for THEIA25 ranges

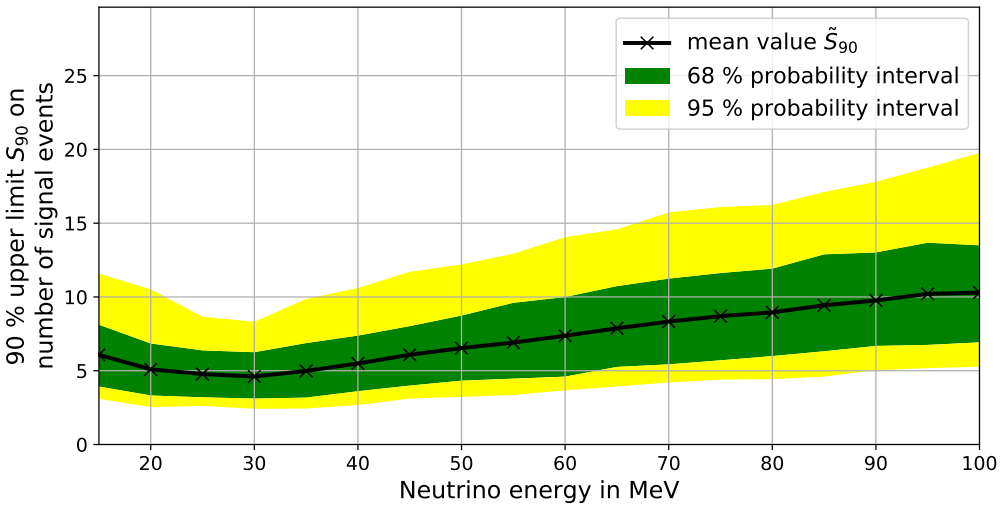

Figure 8.14.: Mean value of the 90 % upper limit on the number of signal events $\tilde{S}_{90}$ in THEIA25 as well as the 68 % and 95 % probability interval as function of the neutrino energy. The mean values and probability intervals are analyzed for DM masses and neutrino energies, respectively, from 15 MeV to 100 MeV in 5 MeV steps.

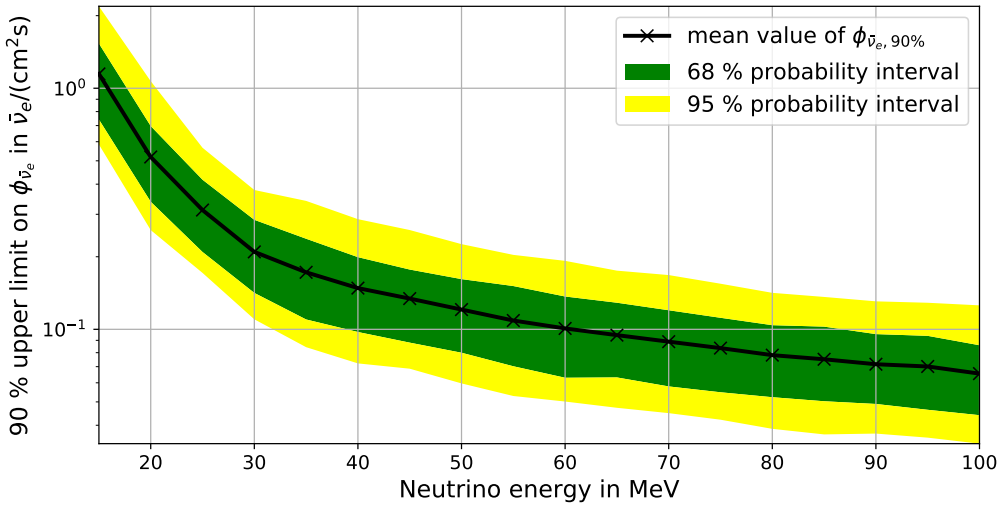

Figure 8.15.: 90 % probability upper limit on a monoenergetic electron antineutrino flux in THEIA25 as function of the neutrino energy. The mean values of $\phi_{\bar{\nu}_e,90\%}$ are displayed in black, the 68 % probability interval is shown in green and the 95 % probability interval in yellow. The mean values and probability intervals are analyzed for neutrino energies from 15 MeV to 100 MeV with steps of 5 MeV.

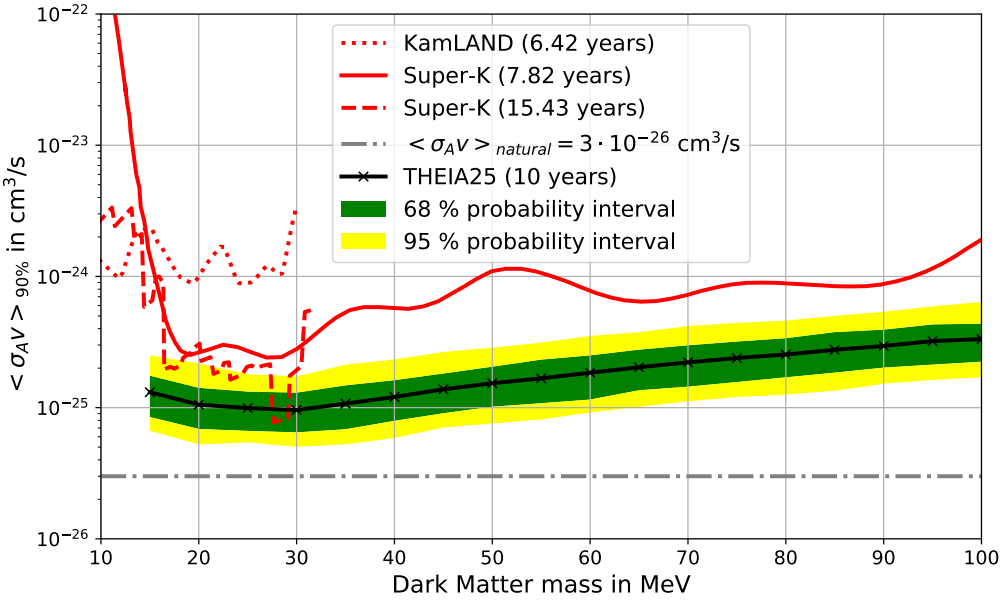

Figure 8.16.: 90 % probability upper limit on the DM self-annihilation cross section $\langle \sigma_A \, \mathrm{v} \rangle$ for the THEIA25 detector. $\langle \sigma_A \, \mathrm{v} \rangle_{90\%}$ for THEIA25 after 10 years of data taking is displayed in black and analyzed for DM masses from 15 MeV to 100 MeV with steps of 5 MeV. The 68 % probability interval is shown in green and the 95 % probability interval in yellow. The best currently existing 90 % C.L. upper limits of KamLAND and Super-K discussed in section 2.4.2 are shown in red. The natural scale of the DM self-annihilation cross section $\langle \sigma_A \, \mathrm{v} \rangle_{natural} = 3 \cdot 10^{-26}$ cm^3/s is displayed as gray line.

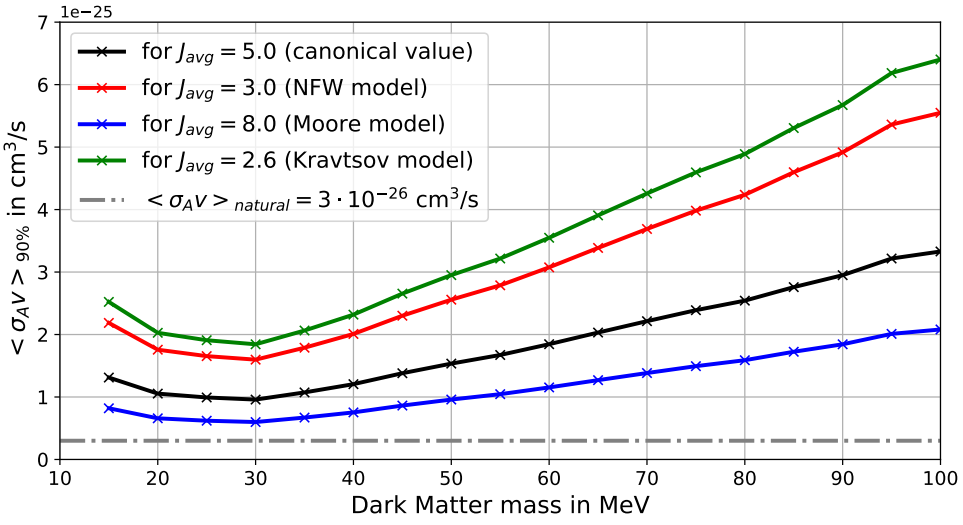

Figure 8.17.: 90 % probability upper limit on the DM self-annihilation cross section $\langle \sigma_A \, \mathrm{v} \rangle$ for the THEIA25 detector for different assumed DM profile models of the Milky Way. $\langle \sigma_A \, \mathrm{v} \rangle_{90\%}$ after 10 years of data taking is displayed assuming $J_{avg}^{Kravtsov} = 2.6$ (green), $J_{avg}^{NFW} = 3.0$ (red) and $J_{avg}^{Moore} = 8.0$ (blue), respectively. The 90 % upper limit of figure 8.16, where $J_{avg} = 5$ is assumed, is shown in black for comparison.

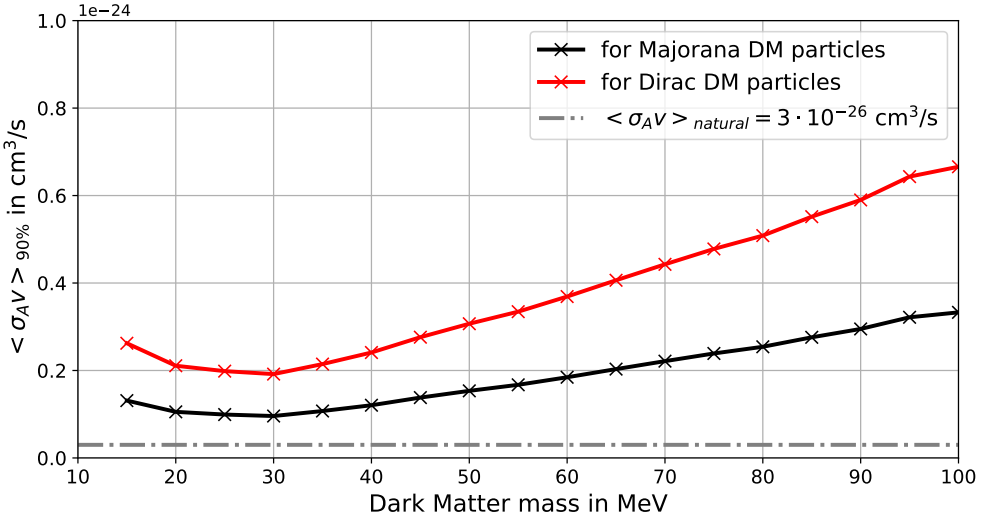

Figure 8.18.: 90 % probability upper limit on the DM self-annihilation cross section $\langle \sigma_A \, \mathrm{v} \rangle$ for the THEIA25 detector assuming Dirac (red) and Majorana (black) DM particles, respectively. The 90 % upper limit for Majorana particles is also shown in figure 8.16.

from $\langle \sigma_A \, \mathrm{v} \rangle_{90\%} (m_{DM} = 30\,\mathrm{MeV}) = 9.6 \cdot 10^{-26}$ cm^3/s to $\langle \sigma_A \, \mathrm{v} \rangle_{90\%} (m_{DM} = 100\,\mathrm{MeV}) = 3.3 \cdot 10^{-25}$ cm^3/s. The upper limit averaged over the DM mass region from 15 MeV to 100 MeV is $\langle \sigma_A \, \mathrm{v} \rangle_{90\%}^{average} = 1.914 \cdot 10^{-25}$ cm^3/s.
The described analysis was also performed assuming prior probabilities of the number of background events defined by equation 7.9 with $\sigma_B = \mu_B/2$, i.e. it is assumed that the uncertainties of the different background contributions are smaller. The resulting 90 % upper limits averaged over the DM mass region from 15 MeV to 100 MeV of both cases match with each other within 0.3 %. So, the choice of σ_B doesn't affect the sensitivity of THEIA25.

THEIA25's Sensitivity for Different DM Properties

$\langle \sigma_A \, \mathrm{v} \rangle_{90\%}$ shown in figure 8.16 is calculated under the assumptions that $J_{avg} = 5$ and DM particles are Majorana particles.
The 90 % upper limit on the DM self-annihilation cross section is also calculated assuming different DM profile models ($J_{avg}^{Kravtsov} = 2.6$, $J_{avg}^{NFW} = 3.0$ and $J_{avg}^{Moore} = 8.0$), which is shown in figure 8.17. $\langle \sigma_A \, \mathrm{v} \rangle_{90\%}$ differs by a factor of around 3 depending on the chosen DM profile model.
The 90 % upper limit on the DM self-annihilation cross section is moreover calculated under the assumption that DM particles are Dirac instead of Majorana particles. The resulting limit assuming Dirac DM particles as well as the limit for Majorana DM particles is shown in figure 8.18 (in both cases $J_{avg} = 5$ is assumed). If DM particles are Majorana particles, the limit on the self-annihilation cross section is more stringent by a factor of around two as expected.

THEIA25's Sensitivity for Different Applied Cuts

The upper limit on the DM self-annihilation cross section of figure 8.16 is analyzed using the signal and background spectra after applying the Cherenkov ring counting and the C/S ratio cut. Applying both cuts leads to the best signal to background ratio of $S/\sqrt{S+B} = 2.293$ as compiled in table 8.5.
To determine the impact of the two different cuts on the resulting 90 % upper limit

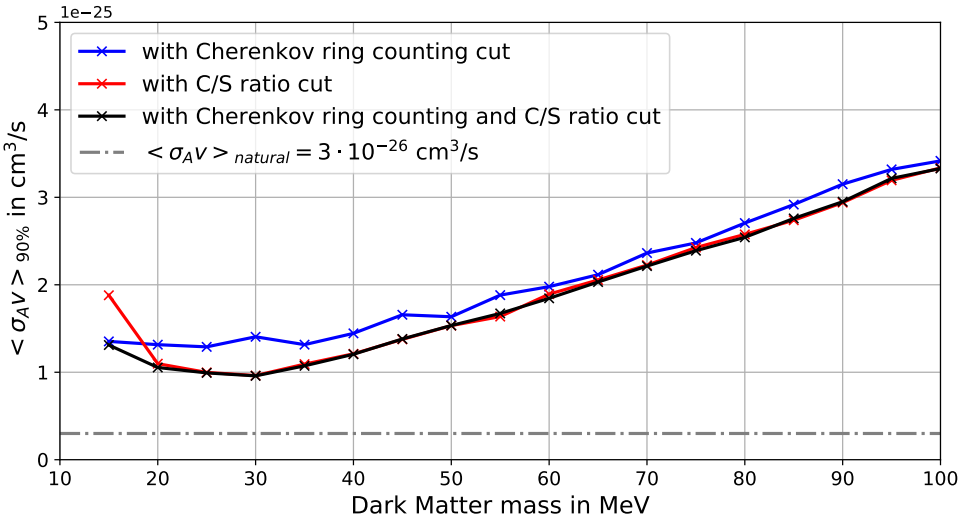

Figure 8.19.: 90 % probability upper limit on the DM self-annihilation cross section $\langle \sigma_A \, \mathrm{v} \rangle$ for the THEIA25 detector applying only the Cherenkov ring counting cut and only the C/S ratio cut, respectively. The upper limits are displayed for applying only the Cherenkov ring counting cut (blue) and for only applying the C/S ratio cut (red). For comparison, $\langle \sigma_A \, \mathrm{v} \rangle_{90\%}$ after applying both cuts already shown in figure 8.16 is displayed in black.

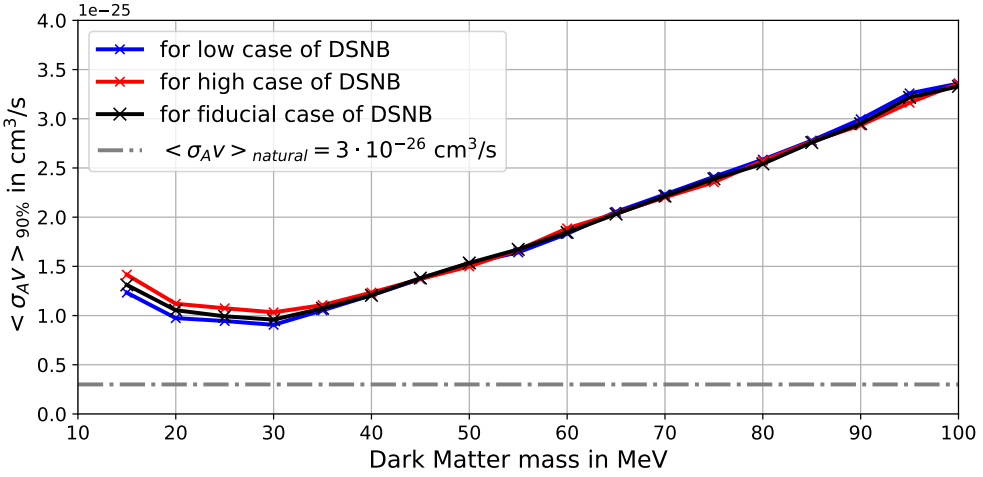

Figure 8.20.: 90 % probability upper limit on the DM self-annihilation cross section $\langle \sigma_A \, \mathrm{v} \rangle$ for the THEIA25 detector for the low (blue) and high (red) case of the DSNB. The 90 % upper limit for the fiducial case (black) of figure 8.16 is also shown.

independently, the analysis described in section 8.5.1 was also performed on the one hand after only applying the Cherenkov ring counting cut introduced in section 8.4.1 and on the other hand after only applying the C/S ratio cut discussed in section 8.4.2. The resulting 90 % upper limits on the DM self-annihilation cross section for the different applied cuts are shown in figure 8.19.
The best 90 % upper limit could be achieved after applying both cuts, the Cherenkov ring counting and C/S ratio cut. The limits after applying the C/S ratio cut only and after applying both cuts agree with each other for $m_{DM} \geq 20$ MeV. For $m_{DM} = 15$ MeV, the limit after only applying the C/S ratio cut is increased by a factor of 1.4. So, the upper limit for these small DM masses is improved by applying the Cherenkov ring counting cut additionally to the C/S ratio cut. The 90 % upper limit after only applying the Cherenkov ring counting cut is by around 10 % worse than the limit after applying both cuts.

THEIA25's Sensitivity for Different DSNB models

So far, the 90 % upper limits for THEIA25 are determined assuming the fiducial case of the DSNB. The same analysis was also performed assuming the low and high case of the DSNB and the resulting 90 % upper limits on the DM self-annihilation cross section are shown in figure 8.20.
The 90 % upper limits clearly differ for DM masses below 35 MeV for the different assumed DSNB models. For the low (high) case, the number of DSNB events is smaller (larger), which results in a better (worse) limit on the DM annihilation cross section. For $m_{DM} >$ 35 MeV, the limits aren't affected by the choice of the DSNB model as expected.

THEIA25's Sensitivity for Different Exposure Times

Here, the dependence of THEIA25's sensitivity on the exposure time is investigated. Therefore, the analysis presented in section 8.5.1 is applied for total exposure times of $t = 1$ year, $t = 5$ years and $t = 20$ years, respectively. The resulting 90 % upper limit on the DM self-annihilation determined with THEIA25 for the different exposure times is presented in figure 8.21. Furthermore, figure 8.21 shows the 90 % upper limits averaged over DM masses from 15 MeV to 100 MeV as function of the exposure times.
The sensitivity of THEIA25 increases, i.e. the 90 % upper limit decreases, for longer exposure times. Especially by increasing the exposure time, i.e. the lifetime of the detector, from $t = 1$ year to $t = 5$ years, the sensitivity could be significantly improved by a factor of 3. Above total exposure times of $t = 10$ years, only a slight improvement of the sensitivity could be gained.

8.5.3. Discussion and Comparison with Limits of other Experiments

Figure 8.22 shows the 90 % upper limits on the DM self-annihilation cross section of THEIA25 and JUNO, which were, for the first time, determined within this thesis. The upper limit of THEIA25 was calculated in this section and shown in figure 8.16. The upper limit of JUNO for a lifetime of 10 years was determined in chapter 7 and presented in figure 7.6. The best currently existing limits in the DM mass region from 10 MeV and 100 MeV of KamLAND and Super-K as well as the prospective upper limit of Hyper-K for a total exposure time of 10 years discussed in section 2.4.2 are also displayed in figure 8.22 for comparison.

THEIA25 could provide an upper limit, which would be a factor of 9 to 37 better than the upper limit of KamLAND in the DM mass region from 15 MeV to 30 MeV mainly because of its larger exposure of 187 kt yr.
Furthermore, the 90 % upper limit on the DM self-annihilation cross section of THEIA25

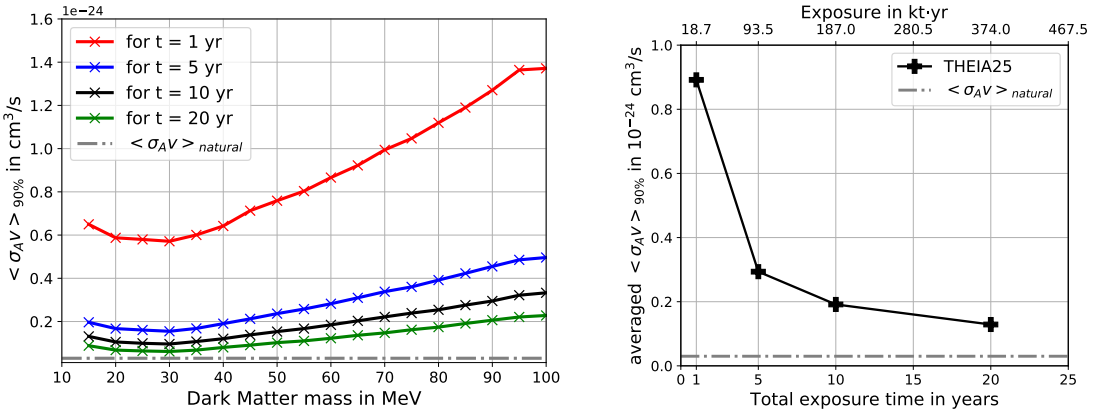

Figure 8.21.: Left: 90 % probability upper limit on the DM self-annihilation cross section $\langle \sigma_A \, \mathrm{v} \rangle$ as function of the DM mass for the THEIA25 detector for different total exposure times t. The upper limits are calculated and shown for $t = 1$ year (red), $t = 5$ years (blue) and $t = 20$ years (green), respectively. For comparison, $\langle \sigma_A \, \mathrm{v} \rangle_{90\%}$ for $t = 10$ years of figure 7.6 is shown in black. Right: 90 % upper limit on the DM self-annihilation cross section of THEIA25 averaged over DM masses from 15 MeV to 100 MeV as function of the total exposure time (and total exposure, respectively).

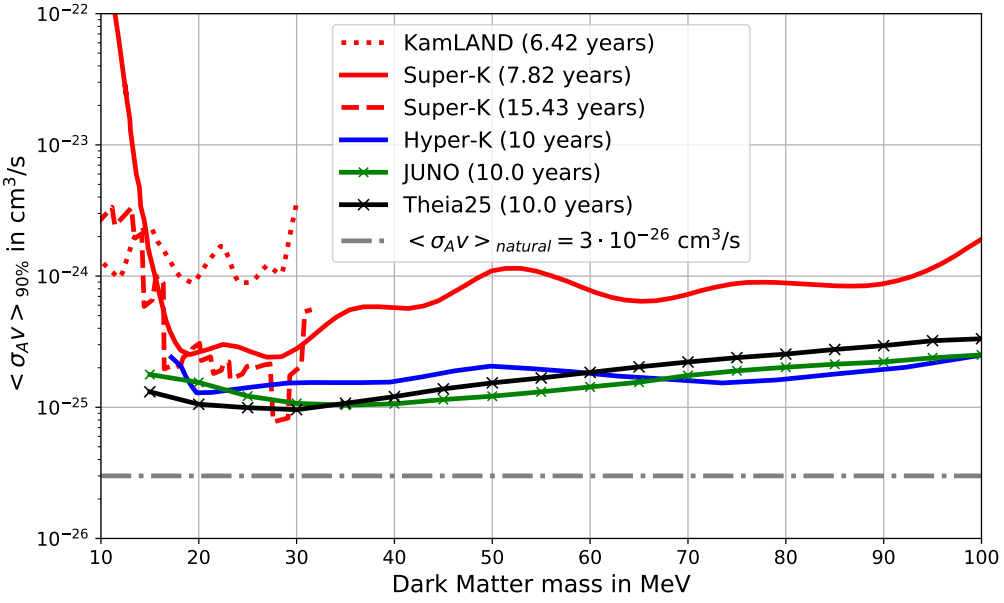

Figure 8.22.: 90 % probability upper limit on the DM self-annihilation cross section $\langle \sigma_A \, \mathrm{v} \rangle$ for the THEIA25 detector compared to limits of JUNO, KamLAND, Super-K and Hyper-K. $\langle \sigma_A \, \mathrm{v} \rangle_{90\%}$ for THEIA25 (black) and JUNO (green), respectively, after a lifetime of 10 years and determined within this thesis are analyzed for DM masses from 15 MeV to 100 MeV with steps of 5 MeV. The 90 % C.L. upper limits of KamLAND (dotted) and Super-K (dashed and solid) discussed in section 2.4.2 are shown in red. The predicted 90 % C.L. upper limit of Hyper-K for a lifetime of 10 years of [121] is displayed in blue.

would be a factor of 2.5 to 11 better than the upper limits of Super-K for 7.82 years and 15.43 years of data taking, respectively (except of the DM mass region between 27.5 MeV and 29.2 MeV due to statistical uncertainties of the Super-K limit, see section 7.3). It was demonstrated that the WbLS detector THEIA25 could reduce non-IBD backgrounds very efficiently compared to Super-K, since it would be able to measure the delayed neutron capture signal of the IBD reaction and, therefore, would benefit from the coincidence between prompt and delayed signal. Moreover, due to the ability to separate Cherenkov from scintillation light, THEIA25 could further reduce non-IBD background events by applying a cut on the number of reconstructed Cherenkov rings per event and by applying a cut on the ratio between Cherenkov and scintillation photons. So, backgrounds in the WbLS detector THEIA25 could be reduced more efficient than in the water Cherenkov detector Super-K, which would yield a better 90 % upper limit on the DM self-annihilation cross section.
The expected sensitivity of THEIA25 would be very similar to JUNO's sensitivity. Below DM masses of 35 MeV, THEIA25 would be slightly more sensitive (by a factor of around 1.3) to measure neutrinos from DM self-annihilation than JUNO, since IBD and atmospheric NC events could be discriminated more effectively in THEIA25. The discrimination performance of the Cherenkov ring counting and C/S ratio cut in THEIA25 described in section 8.4 would be superior to the discrimination performance of the PSD cut in JUNO. It must be mentioned here, that the efficiencies of the Cherenkov ring counting and C/S ratio cut are determined assuming perfect separation between Cherenkov and scintillation light. This might overestimate the discrimination power and, therefore, could slightly overestimate the sensitivity of THEIA25. Above $m_{DM} = 35$ MeV, JUNO provides the better 90 % upper limit on the DM self-annihilation cross section (by a factor of around 1.3) because of the smaller atmospheric CC background. The atmospheric neutrino flux at JUNO site is a factor of around 2 smaller than the atmospheric neutrino flux at SURF (see section 8.3.3), which results in a smaller atmospheric CC background. Nevertheless, THEIA25 with its remarkable background reduction capabilities, which are attributed to the novel used technologies, would provide a sensitivity comparable to JUNO in the observed DM mass region.
THEIA25's sensitivity would be comparable to the sensitivity of the water Cherenkov detector Hyper-K. THEIA25 would profit from the very efficient reduction of background events due to the IBD signal coincidence and the ability to separate between Cherenkov and scintillation light. This would compensate the smaller total exposure (187 kt yr for THEIA25 and 1870 kt yr for Hyper-K) and yield similar sensitivities. Especially for $m_{DM} < 60$ MeV, THEIA25 could provide a higher sensitivity as Hyper-K, since the background of invisible muons can be reduced to a negligible level in THEIA25.

In summary, the proposed detector configuration of THEIA25 described in this thesis would yield a 90 % upper limit on the DM self-annihilation cross section in the DM mass region from 15 MeV to 100 MeV that is a factor of 2.5 to 37 better than the upper limits of KamLAND and Super-K (except for 27.5 MeV$\leq m_{DM} \leq$ 29.2 MeV). Moreover, the sensitivity of THEIA25 would be comparable to the sensitivities of JUNO and Hyper-K.

9. Summary

In this work, the sensitivities of the future neutrino detectors JUNO and THEIA for indirect search of light DM particles with masses ranging from 15 MeV to 100 MeV were determined in detail for the first time. For this purpose, the sensitivities of these two detectors to measure a potential monoenergetic electron antineutrino flux originating from DM self-annihilation in the Milky Way as an excess over backgrounds were studied. It was assumed that DM particles directly annihilate into neutrino-antineutrino pairs with a branching ratio of 100 %. The results of this work demonstrate for the first time that JUNO will provide the highest sensitivity for indirect DM search in the DM mass region between 15 MeV and 100 MeV among existing neutrino detectors. In case of no excess signal is observed, JUNO will set the most stringent upper limit on the DM self-annihilation cross section into neutrinos in the above-mentioned DM mass region. Therefore, JUNO will take a leading role in the indirect search for dark matter particles in the upcoming years. Moreover, it was first shown in this work that the prospective THEIA detector could reach a sensitivity for indirect DM search comparable to JUNO.

In the main part of this work, JUNO's sensitivity for indirect DM search was studied. Electron antineutrinos can be measured with the JUNO detector via the IBD interaction channel with excellent efficiency because of the distinct signature and comparably large neutrino interaction cross section of the IBD. The detection efficiency of IBD events with visible energies between 10 MeV and 100 MeV was determined by simulations of JUNO's detector response done within this work. An IBD detection efficiency of $\epsilon_{IBD} = 67.0$ % is achieved with JUNO as result of the analysis applied on the simulated data. JUNO moreover profits from its large 20 kt liquid scintillator target and its high energy resolution. 7.8 to 50.2 IBD signal events from self-annihilation of DM particles with masses between 15 MeV and 100 MeV are expected in JUNO for 10 years of data taking and an annihilation cross section that corresponds to the best currently existing 90 % C.L. upper limit on the DM self-annihilation cross section. The spectral shape of the DM signal is a peak in the visible energy spectrum.
Furthermore, a complete study of all potential backgrounds in JUNO in the region of interest between visible energies of 10 MeV and 100 MeV was performed in this work. These backgrounds can be divided into IBD and IBD-like backgrounds. IBD backgrounds summarize all backgrounds produced in IBD interactions and state irreducible backgrounds, since they cannot be distinguished from the IBD signal from DM self-annihilation. They include the CC background of atmospheric $\bar{\nu}_e$ interacting with protons, the DSNB and the

reactor electron antineutrino background. IBD-like backgrounds describe all backgrounds that can mimic an IBD signal. IBD-like backgrounds in JUNO can be the atmospheric NC background, CC backgrounds of atmospheric $\nu_e/\bar{\nu}_e$ interacting with ^{12}C and of atmospheric $\nu_\mu/\bar{\nu}_\mu$, muon-induced backgrounds like fast neutrons, cosmogenic isotopes and decaying muons, and non-correlated backgrounds of accidental coincidences.
A detailed simulation of the atmospheric NC background in JUNO was performed in this work, since it exceeds the expected DM signal by at least one order of magnitude in the whole visible energy region from 10 MeV to 100 MeV. These simulated atmospheric NC events were analyzed and IBD selection cuts were applied to determine the background events that mimic IBD signals. As a result of the analysis, the atmospheric NC background is reduced by 92.2 % after applying the IBD selection cuts. This shows the excellent capability of JUNO to reduce the atmospheric NC background effectively due to the distinct IBD signature of prompt and delayed signal coincident in time and space. Furthermore, a veto cut on tracks of cosmic muons in the detector volume was introduced in this work, which reduces backgrounds of cosmogenic isotopes and decaying muons to a negligible level. The fast neutron background is suppressed by 92.5 % due to a cut on the fiducial volume. Moreover, background events of atmospheric $\nu_\mu/\bar{\nu}_\mu$ interacting via CC can be reduced to a negligible level because of JUNO's ability to distinguish between muon and positron events.
IBD-like backgrounds of atmospheric NC and fast neutron events in JUNO can be further reduced using pulse shape discrimination (PSD). The pulse shape is defined as time profile of the photon emission in the liquid scintillator. It depends on the particle type and can be analyzed to discriminate IBD against IBD-like events. Therefore, an advanced pulse shape discrimination of IBD events and IBD-like atmospheric NC and fast neutron events was performed in this work. Realistic pulse shapes were calculated based on the simulation of the detector and electronics response of JUNO and on the reconstruction of PMT waveforms, vertex and energy of each event. It was demonstrated that a simple method only based on the tail-to-total ratio yields excellent background reduction. The PSD survival efficiencies that lead to the best signal to background ratio were determined to be $\epsilon_{PSD,IBD} = 97.4$ % , $\epsilon_{PSD,atmoNC} = 5.0$ % and $\epsilon_{PSD,FN} = 0.6$ %. Thus, atmospheric NC and fast neutron background events are very efficiently reduced in JUNO after applying the studied PSD cut.
The total number of background events in JUNO in the visible energy region from 10 MeV to 100 MeV can be reduced to 85.9 ± 24.9 events for a lifetime of 10 years after applying the described cuts. The remaining background contributions are the atmospheric NC background ($N_{atmoNC} = 37.1 \pm 10.8$), the DSNB ($N^{fid}_{DSNB} = 12.6 \pm 5.0$ for the fiducial case) and the atmospheric CC background of $\bar{\nu}_e$'s interacting with protons ($N_{atmoCC,\bar{\nu}_e+p} = 30.3 \pm 7.6$) and with ^{12}C ($N_{atmoCC,\bar{\nu}_e+^{12}\mathrm{C}} = 5.9 \pm 1.5$). The atmospheric CC background dominates the background spectrum above visible energies of around 35 MeV, while atmospheric NC background and DSNB events have typical visible energies of 10 MeV $\leq E_{vis} \lesssim$ 50 MeV and 10 MeV $\leq E_{vis} \lesssim$ 35 MeV, respectively. The spectral shapes of the backgrounds are broad compared to the sharp DM signal. Therefore, a potential DM signal can be well identified as an excess over backgrounds.
The sensitivity of JUNO was calculated within this work using a Bayesian analysis and MCMC sampling. It is the first detailed determination of JUNO's sensitivity for indirect DM search in the DM mass range from 15 MeV to 100 MeV. In case of no excess signal is observed, JUNO will set a 90 % C.L. upper limit on the electron antineutrino flux in the neutrino energy region between 15 MeV and 100 MeV from $\phi_{\bar{\nu}_e,90\%}(E_{\bar{\nu}_e} = 100\,\mathrm{MeV}) = 0.05$ cm^{-2}s^{-1} to $\phi_{\bar{\nu}_e,90\%}(E_{\bar{\nu}_e} = 15\,\mathrm{MeV}) = 1.55$ cm^{-2}s^{-1}, which provides a model-independent upper limit on a monoenergetic $\bar{\nu}_e$ flux at Earth. Furthermore, JUNO will improve the best currently existing 90 % C.L. upper limit on the DM self-annihilation cross section of neutrino detectors by a factor of 2 to 9 in the considered DM mass region after 10

years of data taking. The 90 % C.L. upper limit determined in this work ranges from $\langle\sigma_A\,\mathrm{v}\rangle_{90\%}(m_{DM} = 35\,\mathrm{MeV}) = 1.04 \cdot 10^{-25}$ cm^3/s to $\langle\sigma_A\,\mathrm{v}\rangle_{90\%}(m_{DM} = 100\,\mathrm{MeV}) = 2.51 \cdot 10^{-25}$ cm^3/s. JUNO's sensitivity will moreover be comparable to the sensitivity of the prospective Hyper-Kamiokande detector. Possible improvements for indirect DM search with JUNO were also studied in this work. The directional information of the electron antineutrino signal with respect to the galactic center could be used to improve JUNO's sensitivity by around 10 % for $m_{DM} \geq 65$ MeV assuming perfect angular resolution of the JUNO detector and a DM density profile of the Milky Way described by the Moore model. A larger fiducial volume and the consideration of an additional detection channel, e.g. $\bar{\nu}_e + {}^{12}\mathrm{C} \rightarrow e^+ + n + {}^{11}\mathrm{B}$, could increase the sensitivity by few percent. A possible improvement of the sensitivity due to an even more efficient PSD was estimated by assuming perfect PSD between IBD events and atmospheric NC and fast neutron events. For perfect PSD, i.e. $\epsilon_{PSD,IBD} = 100$ %, $\epsilon_{PSD,atmoNC} = 0$ % and $\epsilon_{PSD,FN} = 0$ %, JUNO's sensitivity would be further improved by around 4 %.
JUNO's potential to discover an electron antineutrino signal from DM self-annihilation in the Milky Way as an excess over backgrounds was also estimated in this work for the first time. As a result, JUNO's discovery potential will be between 3σ and 5σ for most DM masses from 15 MeV to 100 MeV assuming an annihilation cross section that corresponds to the 90 % C.L. upper limit on the DM annihilation cross section of Super-K.

As another part of this work, a similar sensitivity study was performed for the prospective THEIA detector. THEIA would be the first large-scale water-based liquid scintillator detector and would combine different features of water Cherenkov and liquid scintillator detectors. The main advantage of THEIA for the indirect DM search with neutrinos compared to water Cherenkov detectors would be its ability to measure the prompt and delayed signal coincidence of the IBD signal. Moreover, the novel technologies used in THEIA could allow the separation of Cherenkov and scintillation light.
In this work, the sensitivity of the THEIA25 detector configuration with a 25 kt target containing WbLS with 3 % LS fraction was studied. The detection efficiency of IBD events for THEIA25 was determined based on simulations resulting in $\epsilon_{IBD} = 69.7$ % for visible energies between 10 MeV and 100 MeV. 9.6 to 61.1 IBD signal events from electron antineutrinos produced in DM self-annihilation in the Milky Way are expected for THEIA25 in the DM mass range from 15 MeV to 100 MeV after 10 years of data taking and for the currently existing 90 % C.L. limits on $\langle\sigma_A\,\mathrm{v}\rangle$.
Moreover, potential backgrounds in the visible energy region from 10 MeV to 100 MeV were studied in detail in this work. Atmospheric electron antineutrinos interacting via CC with protons as well as the DSNB would cause irreducible IBD backgrounds, while the reactor $\bar{\nu}_e$ background can be neglected in this energy region. The atmospheric NC background in THEIA25 was determined in this work for the first time based on simulations of a dedicated THEIA25 detector simulation. As a result, atmospheric NC background events could be suppressed by 91.8 % due to the application of IBD selection cuts. Muon-induced cosmogenic isotopes could be reduced to a negligible level by applying a muon veto cut. The same applies for the CC background of atmospheric $\nu_\mu/\bar{\nu}_\mu$ after a discrimination cut between e-like and μ-like events.
Additional approaches to further reduce atmospheric NC and fast neutron backgrounds based on the unique feature of THEIA25 to separate Cherenkov and scintillation light were studied in this work. The C/S ratio is defined as ratio of measured Cherenkov light to measured scintillation light and represents an ideal parameter to distinguish between IBD signal events and atmospheric NC and fast neutron background events. In addition to that, a cut on the number of Cherenkov rings in each event was introduced in this work. To estimate the discrimination performance of both methods, the THEIA25 detector simulation was used. The application of cuts on the C/S ratio and the number of Cherenkov

rings elaborated in this work results in survival efficiencies of $\epsilon_{IBD,ring+C/S} = 97.3$ % , $\epsilon_{atmoNC,ring+C/S} = 0.6$ % and $\epsilon_{FN,ring+C/S} = 0.8$ %. Therefore, atmospheric NC and fast neutron background events could be reduced with excellent efficiency in THEIA25.
The total number of background events in THEIA25 could be reduced to 133.2 ± 36.2 events for 10 years of data taking. The atmospheric CC background of $\bar{\nu}_e$ on protons and of $\bar{\nu}_e$ on ^{16}O would dominate the background spectrum for $E_{vis} \gtrsim 30$ MeV with $N_{atmoCC,\bar{\nu}_e+p} = 86.1 \pm 21.5$ events and $N_{atmoCC,\bar{\nu}_e+^{16}\mathrm{O}} = 17.8 \pm 4.5$ events, respectively. Below visible energies of around 30 MeV, the background spectrum would mainly be composed of the DSNB ($N^{fid}_{DSNB} = 16.1 \pm 6.4$ events for the fiducial case) and the atmospheric NC background ($N_{atmoNC} = 13.2 \pm 3.8$ events).
The sensitivity of THEIA25 for the indirect DM search was determined in the same analysis framework as for JUNO. In case of no excess signal is observed, the 90 % C.L. upper limit of THEIA25 on a model-independent monoenergetic $\bar{\nu}_e$ flux at Earth for neutrino energies between 15 MeV and 100 MeV would range from $\phi_{\bar{\nu}_e,90\%}(E_{\bar{\nu}_e} = 100\,\mathrm{MeV}) = 0.07$ cm^{-2}s^{-1} to $\phi_{\bar{\nu}_e,90\%}(E_{\bar{\nu}_e} = 15\,\mathrm{MeV}) = 1.15$ cm^{-2}s^{-1}. Moreover, THEIA25 would set a 90 % C.L. upper limit on the DM self-annihilation cross section in the DM mass region from 15 MeV to 100 MeV ranging from $\langle \sigma_A \, \mathrm{v} \rangle_{90\%} (m_{DM} = 30\,\mathrm{MeV}) = 9.59 \cdot 10^{-26}$ cm^3/s to $\langle \sigma_A \, \mathrm{v} \rangle_{90\%} (m_{DM} = 100\,\mathrm{MeV}) = 3.33 \cdot 10^{-25}$ cm^3/s. Thus, THEIA25's sensitivity to measure neutrinos from DM self-annihilation in the Milky Way as an excess over backgrounds would be comparable to the sensitivities of JUNO and Hyper-Kamiokande in the DM mass range from 15 MeV to 100 MeV.

Appendix

A. Distributions of the Simulation Data from the JUNO Simulation Framework

A.1. Distributions of Simulated IBD Events

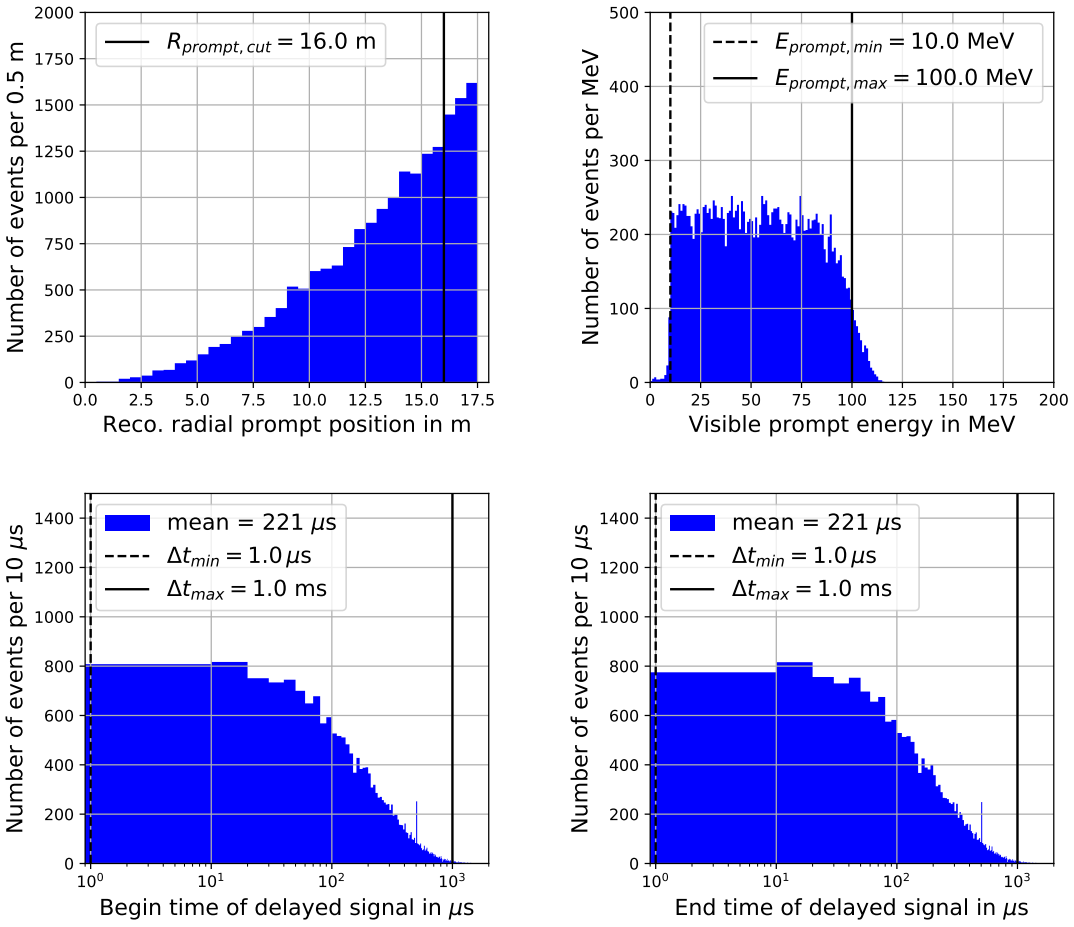

Figure A.1.: Distributions of 20,000 IBD events simulated with JUNO's detector simulation DetSim (version J18v1r1-Pre1). Distributions of the smeared radial position of the prompt signals (upper left), the visible energy of the prompt signals (upper right) and the smeared times, where the delayed signals begin (bottom left) and end (bottom right), are displayed (details about the simulation and analysis are given in section 4.3). Moreover, the IBD selection cut parameters of table 4.1 and the mean values of begin and end time of the delayed signals are shown.

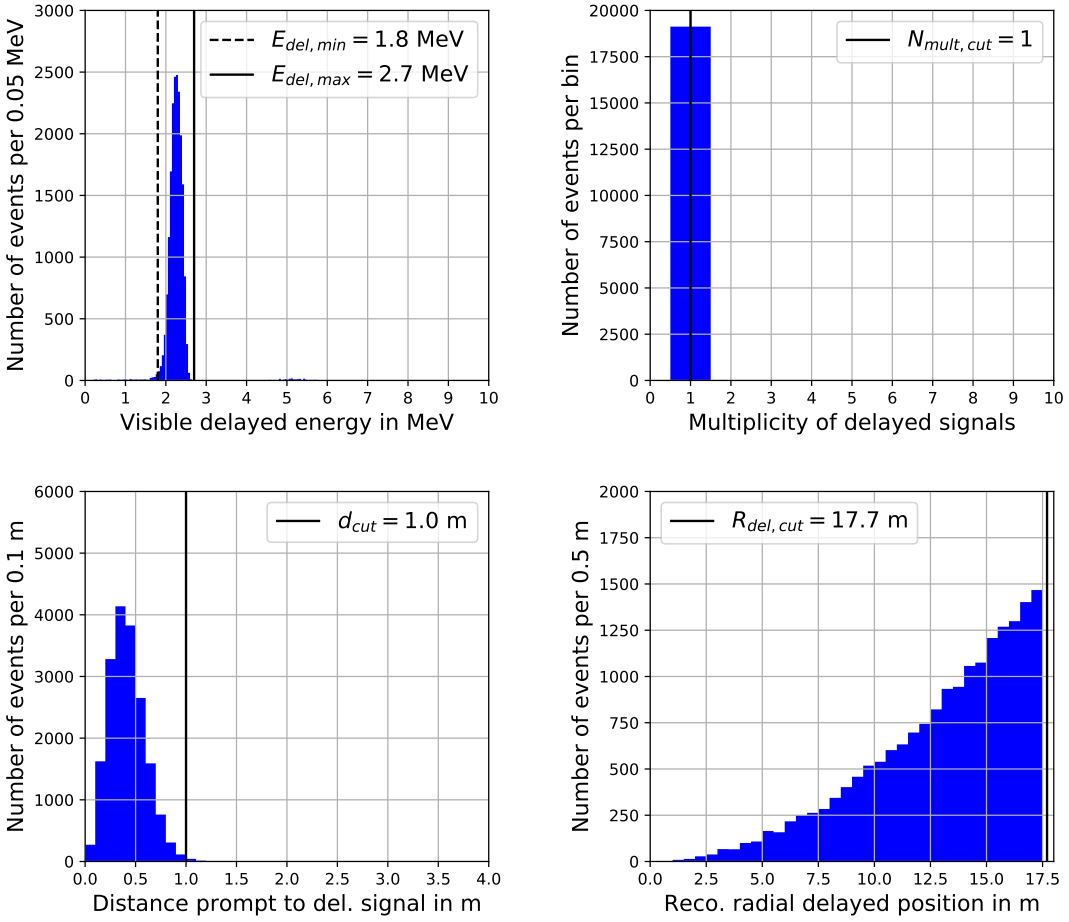

Figure A.2.: Distributions of 20,000 IBD events simulated with JUNO's detector simulation DetSim (version J18v1r1-Pre1). Distributions of the visible energy of the delayed signals (upper left), the multiplicity of delayed signals (upper right), the distance between the smeared positions of prompt and delayed signals (bottom left) and the smeared radial position of the delayed signals (bottom right) are displayed (details about the simulation and analysis are given in section 4.3). The IBD selection cut parameters of table 4.1 are also shown.

A.2. Distributions of Simulated Atmospheric NC Events

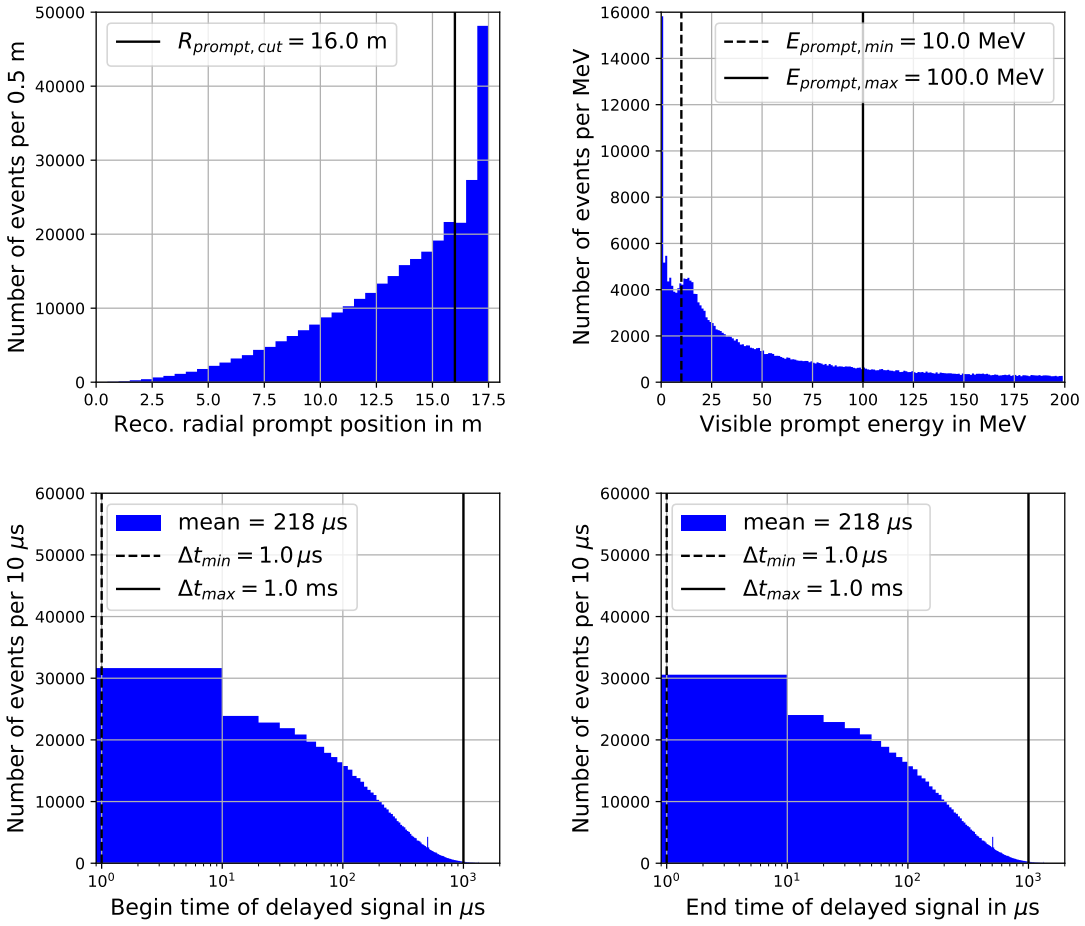

Figure A.3.: Distributions of 400,000 atmospheric NC events simulated with JUNO's detector simulation DetSim (version J18v1r1-Pre1). Distributions of the smeared radial position of the prompt signals (upper left), the visible energy of the prompt signals (upper right) and the smeared times, where the delayed signals begin (bottom left) and end (bottom right), are displayed (details about the simulation and analysis are given in section 5.3.3). Moreover, the IBD selection cut parameters of table 4.1 and the mean values of begin and end time of the delayed signals are shown.

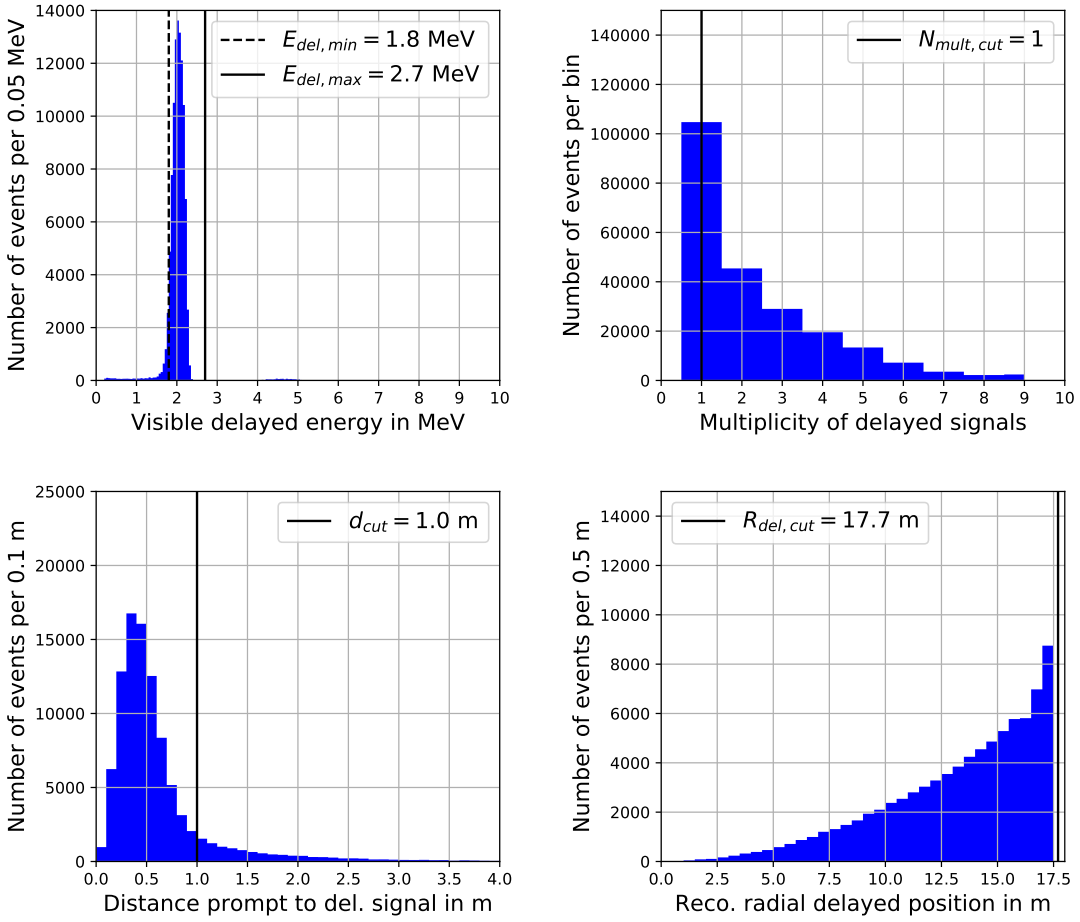

Figure A.4.: Distributions of 400,000 atmospheric NC events simulated with JUNO's detector simulation DetSim (version J18v1r1-Pre1). Distributions of the visible energy of the delayed signals (upper left), the multiplicity of delayed signals (upper right), the distance between the smeared positions of prompt and delayed signals (bottom left) and the smeared radial position of the delayed signals (bottom right) are displayed (details about the simulation and analysis are given in section 5.3.3). The IBD selection cut parameters of table 4.1 are also shown.

B. Total Visible Energy Spectra in JUNO

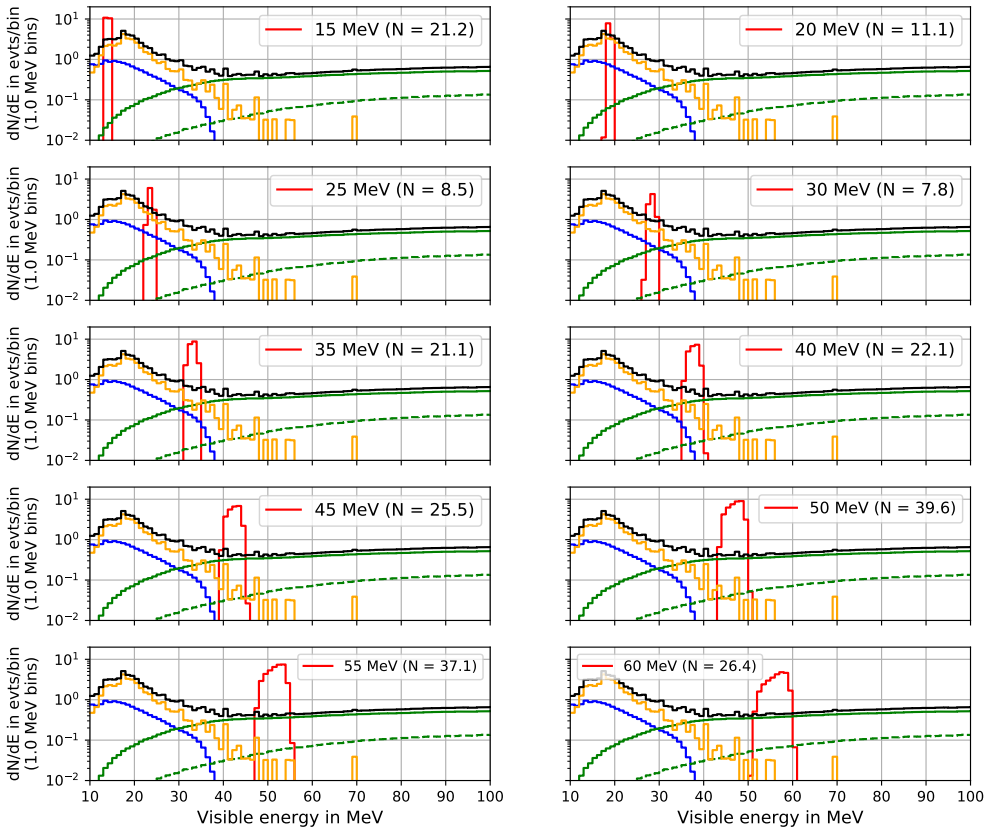

Figure B.5.: Total expected visible energy spectra after applying IBD and PSD cuts in JUNO for 10 years of data taking, a fiducial mass of 14.77 kt and visible energies from 10 MeV to 100 MeV. The IBD selection criteria and PSD cuts are described in section 4.3 and 6.2, respectively. The electron antineutrino signal spectra from DM annihilation and the expected number of signal events are shown in red for DM masses of 15 MeV, 20 MeV, 25 MeV, 30 MeV, 35 MeV, 40 MeV, 45 MeV, 50 MeV, 55 MeV and 60 MeV assuming the currently most stringent 90 % C.L. upper limits of the annihilation cross section from Super-K for each DM mass. The fiducial case of the DSNB is displayed in blue with $N_{DSNB}^{fid,PSD} = 12.6 \pm 5.0$. The atmospheric CC neutrino background spectra on free protons ($N_{atmoCC,\bar{\nu}_e+p}^{PSD} = 30.3 \pm 7.6$) and on ^{12}C ($N_{atmoCC,\bar{\nu}_e+^{12}\mathrm{C}}^{PSD} = 5.9 \pm 1.5$) are shown as solid green and dashed green line, respectively. In orange, the atmospheric NC neutrino background spectrum with $N_{atmoNC}^{PSD} = 37.1 \pm 10.8$ is shown. The total background spectrum is displayed in black.

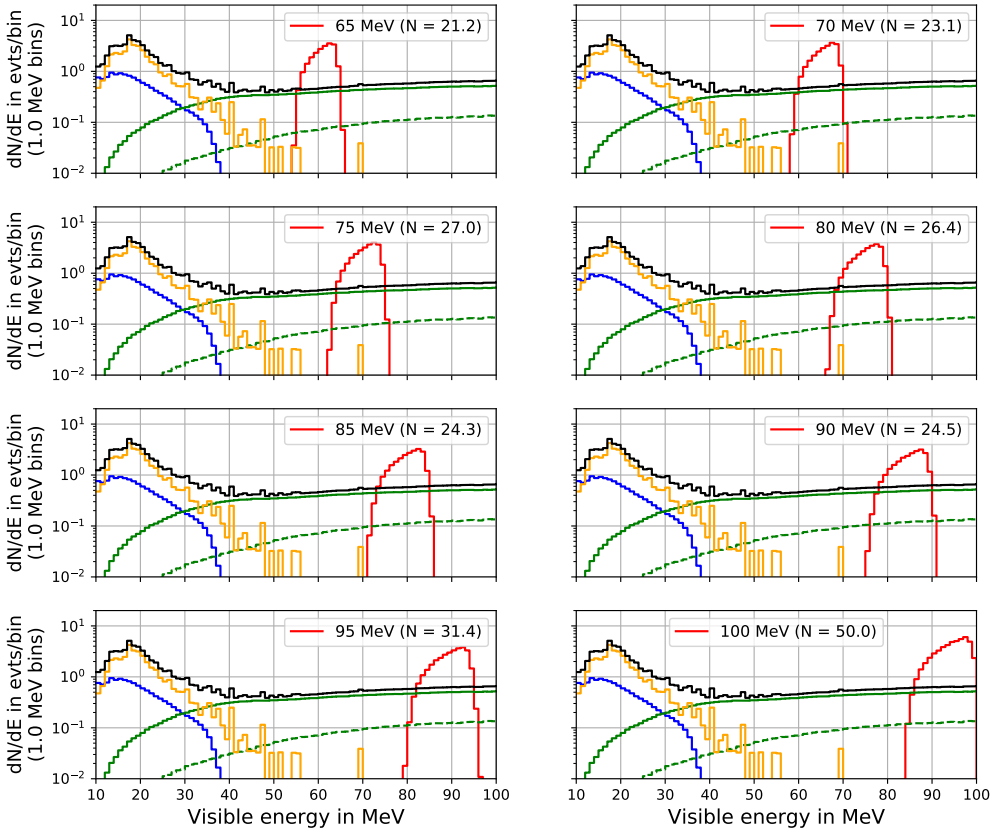

Figure B.6.: Total expected visible energy spectra after applying IBD and PSD cuts in JUNO for 10 years of data taking, a fiducial mass of 14.77 kt and visible energies from 10 MeV to 100 MeV. The IBD selection criteria and PSD cuts are described in section 4.3 and 6.2, respectively. The electron antineutrino signal spectra from DM annihilation and the expected number of signal events are shown in red for DM masses of 65 MeV, 70 MeV, 75 MeV, 80 MeV, 85 MeV, 90 MeV, 95 MeV and 100 MeV assuming the currently most stringent 90 % C.L. upper limits of the annihilation cross section from Super-K for each DM mass. The fiducial case of the DSNB is displayed in blue with $N_{DSNB}^{fid,PSD} = 12.6 \pm 5.0$. The atmospheric CC neutrino background spectra on free protons ($N_{atmoCC,\bar{\nu}_e+p}^{PSD} = 30.3 \pm 7.6$) and on ^{12}C ($N_{atmoCC,\bar{\nu}_e+^{12}\mathrm{C}}^{PSD} = 5.9 \pm 1.5$) are shown as solid green and dashed green line, respectively. In orange, the atmospheric NC neutrino background spectrum with $N_{atmoNC}^{PSD} = 37.1 \pm 10.8$ is shown. The total background spectrum is displayed in black.

C. Distributions of the Simulation Data for THEIA25 from the RAT-PAC Simulation Framework

C.1. Distributions of Simulated IBD Events

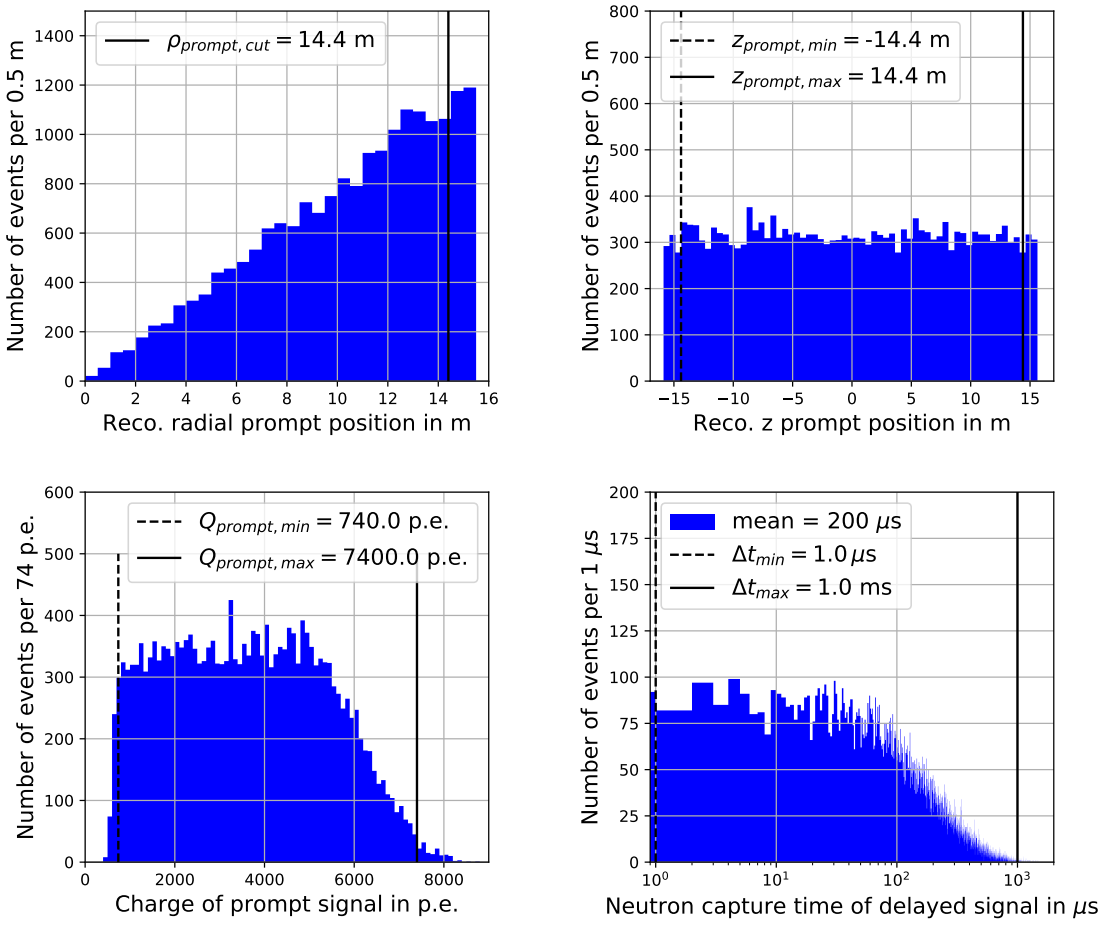

Figure C.7.: Distributions of 20,000 IBD events simulated with the RAT-PAC simulation framework for the THEIA25 detector configuration. Distributions of the smeared radial position $\rho = \sqrt{x^2 + y^2}$ of the prompt signals (upper left), the smeared z position of the prompt signals (upper right), the total charge of the prompt signals (bottom left) and the smeared neutron capture times (bottom right) are displayed (details about the simulation and analysis are given in section 8.2). Moreover, the IBD selection cut parameters of table 8.1 and the mean value of neutron capture times of the delayed signals are shown.

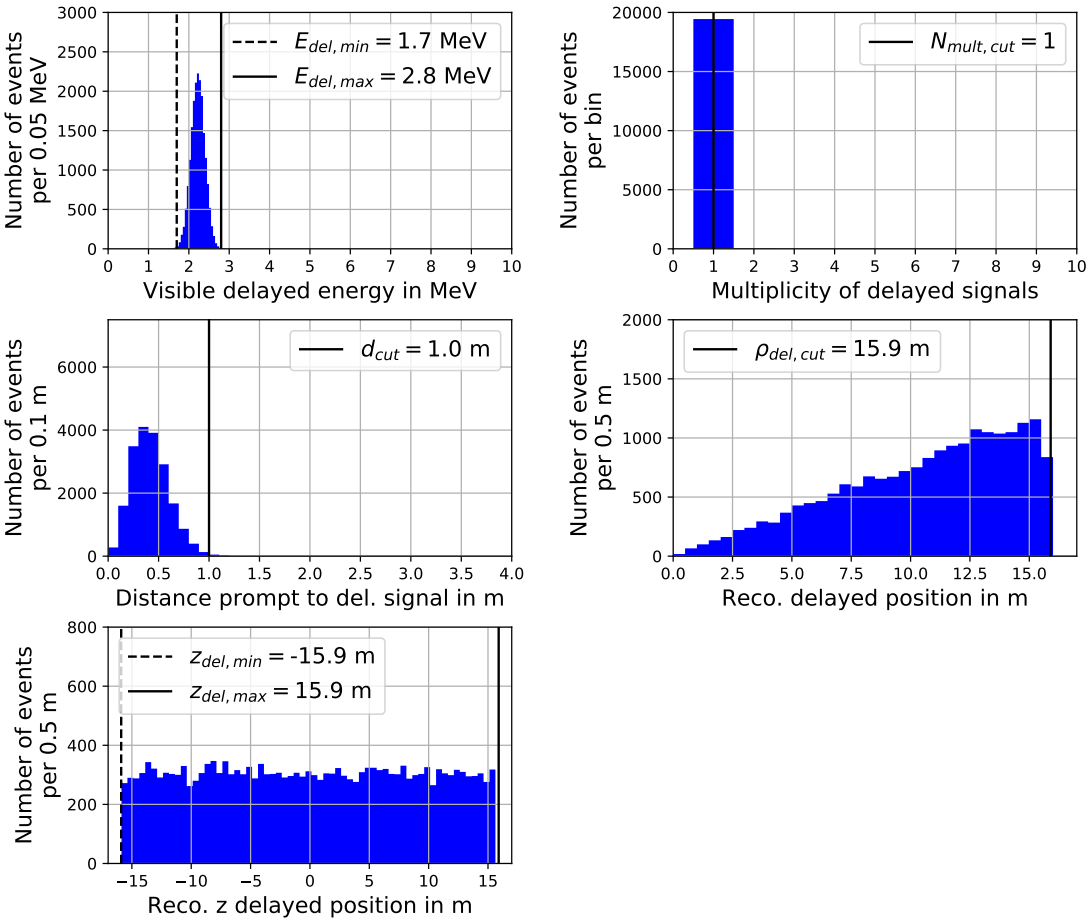

Figure C.8.: Distributions of 20,000 IBD events simulated with the RAT-PAC simulation framework for the THEIA25 detector configuration. Distributions of the visible energy of the delayed signals (upper left), the multiplicity of delayed signals (upper right), the distance between the smeared positions of prompt and delayed signals (middle left), the smeared radial position ρ of the delayed signals (middle right) and the smeared z position of the delayed signals (bottom left) are displayed (details about the simulation and analysis are given in section 8.2). The IBD selection cut parameters of table 8.1 are also shown.

C.2. Distributions of Simulated Atmospheric NC Events

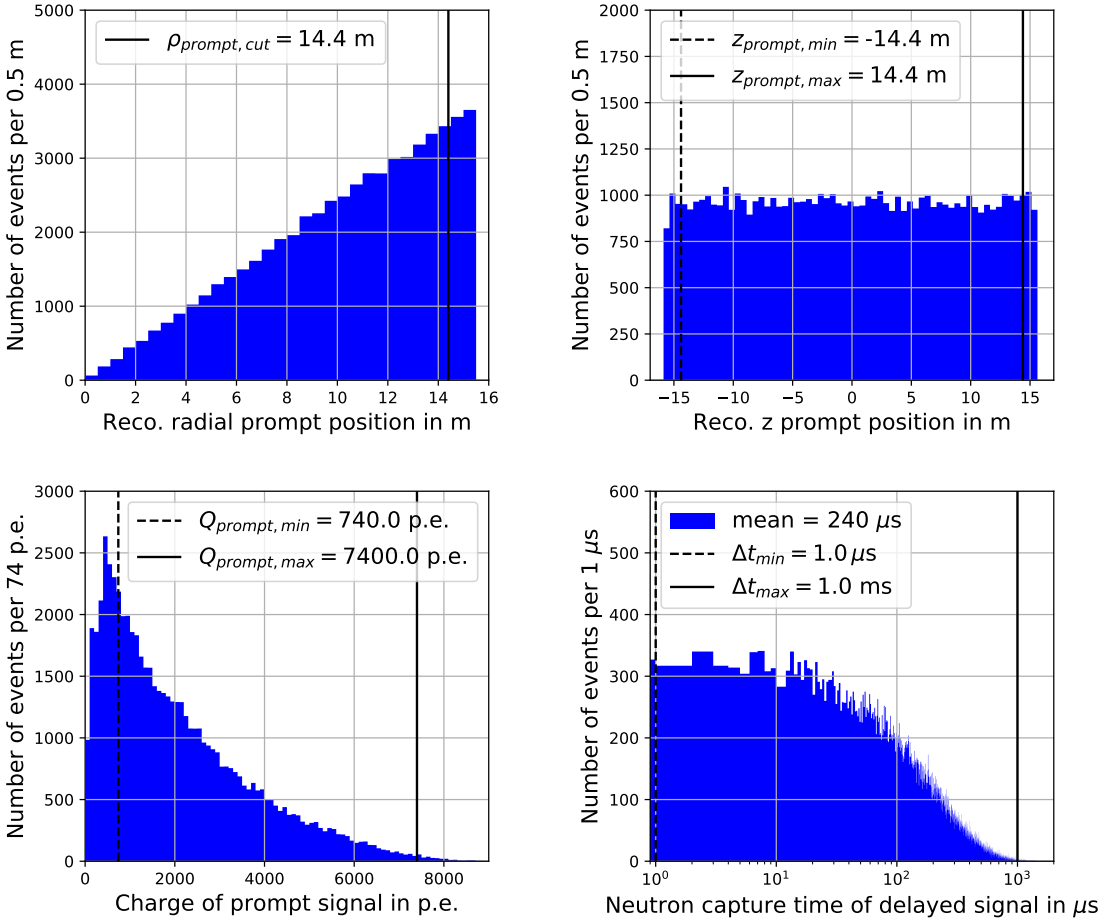

Figure C.9.: Distributions of 104,940 atmospheric NC events simulated with the RAT-PAC simulation framework for the THEIA25 detector configuration. Distributions of the smeared radial position $\rho = \sqrt{x^2 + y^2}$ of the prompt signals (upper left), the smeared z position of the prompt signals (upper right), the total charge of the prompt signals (bottom left) and the smeared neutron capture times (bottom right) are displayed (details about the simulation and analysis are given in section 8.3.4). Moreover, the IBD selection cut parameters of table 8.1 and the mean value of neutron capture times of the delayed signals are shown.

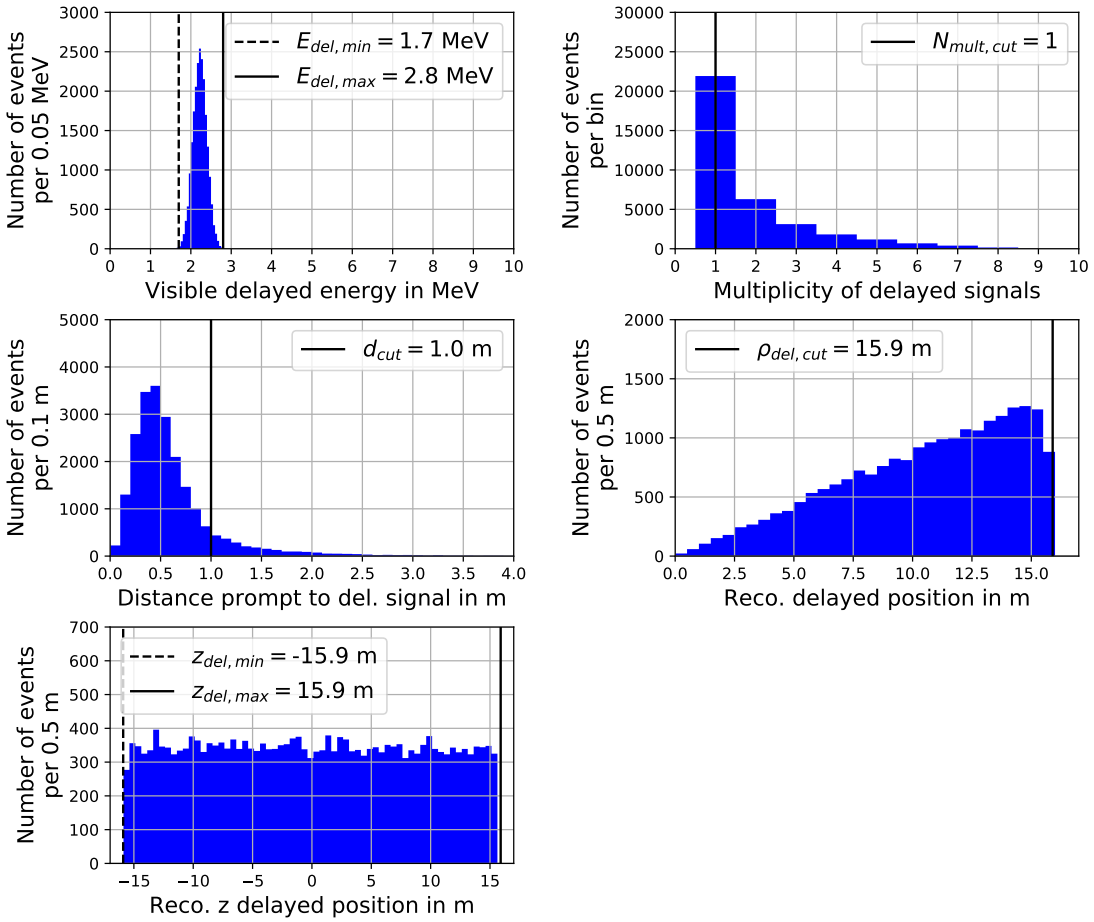

Figure C.10.: Distributions of 104,940 atmospheric NC events simulated with the RAT-PAC simulation framework for the THEIA25 detector configuration. Distributions of the visible energy of the delayed signals (upper left), the multiplicity of delayed signals (upper right), the distance between the smeared positions of prompt and delayed signals (middle left), the smeared radial position ρ of the delayed signals (middle right) and the smeared z position of the delayed signals (bottom left) are displayed (details about the simulation and analysis are given in section 8.3.4). The IBD selection cut parameters of table 8.1 are also shown.

D. Cherenkov Ring in THEIA25

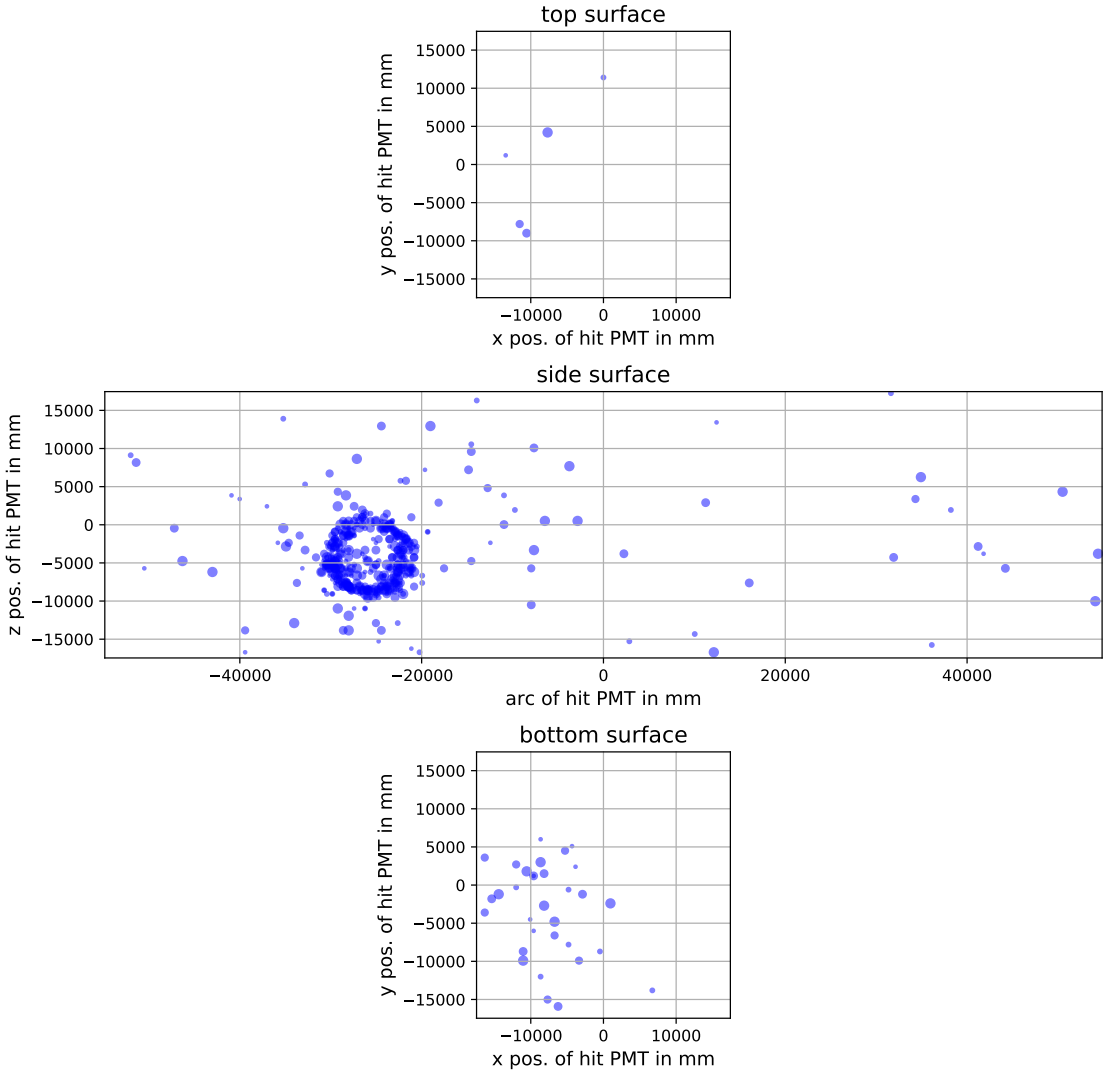

Figure D.11.: Cherenkov ring of a simulated IBD event in THEIA25. The Cherenkov light pattern of a simulated IBD event with visible energy of $E_{vis} = 79.2$ MeV and measured charge from Cherenkov photons of $Q_{pe,cheren} = 824$ p.e. is displayed as example. The positions of PMTs that detected a Cherenkov photon are shown as blue points. The size of the points scales with the number of p.e. measured by the PMT. The top (bottom) plot shows the x and y position of the PMTs on the top (bottom) surface of the detector. The middle plot shows the z position of the PMTs as function of the arc of the PMT position in x and y direction on the side surface of the detector.

E. Total Visible Energy Spectra in THEIA25

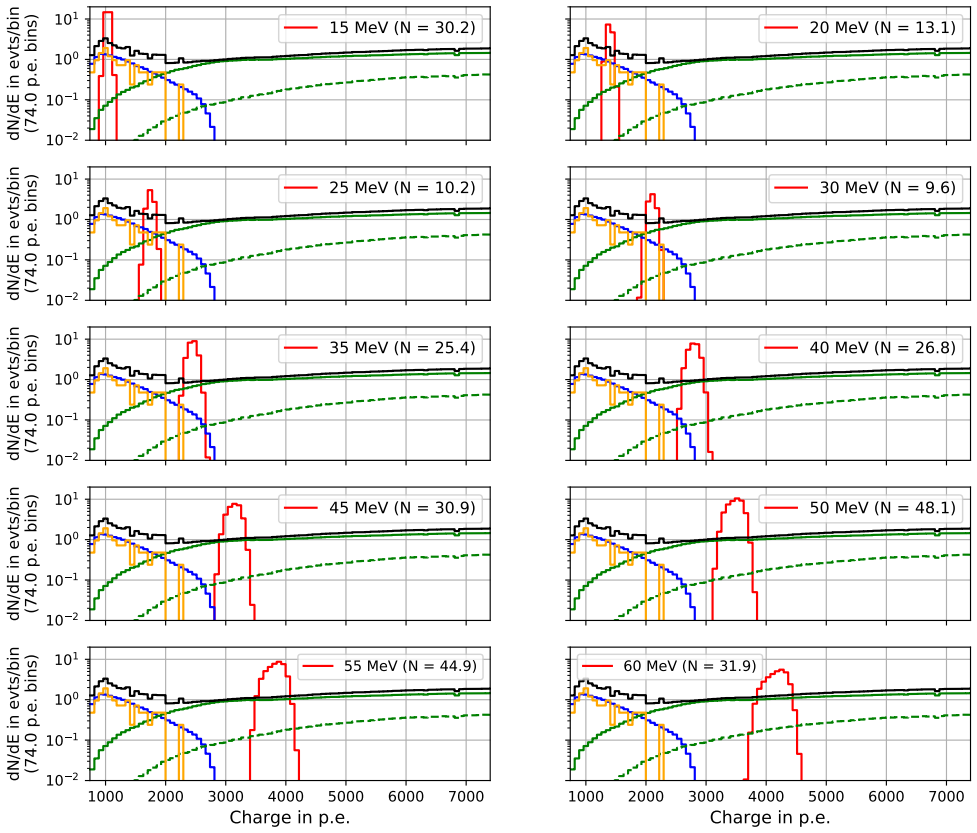

Figure E.12.: Total expected visible energy spectra after applying IBD, Cherenkov ring counting and C/S ratio cuts in THEIA25 for 10 years of data taking, a fiducial mass of 18.7 kt and visible energies from 10 MeV to 100 MeV. The IBD selection criteria, Cherenkov ring counting cut and C/S ratio cut are described in section 8.2, 8.4.1 and 8.4.2, respectively. The electron antineutrino signal spectra from DM annihilation and the expected number of signal events are shown in red for DM masses of 15 MeV, 20 MeV, 25 MeV, 30 MeV, 35 MeV, 40 MeV, 45 MeV, 50 MeV, 55 MeV and 60 MeV assuming the currently most stringent 90 % C.L. upper limits of the annihilation cross section from Super-K for each DM mass. The fiducial case of the DSNB is displayed in blue with $N_{DSNB}^{fid,ring+C/S} = 16.1 \pm 6.4$. The atmospheric CC neutrino background spectra on free protons ($N_{atmoCC,\bar{\nu}_e+p}^{ring+C/S} = 86.1 \pm 21.5$) and on ^{16}O ($N_{atmoCC,\bar{\nu}_e+^{16}\mathrm{O}}^{ring+C/S} = 17.8 \pm 4.5$) are shown as solid green and dashed green line, respectively. In orange, the atmospheric NC neutrino background spectrum with $N_{atmoNC}^{ring+C/S} = 13.2 \pm 3.8$ is shown. The total background spectrum is displayed in black.

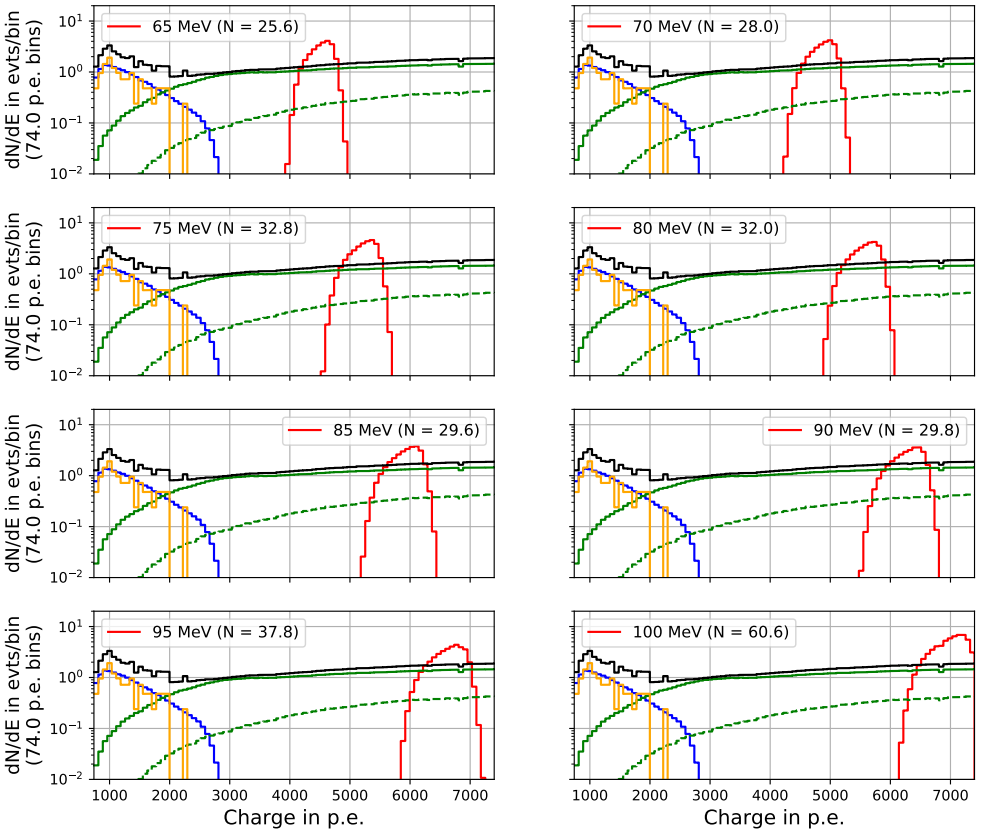

Figure E.13.: Total expected visible energy spectra after applying IBD, Cherenkov ring counting and C/S ratio cuts in THEIA25 for 10 years of data taking, a fiducial mass of 18.7 kt and visible energies from 10 MeV to 100 MeV. The IBD selection criteria, Cherenkov ring counting cut and C/S ratio cut are described in section 8.2, 8.4.1 and 8.4.2, respectively. The electron antineutrino signal spectra from DM annihilation and the expected number of signal events are shown in red for DM masses of 65 MeV, 70 MeV, 75 MeV, 80 MeV, 85 MeV, 90 MeV, 95 MeV and 100 MeV assuming the currently most stringent 90 % C.L. upper limits of the annihilation cross section from Super-K for each DM mass. The fiducial case of the DSNB is displayed in blue with $N_{DSNB}^{fid,ring+C/S} = 16.1 \pm 6.4$. The atmospheric CC neutrino background spectra on free protons ($N_{atmoCC,\bar{\nu}_e+p}^{ring+C/S} = 86.1 \pm 21.5$) and on ^{16}O ($N_{atmoCC,\bar{\nu}_e+^{16}\mathrm{O}}^{ring+C/S} = 17.8 \pm 4.5$) are shown as solid green and dashed green line, respectively. In orange, the atmospheric NC neutrino background spectrum with $N_{atmoNC}^{ring+C/S} = 13.2 \pm 3.8$ is shown. The total background spectrum is displayed in black.

List of Figures

2.1. Measured rotation curve of galaxy NGC 3198. 4
2.2. Composite image of the Bullet cluster. 5
2.3. Sky map of the CMB temperature from 2018 Planck data. 6
2.4. Current experimentally allowed parameter space for spin-independent DM-nucleon scattering cross section as function of the DM mass. 10
2.5. Current experimentally allowed parameter space for spin-dependent DM-nucleon scattering cross section as function of the DM mass. 10
2.6. Current experimental upper limits on the DM annihilation cross section $\langle \sigma_A \, \mathrm{v} \rangle$ in the DM mass region from 1 MeV to 1 GeV. 11

3.1. Expected reactor electron antineutrino spectrum for the location of JUNO. 27
3.2. Illustration of the arrangement of neutrino mass eigenstates in normal and inverted mass ordering. 28
3.3. Expected solar neutrino and geo-neutrino spectra with corresponding backgrounds in JUNO. 29
3.4. Feynman diagrams of charged and neutral current neutrino interactions. . . 31
3.5. Cross sections of neutrino interaction channels for energies up to 100 MeV. 32
3.6. Overview about the setup of the JUNO detector. 34
3.7. Molecular structure and absorption and emission spectra of JUNO's LS. . . 35
3.8. Offline processing chain of the JUNO simulation and analysis framework. . 38

4.1. Radial density profiles of the dark matter halo of the Milky Way for the NFW, Moore and Kravtsov model. 44
4.2. Visible energy distribution of positrons in JUNO. 48
4.3. Total IBD detection efficiency as function of the visible energy. 50
4.4. Visible energy spectra of electron antineutrinos produced by DM self-annihilation in the Milky Way and detected via IBD reactions in JUNO. 52

5.1. Expected reactor electron antineutrino energy spectrum in JUNO for normal and inverted neutrino mass ordering. 55
5.2. Total expected visible energy spectrum of IBD events in JUNO after 10 years of data taking and for visible energies between 10 MeV and 100 MeV. . . . 56
5.3. The expected electron antineutrino flux of the DSNB in the JUNO detector. 59
5.4. Atmospheric neutrino flux of ν_e, $\bar{\nu}_e$, ν_μ and $\bar{\nu}_\mu$ at JUNO site for neutrino energies from 10 MeV to 10 GeV without considering neutrino oscillations. 60
5.5. Charged current interaction cross sections of $\nu_e/\bar{\nu}_e$ interacting with ^{12}C. . . 63
5.6. Expected neutrino energy spectra of atmospheric ν_μ and $\bar{\nu}_\mu$ interacting via CC interactions with free protons and ^{12}C nuclei in JUNO. 65
5.7. Standard deviation $\sigma(t_{pe})$ of the photon emission times t_{pe} of simulated IBD events and simulated atmospheric CC ν_μ and $\bar{\nu}_\mu$ background events. 66
5.8. Simulation procedure of the atmospheric NC neutrino background in JUNO. 68

5.9. Fractions of atmospheric NC neutrino interaction channels on ^{12}C from GENIE simulation before de-excitation. 69
5.10. Occupation of energy levels of the ^{12}C ground state and possible states of ^{11}C after neutron knock out. 70
5.11. Fractions of de-excitation channels of $^{11}C^*$. 71
5.12. Fractions of total atmospheric NC neutrino interaction channels on ^{12}C after considering potential de-excitation. 71
5.13. Fractions of total atmospheric NC neutrino interaction channels on ^{12}C that mimic IBD signals in the JUNO detector. 73
5.14. Radial distribution of prompt signals of IBD-like fast neutron events in the JUNO central detector. 77

6.1. Analytically calculated pulse shapes of different particles types for JUNO's liquid scintillator. 82
6.2. Average pulse shapes of prompt signals of IBD events, atmospheric NC events and neutron events. 84
6.3. Tail-to-total ratio distributions of prompt signals of simulated IBD, IBD-like atmospheric NC and neutron events. 87
6.4. PSD cut efficiency of IBD events and resulting signal to background ratio. . 87
6.5. PSD cut efficiencies of IBD, IBD-like atmospheric NC and fast neutron events. 89
6.6. Total expected visible energy spectrum after PSD in JUNO for 10 years of data taking and visible energies between 10 MeV and 100 MeV. 90

7.1. Expected background-only spectrum in JUNO after PSD. 95
7.2. Example of a dataset generated from the background-only spectrum of JUNO. 95
7.3. Results of MCMC sampling of the posterior probability exemplarily for an assumed DM mass of $m_{DM} = 50$ MeV and for one analyzed dataset. 98
7.4. 90 % C.L. upper limit on the number of signal events $\tilde{S}_{90}$ in JUNO. 98
7.5. 90 % C.L. upper limit on a monoenergetic electron antineutrino flux in JUNO. 99
7.6. 90 % C.L. upper limit on the DM self-annihilation cross section $\langle\sigma_A\,\mathrm{v}\rangle$ for the JUNO experiment. 99
7.7. 90 % C.L. upper limit on the DM self-annihilation cross section $\langle\sigma_A\,\mathrm{v}\rangle$ for the JUNO experiment for different DM profile models of the Milky Way. . . 101
7.8. 90 % C.L. upper limit on the DM self-annihilation cross section $\langle\sigma_A\,\mathrm{v}\rangle$ for the JUNO experiment assuming Dirac and Majorana DM particles. 101
7.9. 90 % C.L. upper limit on the DM self-annihilation cross section $\langle\sigma_A\,\mathrm{v}\rangle$ for the JUNO experiment for different PSD efficiencies. 103
7.10. 90 % C.L. upper limit on the DM self-annihilation cross section $\langle\sigma_A\,\mathrm{v}\rangle$ for the JUNO experiment for different cases of the DSNB. 103
7.11. 90 % C.L. upper limit on the DM self-annihilation cross section $\langle\sigma_A\,\mathrm{v}\rangle$ for the JUNO experiment for different total exposure times. 105
7.12. Discovery potential of JUNO. 105
7.13. 90 % C.L. upper limit on the DM self-annihilation cross section for JUNO compared to limits of KamLAND, Super-Kamiokande and Hyper-Kamiokande. 106
7.14. Galactic $J(\psi)$ and differential IBD interaction cross section $\mathrm{d}\sigma/\mathrm{d}\cos(\theta)$. . . 111
7.15. 90 % C.L. upper limit on the DM self-annihilation cross section $\langle\sigma_A\,\mathrm{v}\rangle$ for the JUNO experiment including a cut on the direction of the neutrinos. . . 113
7.16. Angular distribution and 90 % C.L. upper limit on $\langle\sigma_A\,\mathrm{v}\rangle$ using the positron direction only and the vector between positron and neutron position. 114

8.1. Properties of the 3 % WbLS model implemented into the THEIA RAT-PAC simulation. 118

8.2. Visible energy spectra of electron antineutrinos produced by DM self-annihilation in the Milky Way and detected via IBD reactions in THEIA25. 122
8.3. Total expected visible energy spectrum of IBD events in THEIA25 after 10 years of data taking and for visible energies between 10 MeV and 100 MeV. 124
8.4. Atmospheric neutrino flux of ν_e, $\bar{\nu}_e$, ν_μ and $\bar{\nu}_\mu$ at SURF for neutrino energies from 10 MeV to 10 GeV without considering neutrino oscillations. 126
8.5. Fractions of atmospheric NC interaction channels on protons and ^{16}O. . . . 130
8.6. Fractions of atmospheric NC interaction channels on protons and ^{16}O that mimic IBD signals in the THEIA25 detector. 132
8.7. Cherenkov ring counting cut efficiencies in THEIA25 of IBD, IBD-like atmospheric NC and fast neutron events. 139
8.8. Total expected visible energy spectrum after the Cherenkov ring counting cut in THEIA25. 139
8.9. C/S ratio of IBD and atmospheric NC events and the C/S ratio cut efficiencies of IBD, atmospheric NC and neutron events in THEIA25. 141
8.10. Total expected visible energy spectrum after the C/S ratio cut in THEIA25. 141
8.11. C/S ratio of IBD, atmospheric NC and fast neutron events that pass the Cherenkov ring counting cut and cut efficiencies of Cherenkov ring counting and C/S ratio cut of IBD, atmospheric NC and neutron events in THEIA25. 143
8.12. Total expected visible energy spectrum after the Cherenkov ring counting and C/S ratio cut in THEIA25. 143
8.13. Expected background-only spectrum in THEIA25 after Cherenkov ring counting and C/S ratio cut. 146
8.14. 90 % C.L. upper limit on the number of signal events $\tilde{S}_{90}$ in THEIA25. . . 147
8.15. 90 % C.L. upper limit on a monoenergetic electron antineutrino flux in THEIA25. 147
8.16. 90 % C.L. upper limit on the DM self-annihilation cross section $\langle\sigma_A\,\mathrm{v}\rangle$ for the THEIA25 detector. 148
8.17. 90 % C.L. upper limit on the DM self-annihilation cross section $\langle\sigma_A\,\mathrm{v}\rangle$ for the THEIA25 detector for different DM profile models of the Milky Way. . 148
8.18. 90 % C.L. upper limit on the DM self-annihilation cross section $\langle\sigma_A\,\mathrm{v}\rangle$ for the THEIA25 detector assuming Dirac and Majorana DM particles. 149
8.19. 90 % C.L. upper limit on $\langle\sigma_A\,\mathrm{v}\rangle$ for the THEIA25 detector applying only the Cherenkov ring counting cut and only the C/S ratio cut. 150
8.20. 90 % C.L. upper limit on the DM self-annihilation cross section $\langle\sigma_A\,\mathrm{v}\rangle$ for the THEIA25 detector for different cases of the DSNB. 150
8.21. 90 % C.L. upper limit on the DM self-annihilation cross section $\langle\sigma_A\,\mathrm{v}\rangle$ for the THEIA25 detector for different total exposure times. 152
8.22. 90 % C.L. upper limit on the DM self-annihilation cross section $\langle\sigma_A\,\mathrm{v}\rangle$ for THEIA25 compared to limits of JUNO, KamLAND, Super-K and Hyper-K. 152

A.1. Distributions of 20,000 IBD events simulated with JUNO's detector simulation DetSim for R_{prompt}, E_{prompt}, t_{begin} and t_{end}. 160
A.2. Distributions of 20,000 IBD events simulated with JUNO's detector simulation DetSim for E_{del}, N_{mult}, d and R_{del}. 161
A.3. Distributions of 400,000 atmospheric NC events simulated with JUNO's detector simulation DetSim for R_{prompt}, E_{prompt}, t_{begin} and t_{end}. 162
A.4. Distributions of 400,000 atmospheric NC events simulated with JUNO's detector simulation DetSim for E_{del}, N_{mult}, d and R_{del}. 163
B.5. Total expected visible energy spectra after applying IBD and PSD cuts in JUNO for DM masses from 15 MeV to 60 MeV. 164

B.6. Total expected visible energy spectra after applying IBD and PSD cuts in JUNO for DM masses from 65 MeV to 100 MeV. 165
C.7. Distributions of 20,000 IBD events simulated with the RAT-PAC simulation framework for THEIA25 for ρ_{prompt}, z_{prompt}, Q and $t_{n\,cap}$. 166
C.8. Distributions of 20,000 IBD events simulated with the RAT-PAC simulation framework for THEIA25 for E_{del}, N_{mult}, d, ρ_{del} and z_{del}. 167
C.9. Distributions of 104,940 atmospheric NC events simulated with the RAT-PAC simulation framework for THEIA25 for ρ_{prompt}, z_{prompt}, Q and $t_{n\,cap}$. . 168
C.10. Distributions of 104,940 atmospheric NC events simulated with the RAT-PAC simulation framework for THEIA25 for E_{del}, N_{mult}, d, ρ_{del} and z_{del}. . 169
D.11. Cherenkov ring of a simulated IBD event in THEIA25. 170
E.12. Total visible energy spectra after applying IBD, Cherenkov ring counting and C/S ratio cuts in THEIA25 for DM masses from 15 MeV to 60 MeV. . 171
E.13. Total visible energy spectra after applying IBD, Cherenkov ring counting and C/S ratio cuts in THEIA25 for DM masses from 65 MeV to 100 MeV. 172

List of Tables

3.1. Three flavor oscillation parameters from fit to global data. 24
3.2. Main characteristics of the different PMT types used in the JUNO detector. 36

4.1. Parametrization of the DM profile models NFW, Moore and Kravtsov and the resulting values of the angular-averaged J-factor J_{avg}. 43
4.2. Selection criteria and cut parameters for IBD events together with the resulting cut efficiencies ϵ and the total IBD detection efficiency ϵ_{IBD}. 50

5.1. IBD selection criteria together with the resulting cut efficiencies and the total detection efficiency ϵ_{atmoNC} of atmospheric NC events on ^{12}C. 72
5.2. Estimated decay rates of cosmogenic β-n emitting isotopes in JUNO's liquid scintillator for energies above 10 MeV and for 20 kt. 75
5.3. Number of background events in JUNO for visible energies between 10 MeV and 100 MeV and after 10 years of data taking. 80

6.1. Decay time constants τ_i and weights ω_i of the photon emission of different particle types for the LAB-based liquid scintillator of JUNO. 82
6.2. Survival efficiencies of the PSD cut of IBD-like atmospheric NC, IBD and fast neutron events and the corresponding tail windows that lead to the best signal to background ratio. 88
6.3. Number of background events in JUNO after applying the PSD cut. 91

8.1. Selection criteria and cut parameters for IBD events together with the resulting cut efficiencies ϵ and the total IBD detection efficiency ϵ_{IBD} of THEIA25. 120
8.2. IBD selection criteria together with the resulting cut efficiencies and the total detection efficiency ϵ_{atmoNC} of atmospheric NC events on free protons and ^{16}O. 131
8.3. Number of background events in THEIA25 for visible energies between 10 MeV and 100 MeV and after 10 years of data taking. 135
8.4. Number of IBD, atmospheric NC and fast neutron events depending on the number of Cherenkov rings per event. 138
8.5. Number of background events in THEIA25 after applying the Cherenkov ring counting and C/S ratio cut. 145

List of Acronyms

ΛCDM cosmological standard model.

$0\nu\beta\beta$ neutrino-less double β decay.

AMS-02 Alpha Magnetic Spectrometer.

ANNIE Accelerator Neutrino Neutron Interaction Experiment.

ANTARES Astronomy with a Neutrino Telescope and Abyss environmental RESearch project.

ATIC Advanced Thin Ionization Calorimeter.

ATLAS A Toroidal LHC Apparatus.

AURORA A Unit for Researching Online the LSc Transparency.

BAT Bayesian Analysis Toolkit.

bis-MSB p-bis-(o-methylstyryl)-benzene.

BNL Brookhaven National Laboratory.

Borexino Boron solar neutrino experiment.

C.L. confidence level.

Calib calibration and waveform reconstruction package.

CC charged current.

CDMSlite Cryogenic Dark Matter Search low ionization threshold experiment.

CEνNS coherent elastic neutrino-nucleus scattering.

CERN European Organization for Nuclear Research.

CheSS Cherenkov and Scintillation Separation.

CJPL China Jinping Underground Laboratory.

CKM Cabbibo-Kobayashi-Maskawa.

CMB cosmic microwave background.

CMS Compact Muon Solenoid.

CNO carbon-nitrogen-oxygen.

COMPTEL Imaging Compton Telescope.

CRESST Cryogenic Rare Event Search with Superconducting Thermometers.

DAQ data acquisition.

DayaBay Daya Bay Reactor Neutrino Experiment.

DCR dark count rate.

DetSim detector simulation package.

DIS deep inelastic scattering.

DM dark matter.

DSNB diffuse supernova neutrino background.

DUNE Deep Underground Neutrino Experiment.

e.s. excited state.

ECHo Electron Capture at ^{163}Holmium Experiment.

ElecSim electronics simulation package.

FADC flash analog-to-digital converter.

Fermi-LAT Fermi Large Area Telescope.

FWHM full width at half maximum.

g.s. ground state.

Gallex Gallium Experiment.

GENIE Universal Neutrino Generator.

GERDA Germanium Detector Array Experiment.

GNO Gallium Neutrino Observatory.

H.E.S.S. High Energy Stereoscopic System.

Hyper-K Hyper-Kamiokande.

IBD inverse β decay.

IceCube IceCube Neutrino Observatory.

IceCube-PINGU Precision IceCube Next Generation Upgrade.

IMF initial mass function.

INO India-based Neutrino Observatory.

INTEGRAL International Gamma-Ray Astrophysics Laboratory.

IO inverted neutrino mass ordering.

JUNO Jiangmen Underground Neutrino Observatory.

KamLAND Kamioka Liquid Scintillator Antineutrino Detector.

KamLAND-Zen KamLAND Zero-Neutrino Double-Beta Decay Experiment.

KATRIN Karlsruhe Tritium Neutrino Experiment.

KM3NeT Cubic Kilometre Neutrino Telescope.

LAB linear alkyl-benzene.

LAPPD Large Area Picosecond Photo-Detector.

LBNL Lawrence Berkeley National Laboratory.

LECP Low-Energy Charged Particle experiment.

LEGEND Large Enriched Germanium Experiment for Neutrinoless Double-Beta Decay.

LENA Low Energy Neutrino Astronomy.

LHC Large Hadron Collider.

LNGS Laboratori Nazionali del Gran Sasso.

LS liquid scintillator.

LUX Large Underground Xenon experiment.

m.w.e. meter of water equivalent.

MAGIC Major Atmospheric Gamma-Ray Imaging Cherenkov Telescopes.

MC Monte Carlo.

MCMC Markov Chain Monte Carlo.

MCP microchannel plate.

MINOS Main Injector Neutrino Oscillation Search Experiment.

MOND Modified Newtonian Dynamics.

MSW Mikheyev-Smirnov-Wolfenstein.

NC neutral current.

NFW Navarro-Frenk-White.

NMO neutrino mass ordering.

NNVT Northern Night Vision Technology Ltd..

NO normal neutrino mass ordering.

NOvA NuMI Off-Axis ν_e Appearance Experiment.

NPP nuclear power plant.

OPERA Oscillation Project with Emulsion-tracking Apparatus.

ORCA Oscillation Research with Cosmics in the Abyss.

OSIRIS Online Scintillator Internal Radioactivity Investigation System.

p.e. photo-electron.

PAMELA Payload for Antimatter Matter Exploration and Light-nuclei Astrophysics.

PandaX-II Particle and Astrophysical Xenon Detector.

PDE photon detection efficiency.

PICASSO Project in Canada to Search for Supersymmetric Objects.

PMNS Pontecorvo-Maki-Nakagawa-Sakata.

PMT photomultiplier tube.

pp-chain proton-proton reaction chain.

PPO 2,5-diphenyloxazole.

PSD pulse shape discrimination.

PWR pressurized water reactor.

QE quasielastic.

QES quasielastic scattering.

Reco energy and vertex reconstruction package.

RENO Reactor Experiment for Neutrino Oscillation.

RES resonant neutrino scattering.

SAGE Soviet–American Gallium Experiment.

SD spin-dependent.

SDSS Sloan Digital Sky Survey.

SI spin-independent.

SM Standard Model of Particle Physics.

SNIPER Software for Non-collider Physics ExpeRiments.

SNO Sudbury Neutrino Observatory.

SNOLAB Sudbury Neutrino Observatory Laboratory.

SSM solar standard model.

Super-K Super-Kamiokande.

SURF Sanford Underground Research Facility.

SUSY supersymmetry.

T2K 'Tokai to Kamioka' Experiment.

TAO Taishan Antineutrino Observatory.

TTR tail-to-total ratio.

TTS transit time spread.

WATCHMAN WAter CHerenkov Monitor for ANtineutrinos.

WbLS water-based liquid scintillator.

WIMP weakly interacting massive particle.

Bibliography

[1] P. A. Zyla et al. (Particle Data Group). Review of Particle Physics. *Progress of Theoretical and Experimental Physics*, 2020(8), 08 2020. 083C01.

[2] Gianfranco Bertone, Dan Hooper, and Joseph Silk. Particle dark matter: evidence, candidates and constraints. *Physics Reports*, 405(5-6):279–390, Jan 2005.

[3] Gianfranco Bertone and Dan Hooper. History of dark matter. *Reviews of Modern Physics*, 90(4), Oct 2018.

[4] Carlos A. Argüelles et al. Dark Matter Annihilation to Neutrinos. *arXiv e-prints*, December 2019. arXiv:1912.09486.

[5] F. An et al. Neutrino Physics with JUNO. *J. Phys.*, G43(3):030401, 2016.

[6] M. Askins et al. Theia: an advanced optical neutrino detector. *The European Physical Journal C*, 80(5), May 2020.

[7] Marco Battaglieri et al. US Cosmic Visions: New Ideas in Dark Matter 2017: Community Report. *arXiv e-prints*, 2017. arXiv:1707.04591.

[8] Vera C. Rubin and Jr. Ford, W. Kent. Rotation of the Andromeda Nebula from a Spectroscopic Survey of Emission Regions. *Astrophysical Journal*, 159:379, February 1970.

[9] M. Roberts and A. Rots. Comparison of Rotation Curves of Different Galaxy Types. *Astronomy and Astrophysics*, 26:483–485, August 1973.

[10] V. Rubin, Jr. Ford, W., and N. Thonnard. Rotational properties of 21 SC galaxies with a large range of luminosities and radii, from NGC 4605 (R=4kpc) to UGC 2885 (R=122kpc). *Astrophysical Journal*, 238:471–487, June 1980.

[11] T. van Albada, J. Bahcall, K. Begeman, and R. Sancisi. Distribution of dark matter in the spiral galaxy NGC 3198. *Astrophysical Journal*, 295:305–313, August 1985.

[12] K. Begeman. HI rotation curves of spiral galaxies. I. NGC 3198. *Astronomy and Astrophysics*, 223:47–60, October 1989.

[13] K. G. Begeman, A. H. Broeils, and R. H. Sanders. Extended rotation curves of spiral galaxies: Dark haloes and modified dynamics. *Mon. Not. Roy. Astron. Soc.*, 249:523, 1991.

[14] T. van Albada, J. Bahcall, K. Begeman, and R. Sancisi. Distribution of dark matter in the spiral galaxy NGC 3198. *Astrophysical Journal*, 295:305–313, August 1985.

[15] F. Zwicky. Die Rotverschiebung von extragalaktischen Nebeln. *Helv. Phys. Acta*, 6:110–127, 1933.

[16] J. Anthony Tyson, Greg P. Kochanski, and Ian P. Dell'Antonio. Detailed mass map of CL0024+1654 from strong lensing. *Astrophys. J. Lett.*, 498:L107, 1998.

[17] David M. Wittman, J. Anthony Tyson, David Kirkman, Ian Dell'Antonio, and Gary Bernstein. Detection of weak gravitational lensing distortions of distant galaxies by cosmic dark matter at large scales. *Nature*, 405:143–149, 2000.

[18] Jennifer Adelman-McCarthy et al. The Fourth Data Release of the Sloan Digital Sky Survey. *The Astrophysical Journal Supplement Series*, 162(1):38–48, January 2006.

[19] C. S. Kochanek et al. Clusters of Galaxies in the Local Universe. *Astrophysical Journal*, 585(1):161–181, March 2003.

[20] S. Allen, R. Schmidt, and A. Fabian. Cosmological constraints from the X-ray gas mass fraction in relaxed lensing clusters observed with Chandra. *Monthly Notices of the Royal Astronomical Society*, 334(2):L11–L15, August 2002.

[21] NASA Finds Direct Proof of Dark Matter. `https://www.nasa.gov/mission_pages/chandra/multimedia/photos06-096.html`, 2006.

[22] Douglas Clowe et al. A Direct Empirical Proof of the Existence of Dark Matter. *The Astrophysical Journal*, 648(2):L109–L113, Aug 2006.

[23] M. Markevitch et al. Constraints on the Dark Matter Self-Interaction Cross-Section from the Merging Cluster 1E 0657-56. *The Astrophysical Journal*, 606(2):819–824, May 2004.

[24] X-ray: NASA/CXC/CfA/M.Markevitch et al.; Optical: NASA/STScI; Magellan/U.Arizona/D.Clowe et al.; Lensing Map: NASA/STScI; ESO WFI; Magellan/U.Arizona/D.Clowe et al.

[25] Wayne Hu, Naoshi Sugiyama, and Joseph Silk. The physics of microwave background anisotropies. *Nature*, 386(6620):37–43, Mar 1997.

[26] A. A. Penzias and R. W. Wilson. A Measurement of Excess Antenna Temperature at 4080 Mc/s. *Astrophysical Journal*, 142:419–421, July 1965.

[27] Planck Collaboration. Planck 2018 results - I. Overview and the cosmological legacy of Planck. *A&A*, 641:A1, 2020.

[28] Christian Strandhagen. *Search for Low-Mass Dark Matter with the CRESST-II Experiment*. PhD thesis, Universität Tübingen, December 2016.

[29] Donald G. York et al. The Sloan Digital Sky Survey: Technical Summary. *Astronomical Journal*, 120(3):1579–1587, September 2000.

[30] D. Nathalie and J.-P. Uzan. *Relativity in Modern Physics*. Oxford Scholarship Online, 2018.

[31] Planck Collaboration. Planck 2018 results - VI. Cosmological parameters. *A&A*, 641:A6, 2020.

[32] `https://www.cosmos.esa.int/documents/387566/1753103/Planck_2018_T_CMB.pdf`, 2021.

[33] M. Milgrom. A modification of the Newtonian dynamics as a possible alternative to the hidden mass hypothesis. *Astrophysical Journal*, 270:365–370, July 1983.

[34] Benjamin Audren et al. Strongest model-independent bound on the lifetime of Dark Matter. *Journal of Cosmology and Astroparticle Physics*, 2014(12):028–028, Dec 2014.

[35] Benjamin W. Lee and Steven Weinberg. Cosmological Lower Bound on Heavy-Neutrino Masses. *Phys. Rev. Lett.*, 39:165–168, Jul 1977.

[36] Graciela B. Gelmini. TASI 2014 Lectures: The Hunt for Dark Matter. *arXiv e-prints*, February 2015. arXiv:1502.01320.

[37] M. Tanabashi et al. Review of Particle Physics. *Phys. Rev. D*, 98:030001, Aug 2018.

[38] Katherine Freese. Status of dark matter in the universe. *International Journal of Modern Physics D*, 26(06):1730012, Mar 2017.

[39] C. Bœhm and P. Fayet. Scalar dark matter candidates. *Nuclear Physics B*, 683(1-2):219–263, Apr 2004.

[40] C. Bœhm, P. Fayet, and J. Silk. Light and heavy dark matter particles. *Phys. Rev. D*, 69:101302, May 2004.

[41] Céline Boehm, Dan Hooper, Joseph Silk, Michel Casse, and Jacques Paul. MeV Dark Matter: Has It Been Detected? *Phys. Rev. Lett.*, 92:101301, Mar 2004.

[42] Céline Bœhm. Implications of a new light gauge boson for neutrino physics. *Phys. Rev. D*, 70:055007, Sep 2004.

[43] Marc Schumann. Direct detection of WIMP dark matter: concepts and status. *Journal of Physics G: Nuclear and Particle Physics*, 46(10):103003, Aug 2019.

[44] E. Aprile et al. Light Dark Matter Search with Ionization Signals in XENON1T. *Physical Review Letters*, 123(25), Dec 2019.

[45] E. Aprile et al. Dark Matter Search Results from a One Ton-Year Exposure of XENON1T. *Phys. Rev. Lett.*, 121:111302, Sep 2018.

[46] D. S. Akerib et al. Results from a Search for Dark Matter in the Complete LUX Exposure. *Phys. Rev. Lett.*, 118:021303, Jan 2017.

[47] Xiangyi Cui et al. Dark Matter Results from 54-Ton-Day Exposure of PandaX-II Experiment. *Phys. Rev. Lett.*, 119:181302, Oct 2017.

[48] P. Agnes et al. DarkSide-50 532-day dark matter search with low-radioactivity argon. *Phys. Rev. D*, 98:102006, Nov 2018.

[49] R. Agnese et al. Search for low-mass dark matter with CDMSlite using a profile likelihood fit. *Phys. Rev. D*, 99:062001, Mar 2019.

[50] A. H. Abdelhameed et al. First results from the CRESST-III low-mass dark matter program. *Phys. Rev. D*, 100:102002, Nov 2019.

[51] E. Behnke et al. Final results of the PICASSO dark matter search experiment. *Astroparticle Physics*, 90:85–92, Apr 2017.

[52] C. Amole et al. Dark matter search results from the complete exposure of the PICO-60 C3F8 bubble chamber. *Physical Review D*, 100(2), Jul 2019.

[53] E. Aprile et al. Light Dark Matter Search with Ionization Signals in XENON1T. *Phys. Rev. Lett.*, 123:251801, Dec 2019.

[54] M. Aaboud et al. Constraints on mediator-based dark matter and scalar dark energy models using $\sqrt{s} = 13$ TeV pp collision data collected by the ATLAS detector. *Journal of High Energy Physics*, 2019(5), May 2019.

[55] K. Choi et al. Search for neutrinos from annihilation of captured low-mass dark matter particles in the Sun by Super-Kamiokande. *Phys. Rev. Lett.*, 114(14):141301, 2015.

[56] S. Adrián-Martínez et al. Limits on dark matter annihilation in the sun using the ANTARES neutrino telescope. *Physics Letters B*, 759:69–74, Aug 2016.

[57] J. Billard, E. Figueroa-Feliciano, and L. Strigari. Implication of neutrino backgrounds on the reach of next generation dark matter direct detection experiments. *Phys. Rev. D*, 89:023524, Jan 2014.

[58] E. Aprile et al. Constraining the Spin-Dependent WIMP-Nucleon Cross Sections with XENON1T. *Physical Review Letters*, 122(14), Apr 2019.

[59] D. S. Akerib et al. Limits on Spin-Dependent WIMP-Nucleon Cross Section Obtained from the Complete LUX Exposure. *Phys. Rev. Lett.*, 118:251302, Jun 2017.

[60] Jingkai Xia et al. PandaX-II Constraints on Spin-Dependent WIMP-Nucleon Effective Interactions. *Phys. Lett. B*, 792:193–198, 2019.

[61] Search for new phenomena in events with jets and missing transverse momentum in pp collisions at $\sqrt{s} = 13$ TeV with the ATLAS detector. Technical Report ATLAS-CONF-2020-048, CERN, Geneva, Aug 2020.

[62] M.G. Aartsen et al. Improved limits on dark matter annihilation in the Sun with the 79-string IceCube detector and implications for supersymmetry. *Journal of Cosmology and Astroparticle Physics*, 2016(04):022–022, Apr 2016.

[63] Nicolò Trevisani. Collider Searches for Dark Matter (ATLAS + CMS). *Universe*, 4(11), 2018.

[64] N Ilic. Searching for Dark Matter with the ATLAS detector. *Journal of Physics: Conference Series*, 1690:012153, dec 2020.

[65] Antonio Boveia and Caterina Doglioni. Dark Matter Searches at Colliders. *Annual Review of Nuclear and Particle Science*, 68(1):429–459, Oct 2018.

[66] Albert M Sirunyan et al. Search for dark matter produced in association with a leptonically decaying Z boson in proton-proton collisions at $\sqrt{s} = 13$ TeV. *Eur. Phys. J. C*, 81(1):13, 2021.

[67] Antonio Boveia et al. Recommendations on presenting LHC searches for missing transverse energy signals using simplified s-channel models of dark matter. *arXiv e-prints*, 2016. arXiv:1603.04156.

[68] Reinard Primulando and Patipan Uttayarat. Dark Matter-Neutrino Interaction in Light of Collider and Neutrino Telescope Data. *JHEP*, 06:026, 2018.

[69] M. Aaboud et al. Search for a new heavy gauge-boson resonance decaying into a lepton and missing transverse momentum in 36 fb^{-1} of pp collisions at $\sqrt{s} = 13$ TeV with the ATLAS experiment. *The European Physical Journal C*, 78(5), May 2018.

[70] K.A. Olive. Review of Particle Physics. *Chinese Physics C*, 40(10):100001, oct 2016.

[71] Marco Cirelli et al. INTEGRAL x-ray constraints on sub-GeV dark matter. *Physical Review D*, 103(6), Mar 2021.

[72] Rouven Essig et al. Constraining light dark matter with diffuse X-ray and gamma-ray observations. *Journal of High Energy Physics*, 2013(11), Nov 2013.

[73] Mathieu Boudaud, Julien Lavalle, and Pierre Salati. Novel Cosmic-Ray Electron and Positron Constraints on MeV Dark Matter Particles. *Physical Review Letters*, 119(2), Jul 2017.

[74] A. Gando et al. Search for Extraterrestrial Antineutrino Sources with the KamLAND Detector. *The Astrophysical Journal*, 745(2):193, Jan 2012.

[75] Andrés Olivares-Del Campo, Céline Bœhm, Sergio Palomares-Ruiz, and Silvia Pascoli. Dark matter-neutrino interactions through the lens of their cosmological implications. *Phys. Rev. D*, 97(7):075039, 2018.

[76] Gary Steigman, Basudeb Dasgupta, and John F. Beacom. Precise relic WIMP abundance and its impact on searches for dark matter annihilation. *Physical Review D*, 86(2), Jul 2012.

[77] Carlos Pérez de los Heros. Status, Challenges and Directions in Indirect Dark Matter Searches. *Symmetry*, 12(10):1648, Oct 2020.

[78] Jennifer M. Gaskins. A review of indirect searches for particle dark matter. *Contemporary Physics*, 57(4):496–525, Jun 2016.

[79] Javier Rico. Gamma-Ray Dark Matter Searches in Milky Way Satellites—A Comparative Review of Data Analysis Methods and Current Results. *Galaxies*, 8(1), 2020.

[80] H. Abdallah et al. Search for dark matter signals towards a selection of recently detected DES dwarf galaxy satellites of the Milky Way with H.E.S.S. *Physical Review D*, 102(6), Sep 2020.

[81] H. Abdallah et al. Search for gamma-Ray Line Signals from Dark Matter Annihilations in the Inner Galactic Halo from 10 Years of Observations with H.E.S.S. *Physical Review Letters*, 120(20), May 2018.

[82] Javier Rico. Overview of MAGIC results. *Nuclear and Particle Physics Proceedings*, 273-275:328–333, 2016. 37th International Conference on High Energy Physics (ICHEP).

[83] MAGIC Collaboration. Limits to dark matter annihilation cross-section from a combined analysis of MAGIC and Fermi-LAT observations of dwarf satellite galaxies. *Journal of Cosmology and Astroparticle Physics*, 2016(2):039, February 2016.

[84] Charles Thorpe-Morgan et al. Annihilating Dark Matter Search with 12 Years of Fermi LAT Data in Nearby Galaxy Clusters. *arXiv e-prints*, 10 2020. arXiv:2010.11006.

[85] J. den Herder et al. COMPTEL: instrument description and performance. In *NASA Conference Publication*, volume 3137 of *NASA Conference Publication*, pages 85–94, February 1992.

[86] A Galper et al. The PAMELA experiment: a decade of Cosmic Ray Physics in space. *Journal of Physics: Conference Series*, 798:012033, 01 2017.

[87] M. Aguilar et al. The Alpha Magnetic Spectrometer (AMS) on the international space station: Part II — Results from the first seven years. *Physics Reports*, 894:1–116, 2021.

[88] Jin Chang et al. An excess of cosmic ray electrons at energies of 300–800 GeV. *Nature*, 456:362–5, 12 2008.

[89] I. Allekotte et al. The Surface Detector System of the Pierre Auger Observatory. *Nucl. Instrum. Meth. A*, 586:409–420, 2008.

[90] Esteban Alcantara, Luis A. Anchordoqui, and Jorge F. Soriano. Hunting for superheavy dark matter with the highest-energy cosmic rays. *Phys. Rev. D*, 99(10):103016, 2019.

[91] S. Krimigis et al. The Low Energy Charged Particle (LECP) Experiment on the Voyager Spacecraft. *Space Science Reviews*, 21(3):329–354, December 1977.

[92] E. C. Stone et al. Voyager 1 Observes Low-Energy Galactic Cosmic Rays in a Region Depleted of Heliospheric Ions. *Science*, 341(6142):150–153, 2013.

[93] M. Aartsen et al. Search for neutrinos from decaying dark matter with IceCube. *The European Physical Journal C*, 78(10), Oct 2018.

[94] Arman Esmaili, Alejandro Ibarra, and Orlando L.G Peres. Probing the stability of superheavy dark matter particles with high-energy neutrinos. *Journal of Cosmology and Astroparticle Physics*, 2012(11):034–034, Nov 2012.

[95] Laura Covi, Michael Grefe, Alejandro Ibarra, and David Tran. Neutrino Signals from Dark Matter Decay. *Journal of Cosmology and Astroparticle Physics*, 2010:017, 04 2010.

[96] Sergio Palomares-Ruiz and Silvia Pascoli. Testing MeV dark matter with neutrino detectors. *Physical Review D*, 77, 11 2007.

[97] A. Albert et al. Results from the search for dark matter in the Milky Way with 9 years of data of the ANTARES neutrino telescope. *Physics Letters B*, 769:249–254, Jun 2017.

[98] M. G. Aartsen et al. Search for neutrinos from dark matter self-annihilations in the center of the Milky Way with 3 years of IceCube/DeepCore. *The European Physical Journal C*, 77(9), Sep 2017.

[99] Katarzyna Frankiewicz. Dark matter searches with the Super-Kamiokande detector. *Journal of Physics: Conference Series*, 888:012210, 09 2017.

[100] A. Albert et al. Combined search for neutrinos from dark matter self-annihilation in the Galactic Center with ANTARES and IceCube. *Physical Review D*, 102(8), Oct 2020.

[101] Andrew Gould. Weakly Interacting Massive Particle Distribution in and Evaporation from the Sun. *Astrophysical Journal*, 321:560, October 1987.

[102] Dan Hooper, Frank Petriello, Kathryn M. Zurek, and Marc Kamionkowski. New DAMA dark-matter window and energetic-neutrino searches. *Physical Review D*, 79(1), Jan 2009.

[103] Wan-Lei Guo. Detecting electron neutrinos from solar dark matter annihilation by JUNO. *JCAP*, 01:039, 2016.

[104] K. Griest and D. Seckel. Cosmic Asymmetry, Neutrinos and the Sun. *Nucl. Phys. B*, 283:681–705, 1987. [Erratum: Nucl.Phys.B 296, 1034–1036 (1988)].

[105] A. Albert et al. Search for dark matter annihilation in the earth using the ANTARES neutrino telescope. *Physics of the Dark Universe*, 16:41–48, 2017.

[106] M. Aartsen et al. First search for dark matter annihilations in the Earth with the IceCube detector. *The European Physical Journal C*, 77(2), Feb 2017.

[107] Piotr Mijakowski. Dark Matter Searches at Super-Kamiokande. *J. Phys. Conf. Ser.*, 1342(1):012075, 2020.

[108] Hasan Yüksel, Shunsaku Horiuchi, John F. Beacom, and Shin'ichiro Ando. Neutrino constraints on the dark matter total annihilation cross section. *Physical Review D*, 76(12), Dec 2007.

[109] K. Eguchi et al. First Results from KamLAND: Evidence for Reactor Antineutrino Disappearance. *Phys. Rev. Lett.*, 90:021802, Jan 2003.

[110] S. Fukuda et al. The Super-Kamiokande detector. *Nuclear Instruments and Methods in Physics Research Section A: Accelerators, Spectrometers, Detectors and Associated Equipment*, 501(2):418–462, 2003.

[111] Pavel A Cherenkov. Visible light from clear liquids under the action of gamma radiation. *Comptes Rendus (Doklady) de l'Aeademie des Sciences de l'URSS*, 2(8):451–454, 1934.

[112] K. Abe et al. Solar neutrino results in Super-Kamiokande-III. *Physical Review D*, 83(5), Mar 2011.

[113] Yoichiro Suzuki. The Super-Kamiokande experiment. *The European Physical Journal C*, 79, 04 2019.

[114] J. Caravaca, B. J. Land, M. Yeh, and G. D. Orebi Gann. Characterization of water-based liquid scintillator for Cherenkov and scintillation separation. *The European Physical Journal C*, 80(9), Sep 2020.

[115] Andres Olivares-Del Campo, Sergio Palomares-Ruiz, and Silvia Pascoli. Implications of a Dark Matter-Neutrino Coupling at Hyper-Kamiokande. *arXiv e-prints*, 2018. arXiv:1805.09830.

[116] Introduction of Gadolinium into Super-Kamiokande and the Start of New Observations. `http://www-sk.icrr.u-tokyo.ac.jp/sk/news/2020/08/sk-gd-detail-e.html`, 2020.

[117] Wan Linyan. *Experimental Studies on Low Energy Electron Antineutrinos and Related Physics*. PhD thesis, Tsinghua U., Beijing, 2018.

[118] Wolfgang A. Rolke, Angel M. Lopez, and Jan Conrad. Limits and confidence intervals in the presence of nuisance parameters. *Nuclear Instruments and Methods in Physics Research A*, 551(2-3):493–503, October 2005.

[119] I. Antcheva et al. ROOT — A C++ framework for petabyte data storage, statistical analysis and visualization. *Computer Physics Communications*, 180(12):2499–2512, Dec 2009.

[120] E. Richard et al. Measurements of the atmospheric neutrino flux by Super-Kamiokande: Energy spectra, geomagnetic effects, and solar modulation. *Phys. Rev. D*, 94:052001, Sep 2016.

[121] Nicole F. Bell, Matthew J. Dolan, and Sandra Robles. Searching for Sub-GeV dark matter in the galactic centre using Hyper-Kamiokande. *Journal of Cosmology and Astroparticle Physics*, 2020(09):019–019, Sep 2020.

[122] K. Abe et al. Hyper-Kamiokande Design Report. *arXiv e-prints*, 2018. arXiv:1805.04163.

[123] Alexander Felix Tietzsch. *Development, Installation and Operation of a Container-based Mass Testing System for 20-inch Photomultiplier Tubes for JUNO*. PhD thesis, Universität Tübingen, October 2020.

[124] Zelimir Djurcic et al. JUNO Conceptual Design Report. *arXiv e-prints*, 8 2015. arXiv:1508.07166.

[125] W. Pauli. Dear radioactive ladies and gentlemen. *Phys.Today*, 31N9:27, 1978.

[126] C. L. Cowan, F. Reines, F. B. Harrison, H. W. Kruse, and A. D. McGuire. Detection of the Free Neutrino: a Confirmation. *Science*, 124(3212):103–104, July 1956.

[127] Mary K. Gaillard, Paul D. Grannis, and Frank J. Sciulli. The standard model of particle physics. *Rev. Mod. Phys.*, 71:S96–S111, Mar 1999.

[128] T. D. Lee and C. N. Yang. Question of Parity Conservation in Weak Interactions. *Physical Review*, 104(1):254–258, October 1956.

[129] C. S. Wu, E. Ambler, R. W. Hayward, D. D. Hoppes, and R. P. Hudson. Experimental Test of Parity Conservation in Beta Decay. *Physical Review*, 105(4):1413–1415, February 1957.

[130] M. Goldhaber, L. Grodzins, and A. W. Sunyar. Helicity of Neutrinos. *Physical Review*, 109(3):1015–1017, February 1958.

[131] J. A. Formaggio and G. P. Zeller. From eV to EeV: Neutrino cross sections across energy scales. *Rev. Mod. Phys.*, 84:1307–1341, Sep 2012.

[132] Raymond Davis, Don S. Harmer, and Kenneth C. Hoffman. Search for Neutrinos from the Sun. *Phys. Rev. Lett.*, 20:1205–1209, May 1968.

[133] Bruce T. Cleveland et al. Measurement of the Solar Electron Neutrino Flux with the Homestake Chlorine Detector. *The Astrophysical Journal*, 496(1):505–526, March 1998.

[134] John N. Bahcall et al. Standard solar models and the uncertainties in predicted capture rates of solar neutrinos. *Rev. Mod. Phys.*, 54:767–799, Jul 1982.

[135] P. Anselmann et al. Solar neutrinos observed by GALLEX at Gran Sasso. *Phys. Lett. B*, 285:376–389, 1992.

[136] M. Altmann et al. GNO solar neutrino observations: Results for GNO I. *Phys. Lett. B*, 490:16–26, 2000.

[137] J. N. Abdurashitov et al. Measurement of the solar neutrino capture rate by SAGE and implications for neutrino oscillations in vacuum. *Phys. Rev. Lett.*, 83:4686–4689, 1999.

[138] Q. R. Ahmad et al. Measurement of the Rate of $\nu_e + d \rightarrow p + p + e^-$ Interactions Produced by ^8B Solar Neutrinos at the Sudbury Neutrino Observatory. *Phys. Rev. Lett.*, 87:071301, Jul 2001.

[139] Q. R. Ahmad et al. Direct Evidence for Neutrino Flavor Transformation from Neutral-Current Interactions in the Sudbury Neutrino Observatory. *Phys. Rev. Lett.*, 89:011301, Jun 2002.

[140] Y. Fukuda et al. Evidence for Oscillation of Atmospheric Neutrinos. *Phys. Rev. Lett.*, 81:1562–1567, Aug 1998.

[141] Y. Ashie et al. Evidence for an Oscillatory Signature in Atmospheric Neutrino Oscillations. *Phys. Rev. Lett.*, 93:101801, Sep 2004.

[142] K. Abe et al. Measurement of neutrino and antineutrino oscillations by the T2K experiment including a new additional sample of ν_e interactions at the far detector. *Phys. Rev. D*, 96:092006, Nov 2017.

[143] M. A. Acero et al. First measurement of neutrino oscillation parameters using neutrinos and antineutrinos by NOvA. *Phys. Rev. Lett.*, 123:151803, Oct 2019.

[144] P. Adamson et al. Measurement of Neutrino and Antineutrino Oscillations Using Beam and Atmospheric Data in MINOS. *Phys. Rev. Lett.*, 110:251801, Jun 2013.

[145] Y. Abe et al. Improved measurements of the neutrino mixing angle θ_{13} with the Double Chooz detector. *Journal of High Energy Physics*, 2014(10), Oct 2014.

[146] D. Adey et al. Measurement of the Electron Antineutrino Oscillation with 1958 Days of Operation at Daya Bay. *Phys. Rev. Lett.*, 121:241805, Dec 2018.

[147] J. K. Ahn et al. Observation of Reactor Electron Antineutrinos Disappearance in the RENO Experiment. *Phys. Rev. Lett.*, 108:191802, May 2012.

[148] N. Agafonova et al. Observation of a first ν_τ candidate event in the OPERA experiment in the CNGS beam. *Physics Letters B*, 691(3):138–145, 2010.

[149] Ivan Esteban, M.C. Gonzalez-Garcia, Michele Maltoni, Thomas Schwetz, and Albert Zhou. The fate of hints: updated global analysis of three-flavor neutrino oscillations. *Journal of High Energy Physics*, 2020(9), Sep 2020.

[150] Ivan Esteban et al. Nufit 5.0 (2020). `http://www.nu-fit.org/`. Accessed on February 25th, 2021.

[151] M. A. Acero et al. First measurement of neutrino oscillation parameters using neutrinos and antineutrinos by NOvA. *Phys. Rev. Lett.*, 123:151803, Oct 2019.

[152] R. Acciarri et al. Long-Baseline Neutrino Facility (LBNF) and Deep Underground Neutrino Experiment (DUNE) Conceptual Design Report Volume 1: The LBNF and DUNE Projects. *arXiv e-prints*, 2016. arXiv:1601.05471.

[153] R. Acciarri et al. Long-Baseline Neutrino Facility (LBNF) and Deep Underground Neutrino Experiment (DUNE) Conceptual Design Report Volume 2: The Physics Program for DUNE at LBNF. *arXiv e-prints*, 2016. arXiv:1512.06148.

[154] M. G. Aartsen et al. PINGU: A Vision for Neutrino and Particle Physics at the South Pole. *J. Phys. G*, 44(5):054006, 2017.

[155] M. Aker et al. Improved Upper Limit on the Neutrino Mass from a Direct Kinematic Method by KATRIN. *Phys. Rev. Lett.*, 123:221802, Nov 2019.

[156] M. Galeazzi et al. The Electron Capture Decay of 163-Ho to Measure the Electron Neutrino Mass with sub-eV Accuracy (and Beyond). *arXiv e-prints*, 2012. arXiv:1202.4763.

[157] Matteo Agostini et al. Background-free search for neutrinoless double-β decay of 76Ge with GERDA. *Nature*, 544:47–52, 04 2017.

[158] N. Abgrall et al. The large enriched germanium experiment for neutrinoless double beta decay (legend). *AIP Conference Proceedings*, 2017.

[159] A. Gando et al. Search for Majorana Neutrinos Near the Inverted Mass Hierarchy Region with KamLAND-Zen. *Phys. Rev. Lett.*, 117:082503, Aug 2016.

[160] Planck Collaboration. Planck 2018 results - I. Overview and the cosmological legacy of Planck. *A&A*, 641:A1, 2020.

[161] E Majorana. Teoria simmetrica dell'elettrone e del positrone. *Nuovo Cimento*, 14:171–184, 1937.

[162] T. Mueller et al. Improved predictions of reactor antineutrino spectra. *Phys. Rev. C*, 83:054615, May 2011.

[163] P. Huber. Determination of antineutrino spectra from nuclear reactors. *Phys. Rev. C*, 84:024617, Aug 2011.

[164] M. Fallot et al. New Antineutrino Energy Spectra Predictions from the Summation of Beta Decay Branches of the Fission Products. *Phys. Rev. Lett.*, 109:202504, Nov 2012.

[165] P. Novella. The antineutrino energy structure in reactor experiments. *Adv. High Energy Phys.*, 2015:364392, 2015.

[166] D. Adey et al. Improved measurement of the reactor antineutrino flux at Daya Bay. *Phys. Rev. D*, 100:052004, Sep 2019.

[167] M. Agostini et al. Comprehensive measurement of *pp*-chain solar neutrinos. *Nature*, 562(7728):505–510, 2018.

[168] Aldo Ianni. Solar neutrinos and the solar model. *Physics of the Dark Universe*, 4:44–49, 2014. DARK TAUP2013.

[169] M. Agostini et al. Simultaneous precision spectroscopy of *pp*, ^{7}Be, and *pep* solar neutrinos with Borexino Phase-II. *Phys. Rev. D*, 100:082004, Oct 2019.

[170] M. Agostini et al. Experimental evidence of neutrinos produced in the CNO fusion cycle in the Sun. *Nature*, 587:577–582, 2020.

[171] Angel Abusleme et al. Feasibility and physics potential of detecting 8B solar neutrinos at JUNO. *Chinese Physics C*, 45(2):023004, Jan 2021.

[172] O. Smirnov. Experimental aspects of geoneutrino detection: Status and perspectives. *Progress in Particle and Nuclear Physics*, 109:103712, Nov 2019.

[173] T. Araki et al. Experimental investigation of geologically produced antineutrinos with KamLAND. *Nature*, 436(7050):499–503, July 2005.

[174] A. Gando et al. Partial radiogenic heat model for Earth revealed by geoneutrino measurements. *Nature Geoscience*, 4(9):647–651, September 2011.

[175] G. Bellini et al. Observation of geo-neutrinos. *Physics Letters B*, 687(4-5):299–304, April 2010.

[176] M. Agostini et al. Spectroscopy of geoneutrinos from 2056 days of Borexino data. *Phys. Rev. D*, 92(3):031101, August 2015.

[177] Ran Han et al. Potential of geo-neutrino measurements at JUNO. *Chinese Physics C*, 40(3):033003, Mar 2016.

[178] Pietro Antonioli et al. SNEWS: the SuperNova Early Warning System. *New Journal of Physics*, 6:114–114, sep 2004.

[179] Julia Sawatzki. *Towards the Detection of the Diffuse Supernova Neutrino Background in the Large Volume Scintillator Experiment JUNO*. Dissertation, Technische Universität München, München, 2020.

[180] K. Bays et al. Supernova relic neutrino search at Super-Kamiokande. *Phys. Rev. D*, 85:052007, Mar 2012.

[181] T. Gaisser and M. Honda. FLUX OF ATMOSPHERIC NEUTRINOS. *Annual Review of Nuclear and Particle Science*, 52(1):153–199, 2002.

[182] Angel Abusleme et al. JUNO sensitivity to low energy atmospheric neutrino spectra. *The European Physical Journal C*, 81(10), Oct 2021.

[183] E. Richard et al. Measurements of the atmospheric neutrino flux by Super-Kamiokande: Energy spectra, geomagnetic effects, and solar modulation. *Phys. Rev. D*, 94:052001, Sep 2016.

[184] M. G. Aartsen et al. Determining neutrino oscillation parameters from atmospheric muon neutrino disappearance with three years of IceCube DeepCore data. *Phys. Rev. D*, 91:072004, Apr 2015.

[185] P. Adamson et al. Combined Analysis of ν_μ Disappearance and $\nu_\mu \rightarrow \nu_e$ Appearance in MINOS Using Accelerator and Atmospheric Neutrinos. *Phys. Rev. Lett.*, 112:191801, May 2014.

[186] A Kumar et al. Invited review: Physics potential of the ICAL detector at the India-based Neutrino Observatory (INO). *Pramana*, 88(5), Apr 2017.

[187] S Adrián-Martínez et al. Letter of intent for KM3NeT 2.0. *Journal of Physics G: Nuclear and Particle Physics*, 43(8):084001, Jun 2016.

[188] Sandhya Choubey. Atmospheric neutrinos: Status and prospects. *Nuclear Physics B*, 908:235–249, 2016. Neutrino Oscillations: Celebrating the Nobel Prize in Physics 2015.

[189] JUNO Collaboration. JUNO Physics and Detector. *arXiv e-prints*, 2021. arXiv:2104.02565.

[190] Wan-lei Guo. Detecting electron neutrinos from solar dark matter annihilation by juno. *Journal of Cosmology and Astroparticle Physics*, 2016, 11 2015.

[191] Fabrizio Cei. Neutrinos from supernovae: Experimental status and perspectives. *Int. J. Mod. Phys. A*, 17:1765–1776, 2002.

[192] A. Strumia and F. Vissani. Precise quasielastic neutrino/nucleon cross-section. *Physics Letters B*, 564(1-2):42–54, Jul 2003.

[193] *Database of Prompt Gamma Rays from Slow Neutron Capture for Elemental Analysis*. Non-serial Publications. International Atomic Energy Agency, Vienna, 2007.

[194] Said Mughabghab. *Atlas of neutron resonances: resonance parameters and thermal cross sections Z= 1-100*. 01 2006.

[195] A. Gando et al. Search for extraterrestrial antineutrino sources with the KamLAND detector. *The Astrophysical Journal*, 745(2):193, Jan 2012.

[196] J. Xu. JUNO site muon flux update (2020). *internal JUNO collaboration document: JUNO-doc-6399-v2*, Dez 2020.

[197] A. Abusleme et al. Optimization of the JUNO liquid scintillator composition using a Daya Bay antineutrino detector. *Nuclear Instruments and Methods in Physics Research Section A: Accelerators, Spectrometers, Detectors and Associated Equipment*, 988:164823, 2021.

[198] D. Xu. NeuTel 2021: plenary talk on status and prospects of JUNO. *internal JUNO collaboration document: JUNO-doc-6523-v5*, Jan 2021.

[199] S. Ajimura et al. Technical Design Report (TDR): Searching for a Sterile Neutrino at J-PARC MLF (E56, JSNS2). *arXiv e-prints*, 2017. arXiv:1705.08629.

[200] Y. Zhang, Z.Y. Yu, X.Y. Li, Z.Y. Deng, and L.J. Wen. A complete optical model for liquid-scintillator detectors. *Nuclear Instruments and Methods in Physics Research Section A: Accelerators, Spectrometers, Detectors and Associated Equipment*, 967:163860, 2020.

[201] Michael Wurm et al. The next-generation liquid-scintillator neutrino observatory LENA. *Astroparticle Physics*, 35:685–732, 04 2012.

[202] A. Tietzsch. Recalibration Analysis for the Container System - final update. *internal JUNO collaboration document: Juno-doc-7260-v2*, Jul 2021.

[203] A. Tietzsch. Update on TTS data analysis and results from the container system. *internal JUNO collaboration document: Juno-doc-7294-v1*, Jul 2021.

[204] M. He. Introduction to the small PMT system. *internal JUNO collaboration document: Juno-doc-3955-v3*, Nov 2018.

[205] M. Li. Parameters Distribution of LPMT on Pan-Asia. *internal JUNO collaboration document: Juno-doc-7241-v3*, Jul 2021.

[206] Photomultiplier Tubes - Basics and Applications, 4th Ed. `https://www.hamamatsu.com/resources/pdf/etd/PMT_handbook_v4E.pdf`, 2017.

[207] Ling Ren et al. Mass Production of MCP-PMT for JUNO and Development of 20-inch MCP-PMT with TTS Improved. *Proceedings of the 5th International Workshop on New Photon-Detectors (PD18)*.

[208] HZC Photonics Technology Co. Ltd. Photomultiplier Tubes Product Manual. `http://www.hzcphotonics.com/products/ProductManual.pdf`, 2017.

[209] Jilei Xu. The JUNO double calorimetry system. *PoS*, NuFact2019:117, 2020.

[210] B. Wonsak et al. A container-based facility for testing 20'000 20-inch PMTs for JUNO. *Journal of Instrumentation*, 16(08):T08001, aug 2021.

[211] Peng Zhang. Progress of Veto Detector of JUNO. *Journal of Physics: Conference Series*, 1468:012188, 02 2020.

[212] Angel Abusleme et al. Calibration Strategy of the JUNO Experiment. *JHEP*, 03:004, 2021.

[213] JUNO Collaboration. The Design and Sensitivity of JUNO's scintillator radiopurity pre-detector OSIRIS. *arXiv e-prints*, 2021. arXiv:2103.16900.

[214] JUNO Collaboration. TAO Conceptual Design Report: A Precision Measurement of the Reactor Antineutrino Spectrum with Sub-percent Energy Resolution. *arXiv e-prints*, 2020. arXiv:2005.08745.

[215] G. Huang. Status of energy reconstruction. *internal JUNO collaboration document: Juno-doc-5408-v1*, Jan 2020.

[216] Tao Lin et al. The Application of SNiPER to the JUNO Simulation. *Journal of Physics: Conference Series*, 898:042029, oct 2017.

[217] Tao Lin et al. Parallelized JUNO simulation software based on SNiPER. *Journal of Physics: Conference Series*, 1085:032048, sep 2018.

[218] Leif Lönnblad. CLHEP—a project for designing a C++ class library for high energy physics. *Computer Physics Communications*, 84(1):307–316, 1994.

[219] S. Agostinelli et al. Geant4—a simulation toolkit. *Nuclear Instruments and Methods in Physics Research Section A: Accelerators, Spectrometers, Detectors and Associated Equipment*, 506(3):250–303, 2003.

[220] J. H. Zou et al. SNiPER: an offline software framework for non-collider physics experiments. *Journal of Physics: Conference Series*, 664(7):072053, dec 2015.

[221] G. Cao et al. New PMT Optical Model. *internal JUNO collaboration document: Juno-doc-6762-v1*, Feb 2021.

[222] G. Cao et al. CD Simulation Updates in New Software Release. *internal JUNO collaboration document: Juno-doc-6276-v1*, Oct 2020.

[223] A. Giaz. Status and perspectives of large PMT electronics of the JUNO experiment. *Nuovo Cim. C*, 42(4):193, 2019.

[224] Michaela Schever. Waveform Reconstruction of IBD and Muon Events in JUNO. In *XXVIII International Conference on Neutrino Physics and Astrophysics*, page 315, June 2018.

[225] Z. Yu. Review of PMT reconstruction. *internal JUNO collaboration document: Juno-doc-3103-v2*, Jan 2018.

[226] Christoph Genster et al. Muon reconstruction with a geometrical model in JUNO. *Journal of Instrumentation*, 13:T03003–T03003, 03 2018.

[227] Tao Lin et al. Fast Muon Simulation in the JUNO Central Detector. *Chinese Physics C*, 40, 01 2016.

[228] Björn Wonsak. 3D Topological Reconstruction for the JUNO Detector. In *XXVIII International Conference on Neutrino Physics and Astrophysics*, page 158, June 2018.

[229] H. Rebber, L. Ludhova, B. Wonsak, and Y. Xu. Particle identification at MeV energies in JUNO. *Journal of Instrumentation*, 16(01):P01016–P01016, jan 2021.

[230] Q. Liu, M. He, X. Ding, W. Li, and H. Peng. A vertex reconstruction algorithm in the central detector of JUNO. *Journal of Instrumentation*, 13(09):T09005–T09005, sep 2018.

[231] W. Wu, M. He, X. Zhou, and H. Qiao. A new method of energy reconstruction for large spherical liquid scintillator detectors. *Journal of Instrumentation*, 14(03):P03009–P03009, mar 2019.

[232] Zhen Qian et al. Vertex and Energy Reconstruction in JUNO with Machine Learning Methods. *arXiv e-prints*, 2021. arXiv:2101.04839.

[233] Ziyuan Li et al. Event vertex and time reconstruction in large volume liquid scintillator detector. *arXiv e-prints*, 2021. arXiv:2101.08901.

[234] The GRAVITY Collaboration, Abuter, R., et al. A geometric distance measurement to the Galactic center black hole with 0.3% uncertainty. *A&A*, 625:L10, 2019.

[235] IAU XIX GA, 1985.

[236] Hai-Nan Lin and Xin Li. The dark matter profiles in the Milky Way. *Monthly Notices of the Royal Astronomical Society*, 487(4):5679–5684, August 2019.

[237] A. Burkert. The Structure of Dark Matter Halos in Dwarf Galaxies. *Astrophysical Journal Letters*, 447:L25–L28, July 1995.

[238] Hasan Yuksel, Shunsaku Horiuchi, John Beacom, and Shin'ichiro Ando. Neutrino Constraints on the Dark Matter Total Annihilation Cross Section. *Physical Review D*, 76, 08 2007.

[239] P. Belli, R. Cerulli, N. Fornengo, and S. Scopel. Effect of the galactic halo modeling on the DAMA-NaI annual modulation result: An extended analysis of the data for weakly interacting massive particles with a purely spin-independent coupling. *Physical Review D*, 66(4), Aug 2002.

[240] Julio F. Navarro, Carlos S. Frenk, and Simon D. M. White. The Structure of Cold Dark Matter Halos. *The Astrophysical Journal*, 462:563, May 1996.

[241] B. Moore, T. Quinn, F. Governato, J. Stadel, and G. Lake. Cold collapse and the core catastrophe. *Monthly Notices of the Royal Astronomical Society*, 310(4):1147–1152, Dec 1999.

[242] Andrey V. Kravtsov, Anatoly A. Klypin, James S. Bullock, and Joel R. Primack. The Cores of Dark Matter–Dominated Galaxies: Theory versus Observations. *The Astrophysical Journal*, 502(1):48–58, Jul 1998.

[243] P. Vogel and J. F. Beacom. Angular distribution of neutron inverse beta decay. *Phys. Rev. D*, 60:053003, Jul 1999.

[244] Z. Li. Review of vertex reconstruction in 2020. *internal JUNO collaboration document: JUNO-doc-5405-v2*, Jan 2020.

[245] Z. Li. Vertex Reconstruction Study. *internal JUNO collaboration document: JUNO-doc-4769-v1*, Jul 2019.

[246] P Vogel et al. Reactor antineutrino spectra and their application to antineutrino-induced reactions. II. *Phys. Rev. C; (United States)*, 24:4, Oct 1981.

[247] Alankrita Priya and Cecilia Lunardini. Diffuse neutrinos from luminous and dark supernovae: prospects for upcoming detectors at the $\mathcal{O}(10)$ kt scale. *Journal of Cosmology and Astroparticle Physics*, 2017(11):031–031, Nov 2017.

[248] Lorenz Hudepohl. *Neutrinos from the Formation, Cooling and Black Hole Collapse of Neutron Stars*. PhD thesis, Munich, Tech. U., 10 2013.

[249] A. Mirizzi et al. Supernova neutrinos: production, oscillations and detection. *Riv. Nuovo Cim.*, 39:1–112, 2016.

[250] Edwin E. Salpeter. The Luminosity Function and Stellar Evolution. *The Astrophysical Journal*, 121:161, January 1955.

[251] Andrew M. Hopkins and John F. Beacom. On the Normalization of the Cosmic Star Formation History. *The Astrophysical Journal*, 651(1):142–154, Nov 2006.

[252] S. Horiuchi et al. The red supergiant and supernova rate problems: implications for core-collapse supernova physics. *Monthly Notices of the Royal Astronomical Society: Letters*, 445(1):L99–L103, 09 2014.

[253] Marcella Ugliano, Hans-Thomas Janka, Andreas Marek, and Almudena Arcones. Progenitor-explosion connection and remnant birth masses for neutrino-driven supernovae of iron-core progenitors. *The Astrophysical Journal*, 757(1):69, Sep 2012.

[254] Shin'ichiro Ando and Katsuhiko Sato. Relic neutrino background from cosmological supernovae. *New Journal of Physics*, 6:170–170, Nov 2004.

[255] Shunsaku Horiuchi, John F. Beacom, and Eli Dwek. Diffuse supernova neutrino background is detectable in Super-Kamiokande. *Physical Review D*, 79(8), Apr 2009.

[256] Atmospheric Neutrino Flux Tables for One-Year-Average (HAKKM, 2014). `http://www.icrr.u-tokyo.ac.jp/~mhonda/nflx2014/index.html`, 2014.

[257] M. Honda et al. Atmospheric neutrino flux calculation using the NRLMSISE-00 atmospheric model. *Phys. Rev.*, D92(2):023004, 2015.

[258] Yusuke Koshio. Observation of Atmospheric Neutrinos. *Universe*, 6(6), 2020.

[259] T. K. Gaisser, Todor Stanev, and Giles Barr. Cosmic-ray neutrinos in the atmosphere. *Phys. Rev. D*, 38:85–95, Jul 1988.

[260] G. Battistoni et al. The atmospheric neutrino flux below 100 MeV: The FLUKA results. *Astropart. Phys.*, 23:526–534, 2005.

[261] G. Fogli et al. Three generation flavor transitions and decays of supernova relic neutrinos. *Phys. Rev. D*, 70:013001, 2004.

[262] G. Fogli et al. Addendum to "solar neutrino oscillation parameters after first KamLAND results". *Phys. Rev. D*, 69:017301, Jan 2004.

[263] T. Yoshida et al. Neutrino-Nucleus Reaction Cross Sections for Light Element Synthesis in Supernova Explosions. *The Astrophysical Journal*, 686:448, Dec 2008.

[264] C. Andreopoulos et al. The GENIE Neutrino Monte Carlo Generator: Physics and User Manual, 2015. arXiv:1510:05494.

[265] GENIE: Event Generator and Global Analysis of Neutrino Scattering Data. `https://hep.ph.liv.ac.uk/~costasa/genie/index.html`, 2021.

[266] C. Llewellyn Smith. Neutrino Reactions at Accelerator Energies. *Phys. Rept.*, 3:261–379, 1972.

[267] D. Rein and L. Sehgal. Neutrino-excitation of baryon resonances and single pion production. *Annals of Physics*, 133(1):79 – 153, 1981.

[268] G. Settanta et al. Atmospheric neutrino spectrum reconstruction with JUNO. *internal JUNO collaboration document: JUNO-doc-4965-v1*, Jul 2019.

[269] E. Paschos and J. Yu. Neutrino interactions in oscillation experiments. *Phys. Rev. D*, 65:033002, Jan 2002.

[270] L. Ahrens et. al. Measurement of neutrino-proton and antineutrino-proton elastic scattering. *Phys. Rev. D*, 35:785–809, Feb 1987.

[271] Y. Kamyshkov and E. Kolbe. Signatures of nucleon disappearance in large underground detectors. *Physical Review D*, 67(7), Apr 2003.

[272] TALYS - simulation of nuclear reactions. `https://tendl.web.psi.ch/tendl_2019/talys.html`, 2021.

[273] J. Cheng. Atmospheric Neutrino Background Generator. *internal JUNO collaboration document: JUNO-doc-3836-v1*, Sep 2018.

[274] TUNL Nuclear Data Evaluation Group. `https://nucldata.tunl.duke.edu/`, 2021.

[275] H. Wulandari, J. Jochum, W. Rau, and F. von Feilitzsch. Neutron flux at the Gran Sasso underground laboratory revisited. *Astroparticle Physics*, 22(3-4):313–322, Nov 2004.

[276] Double Chooz collaboration. Double Chooz θ_{13} measurement via total neutron capture detection. *Nat. Phys.*, Apr 2020.

[277] J. Cheng et al. Status of Fast Neutron Simulation at JUNO. *internal JUNO collaboration document: JUNO-doc-2274-v1*, Feb 2017.

[278] D. Webber. An improved measurement of electron antineutrino disappearance at Daya Bay. *Nuclear Physics B - Proceedings Supplements*, 233:96 – 101, 2012.

[279] Nuclear Data Services. `https://www-nds.iaea.org/`, 2021.

[280] National Nuclear Data Center. `https://www.nndc.bnl.gov/`, 2021.

[281] Paolo Lombardi et al. Decay time and pulse shape discrimination of liquid scintillators based on novel solvents. *Nucl. Instrum. Meth. A*, 701:133–144, 2013.

[282] T. Marrodán Undagoitia et al. Fluorescence decay-time constants in organic liquid scintillators. *Review of Scientific Instruments*, 80(4):043301, Apr 2009.

[283] G. Cao et al. Particle Discrimination. *internal JUNO collaboration document: JUNO-doc-1359-v1*, Jan 2016.

[284] R. Zhao et al. After-pulse Model of 20"PMT. *internal JUNO collaboration document: JUNO-doc-6185-v1*, Aug 2020.

[285] Stefan Wagner. *Energy non-linearity studies and pulse shape analysis of liquid scintillator signals in the Double Chooz experiment*. PhD thesis, Heidelberg U., 2014.

[286] J. Ashenfelter et al. Light collection and pulse-shape discrimination in elongated scintillator cells for the PROSPECT reactor antineutrino experiment. *Journal of Instrumentation*, 10(11):P11004–P11004, nov 2015.

[287] H.O. Back et al. Pulse-shape discrimination with the Counting Test Facility. *Nuclear Instruments and Methods in Physics Research Section A: Accelerators, Spectrometers, Detectors and Associated Equipment*, 584:98–113, 01 2008.

[288] E. Gatti and F. De Martini. A new linear method of discrimination between elementary particles in scintillation counters. *International Atomic Energy Agency (IAEA)*, 04 1962.

[289] J. Griffiths et al. Pulse Shape Discrimination and Exploration of Scintillation Signals Using Convolutional Neural Networks. *arXiv e-prints*, 2018. arXiv:1807.06853.

[290] A. Caldwell and K. Kröninger. Signal discovery in sparse spectra: A Bayesian analysis. *Phys. Rev. D*, 74:092003, Nov 2006.

[291] Daniel Foreman-Mackey, David Hogg, Dustin Lang, and Jonathan Goodman. emcee: the MCMC hammer. *Publications of the Astronomical Society of the Pacific*, 125:306–312, 03 2013.

[292] Jonathan Goodman and Jonathan Weare. Ensemble samplers with affine invariance. *Communications in Applied Mathematics and Computational Science*, 5(1):65 – 80, 2010.

[293] Daniel Foreman-Mackey. corner.py: Scatterplot matrices in Python. *The Journal of Open Source Software*, 1, 06 2016.

[294] Allen Caldwell, Daniel Kollár, and Kevin Kröninger. BAT – The Bayesian analysis toolkit. *Computer Physics Communications*, 180(11):2197–2209, Nov 2009.

[295] Jie Cheng, Yu-Feng Li, Hao-Qi Lu, and Liang-Jian Wen. Neutral-current background induced by atmospheric neutrinos at large liquid-scintillator detectors. II. Methodology for in situ measurements. *Phys. Rev. D*, 103:053002, Mar 2021.

[296] B. Wonsak. Directionality of MeV Electron Events in JUNO. *internal JUNO collaboration document: JUNO-doc-5909-v2*, Jun 2020.

[297] M. Apollonio et al. Determination of neutrino incoming direction in the CHOOZ experiment and its application to supernova explosion location by scintillator detectors. *Phys. Rev. D*, 61:012001, Dec 1999.

[298] Ya. Nikitenko. Determination of the direction to a source of antineutrinos via inverse beta decay in Double Chooz. *Physics of Particles and Nuclei*, 47(6):1009–1013, November 2016.

[299] J. R. Alonso et al. Advanced Scintillator Detector Concept (ASDC): A Concept Paper on the Physics Potential of Water-Based Liquid Scintillator. *arXiv e-prints*, 2014. arXiv:1409.5864.

[300] M. Yeh et al. A new water-based liquid scintillator and potential applications. *Nucl. Instrum. Meth. A*, 660:51–56, 2011.

[301] Julia Sawatzki, Michael Wurm, and Daniel Kresse. Detecting the diffuse supernova neutrino background in the future water-based liquid scintillator detector Theia. *Phys. Rev. D*, 103:023021, Jan 2021.

[302] J. Brack et al. Characterization of the Hamamatsu R11780 12 in. photomultiplier tube. *Nuclear Instruments and Methods in Physics Research Section A: Accelerators, Spectrometers, Detectors and Associated Equipment*, 712:162–173, Jun 2013.

[303] A.V. Lyashenko et al. Performance of Large Area Picosecond Photo-Detectors (LAPPD). *Nuclear Instruments and Methods in Physics Research Section A: Accelerators, Spectrometers, Detectors and Associated Equipment*, 958:162834, Apr 2020.

[304] Michael J. Minot, Mark A. Popecki, and Matthew J. Wetstein. Large Area Picosecond Photodetector (LAPPD) Performance Test Results. In *2018 IEEE Nuclear Science Symposium and Medical Imaging Conference Proceedings (NSS/MIC)*, pages 1–4, 2018.

[305] B. Land et al. MeV-scale performance of water-based and pure liquid scintillator detectors. *Physical Review D*, 103(5), Mar 2021.

[306] Tanner Kaptanoglu et al. Spectral photon sorting for large-scale Cherenkov and scintillation detectors. *Phys. Rev. D*, 101:072002, Apr 2020.

[307] T. Kaptanoglu, M. Luo, and J. Klein. Cherenkov and scintillation light separation using wavelength in LAB based liquid scintillator. *Journal of Instrumentation*, 14(05):T05001–T05001, May 2019.

[308] Andrew D. Missert et al. Improving the T2K Oscillation Analysis With fiTQun: A New Maximum-Likelihood Event Reconstruction for Super-Kamiokande. *Journal of Physics: Conference Series*, 888:012066, Sep 2017.

[309] B.S. Wonsak et al. Topological track reconstruction in unsegmented, large-volume liquid scintillator detectors. *Journal of Instrumentation*, 13(07):P07005–P07005, Jul 2018.

[310] L.J. Bignell et al. Characterization and modeling of a Water-based Liquid Scintillator. *Journal of Instrumentation*, 10(12):P12009–P12009, dec 2015.

[311] J. Caravaca et al. Experiment to demonstrate separation of Cherenkov and scintillation signals. *Physical Review C*, 95(5), May 2017.

[312] A. R. Back et al. Accelerator Neutrino Neutron Interaction Experiment (ANNIE): Preliminary Results and Physics Phase Proposal, 2017. arXiv:1707.08222.

[313] S. Andringa et al. Current Status and Future Prospects of the SNO+ Experiment. *Advances in High Energy Physics*, 2016:1–21, 2016.

[314] M. Askins et al. The Physics and Nuclear Nonproliferation Goals of WATCHMAN: A WAter CHerenkov Monitor for ANtineutrinos. *arXiv e-prints*, 2015. arXiv:1502.01132.

[315] RATPAC - A flexible package for detector simulation and analysis. `https://github.com/rat-pac/rat-pac/`, 2021.

[316] Drew R. Onken et al. Time response of water-based liquid scintillator from x-ray excitation. *Mater. Adv.*, 1:71–76, 2020.

[317] SNO+ collaboration. Internal SNO+ collaboration document, 2020.

[318] Raymond C. Smith and Karen S. Baker. Optical properties of the clearest natural waters (200-800 nm). *Appl. Opt.*, 20(2):177–184, Jan 1981.

[319] Robin M. Pope and Edward S. Fry. Absorption spectrum (380-700 nm) of pure water. II. Integrating cavity measurements. *Appl. Opt.*, 36(33):8710–8723, Nov 1997.

[320] https://reactors.geoneutrinos.org/. `https://reactors.geoneutrinos.org/`, 2021.

[321] Z. Li et al. Measurement of the tau neutrino cross section in atmospheric neutrino oscillations with Super-Kamiokande. *Phys. Rev. D*, 98:052006, Sep 2018.

[322] Sanford Underground Research Facility. `https://www.sanfordlab.org/`, 2021.

[323] Toshio Suzuki, Satoshi Chiba, Takashi Yoshida, Koh Takahashi, and Hideyuki Umeda. Neutrino-nucleus reactions on ^{16}O based on new shell-model Hamiltonians. *Phys. Rev. C*, 98:034613, Sep 2018.

[324] H. Ejiri. Nuclear deexcitations of nucleon holes associated with nucleon decays in nuclei. *Phys. Rev. C*, 48:1442–1444, Sep 1993.

[325] K. Kobayashi et al. De-excitation gamma-rays from the s-hole state in N-15 associated with proton decay in O-16. *nucl-ex/0604006*, 4 2006.

[326] L. Wan et al. Measurement of the neutrino-oxygen neutral-current quasielastic cross section using atmospheric neutrinos at Super-Kamiokande. *Physical Review D*, 99(3), Feb 2019.

[327] G Bellini et al. Cosmogenic Backgrounds in Borexino at 3800 m water-equivalent depth. *Journal of Cosmology and Astroparticle Physics*, 2013(08):049–049, Aug 2013.

[328] Y. Zhang et al. First measurement of radioactive isotope production through cosmic-ray muon spallation in Super-Kamiokande IV. *Physical Review D*, 93(1), Jan 2016.

[329] T. Hagner et al. Muon induced production of radioactive isotopes in scintillation detectors. *Astropart. Phys.*, 14:33–47, 2000.

[330] S. Abe et al. Production of radioactive isotopes through cosmic muon spallation in KamLAND. *Phys. Rev. C*, 81:025807, Feb 2010.

[331] Marco Grassi et al. Vetoing Cosmogenic Muons in A Large Liquid Scintillator. *JHEP*, 10:032, 2015.

[332] R. Möllenberg et al. Detecting the diffuse supernova neutrino background with LENA. *Phys. Rev. D*, 91:032005, Feb 2015.

[333] J. Heise. The Sanford underground research facility at Homestake. *Journal of Physics: Conference Series*, 2014.

[334] Michael F. L'Annunziata. 7 - Cherenkov Radiation. In Michael F. L'Annunziata, editor, *Radioactivity*, pages 465–495. Elsevier Science B.V., Amsterdam, 2007.

Danksagung

Abschließend möchte ich an dieser Stelle allen DANKE sagen, die zum Entstehen dieser Arbeit beigetragen haben und mir während meiner Doktorandenzeit unterstützend zur Seite standen.

Zuallererst gilt mein Dank Prof. Tobias Lachenmaier für die Möglichkeit diese Arbeit an seinem Lehrstuhl anzufertigen, für sein entgegengebrachtes Vertrauen, die vielen hilfreichen Ratschläge und lehrreichen Diskussionen. Angefangen als Student in den Vorlesungen Physik I und Neutrinophysik, über meine Bachelor- und Masterarbeit bis hin zu meiner Doktorarbeit möchte ich mich sehr für die gute Betreuung bedanken.

Ein weiterer Dank gilt der gesamten Arbeitsgruppe Lachenmaier/Jochum für die sehr hilfreiche Zusammenarbeit und kollegiale Arbeitsatmosphäre auf fachlicher, aber auch freundschaftlicher Ebene. Danke an meinen Zweitbetreuer Prof. Josef Jochum und vielen Dank an Gaby und Günter für die Hilfe bei allen bürokratischen und organisatorischen Fragen.

Mein Dank gilt auch der gesamten deutschen JUNO Forschergruppe für die tolle und interessante Zeit bei den zahlreichen Meetings. Unsere gemeinsamen Reisen nach China, Brüssel, Hamburg, Aachen oder München haben immer sehr viel Spaß gemacht. Ich werde mich sicher noch lange an die Ausflüge zur chinesische Mauer und den Sommerpalast, Basketballspiele in Shanghai, Bootfahren um die Verbotene Stadt oder die gemeinsamen Biere in den Bars dieser Welt erinnern.
Darüber hinaus möchte ich mich auch bei Prof. Michael Wurm und Michael Nieslony von der Uni Mainz für die sehr gute, unkomplizierte und produktive Zusammenarbeit bei den Studien zum THEIA Experiment bedanken.

Ein besonderer Dank gilt auch meinen Bürokollegen Axel Müller, Alexander Tietzsch, Michael Gschwender, Benedict Kaiser und dem externen Büromitglied Andreas Zschocke für die vielen Tipps, Diskussionen und Gespräche über Physik im Allgemeinen und über meine Arbeit im Speziellen. Außerdem ist es mir eine Ehre mit euch die aufstrebenden Sportarten Magnetdart und Regalball erfunden zu haben und Teil der deutschen Magnetdart-Nationalmannschaft zu sein.

Zu guter Letzt ein rießiges Dankeschön an meine Eltern, meine Familie und meine Freunde. Vielen Dank für eure Unterstützung, euren Rückhalt, eure Ratschläge und eure Hilfe bei allem. Danke!